Design, Construction, and Applications of a High-Resolution Terahertz Time-Domain Spectrometer

Thesis by

Daniel B. Holland

In Partial Fulfillment of the Requirements
for the Degree of
Doctor of Philosophy

California Institute of Technology
Pasadena, California

2014
(Defended April 18, 2014)

The effort put into this thesis is dedicated to the person who would have most wanted to read it, but who never had the chance. Thanks for everything, Mom.

Acknowledgments

To my adviser, Professor Geoffrey A. Blake, thank you for your patience, time, and support. I greatly appreciate the freedom you've given me over the past few years to branch out, broaden my interests, and in particular, explore the fields of biology, bio-imaging, and biophysical chemistry that I intend to move into. I hope that we can continue to collaborate—there is much interesting work to be done with THz radiation in physical chemistry, including many applications with biological relevance!

Along the way, I have had the privilege of working with many knowledgeable and helpful colleagues and collaborators, both within and outside of the Blake group. And I'd like to thank them, in no particular order!

My former labmate Matthew Kelley and I have had countless discussions, even good-natured arguments, about various aspects of THz science and technology, and I am better and more knowledgeable for it. I hope that we will have the opportunity to continue our chats occasionally, even if he moves back home to Ohio at some point. Marco Allodi, another Blake group member, has been a great conversation partner for thinking about applying THz spectroscopy to larger molecules and biological systems, and I look forward to consulting with him on this in the future. I also appreciate the discussions with labmates Brandon Carrol and Brett McGuire. And to labmate Ian Finneran, I appreciate our chemical physics discussions, which were a pleasant complement to the technical/instrumental issues I was otherwise having. And these chats turned out to be quite useful, not just for identifying future research directions with the new instrumentation, but also in leading us to realize I already had, in my instrument, a simple solution for one of your microwave problems, thus leading us together to a provisional patent, a conference talk [1], and new instrument paper [2]!

As part of my exploration of biology, Geoff and I set up a collaboration with the group of Prof. Guo in bioengineering and his graduate student Jiun-Yann Yu, to develop a new kind of wide-field, optical-sectioning fluorescence microscopy. This may seem like an odd collaboration, but the high-power laser system used in our THz efforts has more than sufficient power to excite multi-photon fluorescence in microscope samples across a wide field of view; indeed a paper from this collaboration was the first experimental publication based on our THz equipment [3]. This microscopy aspect of biology is perhaps a natural 'entry point' to the field for me, given my experience in developing the THz instrumentation from scratch. And it has been both exciting and an excellent learning experience; we followed up our first collaborative paper with a co-first authored purely theoretical/numerical study on the diffraction-limited imaging performance of our proposed technique [4], and also had a couple of conference presentations of the work [5, 6]. Recent experimental results show significantly improved performance; I hope this collaboration can continue a bit longer to fully realize the potential of the technique.

I'd also like to thank our collaborators on the application of the ASOPS system, Prof. Austin Minnich and Xiangwen Chen. Thank you for helping us to see that this instrument is useful for much more beyond terahertz spectroscopy, and special thanks to Xiangwen for spending a lot of extra time explaining various aspects of the TTR measurements to me!

More recently, I have had the great opportunity to collaborate to a small extent with the research group of Prof. Scott Fraser, particularly with staff scientist Thai Truong, as well as other group members including John Choi, Francesco Cutrale, and Vikas Trivedi. This was also for microscopy development, for a different type of optical sectioning microscopy. Our efforts are still in a somewhat early phase, but have yielded several conference papers/presentations [7–12], and are advancing fast. It was through these recent efforts, in particular, that my scientific interest in the field of immunology was stimulated, and I started to realize, for myself, the experimental potential for model organisms and advanced microscopy techniques to shed light on this important and still not well understood field. So it is with great anticipation that I look forward to starting post-doctoral studies with this group in the very near future! And thank you very much to Prof. Scott Fraser for agreeing to take a chance on me!

I think the Blake group is in very goods hands going forward, I thank you all. And as for a closing thought, I'd like to refer to a quote:

> We have a habit in writing articles published in scientific journals to make the work as finished as possible, to cover up all the tracks, to not worry about the blind alleys or describe how you had the wrong idea first, and so on. So there isn't any place to publish, in a dignified manner, what you actually did in order to get to do the work.
>
> -Richard P. Feynman Nobel Lecture, 1966

I hope that this thesis can, in part, serve as a place to reveal some of our tracks, blind alleys, and wrong ideas, as we moved into the field of THz spectroscopy, and do so in a dignified manner! Now that things are working, it is important to record such things so the experiments can stay working and so that others may build upon them. I look forward to consulting and assisting in the further use of this ASOPS THz-TDS instrumentation.

I would also like to thank my girlfriend Min for all of her love and support; this thesis work would have been much more difficult without her.

And yes, Dad, I'm done (with this step).

Daniel Holland
Pasadena, CA

Abstract

This thesis reports on the design, construction, and initial applications of a high-resolution terahertz time-domain ASOPS spectrometer. The instrument employs asynchronous optical sampling (ASOPS) between two Ti:sapphire ultrafast lasers operating at a repetition rate of approximately 80 MHz, and we thus demonstrate a THz frequency resolution approaching the limit of that repetition rate. This is an order of magnitude improvement in resolution over typical THz time-domain spectrometers. The improved resolution is important for our primary effort of collecting THz spectra for far-infrared astronomy. We report on various spectroscopic applications including the THz rotational spectrum of water, where we achieve a mean frequency error, relative to established line centers, of 27.0 MHz. We also demonstrate application of the THz system to the long-duration observation of a coherent magnon mode in a anti-ferromagnetic yttrium iron oxide ($YFeO_3$) crystal. Furthermore, we apply the all-optical virtual delay line of ASOPS to a transient thermoreflectance experiment for quickly measuring the thermal conductivity of semiconductors.

Contents

Acknowledgments **iv**

Abstract **vi**

List of Figures **xv**

List of Tables **xvi**

1 Introduction to Terahertz Science and Technology **1**

1.1 The Electromagnetic Spectrum and Its Interactions with Matter 1

1.2 Astrochemical Application of THz Spectroscopy 5

1.3 The Modern THz-TDS Experimental Paradigm 7

1.4 THz-TDS in the Blake Lab and My Thesis Work 10

2 ASOPS THz-TDS Instrumentation **12**

2.1 ASOPS: A Virtual Delay Line 16

2.1.1 Overview of Time- and Frequency-Scaling in ASOPS 18

2.1.2 Historical Development and Uses 20

2.2 Overview of the Instrument 22

2.2.1 Ultrafast Lasers Subsystem 26

2.2.2 Asynchronization Control 28

2.2.3 Scan Triggering 28

2.2.4 Delay Scan Calibration 29

2.2.5 THz Pulse Generation 30

2.2.6 THz Spectroscopy Area 30

2.2.7 THz Detection & Recording 31

2.3 Laser Systems and their Repetition Rate Control 32

2.3.1 Instrument Laser Systems 33

2.3.2 Passive Stabilization 34

2.3.3 Instrumental Implementation 35

2.4 Optical Scan Triggering: T0 Detection 38
2.5 Time-Domain Characterization of System Performance with an Optical Cross-Correlator . . 40
2.6 THz Emitter Array 41
2.7 Purge Box and Sampling Handling 43
2.8 THz Routing Optics 44
    2.8.1 ITO dichroic mirror 44
2.9 THz Electro-Optic Detection 45
2.10 EO Balanced Detector 47
2.11 Signal Acquisition 47

3 THz Time Domain Spectroscopy of Water Vapor 50
3.1 The Nature of Time-Domain THz Waveforms 51
    3.1.1 The Superposition Principle 52
    3.1.2 Fourier Analysis 52
    3.1.3 Electric Field Frequency Components and Dielectric Properties 56
    3.1.4 Implementation and Characteristics of the Fourier transform in Spectroscopy 62
        3.1.4.1 Bandwidth and Spectral Resolution 62
3.2 Overview of Experimental Procedure 65
3.3 THz Time-Domain Waveform Preparation 67
    3.3.1 Acquisition of THz-TDS Waveforms 68
        3.3.1.1 Sample Gas Handling 68
        3.3.1.2 Digitizer Acquisition Settings 72
        3.3.1.3 The Acquired Time-Domain Waveforms 73
    3.3.2 Creating a Timebase for THz Waveforms 76
3.4 Discrete Fourier Transform 79
    3.4.1 Numerical Algorithm for Fourier Analysis 79
    3.4.2 The FFT and Measures of Spectral Content 81
    3.4.3 Zero-Padding the Waveform 82
    3.4.4 Selecting the Waveform Time Window 83
    3.4.5 'Windowing': Apodizing the Waveform 86
3.5 Spectrum Analysis 89
    3.5.1 Referencing the Spectrum 90
    3.5.2 Finding Spectral Peak Frequencies 93
    3.5.3 Results of Peak Frequency Analysis 94
    3.5.4 Fitting Spectral Linewidths 98

4 Applications in Materials Science **100**
4.1 Measurement of Thermal Conductivity 100
4.1.1 Experimental Measurement of Phonon Mean Free Paths 101
4.1.2 Experimental Design of an ASOPS-based TTR Instrument 103
4.1.2.1 Pump and Probe Separation by Noncollinear Beams 103
4.1.2.2 Pump and Probe Separation by Polarization 106
4.1.3 Results 108
4.1.4 Future ASOPS TTR Work 109
4.2 Watching a Coherent Magnon in a Spintronics Material 110

5 Future Directions for ASOPS and Higher Resolution THz Spectroscopy **113**
5.1 Technical Improvements to the Blake Group ASOPS THz-TDS Instrument 113
5.1.1 Improve Data Acquisition Averaging Capability 114
5.1.2 Instrument ‘Loop-Stop Code’ 115
5.1.3 Ease of Use Improvements to the Instrument 116
5.1.4 Setup Master Repetition Rate Control 117
5.1.5 Vibration Isolation Through Table-Floating 117
5.1.6 Measure Pulse Durations at Key Points 118
5.1.7 Evaluate Different Detection Crystals and Schemes 118
5.1.8 Monitoring of Nitrogen-Purging in the THz Spectroscopy Area 119
5.1.9 Improve Sample Cell and Gas Handling Apparatus 119
5.2 Scientific Applications for the Blake Group ASOPS THz-TDS Instrument 120
5.2.1 Pseudorotational Modes in THF 120
5.2.2 Laboratory Molecular Astrophysics 120
5.2.3 Additional ASOPS-TTR Measurements 121

APPENDICES **122**

A MATLAB Scripts and Functions **122**
A.1 Script ‘fig_timeWaveform.m’, used to make Figure 3.5 123
A.2 Function ‘asopsRate.m’ 127
A.3 Function ‘timebase.m’ 128
A.4 Script ‘fig_delayWaterFID.m’, used to make Figure 3.6 128
A.5 Script ‘test_timecut.m’ for Evaluating the FFT of Different Scan Durations 132
A.6 Function ‘fft_plus.m’ for Discrete Fourier Transforms 138
A.7 Script ‘test_zeroPad.m’ 141
A.8 Function ‘peakAnalyzer.m’ 145

A.9 Script ‘test_background.m’ 147
A.10 Script ‘test_apodize_field.m’ 152
A.11 MATLAB Code for Linewidth Measurement 158
  A.11.1 Script ‘test_linewidth.m’ for Linewidth Measurement 158
  A.11.2 Function ‘peakOne_createFit.m’ for a Lorentzian Fit to a Peak 159

Bibliography **162**

List of Figures

1.1 The electromagnetic spectrum from radio waves to gamma rays. The THz spectral region is generally defined from 0.1 to 30 THz, or from a wavelength of 3 mm to 10 μm. Various common objects are depicted at top for size reference. The range of human vision, illustrated at lower right, is generally ∼430–770 THz. A few other common electromagnetic frequencies are listed at lower left in both of THz and their 'native' units. 2

1.2 Optical schematic for a typical THz-TDS instrument. Optical excitation for THz emission is provided by an ultrafast Ti:sapphire laser at left (either oscillator or amplified). Time delay for electro-optic sampling of the THz waveform is provided by a mechanical delay stage. EO detection of the THz pulse, at right, in ZnTe or another nonlinear crystal (marked as DETECTOR), enables the use of regular visible photodiodes, also at right. Note: HR = high reflector, SAMPLER = beam sampler, OAPM = off-axis paraboloidal mirror, $\lambda/4$ = quarter-wave plate, and ITO = indium tin oxide dichroic mirror. Figure adapted from [13]. 9

2.1 Mechanical delay lines that physically move a mirror pair(s) to achieve time delay are widely used in THz-TDS and pump-probe experiments. 14

2.2 Comparison of delay sweep rate and range for typical mechanical delay lines (e.g., as shown in Figure 2.1) and ASOPS based on 80 MHz pulsed lasers. The temporal scan range of ASOPS, while fixed, is covered much more rapidly than is possible with traditional delay lines. Guide lines are drawn in for various scan rates; theoretical time resolutions are shown as well. Given the long delays and moderate time resolution requirements of THz-TDS, the ASOPS technique is in a much better position than delay lines in this scan range-sweep rate parameter space. (Figure adapted from [14]) 15

2.3 The ASOPS 'time-scaling' effect, or operating principle. The pump laser (at top), firing at a rate of f_{pump}, generates an ultrafast process. This process is probed (middle row) by a second pulse train, slightly lower in repetition rate by Δf. The original ultrafast waveform is measured in an iterative manner, over the course of an amount of lab time $\frac{1}{\Delta f}$. (Figure adapted from [15]) 17

2.4 The overall optical schematic for the instrument. The ultrafast lasers for pumping THz emission and probing in its detection are shown at left. At right is the enclosure for THz spectroscopic measurements in a controlled environment. That region of the schematic shows the routing optics from the lasers to towards THz generation and detection, as well as the various photodetectors used for monitoring and controlling the instrument. Note that HR = ultrafast, broadband high-reflecting mirrors, OAPM = off-axis paraboloidal mirror, BBO = nonlinear crystal type, PMT = photomultiplier tube and $\lambda/4$, quarter-wave plate. 24

2.5 A picture of the Blake group ASOPS THz-TDS instrument. Most of the instrument's components are located on a single optical table. The dual ultrafast oscillators are at back, center. The THz spectroscopy enclosure is at bottom-right. Routing optics in the center of the figure direct the ultrashort light pulses from the lasers to the THz emitter and detection setups. Portions of those beams are split off or sampled in the central area, for use by the monitor photodiodes and cross-correlator devices for feedback and instrument control. 25

2.6 Schematic of the instrument, as in Figure 2.4, with components grouped into subsystems by functional relationships; the definitions of these subsystems guide the layout of this chapter. Generally, the 'Ultrafast Lasers' and 'Asynchronization Control' subsystems at left work together to supply ultrashort optical pulses to both of the 'THz Pulse Generation' and 'THz Detection & Recording' subsystems at right. The 'THz spectroscopy area' at right includes the sample holder or cell. In the center of the instrument, the 'Scan Triggering' and 'Delay Scan Calibration' subsystems serve to coordinate the acquisition system and ensure the quality of the scans. 27

2.7 Micra laser head internal optics, showing the three actuators available. 33

2.8 The asynchronization circuit that maintains the rep rate offset in the THz-TDS instrument. . . 36

2.9 The noncollinear cross correlator for scan start triggers. 39

2.10 Instrument delay scans can be checked with cross-correlator timings. Repetitive etalon ringdowns, top, are aligned to the first peak, as a start trigger, then the between-scan jitter of later peaks is measured and plotted, at bottom. The upper (blue) line is the RMS jitter in picoseconds; the lower (red) line is a measure of the error in the fitting of the peak centers and should remain below the jitter measurements. 42

2.11 The electro-optic detection and recording subsystem; the path of the probe laser beam towards the balanced detector is shown in orange-red. 46

3.1 A water vapor THz-TDS time-domain waveform, with the sample duration, T, and sampling time Δt illustrated. 66

3.2 The overall experimental procedure in terms of the collection, processing and analysis of THz waveforms. There are three general areas of work, as shown in the shaded boxes. The THz time-domain waveforms are first acquired and prepared for subsequent Fourier transform to the frequency domain, followed by various spectral analyses. 67

3.3 The schematic of the gas handling apparatus. Note the optical input of pump and probe beams at left, as shown further in Figure 2.4. A sample cell is inserted between the two 4f telescopes for minimal beam size. A network of tubing and valves connects the sample cell to a pressure gauge, sample reservoir, and vacuum pumps, as described further in the main text. 70

3.4 Picture of the gas handling apparatus diagrammed in Figure 3.3, with a common labeling scheme; this view is from the bottom side of that figure. Note the placement of the cell between the two OAPMs at right, and its optically opaque polyethylene windows. The gas tubing at right is normally connected to each of a gauge and the sample reservoir and vacuum pumps (not shown). This picture is taken through the clear wall of the nitrogen-purge box (note the box latches at top). 71

3.5 A THz-TDS time-domain waveform of water vapor, from the balanced detector scheme. The inset provides a much zoomed-in view of the first THz pulse at left. Even in the inset, though, the limited dynamic range of the printed image prevents a clear view of the small signal-dependent oscillations after the initial pulse. The secondary peak at right is a reflection, and is described further in the main text. 74

3.6 The time-domain THz waveform for both of water vapor and a reference scan. The main view is zoomed-in to the period at and just after the main THz pulse. The inset shows a further-zoomed period, just after the main pulse, so as to clearly show the continued THz-frequency ringing from the water vapor. 78

3.7 Comparison of zero-padding levels upon a water vapor spectrum. Higher levels provide increasingly dense interpolation of the frequency-domain data, with the highest level shown providing more than adequate coverage of the peak shape given the sample peak linewidth. . . . 84

3.8 A time-domain THz waveform from a water vapor sample. Different extents of the delay scan are highlighted, with shorter extents plotted over the longer durations of the scan. These different durations of the waveform are each Fourier transformed, with their spectra plotted in 3.9, to look for duration-dependent changes in the FFT result, particularly upon inclusion of the reflection pulse at ∼6500 ps. Note that the y-axis is zoomed so as to clip the full extent of the main THz pulse. 86

3.9 The water vapor FFT results from the differing extents of scan duration that were illustrated in Figure 3.8 (colors matched between figures). The shorter scans generally have less frequency-domain ringing, albeit at a cost of instrument spectral resolution. See the main text for further details. 87

3.10 Windowing in the time domain. The waveform is the THz signal from water vapor, shortly after the main THz peak. A Hanning window type is illustrated on the scale at right, and the resulting, windowed waveform shown over the original data. 88

3.11 Frequency domain results of the time-domain windowing performed in Figure 3.10. Note that the time range considered excludes the main THz peak, so these spectral peaks derive only from the later ringing signal from the water vapor, and no referencing has been performed. . . 89

3.12 Comparison of water vapor and reference spectra; note the sharp water vapor absorption lines dipping down beneath the curve of the reference spectrum. Both sample and reference have a wavy baseline, likely from multiple THz pulse reflections in the instrument. The baseline largely divides out between sample and reference, as shown in the referenced spectrum in Figure 3.13 91

3.13 A referenced water vapor spectrum, the result of dividing the relative power of the water vapor and reference scans of Figure 3.12. The wavy baseline of the un-referenced data has disappeared. The noise levels are low enough for productive measurement of water vapor rotational transitions in the range of ∼0.25-2.6 THz. 92

3.14 The experimental THz-TDS spectrum of water vapor, from 0.5-2 THz, plotted to show the peak center frequencies. The peak centers are found by using a high level of zero-padding in the FFT so as to interpolate the frequency-domain data, then locating maximum values. 95

3.15 The experimental THz-TDS spectrum of water vapor, continued from Figure 3.14, to show the 2-2.5 THz spectral region and the peak center frequencies in the range. The noise levels are slightly higher, relative to the 0.5-2 THz region, but peak centers are nonetheless easily found. 95

3.16 Lorentzian fit to a water vapor peak, obtained from a long (10,000 ps) waveform and zero-padding only to the next power of 2 in the scan record length. The linewidth was fitted as 98.8 MHz; see main text for further details. 99

4.1 A traditional TTR instrument, as employed in the Minnich lab. Pump-probe delays are achieved via the use of a long range, quadruple-pass optical delay line; the beam is magnified for the delay line, to minimize delay-dependent changes in laser spot size. The optical pump pulses are doubled in a nonlinear crystal (BIBO) to enable clean spectral rejection of these pulses in the detection of the 800 nm probe pulses. (Figure courtesy of Xiangwen Chen) 102

4.2 The complete ASOPS-based TTR instrument. The pump and probe beams of the ASOPS system (optical beams, before THz emission) are redirected to the TTR system, at bottom. Note that the two beam colors are for the reader's ease; the pulses are of the same wavelength. Separation of pump and pump in reflection from the sample is achieved via different angles of incidence and spatial filtering. 105

4.3 The newer version of the ASOPS-based TTR instrument, now in a collinear pump-probe geometry. The pump and probe beams of the ASOPS system (optical beams, before THz emission) are redirected to the TTR system as before (with the ASOPS synchronization as before). The two beam colors are of the same wavelength, as in Figure 4.2. Separation of pump and pump in reflection from the sample, though, is now achieved based on cross-polarization of the two beams with respect to each other. 107

4.4 The result of the fitting routines for the transient thermoreflectance time-domain data; the sample is GaAs. The experimental data is plotted in red, with the original sharp rise from the pump pulse excluded from the analysis. See text for details. 109

4.5 Time-Domain plot of the $YFeO_3$ emission; most of the original THz pulse is excluded here. This waveform has been further processed - see main text. It appears that multiple reflections in the instrument may be piling up on each other in the time domain. Nonetheless, the emission can be seen to continue for longer than the 60 ps previously reported [16]. 112

4.6 The spectrum of the $YFeO_3$ emission time-domain data in Figure 4.5. The longer time-domain scan possible with the present instrument is indeed useful for accurate characterization of the long-term coherent emission. Further improvements to the instrument signal levels and scan processing will be of help. 112

List of Tables

1.1 Basic time, energy, and wavelength characteristics of various terahertz frequencies. Terahertz oscillations are generally classified as having picosecond and sub-picosecond timescales, wavenumbers in the range of several tens of cm^{-1}, wavelengths in the several 10s of microns, and photon energies in milli-electron volts. 3
1.2 Physical-chemical phenomena with terahertz/far-IR spectra. Table from [17] 4

3.1 A comparison of the presently determined peak frequencies for water vapor to accepted values from the HITRAN database [18]. Note that the 'line number' field is for internal reference. The transition notation is JK_aK_c. The average frequency deviation between the new centers and those in HITRAN is approximately 27.0 MHz. 96

Chapter 1

Introduction to Terahertz Science and Technology

Research in the Blake group spans chemical physics to laboratory astrophysics and astrochemical modeling. The focus of this thesis is upon the design, development and application of a broadband but high resolution time domain spectrometer in support of this research. More specifically, this thesis is concerned with terahertz or far-IR spectroscopy, generally for far-IR rotational and torsional transitions. As such, we open with a discussion of the electromagnetic spectrum, with an emphasis on the terahertz region and its interactions with matter.

1.1 The Electromagnetic Spectrum and Its Interactions with Matter

The electromagnetic spectrum is an infinite span of frequencies and wavelengths, ranging over the possible energies of light. This spectrum, from radio waves to gamma rays, is illustrated in Figure 1.1. The terahertz region falls into the middle of this figure, and is generally defined from 0.1 to 30 THz; it is sometimes defined from 0.1 to 10 THz, with the specific limits used in the research literature often depending on the techniques and applications favored by the author. This frequency range for terahertz waves is associated with a wavelength range of 3 mm to 10 μm, such that this radiation has a characteristic size comparable to that of biological cells or small tissues. As a familiar point of comparison, the range of human vision extends from 390 nm to 700 nm, or about 770 THz to 430 THz. In this regard, the units of THz are a convenient, viable replacement for replacing other commonly used units of frequency or wavelength (note that the author may be biased in this regard).

Looking more closely at the terahertz region, in Table 1.1, we list the characteristics of various THz wavelengths, in terms of energy, period, etc. (the wavelengths chosen are often given as the edges of various areas of study). We see that terahertz-range electromagnetic oscillations occur on a picosecond or sub-picosecond

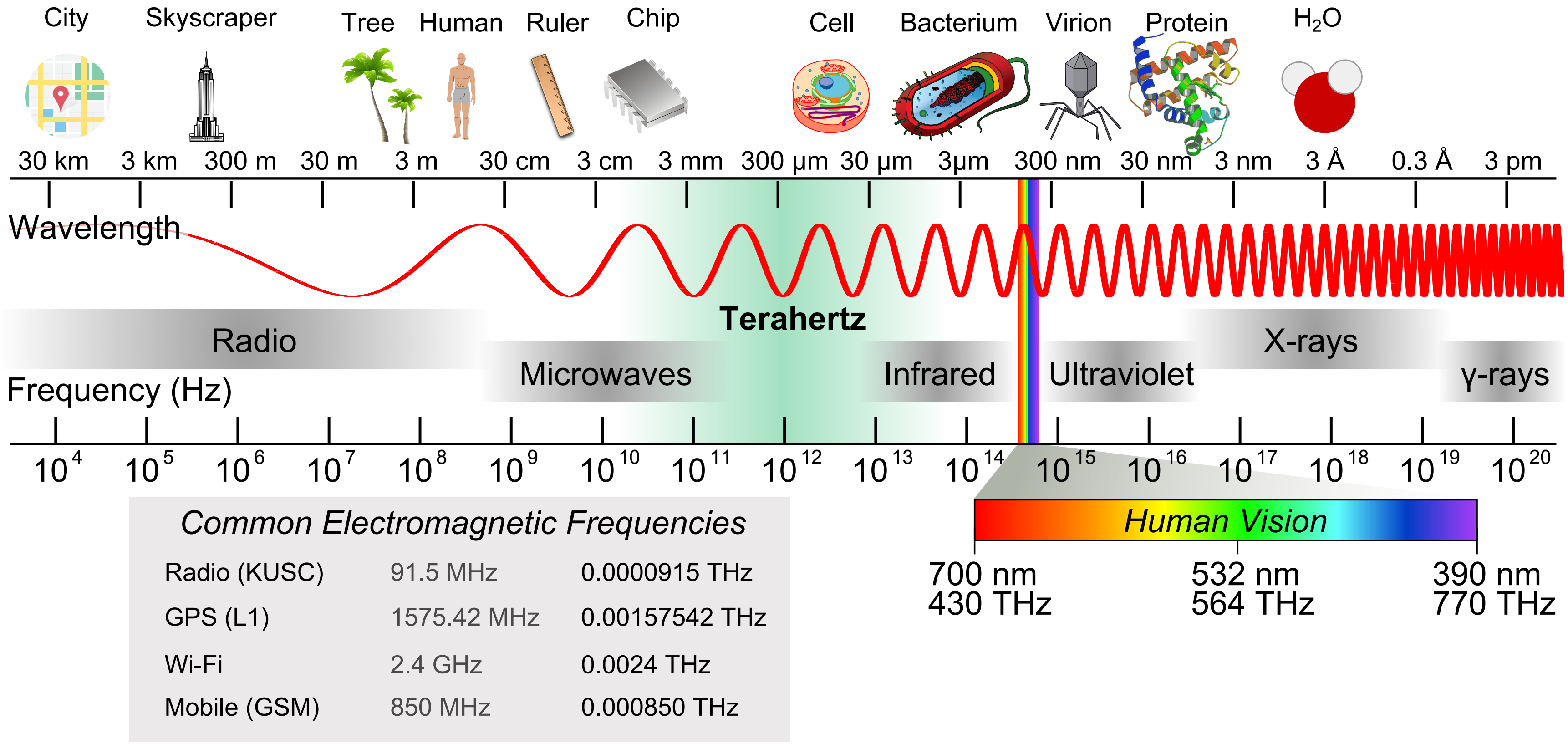

Common Electromagnetic Frequencies

Radio (KUSC)	91.5 MHz	0.0000915 THz
GPS (L1)	1575.42 MHz	0.00157542 THz
Wi-Fi	2.4 GHz	0.0024 THz
Mobile (GSM)	850 MHz	0.000850 THz

Figure 1.1: The electromagnetic spectrum from radio waves to gamma rays. The THz spectral region is generally defined from 0.1 to 30 THz, or from a wavelength of 3 mm to 10 μm. Various common objects are depicted at top for size reference. The range of human vision, illustrated at lower right, is generally ∼430–770 THz. A few other common electromagnetic frequencies are listed at lower left in both of THz and their 'native' units.

THz Frequency	0.1 THz	0.3 THz	1 THz	3 THz	10 THz	30 THz
Frequency (GHz)	100	300	1000	3000	10000	30000
Cycle Period (ps)	100	3.33	1	0.33	0.1	0.033
Wavenumber (cm-1)	3.33	10.01	33.36	100.07	333.56	1000.69
Wavelength (um)	2997.92	999.31	299.79	99.93	29.98	9.99
Photon Energy	0.41	1.24	4.14	12.41	41.36	124.07

Table 1.1: Basic time, energy, and wavelength characteristics of various terahertz frequencies. Terahertz oscillations are generally classified as having picosecond and sub-picosecond timescales, wavenumbers in the range of several tens of cm^{-1}, wavelengths in the several 10s of microns, and photon energies in milli-electron volts.

timescale and a length scale spanning from a few millimeters or few thousand microns to just several microns. Terahertz waves are rather low energy compared to visible light, having only milli-electron volt energies instead of simply electron volts of energy. Despite their small energies, though, terahertz photons are of great importance in the sciences!

The different energies of photons across the electromagnetic spectrum provide a convenient basis upon which to divide or discuss the spectrum in terms of its characteristic resonant interactions with matter. For example, gamma rays are associated with nuclear transitions, ultraviolet light with electronic transitions, while visible light is typically associated with both electronic transitions and vibrational overtones [19]. There are of course, exceptions to the these general trends, but they nonetheless provide a useful way to think about the electromagnetic spectrum. Moving lower in frequency, the infrared spectral region is generally characteristic of molecular vibrations, while the microwave and radio regions are typically associated with transitions between molecular rotational states for gas phase samples.

In between the infrared and microwave regions of the spectrum is the terahertz region. It is worth noting that the terminology in this region of the spectrum has changed over the past several years. Just above the THz region, the infrared (IR) region has typically been divided into three sub-regions: the near-, mid-, and far-IR. These spectral regions are typically noted as spanning 120-400 THz, 30-120 THz, and 0.3-30 THz, respectively. Historically, then, what we presently call the terahertz region has been known simply as the ‘far-IR’. Indeed, this name is still widely, perhaps even predominantly used in place of ‘terahertz’. In general, the terms of ‘far-IR’ and ’terahertz’ are interchangeable. The choice to use one term or the other is often driven by the type of instrumentation used. For example, if one is performing spectroscopy in this spectral region with the use of a Fourier-transform infrared (FT-IR) spectrometer, the use of the ‘far-IR’ term may be prevalent, whereas if one is using the time-domain methods that are the focus of this work, then the term ’terahertz’ is generally used.

Regardless of the terminology employed, far-IR or terahertz radiation probes low energy light-matter interactions, including phonons in solids, rotational transitions in molecules, and soft vibrational modes in

Type of Terahertz-related phenomena	Example
Regular (nearly harmonic) vibrations	$AsBr_3$
Slightly hindered internal rotations	H_3C-CHO (acetaldehyde)
Inversions	H_2N-CHO (formamide)
Puckering of nearly planar rings	cyclopentene
Hydrogen bonding	$(CH_3)_2O$-$HONO_2$ (nitric acid, dimethyl ether complex)
Molecular rotation in gases	H_2S_2 (hydrogen disulfide)
Dipole-dipole absorption	Polar liquids
Phonons (lattice modes)	Most crystals

Table 1.2: Physical-chemical phenomena with terahertz/far-IR spectra. Table from [17]

large molecules or weakly bound clusters and hydrogen-bonding interactions. As a very general guide, a list of various sources of terahertz/far-IR spectral features is provided in Table 1.2, derived from [17], and discussed briefly herein.

For example, in terms of 'regular' intramolecular vibrations, for the associated transitions to fall into the relatively low frequency terahertz region, the vibrations must be of large-mass atoms and/or be associated with small restoring forces [17]; inorganic molecules with single bonds are often a good example. In terms of small molecules (and of more relevance to the present instrumentation), hindered internal rotations fall into the THz region. This is the term for the rotation of a small group, such as a methyl group, relative to another, asymmetric part of the same molecule (e.g., the methyl group in acetaldehyde, H3C-CHO). This rotation environment can create a periodic n-fold (here 3-fold) potential barrier; spectroscopy can reveal the shape of the potential curve and the height of the barrier. Inversions and the puckering of planar rings also yield terahertz spectral features; spectroscopy here can also help to characterize the potential curve and this is an area likely to be pursued within the Blake group using the present instrument.

Hydrogen-bonding, particularly involving heavy atoms, may produce terahertz absorption though the features would generally be >3 THz in the 'high' range of the terahertz region. Dipole-dipole absorption in liquids, and phonons or lattice modes in crystalline solids can also absorb in the far-IR/terahertz region. Of particular relevance to the present work, molecular rotation in gases also produces terahertz-range spectral features. Rotational transitions typically have very low energy ($< 10\,\text{cm}^{-1}$) and thus show up in the microwave region; indeed, microwave rotational spectroscopy is an area in which the Blake lab has significant experience. However, if a molecule has a permanent dipole moment and at least one of its moments of inertia is small, it will have high-lying rotational transitions, including into the terahertz-region. For example, the rotational spectroscopy of water was performed with the present instrument and is described in Chapter 3. Overall, the above list by no means covers all physical-chemical interactions that may result in the absorption of terahertz light; but clearly we can already see that many aspects of nature are meant to be viewed in this spectral region. In particular, we note that molecular rotation spectra and hindered internal rotations are of particular importance to the Blake group and underlie much of our previous microwave-region, laboratory astrophysics work. These sources of terahertz spectra will continue, in large part, to guide our future terahertz studies with the present instrumentation.

1.2 Astrochemical Application of THz Spectroscopy

Terahertz spectroscopy is of central importance in the remote sensing necessary to characterize astronomical and (exo)planetary environments. For example, in the dense regions of the interstellar medium (ISM) where stars are born, dust grains of sub-micron size scatter visible and ultraviolet light. The clouds become optically opaque and and their internal temperatures are reduced to $\lesssim$30 K. In this temperature range, the clouds' thermal radiation peaks in the far-IR. Further, the clouds are optically thin only at longer wavelengths [20]. Overall, then, THz light is often an informative probe, and sometimes the only such probe, for these astronomical environments of importance to understanding our own solar system and its formation.

Indeed, it is the understanding of our own planetary system and place in the universe that makes terahertz spectroscopy so attractive to astronomers, and which provides a primary motivation for the development of the present instrumentation. Within the field of astrochemistry, researchers engage in 'astrochemical modeling', wherein they use spectral lines in astronomical objects to try to figure out their chemical composition; the molecular line shapes and strengths can also reveal physical information. They can then use knowledge of the physical environment (e.g., temperature, radiation, ice/dust grains) to predict what other chemical species may be present, given the possible reaction networks. They can generate calculated spectra, from their models, to match against observed values, and they can search for new, predicted species. The Blake group in particular is interested in this type of modeling and analysis as it applies to protoplanetary disks, including their formation, the accretion of planets, and where water and other molecular material forms before delivery to early planetesimals and protoplanets. Broadly speaking, the general question is one of the physical and chemical evolution of solar systems. Further, an important question driving such research is how far reaction networks can move towards producing molecules typically associated with life, such as sugars and amino acids. This question of the extent of *pre-biotic chemistry* informs theories on the origin of life on Earth [21] as well as the probability of there being life elsewhere in the universe.

Astronomical observations, coupled with laboratory astrophysics and spectroscopy, have been very successful in identifying molecules in outer space. Focusing on the 'submillimeter' (i.e., low terahertz) and 'millimeter' frequency range most familiar to our group, this kind of rotational spectroscopy has been studied since the early 1950s [22] [23] and now more than 150 different molecules, including some of up to 13 or more atoms, have been found in the ISM. In an interesting problem, it appears that that in dense clouds, there are *too many transitions*. While there appear to be many complex organics in these clouds (e.g., [24]), there are so many lines in the spectrum that they start to overlap and one reaches the 'line confusion limit' where it is difficult to make any assignments and progress further. So it is exciting to realize that pre-biotic chemistry can become quite complex even before the development of planets; some of these materials may have reached Earth's surface by impact or dust and may have been involved with the start of life on Earth [21]. However, astronomers and chemists would very much like to be able to solve the mystery of all of the compounds that are present and to understand their physical and chemical evolution.

By moving into the terahertz spectroscopy of astronomical features, astronomers hope to be able to avoid line confusion; it is believed that for Boltzmann-like population distributions, that the line density may decrease at high frequencies of spectral transitions. High-lying rotation transitions of smaller molecules and the softest terahertz vibrational modes of organic compounds may therefore allow better insight into pre-biotic chemistry. The gas phase torsional bands of complex molecules should offer specificity in assignment. Results from a new far-IR space-based telescope lend support the idea of decreasing line densities at higher frequencies; a study of the Orion KL nebula found that 23% of the frequency space from $\sim$858-958 GHz was occupied by lines while only 7% of frequency space from $\sim$1788-1898 GHz was occupied [25].

One of the factors behind the line confusion in lower-frequency measurements, besides simply the presence of many different species, is that larger molecules tend to have more lines per molecule. Less than $\sim$10% of the molecules found in the ISM have $>$10 atoms—this is a problem as the larger, more complex molecules are naturally more interesting in terms of charting the progress of complexity in pre-biotic chemistry. Based on the theory of rotational spectroscopy [19], as molecules become more complex and likely create asymmetries among their moments of inertia, their energy levels become more complicated and more transitions are allowed. These energy levels can be further split by two phenomena noted earlier on Table 1.2, those of the internal rotation of a methyl group, as well as inversion. These additional lines and splittings serve to make the spectra more complex, with more lines placed closely together in frequency space. The problem is further exacerbated by the fact that with more states available, there will be fewer molecules partitioned into each state and thus the peaks will be weaker.

These problems, and the potential terahertz solution, have been recognized for many years in the field of astronomy. And a new generation of telescopes that can see into the far-IR has been built. These include three main new telescopes: the Herschel Space telescope, the Stratospheric Observatory for Infrared Astronomy (SOFIA), and the Atacama Large Millimeter/sub-millimeter Array (ALMA). Between these telescopes, there is spectral coverage from the sub-THz to $\sim$6 THz with spectral resolutions, depending on the frequency range, which are often sub-MHz. A major obstacle now at this point in the progress of the field is that most of the pre-biotic molecules considered do not yet have lab spectra for fitting or comparison purposes with the astronomical data. New instrumentation for laboratory astrophysics is needed so that the datasets produced by these telescopes can be put to full use, and that is a primary motivation for the present work.

1.3 The Modern THz-TDS Experimental Paradigm

The terahertz spectral region, long recognized to be full of scientific promise, has historically suffered technical challenges in terms of robust, bright and tunable sources and sensitive detectors [26]. This has led many researchers to speak of a 'terahertz gap', a hole in our technological capabilities to access the electromagnetic spectrum. This may be something of an exaggeration, as far-IR dispersive and FT-IR instruments, as well as sub-mm astronomy receivers, for example, have been working in the terahertz region for decades. So perhaps as suggested by a leading terahertz researcher, Professor Charles Schmuttenmaer of Yale University, the term 'terahertz dip' is more appropriate. Nonetheless, for many years there was an acknowledged deficit in terms of technology to access and control this spectral region, and difficulties in moving beyond that point.

Fortunately, scientific and technical advances in the past decade have substantially raised the performance of terahertz instrumentation. During this time, the technique of terahertz time-domain spectroscopy (THz-TDS) has made great advances in bandwidth, sensitivity and widespread acceptance. As the name of the technique implies, terahertz signals are detected directly in the time domain in a pump-probe experiment. The terahertz light is created as ultrashort, near-single cycle pulses on a ∼picosecond timescale. And it is the electric field itself, not the time-averaged power, of the ultrashort terahertz pulses that is measured before and after passage through a sample. This is a radical departure from the use of traditional square-law detectors.

The science and technology of THz-TDS are well reviewed in the literature [13], [26], [27]. To advance our discussion, a schematic of a typical THz-TDS instrument is shown in Figure 1.2. This time-domain implementation of THz spectroscopy is the most commonly used coherent THz technique and the majority of instruments are variations on that shown in the figure. As pictured there, an ultrafast/ultrashort Ti:sapphire laser provides the optical excitation necessary to drive the THz emitter. Most researchers use THz-TDS systems based upon commercially available ultrafast lasers, with average powers of typically a few watts or less, pulse durations of between ∼15-150 femtoseconds, center wavelength of 800 nm and high repetition rates of ∼80 MHz, yielding nanojoule-class pulse energies. However, the strongest THz fields (e.g., [28]), are generated from amplified Ti:sapphire lasers, also commercially available, which trade repetition rate down to ∼1 kHz for pulse energies into the 10s of millijoule range, while maintaining durations as short as <30 fs! These higher peak power pulses lend themselves to much more efficiency in nonlinear optical processes and can product THz fields having >1 MV/cm strength vs., for comparison, the ∼kV/cm (or far less) fields of un-amplified systems. The present discussion concerns itself with the oscillators (i.e., un-amplified lasers) as these were used in the current research; we return to this comparison in §1.4.

Returning to the emitters, we note that there are a variety of types available, producing single-cycle THz pulses, with most devices generally falling into one of two categories: a nonlinear crystal (typically ZnTe [29] [30], or GaP [31]) for optical rectification of the laser pulse down to the THz range, or a photoconductive (PC) emitter [32] for impulsive THz generation (see §2.6 for further details). A portion of the same laser beam used for optical THz generation is sampled and delayed with respect to the THz generation. Given the finite speed of light ($\sim$1 foot/second), optical delay is accomplished with a motorized delay line—simply a moving stage with mirrors to increase the optical pathlength in one arm of the experiment so as to achieve fine (sub-picosecond) time delays (note that the delay line can be in either optical arm). The delayed light is passed to a THz detector co-axially with the THz pulse to be detected. Detectors, as with emitters, can be based on nonlinear crystals or PC devices. In either case, the short, delayed optical pulse (short relative to a THz cycle) optically gates a small portion in time of the THz pulse for detection; in a PC detector, the gating pulse allows the pulsed THz electric field to induce an electrical current for the short time duration of the gating pulse (typically tens of femtoseconds or less). In crystal detectors, the pulsed THz field induces a slight polarization change on the gate pulse, as detected by the polarizer analyzer in the figure. This process is referred to as electro-optic detection, and is discussed further in §2.9.

In all experimental cases described above, the THz waveform is repetitively produced and the delay line is scanned so as to acquire a measurement at all moments of time of the waveform (typical total scan duration is on the order of roughly 50 picoseconds or less). The acquired waveform is then numerically Fourier transformed on a host computer, so as to recover the frequency-domain spectrum. Further details on the nature and processing of the THz waveforms are presented in §3.1 and §3.2, respectively. One of the most significant features of THz-TDS to note, though, is that the transformed spectra are *complex* spectra—they have both amplitude and phase components. It is therefore possible to obtain the full dielectric response of a sample, including both of absorption and refractive index. Further, and of relevance to laboratory astrophysics, these related techniques offer far superior dynamic range as compared to traditional dispersive and FT-IR instruments in this frequency range. THz-TDS signals reaching well in excess of 60 dB in dynamic range in power measurements are routine—this is approximately four orders of magnitude beyond traditional FT-IR instruments, thus offering a much better chance of detecting weak signals and/or collecting scans in a technically feasible acquisition time.

Two of the factors that have traditionally troubled far-IR spectroscopy are the responsivity of the far-IR detectors. And secondly, the source brightness, including the limited emission of blackbody light sources or

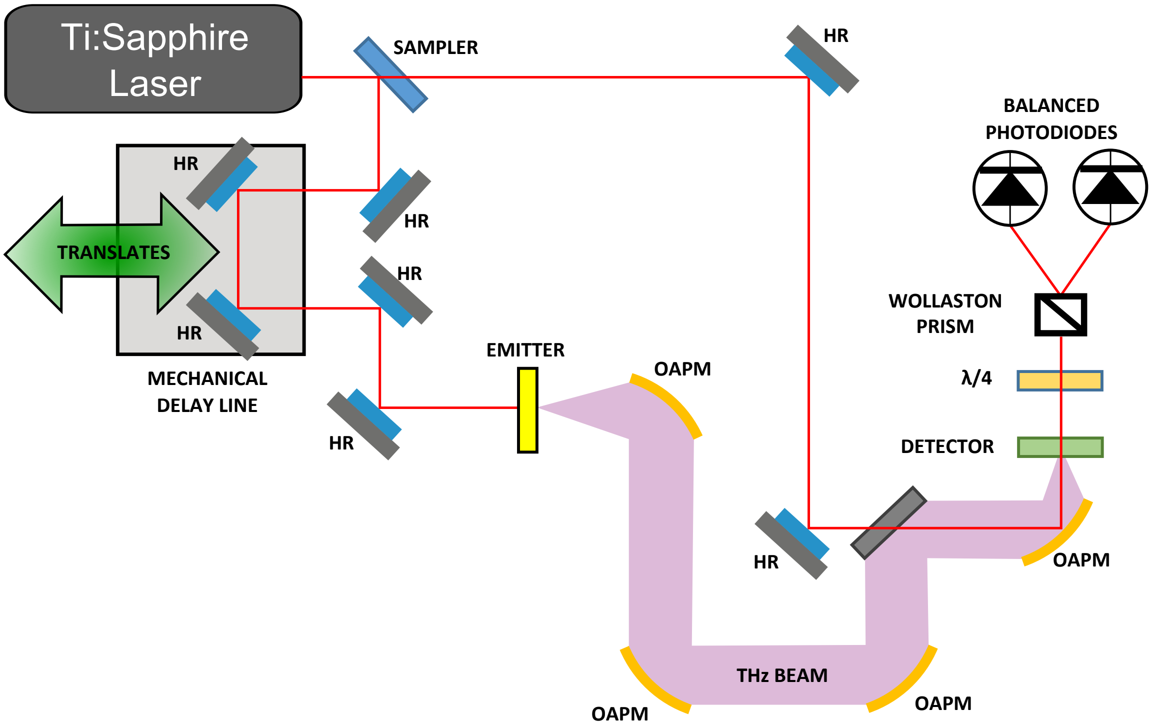

Figure 1.2: Optical schematic for a typical THz-TDS instrument. Optical excitation for THz emission is provided by an ultrafast Ti:sapphire laser at left (either oscillator or amplified). Time delay for electro-optic sampling of the THz waveform is provided by a mechanical delay stage. EO detection of the THz pulse, at right, in ZnTe or another nonlinear crystal (marked as DETECTOR), enables the use of regular visible photodiodes, also at right. Note: HR = high reflector, SAMPLER = beam sampler, OAPM = off-axis paraboloidal mirror, $\lambda/4$ = quarter-wave plate, and ITO = indium tin oxide dichroic mirror. Figure adapted from [13].

the limited wavelengths and technical issues of far-infrared lasers. These issues have been addressed in the development of THz-TDS over the past 30 years with significant improvements in speed, sensitivity, and the technique's user base in the last decade. The resulting benefits can indeed be applied for productive laboratory astrophysics, as our group has recently demonstrated [33]. Even in early THz-TDS technique development papers (e.g., [34], [35]), the exceptional brightness and sensitivity of electro-optic THz sources and detectors was well recognized, with signal-to-noise ratios in the electric field measurements reaching 10000:1 with average THz powers of 10 nW and total acquisition times of just a few minutes; the unity signal-to-noise ratio corresponded to an average THz power of 10^{-16}W! This level of performance, in terms of average power, has been found to exceed the sensitivity of liquid helium-cooled bolometers by more than three orders of magnitude [36], and with no thermal background issues due to the gated and coherent detection in time; these factors contribute to such THz-TDS techniques enabling some of the most accurate absorption cross sections in the far-IR. A direct comparison between the FT-IR and THz-TDS techniques was reported in 2001 [37], finding a crossover point between the two techniques in the range of 3-5 THz. In the previous decade, advances in nonlinear crystals and amplified laser systems are such that this crossover point can reasonably be moved out to higher frequencies.

1.4 THz-TDS in the Blake Lab and My Thesis Work

In the Blake lab we were fortunate to receive support from the National Science Foundation Chemistry Research Instrumentation & Facilities: Instrument Development (CRIF:ID) program, as well as from the National Aeronautics and Space Administration Laboratory Astrophysics program. These funding sources enabled us to build up a strong capability in terahertz time-domain spectroscopy. In terms of major equipment, this capability includes both of oscillator-based and amplified THz-TDS instruments. The initial version of the amplifier-based system was a traditional THz-TDS instrument, much as shown in Figure 1.2. However, it has since been heavily modified to take advantage of higher-power, better bandwidth THz sources to explore nonlinear terahertz spectroscopy. That latter topic is beyond the scope of the present document; the interested reader should look forward to the theses of Marco Allodi and Ian Finneran!

In addition to the traditional THz-TDS instrumentation and variations thereof, we embarked on a project to create a higher-resolution THz-TDS instrument to support the group's efforts in laboratory astrophysics and spectroscopy. As is discussed in much further detail in chapter 2, traditional THz instruments with mechanical delay lines can only scan so far, and thus, because of the Fourier transform time-to-resolution relationship, these mechanical delay line systems generally are limited to low spectral resolution. In practice in our lab, a resolution of $\sim$20 GHz is considered fine. And it indeed is, for condensed phase samples, in particular the model interstellar ices studied to date [38] [33].

However, for gas phase spectroscopy, transitions are much narrower and peaks must be much better localized. And the main goal is to be able to provide spectral line data that will help us to figure out what we are seeing in the spectra sent to us from the Herschel, ALMA, and SOFIA observatories. These instruments have resolutions better than 1 MHz in many bands! In this case, resolution measured in GHz is simple not sufficient. This thesis therefore concerns the development and application of a higher-resolution terahertz time-domain spectrometer, with a resolution intended to reach 100 MHz and perhaps exceed it. To do this, in short for now, we remove the mechanical delay line of Figure 1.2 and all of its limitations of length and speed, and instead add a second laser. This second laser is precisely *asynchronized* with respect to the firing rate of the other, so that with one laser as pump and one as probe, we create a repetitive phase walk-out between the two: a virtual delay line. This instrument is known as an Asynchronous Optical Sampling THz-TDS or ASOPS THz-TDS.

The bulk of the author's present thesis work has been as the sole developer of the present ASOPS THz-TDS instrument. This, and the amplified THz system, are major instrumentation building projects and represent a foray by the Blake group into the previously unfamiliar (to us) areas of ultrafast optics and optically-pumped THz generation, and it is thus a break from the groups earlier electronic synthesizer-based mm-wave and microwave work, as well as diode laser-based near-IR work. The present ASOPS THz-TDS instrument has been built and demonstrated to work, as discussed herein. In collaboration with the research group of Prof. Austin Minnich in mechanical engineering, the all-optical aspects of the instrumentation, as a 'virtual' pump-probe delay line, have been utilized in the measurement of thermal conductivities in semiconductors via a transient thermoreflectance technique; this is discussed in §4.1. And with help from Prof. Jongseok Lee of GIST in S. Korea, we used the ASOPS THZ-TDS instrument to observe the coherent magnon mode of a candidate spintronics material, discussed in §4.2. While the development and initial application of this instrumentation form the bulk of the present thesis work, it is intended that my spectrometer will be a 'work-horse' science instrument for the Blake group for years to come.

Chapter 2

ASOPS THz-TDS Instrumentation

Time-domain THz spectroscopy is essentially an ultrafast, sub-picosecond timescale pump-probe experiment. An ultrashort pump pulse generates a propagating THz transient waveform, and another ultrashort probe pulse interrogates that THz pulse in a nonlinear crystal. By incrementing the pump to probe delay time over and over across the repeating time-domain THz waveform, we can iteratively recover the original THz waveform. Upon a Fourier transform from the time domain to frequency domain, we recover the spectral content of the pulse under the experimental conditions. The precise pump-probe delay scan is inherent in the technique and critical for accurate recovery of the spectral information. To the the extent that we can get more precision, increases in delay time and improvements to the speed of the delay sweeps, we can improve the THz measurement process.

To achieve high resolution spectra in a time-domain technique, we require long optical delays. There are various ways of scanning such time delays, each with a characteristic rate of delay time sampled per unit of laboratory or 'real' time. For example, we may say that a particular delay scanning technique can achieve a sweep of one nanosecond of pump-probe delay time for every millisecond of real time in the laboratory. Importantly, delay scanning methods are also characterized by the total delay scan range they can carry out in each sweep—that is, can a method provide 50 picoseconds of pump to probe delay time at most? Perhaps 10 nanoseconds? There are orders of magnitude of time differences available between techniques, so these are important questions to tailor to one's experimental needs. Further, delay scanning techniques are characterized by an overall sweep rate describing how fast their complete delay sweeps can be repeated. This tells us the round-trip time for the scanning and how fast we can get another scan to co-add or average, or to record so we can see a change in lab time between subsequent delay scans, as part of some dynamical process.

There are many interesting technologies available for optical delays [14], including linearly moving mirrors, rotating mirror pairs, rotating glass blocks, and voice-coil types of devices (also known as 'shakers', basically mirrors on vibrating membranes or acoustic speakers). These methods are collected referred to as being 'optomechanical' in their nature, as they all involve physically or mechanically moving optical elements, so as to change the relative optical pathlengths traversed by each of pump and probe beams. The delay line most commonly used in ultrafast delay scanning methods in general, is that of the mechanical delay line. This is simply a pair of mirrors on a moving stage; two examples of such delay lines are illustrated in Figure 2.1. Here, in Figure 2.1a at left, we see a type of delay line typically used in traditional THz-TDS instruments. It has a travel range on the order of a few inches. The small moving stage is large enough for two mirrors to be mounted to its surface. As shown in the figure, a laser beam can, for example, reflect from the mirror at top, left of center, travel down the page towards the left-side mirror on the delay stage. The light beam is reflected across the small moving stage, and back up the page to another optic at top, right of center and onwards from there. As the delay stage is moved backwards, the light pulses must travel longer in time to reach the moving stages' mirrors and to reflect all of the way back on the opposite side. Given the finite speed of light, $\sim$1 foot per nanosecond, and a double-pass arrangement (i.e., the beam travels down and then back up) as shown, with 6 inches of travel one would achieve a total of 1 foot of delay or about 1 nanosecond of delay time. At right in Figure 2.1, we see a much larger delay line; it is about a meter in length and sufficiently wide enough to enable 4 passes of light for a quadrupling of its available delay line—this model enables up to $\sim$13 nanoseconds of optical delay. Overall, these optomechanical delay systems generally can achieve step sizes of 100 nm or less, enabling delay steps of $\sim$1 fs or less. However, as the delays grow longer and additional passes on the delay line are utilized, the laser beam can become defocused, causing changes in the delivered spot size and its power as a function of the delay position, potentially affecting the results of pump-probe scans. Further, as additional passes of light back and forth on a delay line are added, the complexity of the experimental alignment increases, and a misalignment in the delay line can negatively affect experimental results.

There are benefits in many applications to faster scans through delay time. For example, in scanning quickly, the delay-time associated signals are shifted higher in apparent frequency, thus moving them further away from the baseband frequency-range noise of the source lasers [39]. On a practical level, fast scans enable the experimenter to 'turn the knobs' on various components and receive near real-time feedback so as to better optimize their optical system and its signal levels.

In addition to the optomechanical delay devices, there are 'equivalent time scanning methods' also known as asynchronous sampling techniques. In these systems, there are no moving parts as in Figure 2.1. Instead a 'virtual' pump-probe delay system system is established by using two lasers instead of one, wherein the lasers run at different rates, like two runners at different speeds on a circular race track. The faster runner

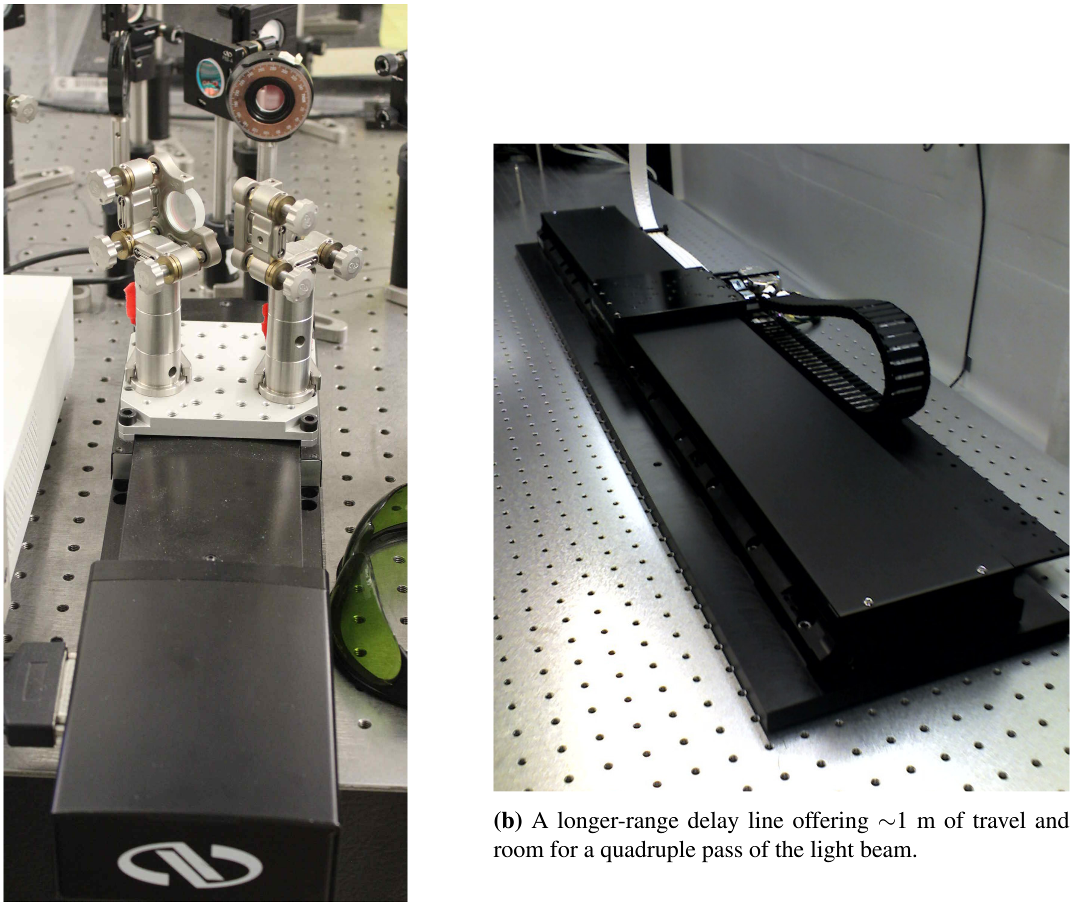

(a) A typical delay line used in THz-TDS experiments; a few inches of travel are usually available, and a double pass of the beam is used.

(b) A longer-range delay line offering ∼1 m of travel and room for a quadruple pass of the light beam.

Figure 2.1: Mechanical delay lines that physically move a mirror pair(s) to achieve time delay are widely used in THz-TDS and pump-probe experiments.

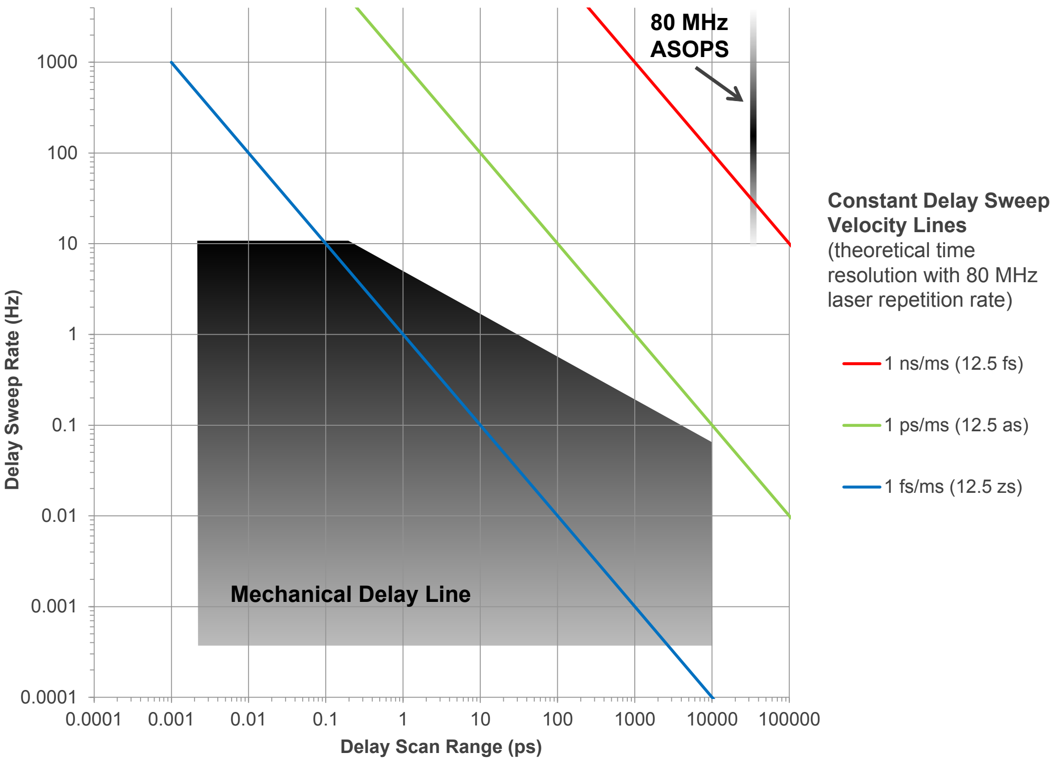

Figure 2.2: Comparison of delay sweep rate and range for typical mechanical delay lines (e.g., as shown in Figure 2.1) and ASOPS based on 80 MHz pulsed lasers. The temporal scan range of ASOPS, while fixed, is covered much more rapidly than is possible with traditional delay lines. Guide lines are drawn in for various scan rates; theoretical time resolutions are shown as well. Given the long delays and moderate time resolution requirements of THz-TDS, the ASOPS technique is in a much better position than delay lines in this scan range-sweep rate parameter space. (Figure adapted from [14])

will periodically sweep past the slower runner, sampling all of the space along the track between them. In this manner, the faster runner is the faster laser and pump pulse, and the slower runner is the slower repetition rate laser and the probe pulse (unless you would like delay time to progress backwards, in which case reverse the runner assignments!). The equivalent time scanning methods are the fastest delay scan techniques, as they are not encumbered by trying to move around mirrors and other masses at increasingly high speeds. With equivalent time approaches, it is readily possible to create virtual delay lines that are the equivalent in scanning speed of mechanical delay lines moving at supersonic speeds and resetting instantaneously at the end of their delay scans.

The question of delay scanning speeds is further addressed in Figure 2.2. Here we see a plot of the useful parameter space for characterizing scanning delay lines. Specifically, we can identify the capabilities of a class of delay lines by comparing their delay sweep rate, in sweeps of full range per Hz (in lab time) along the vertical axis, against their full delay scan range, in picoseconds, along the horizontal axis. Any given point in this two-dimensional space specifies a full delay scanning range swept and the rate at which it can be swept, thus specifying a delay sweep velocity in units of delay time swept per unit of real or laboratory time. In this regard, three constant velocity lines are plotted diagonally across the figure as a guide. Mechanical delay lines, as a class of optical delay technologies, can offer a wide range of delay scan ranges typically covering nearly 7 orders of magnitude in delay scan ranges from the femtosecond level to the level of 10 nanoseconds. The shortest of the delays can be scanned much faster than the longest of delays, which makes sense given the requirement of physically moving a delay stage along its platform and rails. In the upper right we see an interesting linear region, indeed this is an important part of the entire thesis project. This is the region associated with the equivalent time scanning method known as ASOPS or 'ASynchronous Optical Sampling'; it is the technique of dual lasers at different rates as in the analogy above with runners on a racetrack.

The ASOPS line plotted on Figure 2.2 pertains to 80 MHz ASOPS as in ASOPS based on two pulsed lasers with repetition or firing rates of 80 million pulses per second. The full time scan range in ASOPS is the time between two consecutive (faster) pump pulses, just as two runners on a racetrack can never be more than one racetrack apart. At 80 MHz, the time between pulses is 12.5 nanoseconds, hence the vertical line plotted at 12500 picoseconds. The delay sweep rate is the rate at which one laser overtakes the other, that is, how many times per second, it gets 'lapped' by the other laser—this is equal to the repetition rate offset of the two lasers. So if one laser, the pump, is set for an 80 MHz repetition rate and the other, the probe, is a bit slower by 100 Hz, at 79.999900 MHz, then the pump laser will pull ahead of the probe laser 100 times per second, thus completing 100 full delay scans per second between the pump and probe lasers. This offset rate is variable, hence the shaded vertical extent of the line from perhaps several Hz up to $>$1 kHz, depending on one's experimental requirements.

2.1 ASOPS: A Virtual Delay Line

The ASOPS equivalent time scanning method or virtual delay line is the delay technique upon which the present THz-TDS instrumentation has been built. The dual oscillators used in the instrument both have a rep rate of $\sim$80 MHz and are typically run with a 100 Hz repetition offset frequency. The pump-probe experiment that is THz-TDS data recording allows us to monitor up to $\frac{1}{80\text{MHz}} = 12.5\text{ns}$ of delay and the delay sweeps are completed at a rate of 100 Hz; that is, each delay sweep of the 12.5 ns of delay time requires only $\frac{1}{100\text{Hz}} = 10\text{ms}$ of real time in the laboratory. Given the underlying importance of the ASOPS time delay technique to the entire instrument—it is a fundamental principle of operation—an additional explanation of this concept is presented in Figure 2.3.

Here, in Figure 2.3, at top in blue and red, we see the pump and probe laser signals; these signals are along

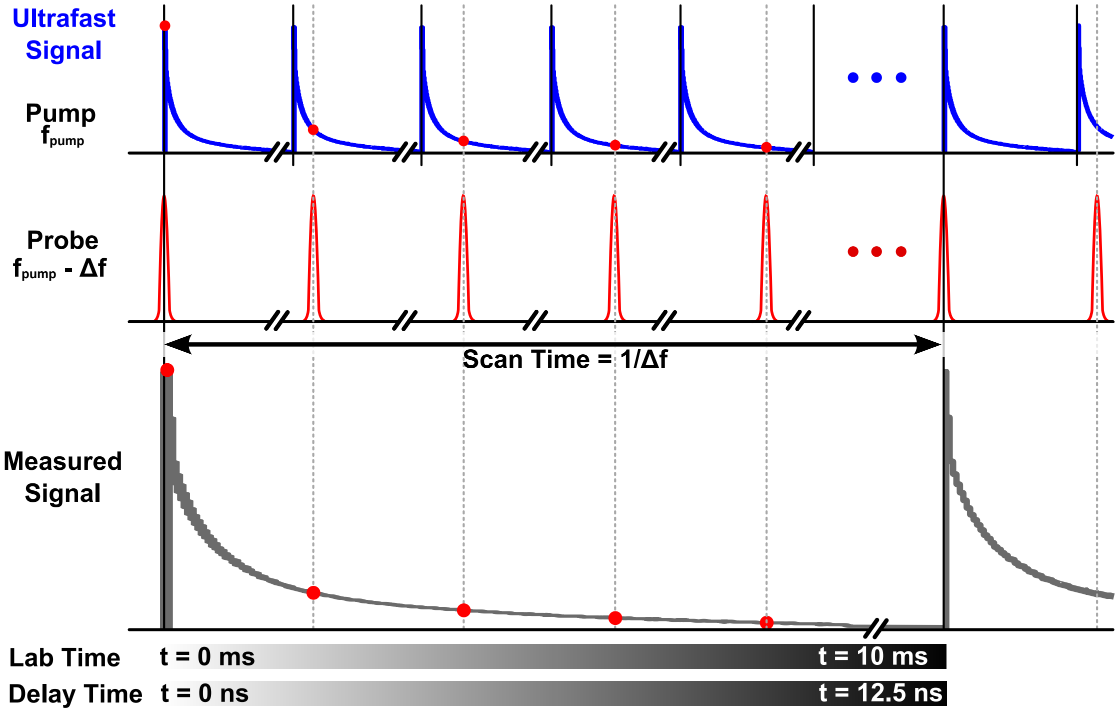

Figure 2.3: The ASOPS 'time-scaling' effect, or operating principle. The pump laser (at top), firing at a rate of f_{pump}, generates an ultrafast process. This process is probed (middle row) by a second pulse train, slightly lower in repetition rate by Δf. The original ultrafast waveform is measured in an iterative manner, over the course of an amount of lab time $\frac{1}{\Delta f}$. (Figure adapted from [15])

a time axis in the ultrafast lab time domain, not delay time. As such, each segmented or windowed view on a pulse has truncated horizontal axes to mark that there is a full period of ultrafast delay associated with each laser pulse. The blue lines are not to represent the pump laser pulse itself, but rather an ultrafast process or signal triggered by that pulse. Every ultrafast waveform at top is separated in time by $\frac{1}{f_{pump}}$ or 12.5 ns for an 80 MHz repetition rate. Each probe pulse, in the row beneath it, is separated in time by $\frac{1}{f_{pump}-\Delta f}$, which for an 80 MHz laser is a period of time about 15.6 fs longer than between pump pulses. So for every pump-probe pair, the probe laser is, on average, arriving 15 fs later and later following the pump pulse. This is indicated by the red dots, showing the spot along the pump-derived ultrafast process that the time-delayed probe pulse would sample. That is, the red dot represents the portion of an ultrafast THz-TDS waveform that a delayed probe pulse would sample in an electro-optic crystal, or the portion of a transient thermoreflectance curve that the probe pulse would sample. These relative steps between pump and probe take time though. Each pump-probe pair comes along every 12.5 ns, but only, on average, advances us (in this case) 15 fs in pump-probe delay time. So it takes many pulses (many! $80\text{MHz pulses} \cdot 10\text{ms scans} = 800,000$ pump pulses) to get through this full stepwise progression of probe through pump or vice versa. Eventually, though, as shown in the measured signal at bottom, we do map out the original ultrafast waveform, just on this much slower laboratory time scale because of our stepwise progression of probe pulse through the pump pulse cycles. This longer lab timescale is noted at bottom as ‘Lab Time’, while the corresponding ‘Delay Time’ explored relatively slowly is beneath. Just as 10 ms of lab time corresponds to the full 12.5 ns of delay time, the 12.5 ns in lab time between pump pulses corresponds to the 15.6 fs of incremental probe beam delayed arrival per pulse. And then at the end of the process, when the curves are acquired, the pump and probe pulses overlap again and the process repeats, seamlessly.

2.1.1 Overview of Time- and Frequency-Scaling in ASOPS

As shown in Figure 2.3 and qualitatively explained above, there is a relationship between the lab-time and delay-time, given by the repetition rates of the pump and probe lasers. The repetition rates of the lasers are held at an offset frequency, defined as:

$$\Delta f = f_{pump} - f_{probe} \tag{2.1}$$

This defines the ‘lapping frequency’ as noted in §2.1, that is, Δf is the rate at which full sweeps or scans of the delay time range will be performed. Or simply rearranged, the amount of lab-time required for a single sweep of delay time will be:

$$T_{scan} = \frac{1}{\Delta f} \tag{2.2}$$

In the scan time T_{scan}, a total delay range of $\tau_{scan} = \frac{1}{f_{pump}}$ will be scanned; there is a linear relationship between the scan time or lab time, and the time in terms of the pump-probe delay. The constant of proportionality, or time scaling ratio between the two time axes is the ratio of the scan and delay time periods, or equivalently, their frequencies [40]:

$$\tau(t) = (t - t_0) \cdot \frac{\Delta f}{f_{pump}} \tag{2.3}$$

where $\tau(t)$ is the delay time expressed as a function of the lab time, t, and the ratio of frequencies at right is the ASOPS scaling ratio. For f_{pump} =80 MHz and Δf =100 Hz, this ratio to scale down time is $1.25 \cdot 10^{-6}$ from lab time to delay (and for the reverse process, it is the reciprocal, a factor of 800,000). The constant t_0 is the amount of lab time between the trigger signal that starts the scan and the moment in lab time when there was actually zero pump-probe delay time, as measured at the sample (or electro-optic detection point, in the case of THz measurements with ASOPS). The actual start time of a scan is arbitrary, such that t_0 can generally be treated as zero; this is discussed further in §3.3.2. It should be noted that equation 2.3 is the ideal relationship between the two domains of time—in reality there may be deviations from this relationship. Such timing errors can distort the measured time-domain waveforms and thus effect any spectra derived from them; the experimental characterization of this relationship is discussed further in §2.5.

To the extent that the ideal linear relationship between delay time and lab time is maintained, then the frequency accuracy of any spectra measured with the ASOPS system will depend on the accuracy of the factors in equation 2.3 [41]. The repetition rates are measured by frequency counters and the lab time t is set by the sampling clock of the data acquisition system; both types of devices can be made very accurate though the use of commercial reference clocks, as utilized herein for the frequency counters.

The time-stretching nature of equation 2.3 is absolutely essential to bringing ultrafast processes within reach of the capabilities of presently available detection electronics. Oscilloscopes and digitizers do not have 1 THz bandwidths, let alone higher as has been observed with the present ASOPS THz-TDS instrument. It is the time stretching of delay time to lab time that multiplies down the frequencies associated with ultrafast processes to a much slower level. With typical scaling ratios on the present instrument approaching a factor of 1 million, then a picosecond of delay time becomes a microsecond of lab time; a 1 THz signal becomes a 1 MHz signal—and the microsecond/MHz timescale/frequency range is addressed by present digitizers, whose bandwidth can extend to many gigasamples per second.

The sampling time of a digitizer, perhaps recording a THz-TDS signal, also scales by equation 2.3. Overall, the temporal resolution, $\Delta\tau$, that one could ideally measure with an ASOPS instrument depends on the coarsest of three quantities on the ultrafast delay timescale [42]:

1. *The pulse duration.* In an extreme example, one can easily imagine that it would not be reasonable to

expect to measure sub-picosecond signals if the probing pulses are of duration a picosecond or longer.

2. *The delay time increment.* The nature of an ASOPS experiment is that from each pump-probe pair to the next, the probe laser pulse falls a little bit in time further behind the pump laser pulse. This size of this increment from pair to pair, the increment in delay time, also can establish a limit on instrumental spectral resolution. It is equal to $\Delta f/(f\cdot(f+\Delta f))$ and for an 80 MHz repetition rate pump laser and $\Delta f = 100$ Hz lower probe laser, this value is equal to 15.6 femtoseconds.

3. *The scaled digitizer bandwidth or sampling rate.* There is the time resolution associated with the sampling rate of one's digitizer system for acquiring the THz waveforms. The time resolution for a given sampling rate f_{ADC} is $\Delta f/(f_{ADC}\cdot(f+\Delta f))$. A note of caution here, as per the Nyquist sampling rule [43], a time-domain waveform must be sampled at least twice as fast as the highest frequency component that one wishes to measure—this rules also applies, via the ASOPS scaling ratio. For example, if the time resolution of the analog to digital convertor is 100 fs when converted to delay time, that is equal to 10 points per picosecond. That does not mean one would have a bandwidth of 10 THz, but rather of 5 THz.

2.1.2 Historical Development and Uses

To the best of the author's knowledge, the first report of ASOPS was the 1987 paper, 'Pump/Probe Spectroscopy by Asynchronous Optical Sampling' by Elzinga et al. [44]. The authors used a mode-locked Nd:YAG laser operating at 81.5970000 MHz and a synchronously pumped dye laser at 81.5870000 MHz as the probe laser. The lasers thus had a 10 kHz offset rate and followed a repetitive relative phase walk-out of the pump and probe pulses which as the authors noted, "replaces the optical delay line used in conventional instruments". This initial ASOPS pump-probe system was used to measure the fluorescence lifetime of rhodamine B, found to be 2.3 ns. In this initial paper, the authors highlighted several key concepts or technical aspects of the technique that remain to the present:

- The probe laser intensity is modulated by the ultrafast waveform under study.
- The ultrafast waveform undergoes a 'time transformation' and repeats continuously at the beat frequency of the two lasers.
- The ASOPS technique is the optical version of a sampling oscilloscope.
- Signals were recorded on an digitizer triggered at the beat frequency

- The probe signal was low-pass filtered to block the individual mode-locked laser pulses and reveal the stretched ultrafast waveform directly.

In terms of the laser locking mechanism between the two lasers, Elzinga et al. used two frequency synthesizers in a master-slave configuration to supply the mode-locking frequencies for the Nd:YAG lasers. The beat frequency was generated by illuminating a photodiode for each laser and feeding the outputs to a double-balanced mixer. In a follow-up paper shortly thereafter, Elzinga et al. [45] provided additional details, but importantly, noted that the cleanness of the trigger signal is important for maintaining sharp time-domain features. Specifically they found that a trigger signal based on cross-correlation of pump and probe beams in a nonlinear crystal was superior to that from illuminating a photodiode for each of pump and probe and electronically mixing the photodiode outputs.

A few years later, Kafka et al. [46] created their own ASOPS system, referring to it as a ‘two-color sub-picosecond optical sampling technique’ or the ’SOS’ technique. Their innovations included the first use of (dual) mode-locked Ti:sapphire lasers, which could be independently tuned in wavelength, hence the importance of ’two-color’ in the technique name. Further, they demonstrated two advancements in timing characterization. First, they treat the cross correlation of pump and probe beams in a nonlinear crystal not just as a trigger signal but they explicitly treat its width as the time resolution of the system. Further, they introduced a ‘calibration étalon’ into the probe beam, before the cross-correlation, in order to introduce a precise delay into the system. This shifted the pattern of the cross correlation, allowing calibration of the timing axis.

In the mid-2000s, German researchers, notably including A. Bartels, started using the ASOPS technique for THz spectroscopy, and improving the laser offset locking electronics to achieve the higher timing stability needed for high frequency THz spectra [47]; they have published numerous papers since that time, greatly expanding ASOPS-based THz-TDS technology and science. As a particularly relevant note, around this time Yasui et al. [48] created an ASOPS time-domain spectroscopy instrument with low repetition rate lasers and claimed to achieve a frequency resolution of 82.6 MHz. However, their laser locking system was likely to have very large amounts of jitter, as the only frequency content they demonstrated was centered at 0.05 THz, or 50 GHz, and ran towards the noise floor not much beyond 100 GHz. Of more significance, Brown et al. [49] created an early $\sim$80 MHz ASOPS system and applied it to water vapor. However, laser locking issues were likely serious, as they had little if any power at 1 THz and presented no referenced spectra. In power spectra of room air, small water peaks could be observed at $\sim$0.55 THz and $\sim$0.75 THz, though the latter peak seemed to barely be above noise levels.

Meanwhile, Bartels et al. continued to improve their laser offset-locking electronics and focused on 1 GHz repetition rate lasers, noting that this kept the scan rates higher above laser baseband noise than would be possible with lower repetition rate lasers (and this is indeed a challenge with ∼80 MHz lasers). They achieved [50] spectra useable to 3 THz in 2005. This was followed with a *Review of Scientific Instruments Paper* in 2007 [40] that detailed the application of their instrument to coherent phonon spectroscopy and the THz-TDS of water vapor (albeit at 1 GHz spectral resolution). A significant improvement followed in 2009 when they redesigned their laser-locking electronics and made other improvements to achieve up to 6 THz of spectral coverage [41]. Design information and a performance characterization for their instrument appeared shortly thereafter [42]; it is this laser-locking electronics design upon which the present higher-resolution THz-TDS instrument is based. Discussion on the laser-locking circuit follows in §2.2.2.

2.2 Overview of the Instrument

The development of the present instrumentation was a difficult process of testing various components individually, assembling them for higher-level tests, while optimizing the overall design. It was an excellent practical education for the author in the areas of electronics and optics, particularly the nuances of ultrafast optics. For the reader interested primarily in the operation and perhaps slight modification of the instrument, it is intended that the discussion herein proves adequate. For the consideration of more substantial changes to the instrument, perhaps as discussed in Chapter 5, review of the references cited herein is recommended. In particular, the interested reader may benefit from a review of electronics, phase-locked loops, basic optics, quasioptics, and ultrafast optics, prior to delving into the research literature. The sections that follow herein nonetheless provide an overview of the instrument, including its development, design and operation principles and usage.

The overall schematic of the Blake group ASOPS THz-TDS instrument and its individual components is presented in Figure 2.4. Taking a high-level tour through the experimental design, we note at left the pair of independent, ultrafast lasers or oscillators used for pumping the THz emission as well as probing it in the detection system. At far right, we have the nitrogen-purged enclosure in which THz spectroscopy is carried out, as well as the components for the electro-optic THz detection. In the middle of the figure, are the routing optics for carrying the light from one side to the other, and also for routing portions of the ultrafast pulse light to various photodetectors for the control of the lasers and spectroscopy system. It should be noted that Figure 2.4, while obviously being a somewhat abstracted view of the instrument, is nonetheless fairly accurate in the number, type and relative positions of optical components; i.e., the real instrument does not have additional turning mirrors, folded paths, etc. that are not shown in the figure. Excluded from the figure are a few important items of note, including the computer for acquisition and control, as well as many of the electronics components used for the locking of the lasers.

In terms of the real-world, overall appearance and setting of the instrument, a picture of the instrument and surrounding area is included in Figure 2.5. The experimental apparatus is, at the time of writing, housed in the Blake group's laboratory in the Linde+Robinson building on the Caltech campus. Essentially all optical components are located on a 5 foot x 10 foot optical table (approximately 1.5 m by 3 m). This table is located adjacent to others (towards lower-right in the figure) that support the Blake groups efforts with THz spectroscopy based on the high-power, amplified laser system, as described in §1.4. This proximity was intentional and practical, designed to place the THz spectroscopy enclosure close to these other tables, so as to enable sharing of the laboratory vacuum system, including turbomolecular pump, as described further in §3.3.1.1.

The ultrafast lasers for THz pumping and detection are located adjacent to one another at the far end of the table; their close proximity was intentional, in the hope that this would help to ensure that any mechanical vibrations or temperature fluctuations they experience are common mode. The power heads for both of the ultrafast lasers are located beneath the optical table, at right though unseen in the figure, and seated on the laboratory floor, with heavy-duty umbilical cables reaching up around the far side of the table (at back in Figure 2.5). The temperature control chillers for the lasers' optical breadboards are also placed underneath the table, at left and unseen in the figure.

The various routing optics are shown in the center of the figure, with the enclosure for THz spectroscopy partially visible at lower-right. At lower-left is the optical breadboard and general area for the transient thermoreflectance (TTR) instrument; this is a collaborative effort with the Minnich Group, also at Caltech, and is described in Chapter 4. The precise repetition rate control of the lasers, as necessary to enable measurements on ultrashort timescales, of course requires various electronics for the monitoring of the laser repetition rates and their active control. Some of these electronics are based on the optical table itself, as shown at left and upper-left in Figure 2.5. Other electronics, particularly the non-RF, lower-frequency loop control electronics, as well as various power supplies, are placed on shelving hanging above the optical table (this is the purpose of the hanging wires at left in the figure). There are also numerous, independent electrical power supply circuits above the table to support the many electrical components, to proactively keep certain components on separate outlets (e.g., lasers on own circuit), and to generally keep cords out of the way of the free-space lasers beams as well as optical components on the table. The computer for instrument control and data acquisition is partially visible at right in the figure; the computer is located close to the table, in range for the cables running to the THz detection system and other components.

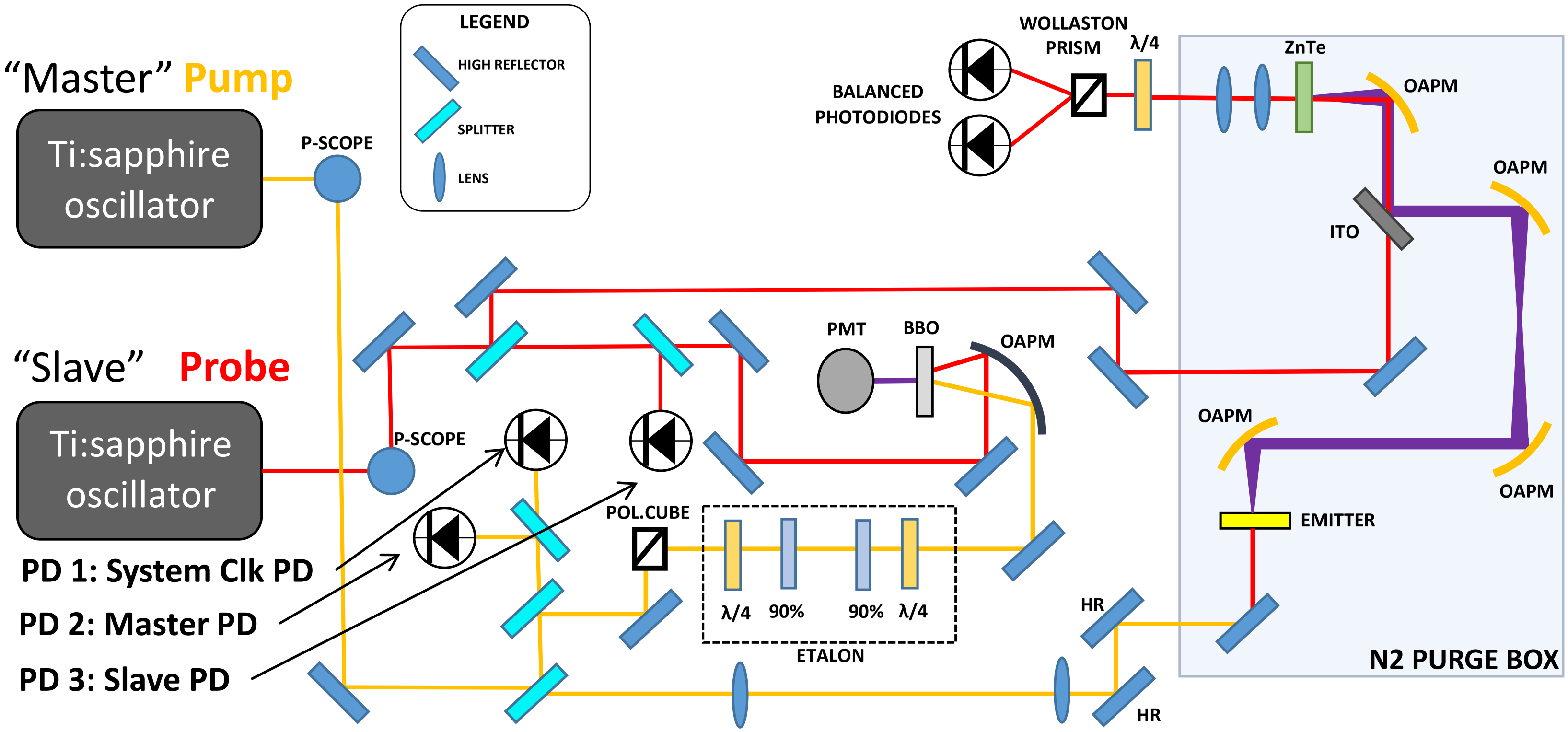

Figure 2.4: The overall optical schematic for the instrument. The ultrafast lasers for pumping THz emission and probing in its detection are shown at left. At right is the enclosure for THz spectroscopic measurements in a controlled environment. That region of the schematic shows the routing optics from the lasers to towards THz generation and detection, as well as the various photodetectors used for monitoring and controlling the instrument. Note that HR = ultrafast, broadband high-reflecting mirrors, OAPM = off-axis paraboloidal mirror, BBO = nonlinear crystal type, PMT = photomultiplier tube and $\lambda/4$, quarter-wave plate.

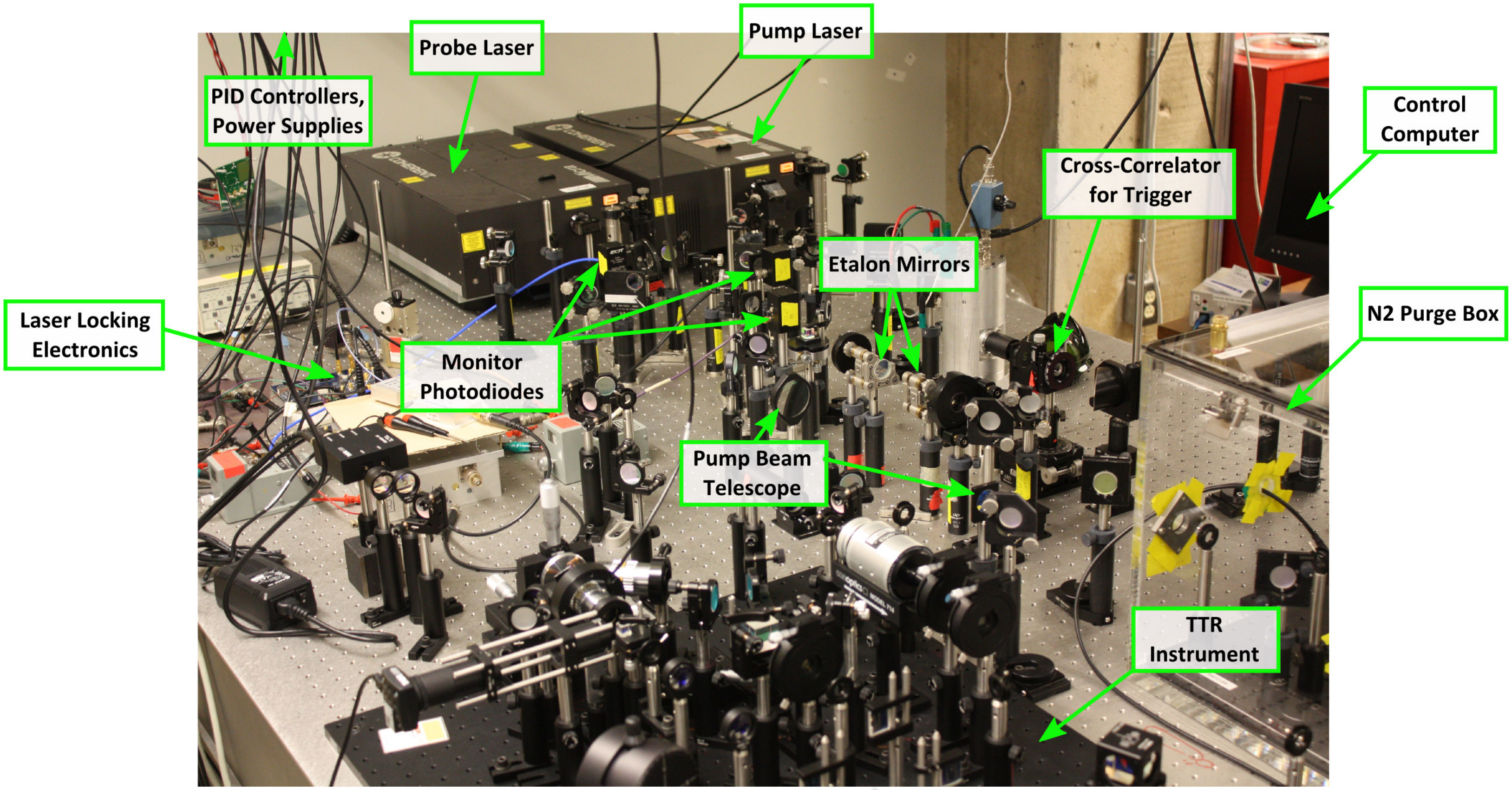

Figure 2.5: A picture of the Blake group ASOPS THz-TDS instrument. Most of the instrument's components are located on a single optical table. The dual ultrafast oscillators are at back, center. The THz spectroscopy enclosure is at bottom-right. Routing optics in the center of the figure direct the ultrashort light pulses from the lasers to the THz emitter and detection setups. Portions of those beams are split off or sampled in the central area, for use by the monitor photodiodes and cross-correlator devices for feedback and instrument control.

Figures 2.4 and2.5, while showing essentially all of the instruments' components, do not necessarily show their functional relationships well. As such, Figure 2.4 has been re-created in Figure 2.6 with functional 'subsystems' defined and highlighted by overlaid blocks upon the instrument schematic. It is hoped that this helps the reader to better understand the overall design of the instrument; indeed, the remaining sections of this chapter are largely organized around the subsystems as graphically defined in Figure 2.6.

Starting at left in the figure, there is the 'Ultrafast Lasers' subsystem; this sends light to and receives electrical control back from the 'Asynchronization Control' subsystem. The light from the laser subsystem pumps THz emission in the 'THz Pulse Generation' subsystem at right; this THz light is then directed through the 'THz Spectroscopy Area' subsystem at far right. After the THz light interacts with the sample in the enclosure area, it is measured in the 'THz Detection & Recording' subsystem at upper-right; this subsystem also includes the host computer (not shown). Portions of the light from the 'Ultrafast Lasers' subsystem are directed to each of the 'Delay Scan Calibration' and 'Scan Triggering' subsystems shown in the center of Figure 2.6; these subsystems help ensure the accuracy of the ASOPS delay-time scan and to provide scan-start triggers to the 'THz Detection & Recording' Subsystem.

As noted above, the definition of these subsystems guides the overall layout of this chapter and the explanations of the instrument's components. Individual subsystems are herein described in further detail, with references to more specialized sections later in this chapter.

2.2.1 Ultrafast Lasers Subsystem

The 'Ultrafast Lasers' subsystem consists of the pair of commercial, mode-locked Ti:sapphire ultrafast lasers. Each laser consists of the laser 'head', placed on the optical table, and the combination power supply and control box, placed below; the two pieces are connected by a somewhat flexible umbilical and cannot, in general, be separated from each other. Each laser has internal photodiodes for coarse monitoring of their repetition rate; these signals are monitored in an open-loop (no feedback) manner by independent frequency counters (not shown in figures). Further, the frequency counters are referenced against a 10 MHz clock standard for accuracy, and it is the output of these frequency counters that is used, in part, to calculate the frequency axis of the THz spectra acquired with the instrument. The ultrafast lasers and their general characteristics, including the repetition rate control actuators essential for the laser asynchronization, are described in detail in §2.3.1; the open-loop frequency counters are described therein as well.

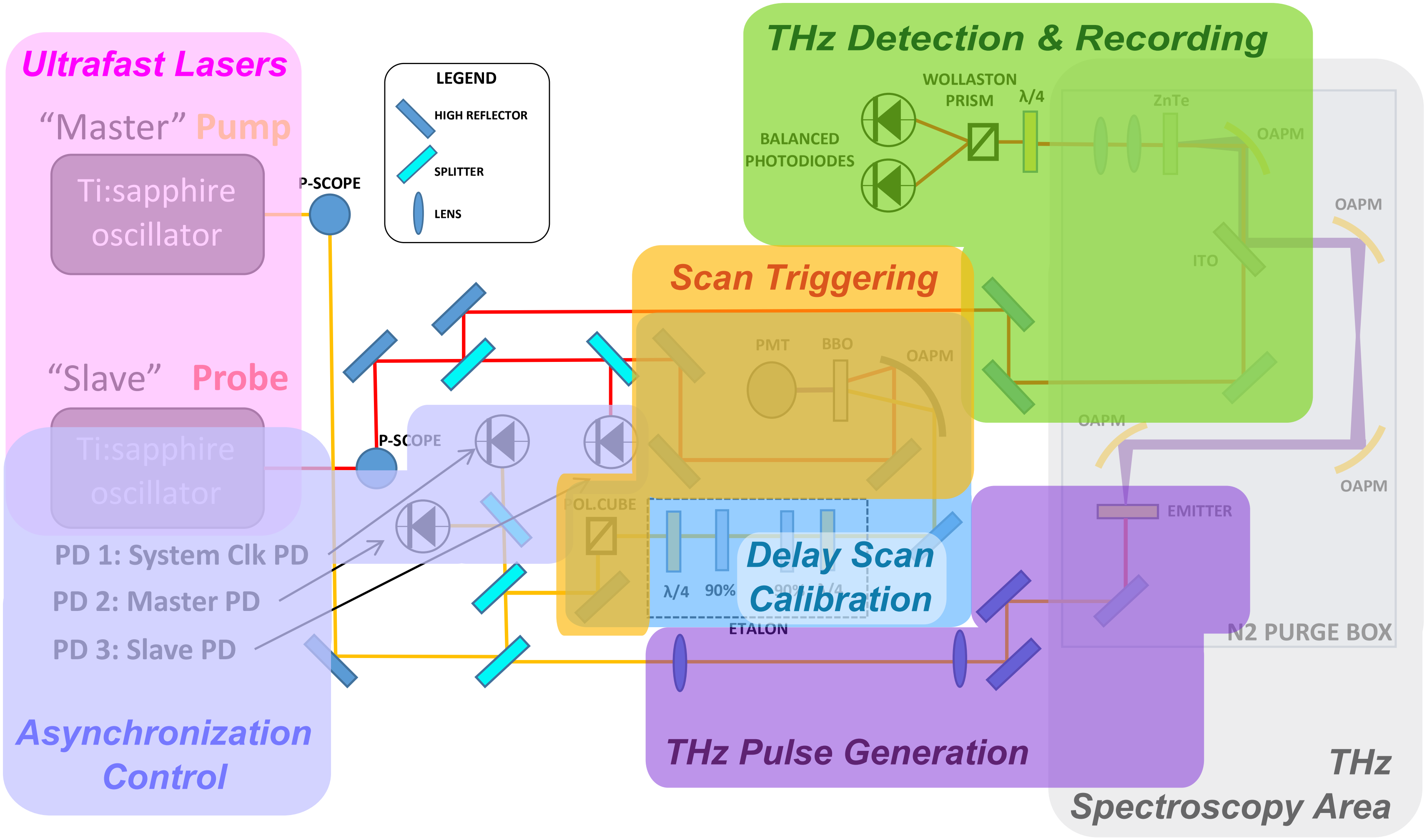

Figure 2.6: Schematic of the instrument, as in Figure 2.4, with components grouped into subsystems by functional relationships; the definitions of these subsystems guide the layout of this chapter. Generally, the 'Ultrafast Lasers' and 'Asynchronization Control' subsystems at left work together to supply ultrashort optical pulses to both of the 'THz Pulse Generation' and 'THz Detection & Recording' subsystems at right. The 'THz spectroscopy area' at right includes the sample holder or cell. In the center of the instrument, the 'Scan Triggering' and 'Delay Scan Calibration' subsystems serve to coordinate the acquisition system and ensure the quality of the scans.

2.2.2 Asynchronization Control

The ‘Asynchronization Control’ subsystem consists of a range of photodiodes, intermediate RF and acoustic-frequency electronics, and laser actuators. In the latter respect there is overlap, as shown in Figure 2.6, between the asynchronization control and ultrafast laser subsystems. The laser actuators themselves are discussed as noted above, in the context of the lasers themselves; their usage pertains to the control subsystem discussion.

A small portion of the output power of the ultrafast pulse trains from both lasers is detected by a set of three photodiodes (‘PD1’, ‘PD2’, and ‘PD3’ as noted in the figures). The master or pump laser is monitored by ‘PD2’, the slave or probe laser by ‘PD 3’; ‘PD 1’ is an additional monitor on the master laser, for use in the asynchronization electronics. The signals from all three photodetectors are used to establish a microwave-frequency phase-lock loop acting on the repetition rate of the slave laser so as to maintain a small and constant offset in rate between the two lasers, typically of 100 Hz. As part of the control loop, an error signal is derived by comparison of the master and slave monitor photodiodes. The signal is conditioned in a proportional-integral-derivative (PID) controller and other circuitry, and the resulting acoustic-frequency range correction signal is used to adjust the repetition rate actuators inside the slave laser, so as to maintain the desired repetition rate offset relative to the rate of the master laser. The technical goal of the asynchronization control subsystem is to minimize phase noise and timing jitter between the master and slave lasers so as to maintain a state of sufficient phase lock between the master and slave lasers to enable the precision delay-time scans required for ultrafast ASOPS-based scans. The technical electronic details of the asynchronization control loop are discussed in §2.3.3.

2.2.3 Scan Triggering

The acquired THz time-domain waveforms are repetitively averaged for an improved signal-to-noise ratio. The acquired scans must be coherently co-added for their signal levels to improve. That is, the starts of sequential scans to be added must align; corresponding points in two different waveforms, representing the same delay time, must be added (averaged) together. Misalignment of scans in this process would diminish the data quality and defeat the purpose of averaging. As such, a ‘scan trigger’ subsystem is provided to generate a trigger signal for the ‘THz Detection & Recording’ subsystem. The trigger signal starts the acquisition of a new scan and serves as a common reference point in time for the co-adding or averaging of subsequent scans. Some readers may be familiar with the concept of triggering off of the data signal itself, however the THz waveforms in the present application are too noisy to be an effective trigger source in this manner.

Recalling the discussion of the ASOPS repetitive phase walk-out in §2.1, a new delay scan could be said to be initiated when both of master (pump) and slave (probe) lasers were firing at the same instant in time. However, what really matters in a pump-probe measurement is the relative delay in arrival time between pump and probe pulses at the interaction region of concern between the two pulse trains. In the present application of a THz spectrometer, that region of concern is at the electro-optic detection crystal in the ‘THz Detection & Recording’ subsystem. In this case, the pump beam first impinges upon the THz emitter to convert a fraction of its energy to THz emission, which is then directed to interact with the optical probe beam in the electro-optic crystal. However, that interaction area, by definition, is already used for the detection. Instead, the optical pump and probe beams (without any THz conversion step) are crossed again to form a new interaction region elsewhere, that is, in the ‘scan triggering’ subsystem. Specifically, the optical pump and probe beams are directed to cross in a beta barium borate (BBO) nonlinear crystal. When the two pulses are spatially and temporally coincident upon the crystal, sum-frequency generation (SFG) light is generated and directed out of the crystal at an angle between the two input beams (i.e., noncollinear SFG). This light is detected on a photomultiplier tube (PMT) and used as a trigger signal for the scan acquisitions.

The components of this subsystem include the optics necessary to focus the pump and probe beams together and the nonlinear crystal in which they interact, as well as the PMT and its associated electronics (e.g., current amplifier). The design and operation of this subsystem is discussed further in §2.4, and is very much related to the ‘Delay Scan Calibration’ subsystem.

2.2.4 Delay Scan Calibration

As shown in Figure 2.6, the ‘delay scan calibration’ and ’scan triggering’ areas overlap. Indeed, the ‘scan trigger’ subsystem is a wholly-contained subset of the ‘delay scan calibration’ subsystem. The start triggering signal provided by the ‘scan triggering’ subsystem is essential for proper instrument functioning in the collection of THz-TDS waveforms. In contrast, the ‘delay scan calibration’ subsystem is not required for normal instrument operation, rather it can be added as a diagnostic on the performance of the ASOPS delay-time scans, and without interfering with normal operation.

The delay scan calibration subsystem consists, in addition to the scan triggering subsystem, simply of a pair of quarter-wave plates, one each before and after, a pair of moderate-reflectivity mirrors (R = 90%). The scan triggering system, without the delay scan calibration components, simply directs pulses from both lasers to overlap on a nonlinear crystal, as noted above in §2.2.3. The addition of a pair of moderately reflective mirrors into one path of one of the pulse trains (in this case, that of the master or pump laser) causes each laser pulse along this path to bounce back and forth between the mirrors. Upon each round trip, a small portion of light leaks through to continue on to the nonlinear crystal where it may interact with a pulse from the slave or probe laser, depending on the timing. The mirrors thus split each master laser pulse into sub-pulses; the timing between these sub-pulses is given by the fixed separation between the two added mirrors and the speed of light (see [14] for further information). Whereas with the scan triggering subsystem alone, there was only one SFG pulse per delay scan, there are now many SFG pulses per scan, in a decaying train of SFG pulses as probe laser pulses interact with later and later pulses in the train of sub-pulses from each pump laser pulse. During the course of a singe scan of delay time, a co-recorded waveform of the PMT's SFG signal will show many pulses - and given the spacing of the added mirrors, we can then know exactly how far apart those pulses should be in delay time, thus providing a check on our delay time to lab time conversion. As for the quarter-wave plates, they are placed about the added mirrors to serve as an optical isolator and prevent strong reflections from bouncing back towards the pump laser, where they may cause instabilities in the even train of pulses from the laser. The design and operation of the delay scan calibration is discussed further in §2.5.

2.2.5 THz Pulse Generation

The 'THz pulse generation' subsystem is shown at the bottom-right of Figures 2.5 and 2.6. While this subsystem may consist of only a few components, it is indeed a very important part of the spectrometer, it is our THz light source! Overall, this subsystem consists of the THz emitter device, a voltage supply for its electrical bias (not shown in the figures), as well as the mirrors and lenses used to route the master or pump laser pulse train onto the emitter's active area. The two lenses, shown in this subsystem, both achromatic doublets, serve as a telescope to scale the pump beam down to the proper size for optimally efficient conversion of optical to THz light in the emitter. Further details on all of these components, including upon the THz emitter and its operating principles, are included in §2.6.

2.2.6 THz Spectroscopy Area

The 'THz spectroscopy area' as a subsystem is shown at right in Figures 2.5 and 2.6. This subsystem notably consists of the nitrogen-purged enclosure used to reduce the amount of water vapor in the THz beam path—the vapor absorbs strongly in this region of the spectrum, as demonstrated in Chapter 3. The system further consists of the other optics in the enclosure and the optical breadboard, attached to the bottom of the enclosure, upon which all components are secured. The spectroscopy area's optics primarily include the four off-axis paraboloidal mirrors (OAPMs) used to collect the THz light from the emitter, focus it down upon and guide it though a sample, and then focus it upon the electro-optic crystal for measurement by the THz detection and recording subsystem. The four OAPMs form a pair of far-infrared telescopes in series, each being of the type known as a 4f or Gaussian beam telescope [51]; a beam 'waist' or focal point at the THz emitter is focused by the first two mirrors down to another waist or focal point (as shown by the purple-colored THz beam path in Figures 2.5 and 2.6) between the two pairs of mirrors, where it is thus convenient to place a sample or sample cell. This beam waist is then projected by the next telescope, with demagnification, onto the electro-optic detection crystal (in this case ZnTe material) as shown in the figures. This subsystem also includes the optical windows (not shown) for passing the pump beam into and probe beam into and out of the purged enclosure area.

There is overlap, of course, between the subsystem of the THz spectroscopy area, and both of the THz pulse generation and THz detection and recording subsystems. The THz emitter and preceding optics are discussed in the context of the THz pulse generation subsystem, as noted above. The breadboard and purge box components of this subsystem are discussed in §2.7. The sample cell and related vacuum components that are used in conjunction with the THz spectroscopy area would technically be considered part of this subsystem, though they are discussed in the context of the THz spectroscopy of water vapor in Chapter 3, in §3.3.1.1. The far-infrared telescopes made from the OAPMs are discussed in §2.8.

2.2.7 THz Detection & Recording

The 'THz Detection and recording' subsystem is shown at upper right in Figures 2.5 and 2.6. This subsystem includes several devices both within and outside of the purged enclosure. The components of this system can be reviewed simply by following the path of the probe beam as it enters the nitrogen-purged enclosure of the THz spectroscopy area. The beam is directed by a high-reflector towards an optic labeled as 'ITO'; this is a piece of glass coated with a transparent, conductive material known as indium tin oxide (ITO). The ITO optic functions as a dichroic mirror, allowing the optical probe light to transmit, while reflecting the much longer wavelength THz light. In doing so, this optic allows for the recombination of the probe and THz pulses onto a common beampath into the electro-optic crystal for THz detection; the ITO mirror is discussed further in 2.8. After the THz and probe light have reflected off of the last OAPM and passed through the electro-optic detection crystal, the THz light is discard/ignored while the probe light is re-sized with a small 2-lens telescope. Subsequently, the probe light is passed through a quarter-wave plate for a bias to its polarization and then though a Wollaston prism for separation of orthogonal polarizations. The separate beams of cross-polarized probe beam light are then directed onto two photodiodes for optical measurement of the THz signal via modulation of the probe light balance across the photodiodes. This is of course a very brief description of the THz electro-optic detection process; it is described in more detail in §2.9. The photodiodes in this detection step may be two completely separate devices, or two photodiodes wired together in a single, balanced photodetector; this is discussed further in §2.10. The electrical signal from the photodiode detector(s) is then connected to a digitizer card in the host or control computer (not shown in figures) for recording and processing, this is described in more detail in §2.11. The trigger and delay calibration signals from the PMT are also passed along to this same digitizer for co-recording of the data.

It should also be noted that there are a few small optics in Figures 2.5 and 2.6 that are not explicitly assigned to any particular instrument subsystem—these are involved in routing light to various subsystems and are discussed as appropriate in the sections that follow.

As noted above in §2.2.2, the key to a viable ASOPS THz-TDS instrument is that the asynchronization electronics are able to establish a microwave-frequency phase-lock loop between the master and slave lasers, rapidly acting on the repetition rate of the slave laser to account for relative changes in the timing of the master and slave laser pulse firings. In the context of electrical engineering, this is a problem of phase noise and timing jitter between the two lasers, as discussed in the next section.

2.3 Laser Systems and their Repetition Rate Control

The core of the ASOPS system is the set of circuits and actuators that maintains the laser repetition rate offset; the asynchronization circuit. This is described in further detail in the next sections. There are essentially three key technical points underlying this discussion. First, passive stabilization is great. The easiest correction is that which you do not have to make—to the extent that noise can be eliminated or insulated against, the demands on the laser actuators and electronics are reduced. Secondly, the mechanism of control that we have upon the laser repetition rates is the physical length of the laser cavity. That is, the repetition rate of the laser can be treated as the time it takes for a short pulse of light to make a round trip through the laser cavity; if that cavity is made shorter, the repetition rate goes up and if it is made longer, the rate goes down. A quick test of this is to put one's hand on top of the laser case while it is on, the rate will go down as the case is warmed and expands (unless the slow loop is on—this is a good way to check that!). And thirdly, through the use of fast electronics, we can make rapid, fine corrections to the cavity size in order to hold the repetition rate where we would like it. Electronic mixers can compare the different laser frequencies and produce an error signal, that properly conditioned, can be used to adjust a laser actuator.

Overall, the ASOPS THz-TDS instrument has two loops and three actuators. There is a small PZT on the 'fast' loop for acoustic and mechanical corrections, and a slower PZT (called the 'galvo' for historical reasons) on the 'slow' loop for temperature changes in the room. And for manual corrections, there is a stepper motor/actuator. These are described in more detail in the next section.

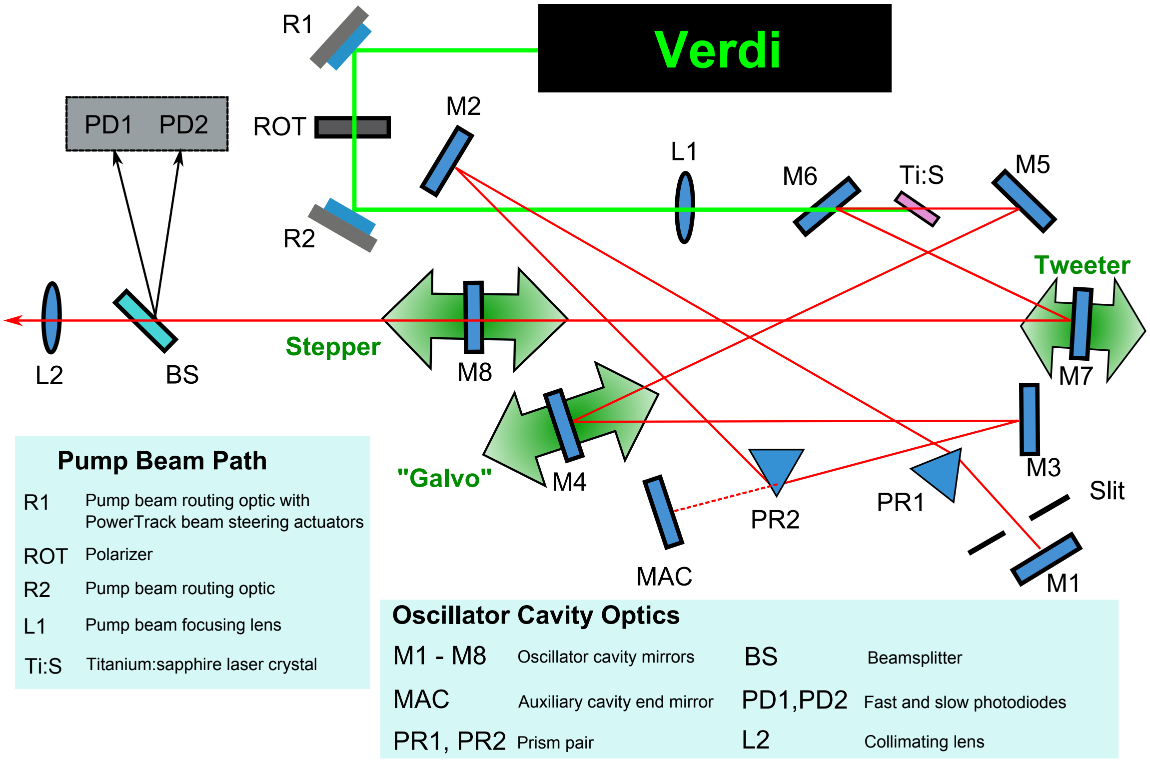

Figure 2.7: Micra laser head internal optics, showing the three actuators available.

2.3.1 Instrument Laser Systems

The Coherent Micra lasers used in the present ASOPS THz-TDS instrument have a few different, optional actuators available. The laser used as master/pump was not explicitly ordered with any such actuators as it was intended to be free-running. However, it was ordered with a more stable starter (mode-locking) mechanism, based on a piezo stack, rather than a spring device; the concern was that the spring device would be less stable during normal operation and be a source of mechanical noise. This starter mechanism, it turns out, is the same device that Coherent Inc. refers to as the 'galvo' actuator. The same device is used for both of starting and for accepting outside signals through a BNC port labeled 'galvo' on the back of the laser. In the case of the master laser, since we did not request this actuator, just the starter, we did get the unit, but the external access needed to supply our own signal to the galvo was not provided. Nonetheless, we could add such access if we wished to gently lock the master laser with that actuator. For in-depth details of the proper electrical engineering work behind phase-locked loops, the interested reader is referred to two theses out of the Ye group at JILA/U. Colorado at Boulder, those of Robert Shelton [52] and Seth Foreman [53].

The other Coherent Micra laser we ordered was specifically to be the slave/probe laser—so we ordered three different kinds of actuators on it. The internal optics of the Micra laser and the positions of these three different actuators therein are illustrated in Figure 2.7. The three actuators on the Micra (slave) system include a stepper motor on the output coupler (that is, on mirror 8 or M8), a tweeter or high-speed PZT on the M3 folding mirror, and a 'galvo' on the M4 folding mirror. 'Galvo' is in quotes for two reasons: firstly, it isn't really a galvo, which actually refers to an older type of actuator not used on these lasers anymore. Coherent continues labeling its electrical port on the back of the laser as 'galvo' for historical reasons; this actuator is really a multi-wafer PZT stack and is good for slow, moderate to large (e.g., several Hz to hundreds of Hz) corrections to the repetition rate. It should be noted that this galvo is also the starter mechanism for the laser; the Micra's internal circuits ignore user signal input to this port during start-up and instead command the galvo PZTs to shake until modelock is achieved. The master laser has this same part, but without the BNC connection on the back face of the laser already attached—so adding this option in the future might be useful for further stabilizing the ASOPS system. Presently, though, the master galvo is unused (aside from start-up) while the slave galvo is controlled as part of the ASOPS THz-TDS instrument's slow loop, that primarily adjusts for changes in temperature over time.

For the stepper motor actuator on the slave Micra system, a custom stepper-motor controller was made and is considered part of this subsystem. It is used on a manual basis in order to get the laser rep rate close enough to that of the master in order for the fast loop to capture when it is engaged. Slight corrections to it can be made during lock (while scans aren't running though) in order to re-center the locking range of the loop, but the slow loop, if working properly, now negates the reasons for trying this. The tweeter or fast PZT system on the slave laser is critical to the ASOPS THz-TDS—it is the actuator that makes the most difference. Indeed the instrument was originally run just using the fast PZT. It was only when it was noticed that the laser could drift out of lock over a few hours, likely due to room temperature issues, that the slow loop control was added to the slave laser's galvo actuator.

2.3.2 Passive Stabilization

Any changes in the ambient environment about the laser can have an effect on the repetition rate of the laser and its phase. Even talking a bit loudly next to the laser can sometimes create a noticeable disturbance to the in-loop error signal. And certainly stomping, slamming doors, etc. Further, temperature variations also require a response. To the extent that these problems can be blocked or insulated, that means less work for the stabilization loops, a better lock and perhaps better THz data. On short time scales (e.g., $<\sim 1$ second), the predominant sources of noise to correct will be acoustic and mechanical. In this regard, the instrument table should be fixed and floated as soon as is reasonably possible. Other students should not be working on the table during scans, and perhaps generally not right next to it either. These concerns will generally be more strict for the ASOPS-TTR experiments, as discussed in §4.1, due to that experiments' concern for baseband data. In contrast, ASOPS for THz purposes will be much more immune to noise. Presently the only real passive stabilization that has been taken is to mount both of the oscillators on large-diameter rubber stoppers on the tabletop. If further noise issues are observed in the future, there are partially constructed heavy walled acrylic boxes available that could be built over the lasers to further isolate them from acoustic effects in the surrounding room. Also, particularly sensitive scans could be done overnight, when such noise is likely much reduced. But overall, it should be stressed that for the ASOPS-based THz work, these measures have not been necessary and the system seems fairly robust.

2.3.3 Instrumental Implementation

The present asynchronization circuit is based on that discussed by Gebs et al. [42], and is presented in Figure 2.8. The novel aspect of this general design of offset-locking circuit was the use of 'DDS boards'; that is, components DDS1 and DDS2 in the schematic. Direct-digital-synthesis (DDS) boards are low phase noise frequency synthesizers. The devices use an external sample clock and a digital tuning word to generate a tunable digital signal that is then converted to an analog sinusoidal output using a digital-to-analog converter. DDS boards can produce a range of frequencies up to nearly half the supplied clock frequency, with a tuning step size of $\sim 4\mu$Hz for the particular model used herein [54]; the external sample clock in the present case is a harmonic of the master laser output.

The tracing of the circuit is perhaps best started at the master laser, as it is presently left free-running, with no active control. Small portions of power from the master laser illuminate two monitor photodiodes; these are the optical inputs to the asynchronization circuitry. PD1 is lower in bandwidth as compared to PD2 and supplies the 12th harmonic of the laser repetition rate, at approximately 960 MHz, though an amplifier and power splitter to provide the clocking signal to both of the DDS boards (DDS1 and DDS2). In this regard, when the DDS boards are initially turned on and programmed with the frequency of their reference clock, the repetition rate of the master laser, as read off of a referenced frequency counter, is used as the clocking frequency ($\sim$960 MHz). During the course of an experiment, the repetition rate of the master laser may drift away from this initial value; perhaps a few hertz or even up to a few tens of Hz. These drifts are generally small compared to the frequency of the master laser, and thus represent a small fractional error, unlikely to significantly affect the definition of the temporal waveform timebase or subsequently, the frequencies of spectral line centers. However, with improvements in frequency performance or simply to make the system more robust, it may be worthwhile to pursue at least loose stabilization of the master laser.

Returning to PD2, this is the other photodiode that the master laser beam illuminates, and is a higher

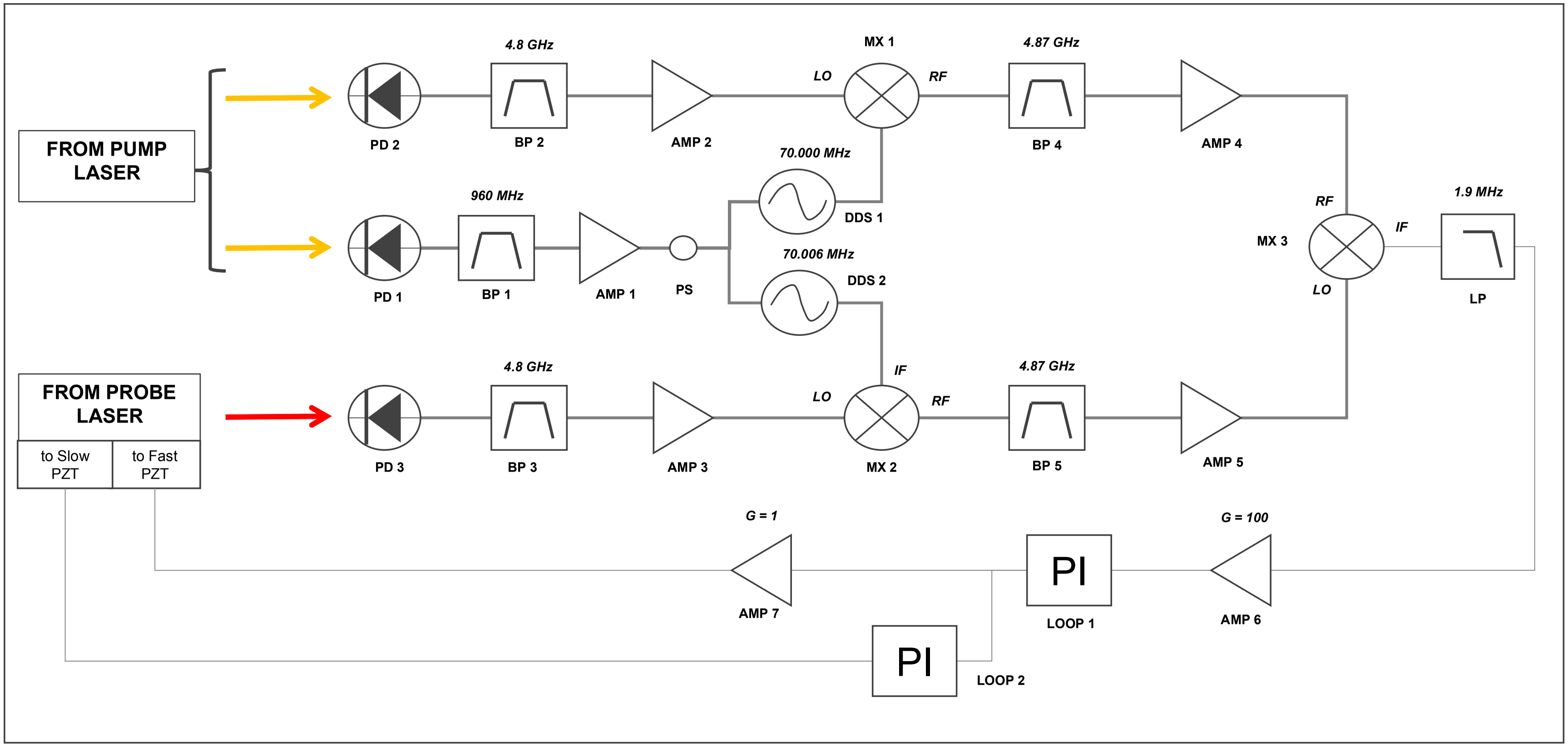

Legend: PD = photodiode, BP = bandpass filter, AMP = amplifier, PS = power splitter, DDS = Direct Digital Synthesizer, MX = Mixer, LP =low-pass filter, PI/LOOP = Proportional-Integral Loop Filter

Figure 2.8: The asynchronization circuit that maintains the rep rate offset in the THz-TDS instrument.

frequency model; PD2 supplies the 80th harmonic of the master laser repetition rate (4.8 GHz) through a bandpass filter and amplifier for mixing against DDS1. The slave laser similarly illuminates PD3 (identical to PD2), the signal (at 4.8 GHz) from which is band-passed and filtered to select a single comb tooth, amplified, and mixed with the output of DDS2. So overall, the master laser is clocking both of the DDS boards, and each of the master and slave lasers is having its 60th harmonic comb tooth at $\sim$4.8 GHz mixed against the output of a DDS board.

As an aside, we point out that in a synchronization circuit, there would be no need for the DDS boards; we could simply and directly mix the matched comb teeth selected from each laser, and use the resulting error signal to close the loop. However, for the precise asynchronization of the lasers, the DDS boards are necessary. In this regard, we point out that the DDS boards, while phase coherent, due to the common (master laser) clocking, are set to different output frequencies: DDS1 to 70.000 MHz and DDS2 to 70.006 MHz—the latter being a 6 kHz increase in frequency. And this is the key point: the asynchronization circuit is basically a synchronization circuit where we 'give' a small, extra amount of frequency to the slave laser, so that when its signal is synchronized against that from the master laser, the slave laser is actually running at a lower repetition rate, in this case 6 kHz lower as measured at the 60th harmonic at which the PLL circuit operates. Dividing 6 kHz by 60 yields 100 Hz, the desired offset.

So when the loop has zero error signal, the slave laser will be operating at a repetition rate that is 100 Hz lower than that of the master. Still under this zero error condition, when the master and slave lasers' 60th harmonic signals are received by the monitor photodiodes, the slave lasers' signal will be 6 kHz lower than that of the master laser. However, after the slave laser is mixed with the output of DDS2, which is 6 kHz higher than that of DDS1 (and the sum frequency output of the mixer selected and amplified) the master and slave laser signals reaching MX3 will be the same and the intermediate frequency (IF) signal leading into the PID controller will be zero.

Any nonzero error voltage at the last mixer would be passed on to the PI controllers for correction to the laser. The first component in the path after the 'last' mixer (MX3) is a 1.9 MHz low-pass filter; this is in place to reject any high frequency components that may have leaked through the circuit to this point. The correction bandwidth of the overall circuit is $<$100 kHz, so any high frequency signals at this point could only serve to potentially saturate later amplifiers or otherwise interfere with circuit operation, and so should be rejected. Following the low-pass filter, the filter is immediately run into a variable voltage amplifier, typically set to a gain of 100 during lock conditions. It should be noted that in Figure 2.8, it looks like there is quite a gap or length of cable from MX3 and the LP over to AMP6, but actually they are all connected straight together in one block. Following the mixer, any noise that is added on the circuit will be interpreted by the loop as something for which a correction is needed. Therefore it is important to place AMP6 as close after MX3 and LP as possible. Following AMP6, the error signal is directed into the PI controlled labeled as Loop1; this is the fast loop attached to the high-speed PZT in the slave laser. This PZT or ‘tweeter’ is attached to the back of a folding mirror inside the laser cavity. The Coherent fast PZTs are known to have a relatively high capacitance, so a gain = 1 line driver, designed for high current, is used as suggested in [55].

2.4 Optical Scan Triggering: T0 Detection

For any sort of THz-TDS work, be it a ’traditional’ delay line-based experiment, or an ASOPS-based technique as in the present effort, it is important to have a well-defined time axis against which all waveform data points are associated. The requirements include a well-defined zero time or start trigger, which may alternatively be defined as the time location of the peak of the time-domain THz waveform in the case of the reference (no sample in path), or as the beginning of the recorded scan period itself, sometime before such a peak; the former definition is often used for traditional experiments, while the author employs the latter for ASOPS work. The zero time signal is simply provided by an ultrafast optical cross-correlation between the master/pump and slave/probe pulse trains, as employed by Elzinga et al. [45] and Kafka et al. [46] as noted above in §2.1.2. Our cross-correlation scheme is illustrated in Figure 2.9.

Referring to Figure 2.9, it may be useful to compare it against Figure 2.4 to follow the beams (colors are matched). In the cross-correlator, portions of the master and pump beams are directed to interact in a thin piece of BBO nonlinear crystal. The majority of the slave/probe beam is directed to the cross correlator; there are two ∼10% pick off mirrors along its path to sample enough power for the monitor photodiodes and the EO detection. Indeed, there probably is more than enough power for the cross correlator now, so it may be worthwhile to replace the EO pathway’s pick off mirror with a splitter. For now, as much as ∼90% of the slave or probe laser power is directed towards the cross correlator. On the other hand, only a small portion of the master or pump laser beam is sent over, as most of that power is desired for pumping THz emission. The only master/pump beam power that goes to the cross correlator is that which was sampled and then split off the main beam, so perhaps about 5%.

After the pump and probe beams cross in the crystal, the blue sum frequency generation (SFG) light is directed between the crossed pump and probe beams (now spatially filtered out on the iris surface) and the SFG light passes through a blue-pass filter on the PMT housing, where it is detected. As shown in Figure 2.9, the etalon mirrors for the delay scan calibration subsystem are not in setup during that picture. In this configuration, there is one main SFG pulse per scan; this pulse is the start trigger for the digitizer electronics.

A well-defined time-axis is of course required for waveform fidelity. A well-defined zero time takes on

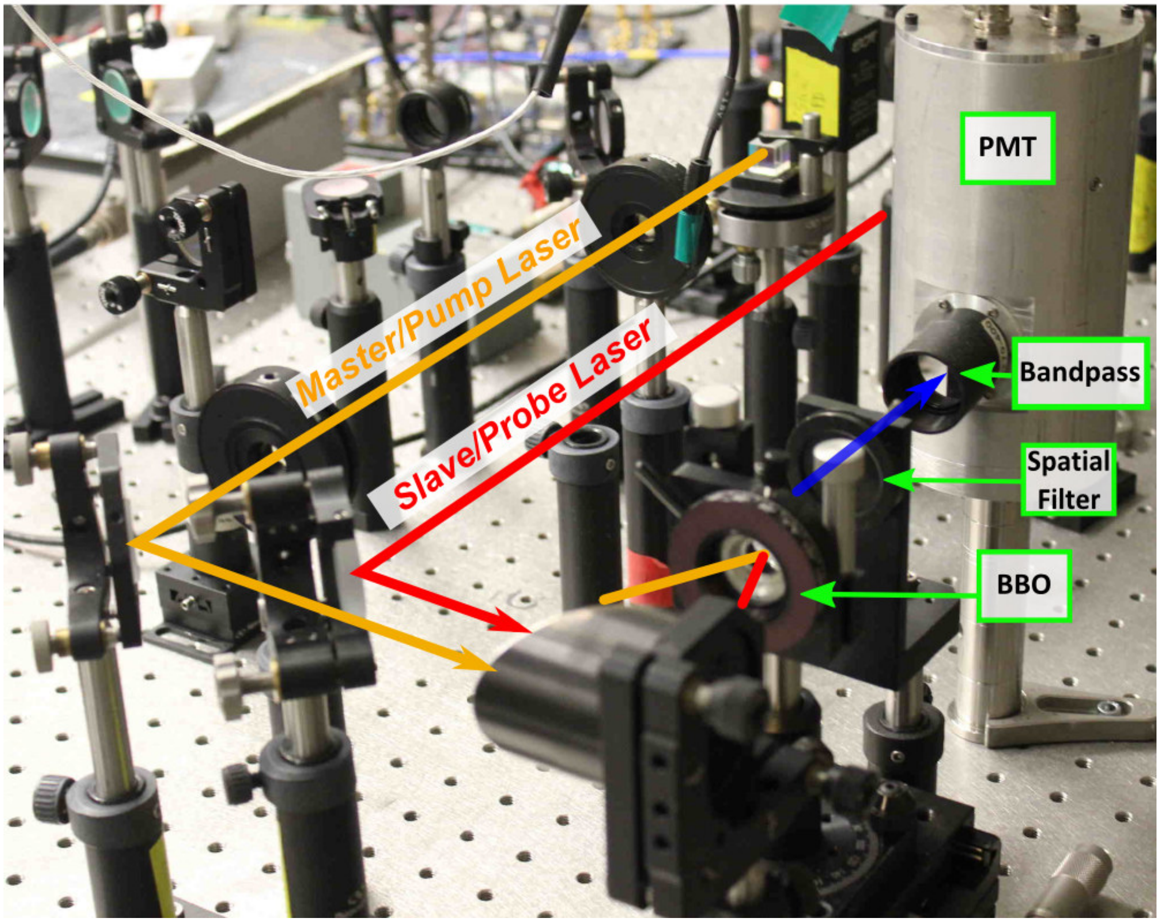

Figure 2.9: The noncollinear cross correlator for scan start triggers.

additional importance over other time points in that this is the reference time for the start of new scans and is thus a guide for the proper coherent addition (averaging) of numerous scans for the improvement of the experimental SNR. In traditional THz-TDS, subsequent swipes of the delay line through the full scan range can be aligned with the T0 point, for the co-adding or averaging of thus-aligned time points. Such a zero time point takes on additional importance in the case of ASOPS-based THz-TDS. With the waveforms acquired in near real-time on a digitizer or oscilloscope, a trigger signal is required for the start of the acquisitions and to align the rapidly swept waveforms for co-adding or averaging on the device or a host computer. Signal averaging on oscilloscopes is a very common activity merely requiring a sharp pulse of a signal supplied to the triggering circuitry of the oscilloscope. For example, a sine wave from a function generator could be conveniently averaged by connecting the function generator's synchronous square-wave/TTL timing signal to the oscilloscope's trigger input. Alternatively, with a 'clean' enough signal, one could trigger off the sine wave itself.

For the present application of the THz-TDS, the THz signal in a single scan is typically too noisy for clean triggering in support of the alignment and coherent addition of repetitive scans, so a synchronized timing signal is required, much like a function generator's synchronous square-wave signal. The sharper the rise-time of the trigger signal the better, as this makes the trigger time less susceptible to noise (which may cause an early or late trigger) by reducing the impact of lower frequency noise (the trigger becomes 'faster' than the noise).

The optical cross-correlator as employed for the time-domain characterization, serves as an effective source for a zero time signal. The full ring-down signal associated with having the etalon mirrors inserted is not required, just one peak, which can be selected by setting the trigger signal level (voltage) to the appropriate level and the scan duration on the digitizer or oscilloscope to the proper number of points and acquisition rate.

As a simple alternative, the fundamental 80 MHz signals from both oscillators' internal (low bandwidth) power monitors were mixed directly. This should yield a frequency component at the repetition rate offset frequency, typically set to 100 Hz. A signal was indeed observed at this frequency, however it was highly noisy and not nearly as stable a trigger source as the SFG cross-correlator with PMT detector.

2.5 Time-Domain Characterization of System Performance with an Optical Cross-Correlator

As noted above in §2.1.1, equation 2.3 is the ideal relationship between the two domains of time—in reality there may be deviations from this relationship. Such timing errors can distort the measured time-domain waveforms and thus effect any spectra derived from them; an experimental check on this timing relationship is important.

An important set of questions concerns how to ensure that the ASOPS system is properly scanning trough delay time, such that the fidelity of the 'true' THz waveforms is preserved. In a typical delay line-based THz-TDS experiment, this would be achieved by utilizing delay stages having high-precision position encoders, such that one can measure stage position changes on the order of several nanometers or less. These encoder signals can be acquired in real-time with the THz data, such that every single THz data point has a precisely measured spatial position which directly corresponds to an amount of optical delay. In the case of ASOPS-based THz-TDS, though, we of course have no such delay line. How else, then, can one measure optical delays to a sub-picosecond precision?

As noted in 2.1.2 above, Kafka et al. [46] with their 'SOS' technique introduced the use of a calibration étalon into the probe arm of a cross-correlator, so as to create a known ultrafast optical delay for time-axis calibration purposes. This general line of thought of using ultrafast delays, in conjunction with cross-correlation, to extract delay-time scan characterization information has been greatly expanded upon since that time. As a reference, G. Sucha reviews [14] a wide range of variations on these techniques. It is therein noted that one can insert an étalon into one arm of the cross-correlator and then acquire, while locked, a continuous run of étalon ring-down scans. Subsequently, peaks can be found, a first-point correction made, much as an oscilloscope trigger would work, and then the RMS variations in arrival times of later, corresponding peaks watched, over the set of scans collected. This is a measurement of scan to scan timing jitter of the system. The plots from such an analysis are recorded in Figure 2.10 as an example of such capabilities. In the dataset shown the scan to scan timing jitter was found to be extremely low over the course of several scans. In this case, there were concerns that the amplifier on the PMT (used to observe the cross-correlations) was of insufficient bandwidth to characterize well beyond the ∼picosecond level, though the measured jitter remained below that floor—this was among the first experimental evidence during the early instrument development that the virtual delay line was working well enough to justify beginning attempts at THz scans. As efforts now turn, in part, to improving upon the THz bandwidth, these types of cross-correlation experiments should be re-examined for the role they can play in helping us to identify the limiting instrumental factors.

2.6 THz Emitter Array

The THz emitter array employed in the present THz-TDS instrument is a commercial product; it is the 'Tera-SED3' from Gigaoptics. Note that this is a company run by A. Bartels and colleagues, who were the first to apply the ASOPS technique to THz-TDS work. The emitter is regarded as a microstructured

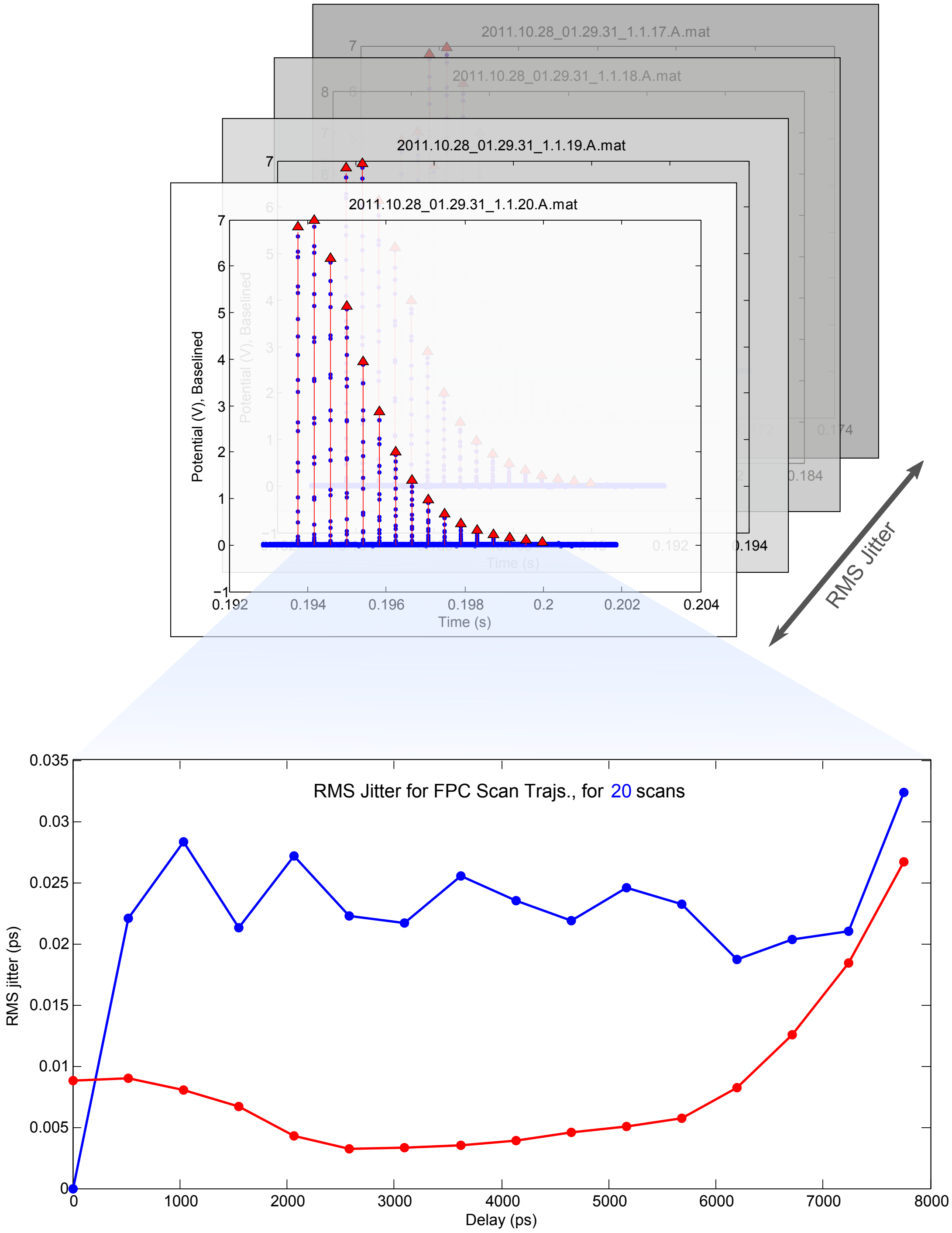

Figure 2.10: Instrument delay scans can be checked with cross-correlator timings. Repetitive etalon ring-downs, top, are aligned to the first peak, as a start trigger, then the between-scan jitter of later peaks is measured and plotted, at bottom. The upper (blue) line is the RMS jitter in picoseconds; the lower (red) line is a measure of the error in the fitting of the peak centers and should remain below the jitter measurements.

large-area photoconductive antenna or photoconductor, and is designed to provide up to, and perhaps slightly beyond, ∼2.5 THz of emission bandwidth using oscillator-class lasers [32]. Such devices can also be used as antenna [56], but it is presently only used as the emitter.

The photoconductive antenna is a widely used method for THz generation and creates THz pulses from transient photocarriers excited by ultrafast laser pulses [57]. In its simplest form, a photoconductive antenna is merely two metal electrodes, spaced by a small gap, and coated on a semi-insulating semiconductor substrate. The electrodes are biased; the required voltage scales with the spacing of the electrodes. Ultrafast lasers illuminate the electrode gap and photoinduce free carriers, so as to act like a very short, transient switch has been closed between the two electrodes. The rush of free carriers across the gap, forced by the applied bias, create a time-varying photocurrent, which in turn creates an electromagnetic pulse with frequency content into the THz. For the interested reader, further technical details are discussed in [57] [27].

In the case of the Tera-SED device, instead of having one large gap, which would require a large external bias, it has many small interdigitated gaps. These much smaller, microscale electrodes enable the creation of high electrical fields at modest bias voltages (e.g., DC 15V).

The model of emitter in the Blake Lab ASOPS-THz TDS instrument can be operated in either of a pulsed or DC/continuous bias mode. Overall, there is an important limit of 0.75 W of total allowable power dissipation on the device that *must* be followed or the device could be destroyed. The product of the bias voltage, the duty cycle, and the average (photo) current must be ≤0.75 W at all times! Further, for the present instrumentation, the electrical bias should be applied continuously. The lower duty cycles enable higher bias voltages and laser powers, but less frequently, so that the time-averaged power dissipation is still ≤0.75 W. Under normal usage, the Tera-SED device is biased with DC 15V and illuminated with approximately a few hundred milliwatts (depending on other experimental conditions), generating a photocurrent of ∼ 50mA; these conditions are similar to those used by A. Bartels with the same type of device [40] [50].

2.7 Purge Box and Sampling Handling

The purge box and sample handling area is of course important for excluding ambient/atmospheric water vapor from the scan path. Further notes on the sample handling, as it pertains to the gas cell and water vapor spectroscopy are discussed further in Chapter 3. The purge box itself is a large acrylic box custom ordered from a company by the name of ‘Cleatech’. This type of enclosure is typically meant to be (and is sold as) a ‘custom desiccator cabinet’, which is appropriate enough, given its function in dry nitrogen purging. The overall box is 25 inches wide by 25 inches deep and 13 inches in height, with one contiguous interior chamber. The side walls are 3/8 of an inch thick and the base was ordered custom with a 3/4-inch thickness.

The latter was done so we could also have deep, custom screw holes put into the base for securing a 2 foot square optical breadboard directly to the bottom of the base. The top of the box functions as a fully removable door, and has foam rubber sealing and latches to help keep a reasonable seal about ambient conditions. The box itself is not directly attached to the table, rather it sits on the table under its own weight (and that of the breadboard, etc.) and small metal plates are screwed into the optical table on sides about the box, so as to prevent lateral motion.

2.8 THz Routing Optics

Recall the overview of the instrument schematic in Figure 2.4. The 'routing optics' term pertains to the optics, primarily off-axis paraboloidal mirrors (OAPMs), in the THz spectroscopy area/subsystem (at right in the figure). The purpose of these mirrors is to collect, size, transport, and deliver the THz beam from emitter to detector, while passing through the sample cell or holder. Paraboloidal mirrors are very convenient for this application; such mirrors have the property that a point source placed at the location of the mirror focus is reflected off the mirror as a nearly collimated beam of light and vice versa [58]. Off-axis mirrors are particularly helpful in this respect, as the focal point lies outside of the mirror body and thus is fully accessible.

The OAPMs in the present design are set up as Gaussian beam telescopes [51] (also known as 4f telescopes), wherein the mirrors are separated by the sum of their focal lengths. Such telescopes, have a few important properties, namely that the magnification is simply the ratio of the second to the first focal length, that the input and output focal lengths remain the same, and that the magnification is wavelength-independent. Overall, these are good qualities in dealing with large bandwidth THz signals. The OAPMs used in the setup are all 2-inch diameter, gold-coated mirrors; some may be protected gold now, and they are generally bought from ThorLabs or EdmundOptics. Metal coated mirrors, in general, act as high-reflectors over a wide bandwidth in the far-IR [59], so THz power losses should not be significant.

Referring to Figure 2.4, the focal lengths of three of the four OAPMs (all but the last/pre-ZnTe OAPM) are four inches; the OAPM just before the EO crystal has a focal length of 2 inches. These OAPMs are positioned to be separated by their focal lengths, so as to create a pair of Gaussian beam telescopes in series.

2.8.1 ITO dichroic mirror

A THz/near-IR dichroic mirror is used within the purged-nitrogen enclosure, in order to recombine the THz and optical probe beams along a common path to the electro-optic crystal; this is the optic labeled as ITO in Figure 2.4. An alternative approach would be to drill a small ($\sim$1 mm) diameter hole straight through an OAPM and take advantage of the fact that the THz beam is generally quite large relative to the optical probe beam, so only a small amount of THz light would be likely to be lost. ITO has been shown to be sufficiently reflective in the far-IR for this purpose up to at least 2.5 THz [60] and Blake group coworkers, using the amplified THz system, have used ITO in the same manner up to several THz. Overall, ITO glass was chosen for its ease of use, wide bandwidth, and of course, its avoidance of having holes drilled in otherwise fine mirrors.

2.9 THz Electro-Optic Detection

The detection of the THz pulses occurs in the 'THz Detection & Recording' subsystem as highlighted in Figure 2.6. Herein, we utilize electro-optic detection to directly measure the electric field—not the average power or intensity—of the propagating THz pulse at a moment in delay time. In the detection process, the probe pulse interacts with a THz pulse via the EO crystal. The electric field of the THz pulse in the crystal at a moment changes the birefringence of the crystal, that is, it changes the refractive index for polarizations along difference crystal axes. The THz field-induced birefringence changes the polarization of the (previously) linearly polarized probe beam. This change in polarization is then converted to a change in intensity upon a detector(s) by a polarization sensitive optical element (a polarization analyzer in general) such as the Wollaston prism shown in Figure 2.4 at upper right before the balanced detectors. During an ASOPS pump-probe delay scan, the changing profile of THz pulses imprints a polarization and thus intensity waveform pattern upon the probe beam, and is read out over lab time [57].

In passing the linearly polarized probe pulse and the THz pulse together through a (for example) [110]-oriented ZnTe crystal (as utilized in the present THz detection scheme), the probe pulse will be probe pulse will experience a phase retardation proportional to the THz electric field at the moment of interaction in the crystal. The probe is then passed on through a quarter wave plate and through a Wollaston prism (generally, a polarizer analyzer). The (single beam) probe transmission is described by [61]:

$$T = \frac{1+\sin\Gamma}{2} \tag{2.4}$$

where the phase retardance of the probe beam is

$$\Gamma = \frac{\pi E_{THz}(t)L}{V_{\lambda/2}} \tag{2.5}$$

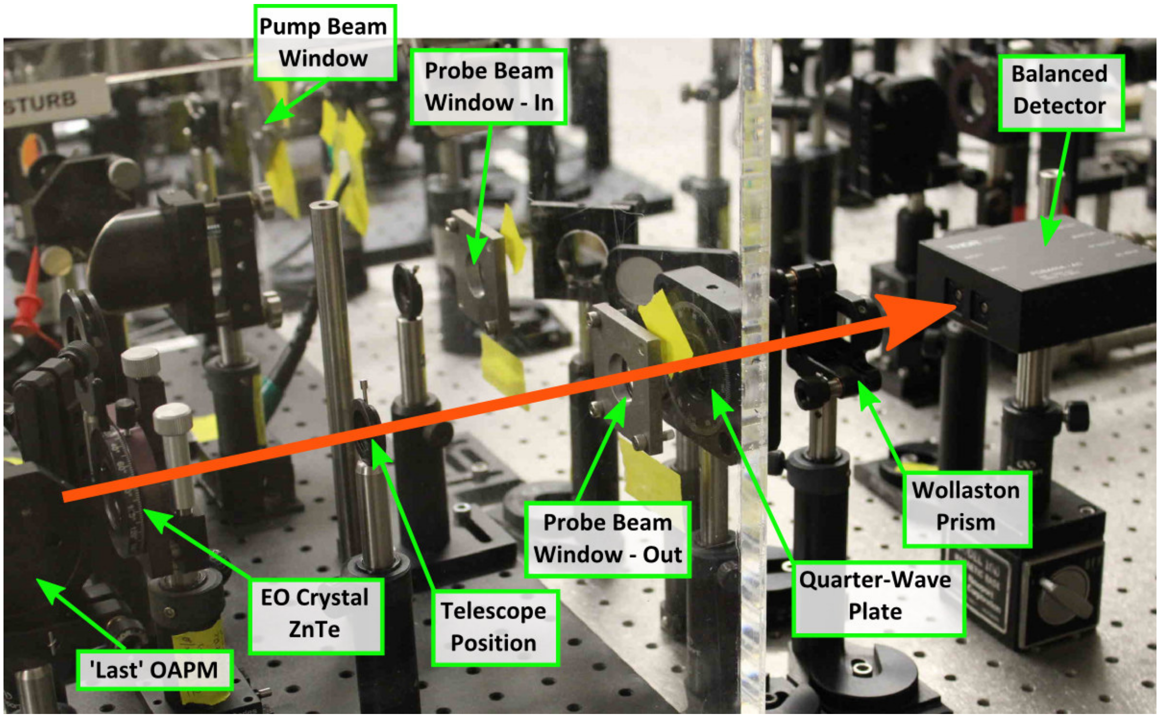

Figure 2.11: The electro-optic detection and recording subsystem; the path of the probe laser beam towards the balanced detector is shown in orange-red.

and L is the length of the EO crystal and $V_{\lambda/2}$ is the half-wave voltage for the EO crystal material. As a reference, $V_{\lambda/2} = 3 \cdot 10^3$ V for ZnTe at a 795 nm probe wavelength. Note that the transmission, T is only approximately linear in response to the THz electric field when $\Gamma \ll 1$, basically a small angle trigonometric approximation. Further ZnTe is typically used as a detector for THz spectroscopy around 2 THz, as the optical-group-velocity is matched to the THz-phase-velocity for light within the tuning range of a Ti:sapphire lasers [31]. The interested reader is referred to [30], for more information on the orientation dependence and alignment of the ZnTe EO crystal in the beampath.

Most all of the THz detection and recording subsystem is shown from a sideways view in Figure 2.11. The orange-red arrow traces out the path of the probe beam as it exits the last OAPM, is focused down upon the EO crystal and passes out of the purging enclosure towards the quarter-wave plate, Wollaston prism and finally, balanced detector. Note that the telescope lenses are absent from the picture, but their position marked—the telescope is set up so the spot size is appropriate for the chosen detector(s) at right. The quarter wave plate is kept outside of the case for ease of adjustment, though the EO crystal mount—which may require adjustment, must stay in the enclosure. Note also in the background, the other windows on the side of the purging enclosure, for the entry of the probe beam as well as the pump beam in the background.

2.10 EO Balanced Detector

In the Bartels et al. Rev. Sci. paper [40], there was a notable difference in the EO setup in their schematic vs. ours. In their instrument the probe beam, following the electro-optic crystal, passed through a half-wave plate and polarizing beamsplitter before being detected by a single detector. This single detector arrangement is an example of a ‘crossed measurement’ [57]. In contrast is the ‘balanced measurement’ as indicated in the main experimental schematic in Figure 2.4. At upper right, in the THz detection subsystem, the probe beam passes through the EO crystal, and after lenses, a quarter waveplate, followed by a Wollaston prism and a pair of balanced photodetectors. The quarter-waveplate is said to ’bias’ the polarization of the probe beam (and this bias can be applied either before or after the EO crystal). The analyzer, a Wollaston prism here, separates out both s and p polarization components so that both may be measured on photodiodes. This balanced arrangement gives better signal, as the signal level is doubled as a difference between two photodiodes, and this differencing also cancels out common mode laser noise (this aspect may perhaps be more important for the present 80 MHz oscillators as opposed to the 1 GHz systems typically used by Bartels et al.). In the cross measurement, the analyzer is set orthogonal to the polarizer before the EO crystal. Any probe light that can leak through the analyzer is then passed on to the detector. Importantly, the measured signal is proportional to the intensity (or square of the field) of the detected THz beam.

Within the balanced measurement scheme, one may use either of two separate photodetectors, or one balanced photodetector. It is generally advantageous to use a balanced detector, as the subtraction of the signal between the two photodiodes is done internally, in a low-noise analog manner, as opposed to after digitization, where the measurement could suffer from additional quantizing noise or additional amplifier noise. In the present instrumentation, a balanced measurement scheme was always employed. However, both of separate photodiodes (ThorLabs PDA36A) and a balanced photodiode (ThorLabs PDB440-AC) have been used. When using the separate photodiodes, each detector gets one of the two input channels on the digitizer and a math channel calculates A-B (after digitization). In this regard, it is more convenient to use the balanced photodetector; only one channel is needed, no extra math channel is required, and the free input channel can be used to simultaneously co-record the cross-correlator data.

2.11 Signal Acquisition

Within the THz detection and recording subsystem, the signal acquisition, as in the digitizer card to use, is an important factor in the quality of the experimental data and the capabilities of the instrument. In looking for a digitizer, had a list of features and specifications in mind:

- *High precision, bit depth $\geq$14 bits:* Preferred at least 14 bits to match capability in Bartels et al. [40] system. Preferred to have low full-scale range options available for weak signals, and a mode(s) where the signal would be digitized as is, without any amplification on the card.

- *Low impedance option, for both of DC and AC inputs:* Having both of AC and DC input is a nice convenience. It seemed that some cards would not offer an AC 50 Ohm port, and that would be useful. In general the AC-coupling and block problematic baseband noise and the low impedance can further reduce noise and improve compatibility with RF electronics.

- *2 channels:* Definitely wanted to have at least 2 channels, as at time of purchase was using separate photodetectors for balanced detection, so that required 2 channels.

- *Sampling rate:* A sampling rate of at least 12.5 MSa/s was desired to ensure sufficient delay time sampling. However, recognized that a sampling rate of $\geq$160 MSa/s would be useful, as would likely be able to measure a frequency domain signal for an 'residual' 80 MHz laser pumping signal that may make it into the ASOPS scan data.

- *External clocking:* For increased accuracy in the timebase for scans, the ability to be externally clocked from a synthesizer or to receive a 10 MHz reference signal at least, would be very useful.

- *Trigger options:* The ability to trigger on either of the sample or on a separate dedicated trigger point is useful, as can then have two real data channels recorded while trigger is watched on a third port.

- *Multiple Records:* The ability to take one scan after another, with little downtime and ideally not having to skip every other scan, does much to save on data acquisition time.

- *Deep memory:* For deep averaging of data on the fly, a lot of memory is necessary, either on card or via streaming to the host computer.

- *Software:* Drivers should be available for the most recent version of computer operating systems. Further there should be drivers and software development kits so the hardware can easily be controlled via C/C++ programming or Labview, at least. And lots of example programs is a plus, as it can cut down substantially on coding time.

This is certainly a technically demanding list of specifications. However, we were indeed able to find a digitizer that satisfied all of these requirements: an AlazarTech ATS9462 digitizer. Specifically, it is a 180 MSa/s 16-bit PCI-express digitizer with 2 data channels. At the time of purchase, this sampling rate was towards the high end of what was available for such a high resolution. All desired input coupling modes were supplied and the sampling rate was more than sufficient. The board could be externally clocked or referenced against our laboratory 10 MHz standard, if need be. The card has a wide variety of trigger options, and scan very quickly, taking records essentially back to back and streaming them all to the memory of its host computer over the fast PCI-e bus. It may seem trivial, but it should be noted that at the time of purchase, this was one of only a few companies that was selling quality digitizers with a PCI-e bus. This level of bus is necessary for sustained streaming of experimental data straight to the host computer's RAM. Otherwise, one would need to start and stop and deep averaging scans would take significantly longer. Or one would have to buy additional on-card memory, which still would take a while to transfer, and which is generally far more expensive than memory for a regular computer. So overall, we have found the technical specifications on this card to be more than sufficient for the ASOPS THz-TDS instrument.

Chapter 3

THz Time Domain Spectroscopy of Water Vapor

The science and technology of THz-TDS are well reviewed in the literature [13, 26, 27] and of course described in chapters 1 and 2 herein. The time-domain implementation of THz spectroscopy is the most commonly used coherent THz technique. The particular details of the experimental implementations will vary, e.g., delay lines or ASOPS may be utilized. In all cases, though, we are acquiring a measurement of the electric field during the time course of the THz waveform. Traditional delay line instruments may typically acquire a total scan duration of roughly 50 ps or less and ASOPS can go much longer, but the underlying principle is the same. The acquired waveform is time domain data and therefore must be Fourier transformed so as to recover the desired frequency-domain spectrum. The present instrumentation is indeed capable of measuring the phase as well as amplitude response of a material, for a full dielectric characterization. However for the present application of the THz time domain spectroscopy of water vapor, and of gases in general for astrochemical studies, the refractive index is generally not of direct concern. Rather, the frequencies of THz transitions are of primary interest. In this manner, we are primarily taking advantage of the broad instantaneous bandwidth and high dynamic range of THz-TDS in general, as well as the higher frequency-domain resolution and frequency precision of the ASOPS technique as applied to THz-TDS.

The spectroscopy of water has been well-studied across the electromagnetic spectrum, from the microwave to the ultraviolet [62], and most of its lines have been incorporated into the the well-known HITRAN database [18], as described further in §3.5.3. Because of the extent of these prior studies, its relatively strong transitions, and its obvious general importance, water is often chosen as a first application of various researchers' THz-TDS instruments, particularly [49] [50] [40] [41]. For example, water was one of the very first molecular samples to be studied by THz-TDS [36]. In our spectroscopy of water vapor we have observed high frequency resolution, accurate line centers, and an apparent free-induction decay (FID) signal [36] [63] in emission. These and other efforts are described herein and our results compared with the prior literature.

3.1 The Nature of Time-Domain THz Waveforms

The instantaneous bandwidth of the THz pulses in THz-TDS are typically quite large (> 1 THz), yet we wish to recover spectroscopic information about each frequency component from the time-domain profile of the pulse. The pulsed THz electromagnetic waveform is composed of a broad spectrum of waves, in phase and propagating together in space. The overall waveform we observe depends on the constituent waves. Each frequency component (and field component, e.g., x, y, z) of the THz electromagnetic wave satisfies the three-dimensional differential wave equation (for free space) [64]:

$$\frac{\partial^2\psi}{\partial x^2}+\frac{\partial^2\psi}{\partial y^2}+\frac{\partial^2\psi}{\partial z^2}=\frac{1}{\upsilon^2}\frac{\partial^2\psi}{\partial t^2} \tag{3.1}$$

or more simply,

$$\nabla^2\psi=\frac{1}{\upsilon^2}\frac{\partial^2\psi}{\partial t^2} \tag{3.2}$$

with the use of the (spatial) Laplacian operator, where x, y, z, and t are spatial coordinates and time, υ is associated with the propagation speed of the wave, and ψ is the wavefunction describing the waves. The simplest waveform, and widely used, is that of a one-dimensional sine or cosine curve, that is sinusoidal waves, also known as harmonic waves [65]. These are generally of the form:

$$\psi = A\sin k_0(x-\upsilon t) \tag{3.3}$$

where A is the amplitude of the wave and k_0 a constant known as the propagation number or wavenumber in vacuum. The wavenumber has a vector form, the wavevector, when using higher-dimensional waves (e.g., plane waves would be an appropriate wavefunction for equation 3.1); the 1D case is sufficient for the present discussion. The wavenumber (or magnitude of a wavevector) is found [65] to satisfy:

$$k=\frac{\omega}{c}=\frac{2\pi\nu}{c}=\frac{2\pi}{\lambda} \tag{3.4}$$

where ω is the angular (temporal) frequency of the wave, ν is the (temporal) frequency of the wave, λ is the spatial period and more commonly known as the wavelength, and c is the speed of light if we now concern ourselves with light waves.

The wavefunction of equation 3.3 consists of just one harmonic wave, that is, a wave having one exactly defined frequency. In this case, the wave defined as such is said to be *monochromatic*. A waveform covering a range of frequencies, such as a broadband THz pulse or white-light optical pulse, can be expressed as a summation over many harmonic terms, each for a different frequency; such a waveform can be said to be *polychromatic*. The polychromatic nature of THz-TDS spectroscopy is one of its benefits, allowing the experimental measurement of optical properties simultaneously over the wide bandwidth for which the probing THz pulses have frequency content. This concept of the physical combination of different light waves to create a net result is known as the *superposition principle*, and it can be said to be the physical manifestation of the Fourier transform.

3.1.1 The Superposition Principle

Referring back to 3.1 and 3.2, it is important to note that this is a linear differential wave equation, in that ψ and its derivatives are only taken to the first power. So if any wavefunction ψ, that is, any single light wave, is a solution of the wavefunction, then any linear combination of such solutions (and light waves) will also be a solution. This concept in optical physics is referred to as the *principle of superposition* [64] and tells us that the resultant or net electromagnetic field at a point in space is an algebraic sum of the separate waves that are simultaneously at that point.

For our large bandwidth THz pulse, as opposed to a theoretical, ideal monochromatic wave, the pulse can be treated as the linear superposition of a continuum of THz frequencies, and mathematically disassembled as such into its component waveforms. Under conditions of very high electric fields, within a medium, the field amplitude may change the properties of the medium in a non-linear manner, and that is the basis of nonlinear optics. For the low THz field strengths involved in the present work (i.e., on the order of a few to 100 V/cm), we are in a linear regime, enabling linear spectroscopy. As such, the overall THz time domain waveform profile will depend, via the superposition principle, on the properties of its component THz waves and their properties of amplitude, phase, and frequency. It is the measurement of these properties that is the core of THz time-domain spectroscopy.

3.1.2 Fourier Analysis

Through the superposition principle, any real wave can be constructed from the appropriate combination of harmonic (e.g., sine or cosine) waves. With proper choice of the frequencies, and corresponding amplitudes and relative phases, to combine in an overall waveform, arbitrary (though mathematically well-behaved) anharmonic, periodic waves can be created. In mathematical terms, this concept is known as *Fourier's Theorem* [64], and the series summation of harmonic terms is known as a Fourier series. The Fourier series has various mathematical representations, including both of a trigonometric and complex form [66, 67]. For the trigonometric form:

$$f(x) \approx \frac{a_0}{2} + \sum_{n=1}^{\infty} (a_n \cos nx + b_n \sin nx) \tag{3.5}$$

where

$$a_n = \frac{1}{\pi} \int_{-\pi}^{\pi} f(x) \cos nx dx \qquad (n = 0, 1, 2, ...) \tag{3.6a}$$

$$b_n = \frac{1}{\pi} \int_{-\pi}^{\pi} f(x) \sin nx dx \qquad (n = 1, 2, ...) \tag{3.6b}$$

And for the complex form:

$$f(x) \approx \sum_{n=-\infty}^{\infty} c_n e^{inx} \tag{3.7}$$

where

$$c_n = \frac{1}{2\pi} \int_{-\pi}^{\pi} f(x) e^{inx} dx \qquad (n = 0, \pm 1, \pm 2, ...) \tag{3.8}$$

The forms are equivalent and related through [67]:

$$c_{\pm n} = \frac{1}{2}(a_n \mp i b_n) \tag{3.9}$$

THz-TDs waveforms, being experimentally acquired, are always real, so that the coefficients c_n and c_{-n} are complex conjugates.

As a brief digression, it is important to stress that the trigonometric and complex forms are equivalent. However, it is the complex form that is typically used in the Fourier analysis of THz (or other) waveforms. In equation 3.7, we see the overall waveform expressed as a summation of exponential terms. Calculations with harmonic waves are can be easier to handle if the harmonic waves are expressed instead in an exponential form (§1.3.3 in [68]). For example, if we have a (monochromatic) harmonic function:

$$V(t) = A \cos(\omega t - \phi) \tag{3.10}$$

It may also be written as:

$$V(t) = \mathscr{R}\left\{\tilde{U} e^{i\omega t}\right\} \tag{3.11}$$

where $\mathscr{R}$ selects the real part and

$$\tilde{U} = A e^{-i\phi} \tag{3.12}$$

$\tilde{U}$ is referred to as the complex amplitude of the monochromatic wave expressed by $e^{i\omega t}$ and consists of an amplitude A and phase ϕ; herein a tilde ($\sim$) is used to denote complex quantities. The amplitude is also known as the modulus or the magnitude of $\tilde{U}$ and the phase is also known as the argument of $\tilde{U}$. Complex coordinates can be expressed in various coordinate systems [66]; the form in (3.12) is the polar representation, given the use of a radius and angle. There is also a Cartesian representation,

$$\tilde{U} = A(\cos(-\phi) + i\sin(-\phi)) = A(\cos\phi - isin\phi) \tag{3.13}$$

where we treat the real and imaginary parts as x and y values, as in $x = A\cos\phi$ and $y = -A\sin\phi$, for the purposes of plotting and vector manipulation. Accordingly,

$$\tilde{U} = x + iy \tag{3.14}$$

$$\overline{\tilde{U}} = x - iy \tag{3.15}$$

(where $\overline{\tilde{U}}$ denotes the complex conjugate of $\tilde{U}$)

$$A = \left|\tilde{U}\right| = \sqrt{x^2 + y^2} \tag{3.16}$$

$$\phi = \arctan\frac{y}{x} \tag{3.17}$$

$$\overline{\tilde{U}}\tilde{U} = x^2 + y^2 = A^2 \tag{3.18}$$

The choice of complex representation, with Cartesian or polar being most popular, is one of convenience for the chosen application; multiplication and division are generally easier in the polar form. This complex representation has its mathematical justification in Euler's formula:

$$e^{ix} = \cos x + i\sin x \tag{3.19}$$

providing the relationship between the perhaps more familiar sin and cos trigonometric functions and the natural logarithm base *e*.

The real part of equation 3.19, as in 3.11, produces just the real $\cos x$, as in 3.10; it should be noted that real-world waveforms will indeed be mathematically real! However, it can be more convenient mathematically to use a complex representation, with the real part being taken at the end of a calculation if calculating a real-world quantity. For example, in this representation, a phase shift of ϕ radians is simply $e^{i\phi}$. This complex representation is used quite frequency in the THz-related research literature.

The observant reader will note that the preceding equations have shifted between the use of x, ωt, and related expressions as the argument of the trigonometric and exponential functions. In all cases, we are representing a quantity of phase (variable or fixed) in radians, with the relationship between angular frequency ω and temporal frequency ν (i.e., the frequency in units of Hz) provided by $\omega = 2\pi\nu$, as in equation (3.4).

Just as waveforms can be physically and mathematically constructed from such series equations, they can also be mathematically decomposed into constituent frequency components of specific amplitude and relative phase. This process of finding the properties of the frequency components for a given waveform is known as Fourier analysis, and a plot of the calculated amplitudes as a function of frequency is a frequency spectrum—and such a plot is the basis of a good deal of spectroscopy! Indeed, it is through Fourier analysis that the experimentally measured THz-TDS electric field waveforms are transformed into the frequency domain for further analysis.

Fourier analysis truly is the mathematical cornerstone of THz-TDS spectroscopy; it is the bridge between our time-domain experiments and our frequency domain analysis, including the extraction of the sample's optical properties. As the THz pump and probe pulses scan past each other in time, we are able to record the THz electric field over a range of delay times, assembling a THz (time-domain) waveform, $E(t)$. An arbitrary THz pulse, or any electromagnetic waveform in one dimension, can be expressed through its Fourier transform representation [69] as:

$$E(t) = \mathscr{R}\left\{\int_0^\infty d\omega\, \tilde{E}(\omega) e^{-i\omega t}\right\} \tag{3.20}$$

In expressing an integration over a continuum of frequencies, we have explicitly moved beyond consideration of a monochromatic wave as in 3.3 or eqs. (3.10) to (3.12), to the general case of a polychromatic, or broadband waveform; equation 3.20 is the polychromatic counterpart to $V(t)$ in 3.11 and is the integral form of the complex Fourier series in 3.7. Also in 3.20, we adopt E as our function name, to remind us we are primarily concerned with an electric field waveform; the use of a tilde as in $\tilde{E}(\omega)$ in 3.20, denotes a complex quantity. $\tilde{E}(\omega)$ is the complex amplitude of each component harmonic and is the polychromatic counterpart of U in 3.12. The complex amplitudes are now found as [57]:

$$\tilde{E}(\omega) \equiv E(\omega) e^{-i\phi(\omega)} = \int_0^\infty dt E(t) e^{-i\phi(\omega)t} \tag{3.21}$$

where $\tilde{E}(\omega)$ is similar to the complex Fourier coefficients of equation 3.8 and provides the 'spectral distribution' of the THz pulse in the (complex) frequency domain; the ω dependence of the amplitude and phase have been made explicit (in contrast to equation(3.12)) to emphasize the polychromatic nature of the waveform—in THz spectroscopy we are very much concerned with both the amplitude and phase as a function of frequency. Indeed, this is the whole basis of THz-TDS.

The Fourier transform converts the temporal domain electric field waveform, as experimentally measured, into a frequency domain spectrum, from which we extract the optical properties of a sample material. The THz pulses we typically use, as noted in chapter 2, consist of only a few cycles of field oscillation or less. Through time-bandwidth relationships, the THz waveforms will have a large bandwidth, typically well exceeding 1 THz.

As with most spectroscopic techniques, it is important to isolate the effects of the sample from the background and to account for all instrumental effects. In terms of instrumental effects, different THz emitters and detectors will have differing emission spectra and response functions. Further, variable humidity along the THz beam path will further effect observed THz signal levels, as noted in chapter 2. THz-TDS, while performed coherently in the time-domain, is nonetheless an absorption technique, and therefore the light source must be well-characterized for proper ratioing of results with a sample in the beam path.

As is typical in spectroscopy, it is thus important to measure the THz waveform of a reference 'sample'. This is simply 'everything' with the exception of the sample, and for solid samples can simply be free space. However, for gases, particularly water vapor as is the present focus, a sample cell is necessary for isolation and pressure control—as discussed in section 3.3.1.1. In this case, the reference sample is the empty cell. The empty cell must first be measured, followed by the gas-loaded cell, yielding sample and reference electric field waveforms $E_s(t)$ and $E_r(t)$. Since this is time-domain data, as opposed to the frequency (equivalently wavelength) data normally obtained in a transmission or absorption experiment, a different analysis procedure must be followed to find the material properties; one cannot simply divide the time-domain data. This processing for material properties is detailed further in section 3.1.3.

3.1.3 Electric Field Frequency Components and Dielectric Properties

It is important, though perhaps obvious, to note that being an absorption technique, we must first obtain both of sample and reference electric field waveforms $E_s(t)$ and $E_r(t)$, respectively, in order to have sufficient information to extract the material properties from the sample.

The Fourier analysis of these waveforms will yield a reference and sample spectra:

$$\mathscr{F}\{E_r(t)\} = \tilde{E}_r(\omega) = E_r(\omega)e^{-i\phi_r(\omega)} \tag{3.22a}$$

$$\mathscr{F}\{E_s(t)\} = \tilde{E}_s(\omega) = E_s(\omega)e^{-i\phi_s(\omega)} \tag{3.22b}$$

where we have defined the operator $\mathscr{F}$ as that of the Fourier transform. And note that in the complex representations above, we can clearly identify the frequency-dependent amplitudes of each of the sample and reference, $E_s(\omega)$ and $E_r(\omega)$, as well as the relative phases of their frequency components, $\phi_s(\omega)$ and $\phi_r(\omega)$.

Proper analysis of sample and reference waveforms requires consideration of the THz detection process and the interactions of the THz pulse with the sample and other optical elements in the beam path. The detection of the THz waveforms, as discussed in chapter 2, relies upon the interaction of the THz pulse and the optical probe pulse (also known as the gate or trigger pulse) simultaneously on the detector. This may result in a transient photocurrent on a PC antenna, or a change in polarization of the probe pulse if an electro-optic detection scheme is employed. However, the EO probe pulse is of finite duration and temporal profile with non-ideal interactions in the detector crystal [57], and a PC detector will, in an analogous manner, experience a transient photoconductance. As in [27, 70, 71], the reception and sampling of the detection process can be modeled as a time-dependent window, $G(t)$ that is mathematically convolved with the 'true' THz time-domain waveforms incident upon the detector and associated with the reference and sample, $E_{r,true}(t)$ and $E_{s,true}(t)$, respectively. This is represented below, where $E_{THz}(t)$ can be either of the observed sample or reference signals:

$$E_{THz}(t) = \int_{-\infty}^{\infty} E_{THz,true}(t') \cdot G(t'-t)dt' \tag{3.23}$$

For spectroscopic purposes, of course, it is desired to obtain the properties of the sample independent of those of the particular detector used or other environmental perturbations and changes, which will effectively change the detector response function. To proceed further in understanding the data processing, it is useful to consider the optical transmission through the sample in terms of frequency domain (and dependent) complex transmission functions. This approach largely follows that of [70]. In this domain, the effect of the detector can be found by taking the Fourier transform of its time response profile, just as we do for the measured THz time-domain waveforms:

$$\mathscr{F}\{G(t)\} = \tilde{G}(\omega) = G(\omega)e^{-i\phi_G(\omega)} \tag{3.24}$$

Likewise, the sample has its own frequency-dependent complex transfer function:

$$\tilde{H}(\omega) = H(\omega)e^{-i\phi_H(\omega)} \tag{3.25}$$

And $\tilde{H}(\omega)$ is of course the unknown quantity we wish to experimentally obtain. From $\tilde{H}(\omega)$, the optical properties of the sample can be calculated; the amplitude $H(\omega)$ plotted as a function of frequency is the THz spectrum of the sample.

The sequential transmission of light, THz or otherwise, through a sample and other optical media can mathematically be expressed as sequential, time-domain convolutions, as in the convolution of the true THz waveform and the detector response in equation 3.23. Rewriting that equation, using the convolution operator, we have:

$$E_{THz}(t) = E_{THz,true}(t) \circledast G(t) \tag{3.26}$$

Importantly, the Fourier transform converts time domain convolutions to frequency domain products, via what is known as the convolution theorem (§15.5 in [66], §11.3.2 in [72]). The theorem states that for a function $g = f \circledast h$,

$$\mathscr{F}\{g\} = \mathscr{F}\{f \circledast h\} = \mathscr{F}\{f\} \cdot \mathscr{F}\{h\} \tag{3.27}$$

In applying this theorem, we change a convolution in one domain into a product in another; this can be quite useful mathematically, as products are generally easier to manipulate than convolutions. Applying this theorem to (3.26) yields:

$$\mathscr{F}\{E_{THz}(t)\} = \mathscr{F}\{E_{THz,true}(t) \circledast G(t)\} = \mathscr{F}\{E_{THz,true}(t)\} \cdot \mathscr{F}\{G(t)\} = E_{THz,true}(\omega) \cdot G(\omega) \tag{3.28}$$

In the frequency domain representation, the light-matter interactions are represented simply by multiplication of the appropriate transfer functions for each optical element, including the sample. As in [70], we can express the measured THz waveforms in terms of their ’true’ waveforms and their interactions with both of the sample and detector:

$$\tilde{E}_r(\omega) = \tilde{E}_{r,true}(\omega) \cdot \tilde{G}(\omega) \tag{3.29}$$

$$\tilde{E}_s(\omega) = \tilde{E}_{s,true}(\omega) \cdot \tilde{G}(\omega) = \tilde{H}(\omega) \cdot \tilde{E}_{r,true}(\omega) \cdot \tilde{G}(\omega) \tag{3.30}$$

In 3.29, we see that the measured reference THz, in the frequency domain, is simply the product of the ’true’ reference signal and the response of the detector (and rest of the instrument). In 3.30, the measured sample waveform, when converted to the frequency domain, is simply the product of the ’true’ sample signal and the detector response. However, in the second part of 3.30, we can see that mathematically, this is equivalent to the observed reference signal 3.29 with the additional factor for passage through the sample as well. (Reflections of the THz pulse by/within the sample can complicate this analysis as discussed later in this section.)

In 3.29 and 3.30, the desired quantity for sample information is $\tilde{H}(\omega)$. It follows simply that,

$$\tilde{H}(\omega) = \frac{\tilde{E}_s(\omega)}{\tilde{E}_r(\omega)} = \frac{E_s(\omega)}{E_r(\omega)} e^{-i(\phi_s - \phi_r)} \tag{3.31}$$

Separating $\tilde{H}(\omega)$ into the amplitude response and the phase change of the sample pulse relative to that of the reference yields:

$$H(\omega) = \frac{E_s(\omega)}{E_r(\omega)} \tag{3.32}$$

$$\phi_H = \phi_s - \phi_r \tag{3.33}$$

The above analysis reveals an important aspect of experimental THz-TDS. In 3.23, and 3.30, it is assumed that the THz detector (and the rest of the instrument) have a linear response to the THz electric field of the THz waveforms detected. Such a linear response, as well as a response with sufficient bandwidth (or speed in the time-domain) are the main requirements for a THz-TDS detector. Whether that fast, linear response is provided by an electro-optic detector or a PC antenna, etc. is not of consequence for the purposes of this analysis. Further, in 3.30, it is also implicit that the response of the material to the probing THz radiation is linear. That is, that the transfer function $\tilde{H}(\omega)$ of the material is independent of THz probing field strength, yielding the same result in 3.32 regardless of the brightness of the THz light source used in the experimental apparatus. For the quantitative treatment of pathlengths and absorption coefficients, it is assumed that the THz pulse is essentially a plane wave illuminating the sample at normal incidence, so that the observed transfer function can properly be related to the experimental pathlength. For all scans, particularly between corresponding pairs of sample of reference scans, it is important that the THz polarization state (e.g., linear, elliptical, etc.) be consistent and fixed with respect to the detector, as both of electro-optic crystal detectors and PC antennas have an optical axis and response function dependent upon its orientation relative to that of the THz polarization. If one is studying condensed phase samples, it is ideal to have a linear polarization in the THz pulse, with attention to sample orientation, in case of any anisotropy in the sample (e.g., birefringence). For the present study of gases, it is sufficient to ensure that the emitter and detector orientations are fixed between corresponding sample and reference scan pairs.

In terms of the extraction of the optical properties of our sample from its transfer function, $\tilde{H}(\omega)$, we require a way to connect the amplitude reduction of 3.32 and the phase change of 3.33, to the more familiar spectroscopic quantities of the absorption coefficient and the index of refraction. The linear response of a sample in a light-matter interaction is typically expressed as a single quantity, the complex index of refraction [73], with real and imaginary parts to describe the phase velocity and absorption properties of an optical medium. This is simply expressed as:

$$\tilde{n} = n - i\kappa \tag{3.34}$$

In (3.34), each of the real index of refraction, n, and the imaginary part, κ, are of course frequency dependent, however this is not explicitly written by convention. The real index is as normal and describes the phase retardation of the THz waveform and its components; the phase velocity of the THz light will differ between that in a vacuum and in a sample. Further κ is defined such that,

$$\alpha = \frac{2\omega}{c}\kappa = 2k\kappa \tag{3.35}$$

where α is the usual absorption coefficient, from Beer-Lambert's law [19]:

$$I = I_0 e^{-\alpha d} \tag{3.36}$$

where I and I_0 are the transmitted and incident light intensities, respectively, d is the pathlength of the medium. The absorption coefficient, α is related to molecular properties via concentration or number densities via:

$$\alpha = \varepsilon p = \sigma N \tag{3.37}$$

where ε is the molar absorption coefficient (typically in units of liter mole^{-1} cm^{-1}), p is the concentration (moles per liter), σ the molecular absorption cross section (cm^2) and N the number density of molecules of the proper type and state to absorb (molecules per cm^3); the latter form is most appropriate for the present work with gaseous samples.

In the frequency-domain, complex transfer function approach to light-matter interactions, as utilized in 3.24 to 3.33 above, the transfer function of the sample, $\tilde{H}(\omega)$, can be expressed as [74]:

$$\tilde{H}(\omega, d) = \exp\left[-i\frac{\tilde{n}\omega d}{c}\right] = e^{-\kappa k d} e^{-inkd} \tag{3.38}$$

This is the propagation coefficient, or transfer function, in a medium of complex index $\tilde{n}$ over a distance d; recall the wavenumber k from equation (3.4). The single exponential in the middle of (3.38) is expanded as a product of exponentials on the right-hand side of that equation, with the first factor characterizing optical attenuation in the sample via the imaginary part κ and the second factor, as a completely imaginary exponential, is a linear phase shift induced by the real part of the index.

The absorption coefficient α and absorption κ can then be calculated, from the experimental data in $\tilde{H}(\omega)$, as [73]:

$$\kappa = \frac{\alpha}{2k} = -\frac{1}{2dk}\ln(\overline{\tilde{H}(\omega)}\tilde{H}(\omega)) \tag{3.39}$$

and the index as (given the index of the reference, n_r):

$$n = n_r - \frac{1}{kd}\phi_H \mod 2\pi \tag{3.40}$$

There is ambiguity in the extraction of the material (real) index as the phase of a frequency component could shift, relative to reference, by periods of 2π, and our Fourier analysis will still yield a phase change in the interval of one such cycle (this is related to the mathematical property that the natural logarithm of a complex number is a multi-valued function). In a single measurement of a single THz waveform, this uncertainty cannot be resolved. There are experimental and modeling approaches to this issue (e.g., [73]), however for the present work in gases, we are generally concerned with the frequencies of spectral peaks, and to some extent with the absorption strength; the index properties are generally beyond the scope of this work. However, a frequency-independent approximation for the real part of the complex index can be made based upon the shift in time, Δt, of the peak THz field in the time domain, between sample and reference waveforms,

$$n \approx n_r + \frac{c\Delta t}{d} \tag{3.41}$$

It is important to note that the equations for the absorption and index of refraction, 3.39 and 3.40, are themselves approximations. This inexact nature is due to THz reflections within the sample, though 3.39 is generally reasonable for gases. In the general case, for any sample, the ratio of the Fourier transforms of sample and reference waveforms, the complex transfer function $\tilde{H}(\omega)$ as in 3.31 (also known as the complex transmission coefficient), does indeed contain complete information about a sample's complex index of refraction. In the general case, though, there are Fresnel reflections at material interfaces, be it between a solid sample and the surrounding air or vacuum, or between a gas sample and its windows, as well as the surrounding interface between those windows and air. The Fresnel reflections are of course a loss mechanism in the incident THz pulse that should be accounted for, with the losses at the sample interface depending on the complex index of the sample which we wish to find. That is, the reflection losses will be different for sample and reference measurements, and this cannot be corrected in the experimental design. The reflections, both backwards and forwards, appear in the time domain as temporal echoes and are the time domain manifestation of the Fabry-Pérot effect.

A complete treatment of these effects, requires a more detailed optical transfer function than that described in equation 3.30. There, we considered the functions of the detector and sample only; additional factors such as optical interfaces were excluded. The full consideration of these factors and the extraction of the complex index of refraction from the ratio of sample and reference Fourier transforms requires the introduction of additional factors into the system transfer equation. This creates a complicated inverse problem to solve and requires a modeling and fitting approach. Some modeling approaches require initial guess values for fitting, the choice of which can bias the results. In other cases, the models may fail to converge on a solution. These issues have been discussed in the literature, and there have been some recent efforts to improve these extraction methods; the interested reader is referred to [73–76]for further information on these procedures. In optically thick samples, where the reflections through the sample are well separated in time, temporal windows, prior to Fourier analysis, can be used to remove Fabry-Pérot considerations from the analysis, though highly dispersive samples can be problematic. For the present case of THz-TDS of gaseous samples, the generally small index change between the sample and its surrounding cell helps to minimize any differences between the sample and reference scans; Fabry-Pérot effects dependent on the sample are greatly reduced. Indeed, previous workers [36] and our present work have found these effects to divide out, in the frequency domain, between sample and reference scans.

3.1.4 Implementation and Characteristics of the Fourier transform in Spectroscopy

In equation 3.21 for the complex amplitudes, $\tilde{E}(\omega)$, a time-domain integration from zero to infinity was employed; similarly, in 3.20, a frequency-domain integration from zero to infinity was made to include contributions of all frequency components from zero (i.e., DC or direct current) to infinity. Needless to say, in the real world we cannot consider infinitely long experiments nor is it reasonable to investigate the gamma-ray contributions to our THz spectra. So the frequency bandwidth and measurement time in our experiments will be appropriately limited. The Fourier transform is a mathematical operation linking the domains of space and time. In the 'mathematical machinery' of Fourier analysis are fundamental relationships between waveform duration, spectral resolution, sampling time, and bandwidth. These relationships are of great importance in the practical application of Fourier transform spectroscopy, and they describe the tradeoffs in considering finite durations in the measurement of the THz waveforms and finite bandwidth spectral contributions to these waveforms.

One of the most important aspects of the Fourier transform to the practicing spectroscopist is that of the frequency-domain spectral resolution. The resolution obtained in Fourier analysis, as well as the bandwidth are determined by the sampling parameters for the THz waveform; this is discussed further in §3.1.4.1 below.

3.1.4.1 Bandwidth and Spectral Resolution

The experimental spectral resolution is of the utmost importance in the present application of gas-phase spectroscopy. Spectral features in the condensed phase considered to be 'sharp' or 'narrow' have linewidths on the order of tens of GHz; features often can exceed 100 GHz in width. In the gas phase, particularly at pressures of order of a few Torr, or much less, pressure broadening of spectral features is much reduced and spectral features can have linewidths of a few hundred MHz or much less, falling below 1 MHz at pressures in the millitorr regime where Doppler broadening, not pressure broadening, is the dominant contribution to the linewidth. The narrow gas-phase spectral features of water vapor and other gases present a technical challenge to traditional THz-TDS, where a spectral resolution of 1 GHz would be considered 'high' and scans are often taken with a resolution an order of magnitude worse (or more). This level of performance is adequate, of course, for condensed phase samples, but has perhaps limited the application of THz-TDS to gas phase samples. High spectral resolution, relative to the spectral linewidths, is of course desired for accurate measurement of the line profiles in pressure broadening studies. However, even if one is interested primarily in peak center frequencies for producing line lists of interest to astronomical studies, as in the present application, peaks can typically be fit to a precision on the order of the measured linewidth divided against the signal to noise of the measurement. If spectral peaks are broadened by limited instrument response, this will then make it more difficult to accurately determine the peak location.

The source of the spectral resolution problem lies in the very time-domain nature of the THz-TDS technique and the Fourier transform. From a mathematical perspective, Fourier analysis is expressing the measured waveform in a basis set of sinusoidal functions of various frequencies. In the Fourier coefficient equations above (see 3.6a, 3.6b and 3.8), we see that the basis functions come in integer multiple frequencies. The lowest nonzero frequency is that having a period equal to the duration of the measurement window (the bounds of integration in the coefficient equations above); all other basis frequencies are integer multiples of this lowest frequency component. The finest frequency step, that is, the resolution, is then that frequency associated with the inverse of the measurement duration [57]:

$$\delta \nu = \frac{1}{T} \tag{3.42a}$$

$$\delta \omega = \frac{2\pi}{T} \tag{3.42b}$$

where we have spectral resolution in terms of the (temporal) frequency and the angular frequency and T is the scanned range or duration of the THz waveform; note the temporal frequency, not the angular version, is typically discussed. For example, if a scan range of 50 ps is used (as is often for condensed phase work), then the spectral resolution will be 20 GHz. Likewise, 1 ns of measurement duration will yield 1 GHz resolution. And for the present instrumentation, a full scan window of 12.5 ns would yield 80 MHz spectral resolution (i.e., the repetition rate of the pump laser). Multiple reflections in the sample, as discussed above, can complicate the analysis of condensed phase samples, and if simple time windowing is used to ignore these effects, this can therefore degrade spectral resolution [27]—though high resolution is typically not required for such samples.

Looking at the spectral resolution from a more physical, qualitative perspective, it may be intuitive that when observing these repetitive THz waveforms, that the lowest frequency we could hope to measure would be one that 'fits' completely, in terms of a full cycle, in our measurement window. With a 12.5 ns time window, for example, we would not actually be measuring any 80 MHz signal, but each frequency step or bin in the Fourier analysis would be 80 MHz apart. So our first frequency bin would be at 0 Hz (DC) and then 80 MHz, 160 MHz, 240 MHz, and so on. In this manner, our regular THz probing can be thought of as a THz frequency comb, with the comb teeth centered at each frequency bin (80 MHz apart in this example).

Our Fourier analysis results will indeed have frequency bins at 0, 80 MHz, 160 MHz, etc., though we do not expect to see any signal at these very low frequencies; they are beyond the ability of the instrument to produce, transmit efficiently, or detect. So there is a difference between the frequencies that we could in principle observe given the mathematics of Fourier analysis, and those that we can actually observe given the experimental apparatus. The frequency range useful for spectroscopy is referred to as the instrumental bandwidth. On the high frequency end of this, the limiting concerns again include the response of the THz emitter and detector. However, as opposed to the low frequency end, we do have a somewhat more important mathematical limitation in terms of the speed of the electro-optic sampling of the THz waveforms, with higher sampling rates required for the measurement and Fourier analysis of higher frequency components of the THz waveform.

In the THz spectroscopy of water vapor or any other material, the THz waveform electro-optically detected will be a waveform of a wide bandwidth. In order to accurately measure all of those frequency components, it is perhaps intuitive that our sampling of that waveform at least be faster than the temporal period of the highest frequency THz component present in the waveform. In electronic measurements, the quantitative formulation of this idea is referred to as the Nyquist sampling theorem [43]. Specifically, we have to sample a waveform twice as fast as the highest frequency that we wish to be able to 'see' in the Fourier analysis of the waveform. In the case of our THz waveform, the situation is a bit more complicated than usual, given the discrete laser pulsing (as discussed in Chapter 2), but overall, we are (via electro-optic detection and digitization) sampling a THz waveform at a finite number of discrete points. Given the (unsampled) time between samples, known as the sampling interval Δt, then the sampling rate is given simply by:

$$\nu_s = \frac{1}{\Delta t} \tag{3.43}$$

and is the temporal frequency at which the waveform is sampled. From the Nyquist sampling theorem and its factor of two, we can simply state the Nyquist frequency:

$$\nu_N = \frac{1}{2\Delta t} = \frac{\nu_s}{2} \tag{3.44}$$

Given a particular sampling rate, we will only be able to 'see' waveform frequency content if its frequency is less than or equal to that of the Nyquist frequency; Fourier analysis of such an acquired signal will yield zero amplitude for all higher frequency components. So for example, if our THz waveform has frequency content up to 3 THz, then we must sample that waveform at ≥ 6 THz, that is, there must be $6 \cdot 10^{1}2$ samples acquired per second, also described as 6 terasamples per second or 6 TSa/s. Frequencies falling above the Nyquist frequency will not be measured at their proper frequency, but will instead 'fold-over' or 'alias' [77] [43] into lower frequencies. Given the high (THz) frequencies presently discussed, this might seem to be a relevant concern. However, given the nature of the ASOPS effect and speed of digitizer employed (as discussed in Chapter 2), the THz waveforms herein are actually well oversampled; this is discussed further below in the experimental details of the water vapor spectrum acquisition.

The sample duration and sampling time are illustrated in Figure 3.1, with the waveform obtained from the actual time-domain trace for low pressure water vapor. In the figure inset, we see a zoomed-in portion of the main THz peak, wherein the actual experimental data points have been marked. The closest spacing between points is the sampling interval, Δt, and sets the mathematical upper limit to the meaningful bandwidth of the THz-TDS measurement. The overall portion of the waveform upon which Fourier analysis is to be performed is enclosed by brackets; this is the sampling duration, T, and defines the spectral resolution of the THz-TDS measurement. A further discussion of the numerical details of this analysis continues below in §3.4.1, and experimental details of the sampling rates are discussed below in §3.3.1.2 and §3.3.2 regarding the 'lab-time' and ASOPS-scaled 'delay-time' sampling rates, respectively.

In summary, the 'physical' THz bandwidths of the instrumentation—the emitters, transmission optics, detectors—is an important factor in the spectra we observe, however the acquisition parameters of that spectrum—including the temporal duration of the measurement, the sampling rate, and other Fourier analysis parameters, will have an important role in ensuring we have sufficient resolution and bandwidth to properly measure spectroscopic information. This is further discussed in below, in the present case of THz-TDS spectroscopy of water vapor, in the experimental section.

3.2 Overview of Experimental Procedure

The overall experimental procedure in terms of the collection, processing and analysis of THz waveforms is diagrammed in Figure 3.2. Overall, the tasks or steps can be grouped into three main areas: the initial preparation, including acquisition, of the THz time-domain waveform(s) (plural as there are both of sample and reference waveforms, as well as perhaps having multiple samples), followed by a discrete Fourier transform, and then the analysis of the spectra. The discrete Fourier transform bridges the time and frequency domains,

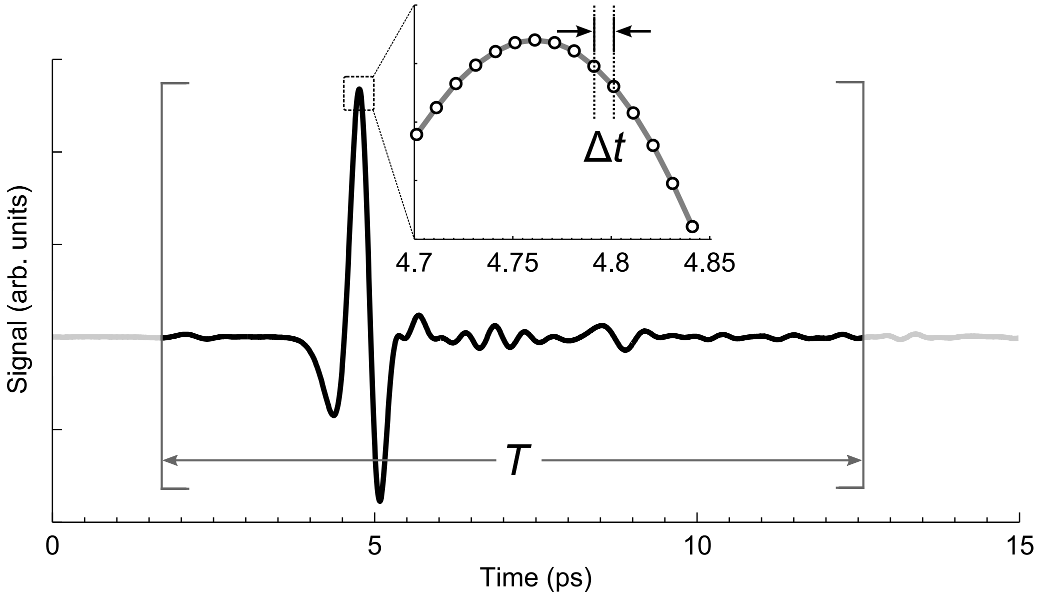

Figure 3.1: A water vapor THz-TDS time-domain waveform, with the sample duration, T, and sampling time Δt illustrated.

from the initial time-domain processing, to the subsequent frequency-domain analysis.

The three main areas of the experimental procedure are discussed in the following sections, including: “THz Time-Domain Waveform Preparation (§3.3), “Discrete Fourier Transform” (§3.4), and “Spectrum Analysis” (§3.5).

As an overview, the general theme is that the experimentally-acquired THz waveforms must be properly prepared for the discrete-sample Fourier transform into the frequency domain. After correction of the spectrum against a reference scan to remove the background, the resulting spectrum is ready for further analysis. It is upon this spectral data that various numerical fitting and measurement techniques can be applied, depending on the desired spectral information.

The first area of work in the experimental procedure is the initial preparation of the time-domain THz waveforms; this is diagrammed in the shaded box at upper left in Figure 3.2. The main goals of this set of tasks include the experimental acquisition and the proper ’pre-processing’ of the acquired time-domain THz waveforms for later Fourier analysis and conversion to frequency-domain data.

The second major area of work in the processing algorithm is the Fourier analysis of the time-domain data to bring it into a frequency-domain representation; this is shown at upper right in Figure 3.2; the data may be further prepared, prior to the transform, by ’zero-padding’, as discussed further in §3.4.3. An important aspect to note is that in the introductory discussion of the theory of Fourier analysis above, those equations assume a function $f(x)$ that is mathematically ’well-behaved’, including that it is a continuous function, in

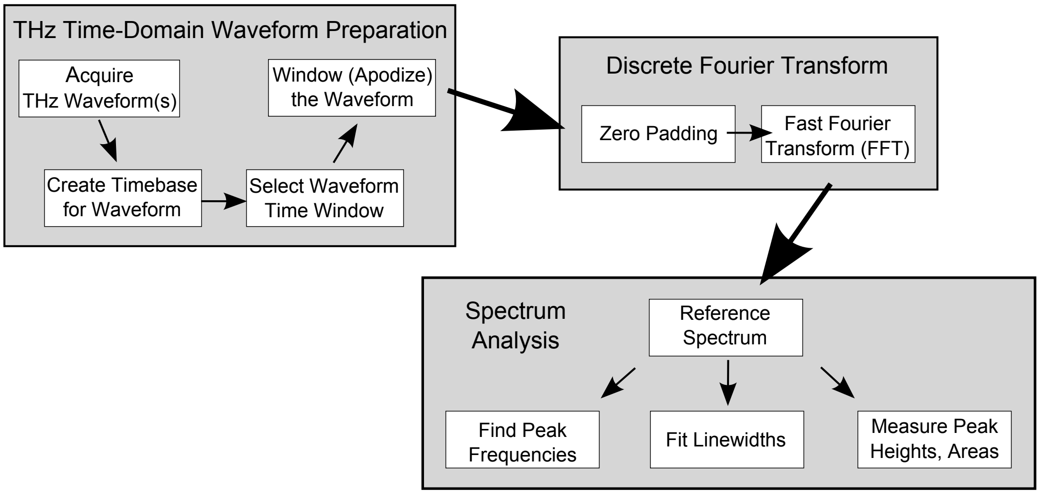

Figure 3.2: The overall experimental procedure in terms of the collection, processing and analysis of THz waveforms. There are three general areas of work, as shown in the shaded boxes. The THz time-domain waveforms are first acquired and prepared for subsequent Fourier transform to the frequency domain, followed by various spectral analyses.

our present case of time. Experimentally acquired data, as noted in 2, consists of discretely sampled time points. As such a different form of Fourier analysis, building on that discussed above, and known as the discrete Fourier transform, is required. This is discussed further, below in §3.4 and §3.4.1.

The third and final major area of work in the processing algorithm is the spectral analysis of the now frequency-domain data; this is diagrammed as the shaded box at lower-right in Figure 3.2. This area of work includes the comparison of the acquired (spectral) data against a reference dataset to remove instrumental effects, followed by one or more spectral analysis techniques. The chosen techniques depend on the desired application; for the present efforts, the frequency locations of spectral peaks of water vapor are sought, so a peak-finding algorithm is applied—this is discussed further in §3.5.

3.3 THz Time-Domain Waveform Preparation

In this first area of work, the goal is the basic experimental acquisition of the sample and reference THz waveforms and the subsequent pre-processing so that we have a time-domain dataset ready for the next part, the Fourier analysis. While all three parts of the experimental procedure as shown in Figure 3.2 are required for a full analysis, this first part should be viewed with particular importance due to its inclusion of the experimental data acquisition. Following the collection of proper reference and sample waveforms, the subsequent analysis steps can be (re-)performed as desired. That is, one can easily re-sample the raw time-domain data, re-run the Fourier transform with different parameters, or perform a different set of spectral analysis techniques. The key is that there must be a quality experimental dataset for these later analysis steps. This is discussed further in the first step of this part, the “Acquisition of THz-TDS Waveforms” in §3.3.1.

The reference and sample waveforms initially acquired are digital waveforms having a timebase in the laboratory time frame. That is, in microseconds or nanoseconds of lab time between samples, instead of picoseconds or femtoseconds between samples in the ASOPS sweep through delay time. The next step in the preparation of the THz waveforms is therefore to create a proper timebase in steps of delay time; this is discussed further in §3.3.2, “Creating a Timebase for THz Waveforms”.

Once the THz waveforms are acquired and provided with a proper timebase, we can then select the time window in these waveforms that we wish to further analyze in later parts and steps. The experimenter may wish to truncate or otherwise select a time-reduced portion of the waveforms for a variety of reasons. In the present effort of THz spectroscopy of water vapor, this step is, in part, motivated by its impact on the results of the FFT analysis. As such, the discussion of this time selection is deferred until after the basics of the FFT analysis have been explained, see §3.4.4, “Selecting the Waveform Time Window”. And lastly, for this first part, there is the related step of potentially ’windowing’ or apodizing the data to effect the peak line-shapes and reduce the potential for frequency domain ’ringing’. As with time-windowing, this step is motivated by the details of its impact upon the FFT analysis, and so is discussed after the FFT analysis, in §3.4.5, “’Windowing’: Apodizing the Waveform”.

3.3.1 Acquisition of THz-TDS Waveforms

There are two main aspects to the acquisition of the THz-TDS waveforms. First, there are the specific digitizer settings selected. And secondly, there are the details of the sample (gas) handling and conditions. These are discussed, in turn, in the following subsections.

3.3.1.1 Sample Gas Handling

Recall that the overall instrumental schematic is shown in Figure 2.4. At right in this figure was the nitrogen-purged enclosure where spectroscopic measurements are to be taken. However, absent from that diagram was any sample or holder, etc. Solid, liquid, and gaseous samples can all be studied with the THz spectrometer, dependent only on the proper sample holder or cell and its placement in the THz beam path. These details are now discussed for the present case of a gaseous sample, particularly the present application of the THz spectroscopy of water vapor.

A new view of the instrumental schematic is shown in Figure 3.3. At left in that figure, we have a (faded) view of some of the optical path for the delivery of the pump and probe (optical) pulses for THz generation and detection. At right, though, we have an expanded view of the nitrogen purge box and additional apparatus for the handling of gaseous samples. Specifically, a sample cell has been placed in the THz beam path (path shown in purple). The cell is placed between the second and third off-axis paraboloidal mirrors (OAPMs) that form the double-4f or double Gaussian-beam telescope that collects, shapes and directs the THz beam. This point puts the cell between the two 4f telescopes, providing access to an (ideally) frequency-independent beam waist. The smaller size of the beam at its waist is advantageous, in general, for smaller samples (e.g., the small spintronics-related sample discussed in 4.2).

In the present case, though, the smaller waist is useful in that the beam remains at a relatively small size, along the axial direction, before and after the location of the waist along the optical axis. The smaller size of the beam around the waist thus enables the use of smaller diameter sample cells for liquid and gas samples, while still allowing the cells to have a reasonable pathlength about the waist position. Smaller diameter sample cells may be advantageous if the sample material is hard to obtain and/or expensive, or if the sample cell windows (or body) are constructed of an expensive material (e.g., large crystalline quartz windows can become prohibitively expensive as compared to smaller diameters). In the present case, the sample cell, as diagrammed in Figure 3.3 and pictured in Figure 3.4, is simply an acrylic tube with thin polyethylene windows epoxied to both ends and an internal in-gas pathlength of 13.7 cm. Placing the cell at the beam waist conveniently allowed the use of this pre-existing cell instead of fabricating something larger in diameter for placement in the collimated beam region between the first pair of OAPMs.

As shown in Figure 3.3, a network of tubing connects the sample cell to additional gas handling apparatus. Attached to one port of the sample cell is a sensor for monitoring its internal pressure from the sample gas/vapor. The pressure gauge is placed as close as possible to the cell to ensure accurate measurements. Further the Baratron-type of pressure sensor, an example of a capacitance manometer, is utilized as this class of sensors is regarded for their ability to operate over a few orders of magnitude, to hold their calibration well, and their fast response time ($\ll$ 1 second) [58]. A mix of $1/4$" polyethylene and stainless-steel tubing is used to make most of the connections between the sample cell and the pressure gauge, valves, and sample reservoir. The connection to the turbopump is through a series combination of the plastic tubing and a $>$1m length of larger-diameter conflat-fitted tubing. In isolation, this would be a less-than-ideal vacuum connection, but in the present setup, this allows the vacuum connection to be connected and disconnected easily as needed so it can be shared between the ASOPS instrument table and another experiment presently on an adjacent table (the astronomical ices project described briefly in 1.2, also see [38], [33], [78]). Potential improvements to this present arrangement are discussed further in chapter 5 concerning future directions.

Returning to the sample, the present study of water vapor enables the liquid sample to be held in a simple

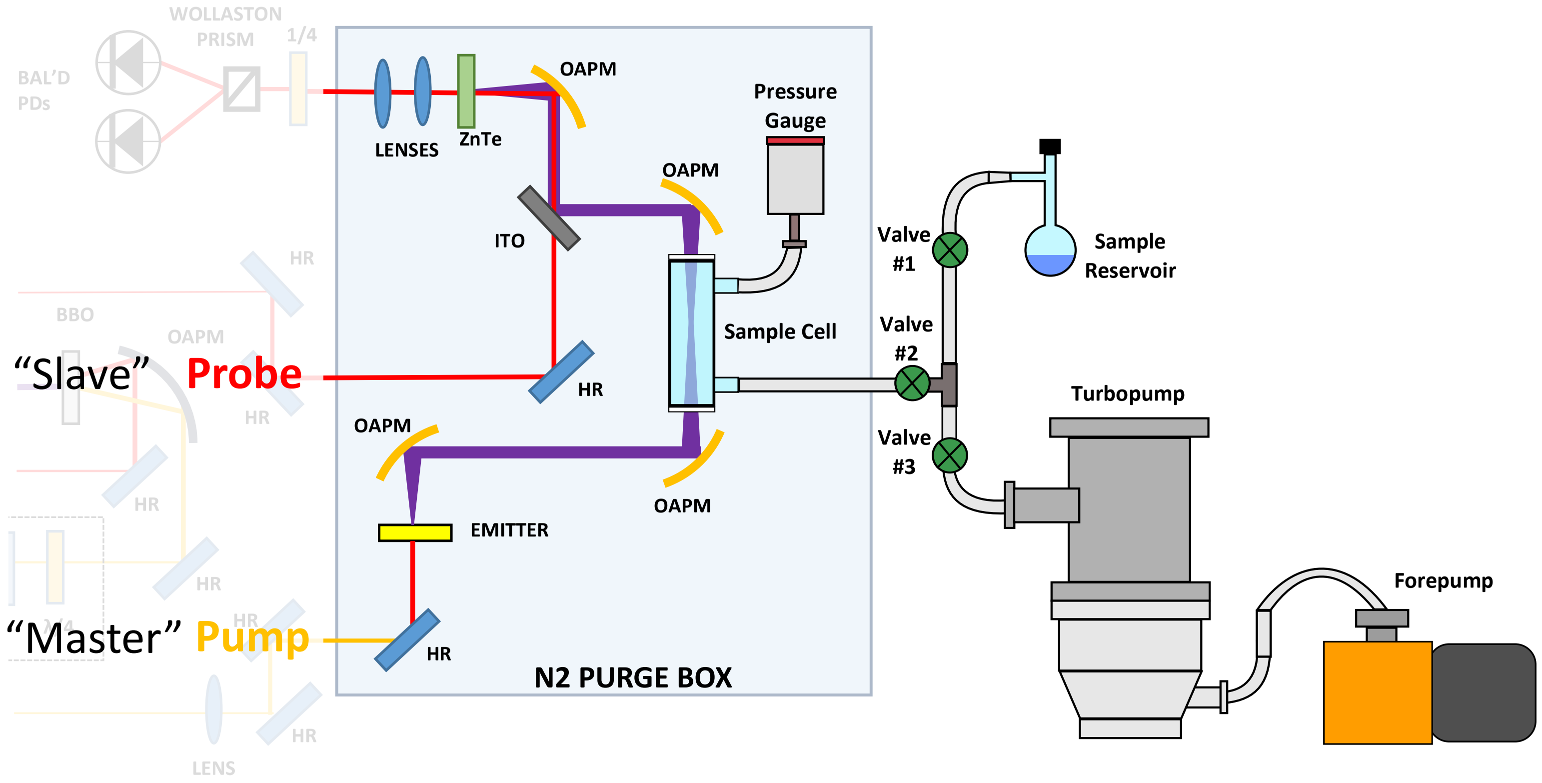

Figure 3.3: The schematic of the gas handling apparatus. Note the optical input of pump and probe beams at left, as shown further in Figure 2.4. A sample cell is inserted between the two 4f telescopes for minimal beam size. A network of tubing and valves connects the sample cell to a pressure gauge, sample reservoir, and vacuum pumps, as described further in the main text.

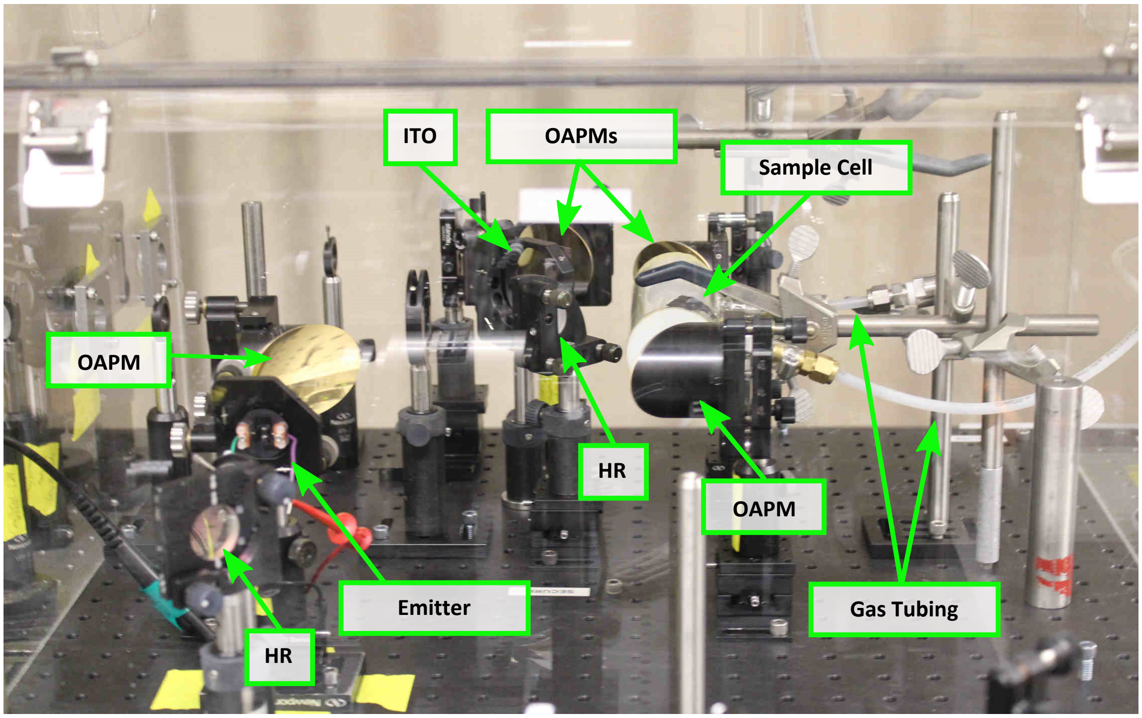

Figure 3.4: Picture of the gas handling apparatus diagrammed in Figure 3.3, with a common labeling scheme; this view is from the bottom side of that figure. Note the placement of the cell between the two OAPMs at right, and its optically opaque polyethylene windows. The gas tubing at right is normally connected to each of a gauge and the sample reservoir and vacuum pumps (not shown). This picture is taken through the clear wall of the nitrogen-purge box (note the box latches at top).

glass vacuum side-arm flask, diagrammed at upper-right in Figure 3.3. Pulling a vacuum on the flask and attached tubing draws water vapor from the sample reservoir, eventually to the cell. The sample flask has a built-in vacuum valve/seal at its neck, allowing the tubing connecting it to the apparatus to be pumped down independently and the sample to be held under vacuum between experimental runs.

In terms of the sample loading procedure, the flask is partially filled with water (or any other liquid to be studied). The flask's internal stopper/valve is closed, whiles valves #1-3 are opened and the rest of the gas system, including sample cell, is pumped down with a turbomolecular pump (model Varian V-250 with Varian Tri-Scroll mechanical forepump). Valve #2 is closed to isolate the sample cell, and the flask's internal stopper opened to pump down the headspace above the fluid level, then that valve is closed again. Valve #2 can be opened again, if needed to finish pumping down the sample cell. Then valves #1-3 are closed and the flask opened to fill the space between it and valve #1. Valve #2 can then be opened and sample gas let into the cell via control of valve #1. In general, it is good practice to do a 'rinse' of the sample cell before spectroscopy. As such, the sample cell can be filled with sample (water) vapor for a few minutes. Subsequently, the above process can be repeated to fill the sample cell to the desired pressure. In this manner, a static gas cell is employed. For the present efforts concerning water vapor, the sample pressure was typically set to approximately 2 Torr; this is a rough measurement of pressure due to limitations of the present sample cell (discussed further in 5). However, the present level of precision in pressure measurements is sufficient for the present focus of measuring peak center frequencies.

3.3.1.2 Digitizer Acquisition Settings

In addition to the sample gas handling and conditions described above, the other main aspect to consider in the acquisition of THz waveforms is that of the electronic measurement settings, notably those concerning the digitizer. The full instrumental details are of course described in detail in chapter 2; the interested reader is referred there for a full description of the electronic and software options and parameters available. In this section, the focus is on the particular settings and configurations employed in the acquisition of THz waveforms for the present study of water vapor, and so is not an exhaustive list of available options. Further, the discussion here is only for options that are readily changed in the routine use of the instrument (with the exception of a brief note about the use of dual vs single detectors). That is, the present discussion is for those settings whose changes are 'user-friendly' and thus may be expected to be changed often.

As described in chapter 2, there is the option of using either of separate photodetectors or a single balanced photodetector. For the results concerning water vapor discussed in the present chapter, both types of detection schemes have been employed. Largely for historical as opposed to technical reasons, the water spectra illustrated in the following sections were generally acquired with the separate photodetectors scheme, while the peak center frequency results discussed in §3.5.3 are obtained from the single balanced detector scheme. In the case of dual detectors, both input channels of the card were required, one for each photodiode. so that a live difference signal, a 'math channel' in the Alazar DSO oscilloscope software, could be calculated; in this case the scan trigger signal from the cross-correlator was recorded via the digitizer's dedicated trigger input. In the case of the single balanced detector, the cross-correlator and photodetector signal were each recorded on a digitizer input. In this case, the trigger signal was supplied on channel A and the balanced detector signal on channel B. This was done as the noise observed on channel A, with no signals connected, was slightly worse than that observed on channel B. In general, the full scale voltage input range was set for ± 2V. Further details of the signal connections, impedances, etc. in these schemes are discussed in Chapter 2.

All scans, in both of single- and dual-detector schemes, were recorded with otherwise similar data acquisition settings. Scans in both cases were acquired with a digitizer sampling rate of 125 MSa/s (with the clocking of the samples determined by the cards internal sample clock, as normal). Record lengths were typically of about 1 million points. In the Alazar DSO oscilloscope software, the memory usage settings were such that there was 1 record per buffer, 10 or more buffers per acquisition and a variable number of acquisitions, with the product of the number of buffers and acquisitions equal to the desired total number of scans. The acquired scans were averaged, with the total number of scans typically ranging from 1000 to 10000; averages were performed with the Alazar DSO scope program's averaging plug-in software. The required acquisition time, including processing time, was roughly 20 seconds to 200 seconds, respectively (much longer scans can be taken in the future work, see chapter 5. The trigger signal was shifted to the approximately 5% record position, providing about 50,000 pre-trigger points as to start the THz waveform towards the beginning of the scan record, so that it was not cut-off by the start or stop of a scan record. In all cases the repetition rate offset of the pump and probe lasers was 100 Hz, with the master repetition rate typically around 79.979 MHz (it was measured to the 1 Hz level in practice with a referenced frequency counter). All scan data was saved to MATLAB-format 'mat' files [79], directly from within the Alazar DSO oscilloscope software, with subsequent analysis performed in MATLAB, as discussed further in the following sections.

3.3.1.3 The Acquired Time-Domain Waveforms

The time-domain waveforms acquired by the digitizer card are recorded as two 1-dimensional matrices; one data point per element of each matrix. One matrix is for the 16-bit (2-byte) signal level in electrical potential, in units of volts, the other for the timestamps generated by the digitizer hardware, in units of seconds. An

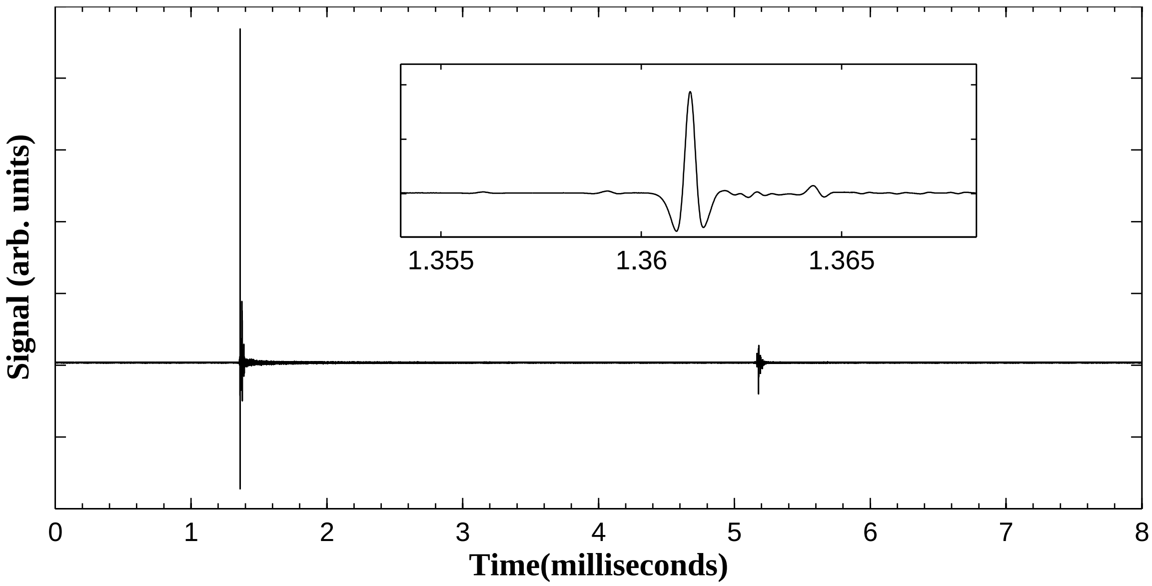

Figure 3.5: A THz-TDS time-domain waveform of water vapor, from the balanced detector scheme. The inset provides a much zoomed-in view of the first THz pulse at left. Even in the inset, though, the limited dynamic range of the printed image prevents a clear view of the small signal-dependent oscillations after the initial pulse. The secondary peak at right is a reflection, and is described further in the main text.

example of such a time-domain waveform is presented in Figure 3.5. Here we see a scan through the nitrogen-purged enclosure, with the sample cell present in the THz beampath and filled with approximately 2 Torr of water vapor, as described above in §3.3.1.1. The signal levels are shown in arbitrary units, linear to measured voltage, as explicit voltage values has little mention without relation to a reference scan. There has been no processing of this waveform, other than the conversion of the timestamps to milliseconds from seconds and setting the initial time in the scan record to zero; this is essentially the 'raw' time-domain waveform upon which all analysis is based, as discussed in the sections that follow. With a 100-Hz repetition rate offset between the pump and probe lasers, as used here, each scan will last for 10 ms. In the present case, the displayed scan runs to a total duration of approximately 8 ms; this was a result of a perhaps overly-cautious attempt to make sure one scan was finished well before a new trigger arrived in the next (scan durations and triggers are discussed further in the chapter 2).

Upon simple inspection of Figure 3.5, three attributes stand out. First, the signal appears zero-valued, or nearly so, for most of the time duration. Secondly, there are two widely-spaced peaks in time. And lastly, the time axis, of course, spans milliseconds not picoseconds. Dealing with this in turn, we first note that much of the zero-valued appearance is a limitation of the dynamic range available in a printed/electronic page, and *not* in the underlying time-domain data. Indeed, in the main plot, we can see a slight 'fuzzy tail' on the later side of the main waveform peak at left. And in the inset, zoomed-in view of this main peak, there are additional oscillations following the peak—even here, the displayed dynamic range is limiting to the data. An important aspect to keep in mind is that this is a relatively large dataset, approximately 1 million datapoints, to be displayed on the page, so that there is a high degree of undersampling in Figure 3.5. For example, the main peak at left is actually a succession of a few peaks that is squeezed in the figure so as to look almost like one; and the 'fuzzy tail' following the peak is the result of many smaller oscillations similarly squeezed, and not just the few small, later peaks shown in the inset plot. In short, this is a dataset best viewed in an interactive plot viewer program.

As noted above, there is clearly a second major peak or set of peaks later in the scan, at a time value of approximately 5.2 milliseconds. This second peak is the result of a relatively strong reflection of the main THz pulse along the beam path. Based on the timing, as discussed more in chapter 2, this is a reflection of the main THz pulse off of the detection crystal, all the way back through the THz beam path and reflected off of the emitter back down the THz beam path towards the detector again. For the purposes of the present analysis, this additional peak can be ignored and will approximately 'divide out' between the sample waveform (as shown in Figure 3.5) and the reference waveform (not shown, but similar in appearance); this issue of pulse reflections and referencing was briefly discussed earlier in §3.1.3.

The reference waveform is not shown herein, as it would appear largely the same as the sample waveform, given the limited dynamic range and undersampling of the image as already discussed; other than an attenuation of the main THz peaks, there would appear to be little, if any, difference. As an instrumental note, it should be pointed out that the near-real time capability of the ASOPS THz-TDS instrument, means that this waveform can be viewed essentially 'live' on a monitor screen. This enables the experimental to optimize the alignment of the optics, the positioning of the sample cell, etc. so as to maximize the peak in the THz time-domain waveform. Further, as the sample is loaded and its pressure increases in the sample cell, the main THz peak can be seen to attenuate. Another important aspect of the THz time-domain waveform shown in Figure 3.5 as noted above, is that the time axis spans milliseconds, not picoseconds. The delay-time scan spans a pump-probe delay time range of up to 12.5 nanoseconds—certainly not milliseconds! Due to the ASOPS time-scaling effect, as discussed in chapter 2, we observe this short delay-time scan over a period of a much longer amount of 'lab time'. An approximate rule-of-thumb, given a rep rate of approximately 80 MHz and an offset of about 100 Hz, is that every millisecond as shown in Figure 3.5 is roughly 1 nanosecond of delay time. For the upcoming Fourier analysis, the quantitative assignment of a proper delay-time axis is required, and that is the subject of the next section. As a closing note to this section, it should be noted that the MATLAB script utilized to generate Figure 3.5 is included in for the interested reader.

3.3.2 Creating a Timebase for THz Waveforms

Referring back to Figure 3.2, our overall schematic for the processing of THz waveforms, it is seen that following the acquisition of sample and reference THz waveforms that the next step in the time-domain waveform preparation is the creation of a timebase for the waveform(s). This is an important part of the pre-processing of the acquired time-domain THz waveforms prior to the Fourier analysis for conversion to frequency-domain data. As noted above in the parent section, §3.3 and immediately above in §3.3.1.3, the reference and sample waveforms are discrete time-sampled waveforms having a timebase in the laboratory timeframe. For example, the time axis in Figure 3.5 is in units of milliseconds as, at a 100 Hz repetition rate offset, a total of 10 milliseconds of ‘real-world’ laboratory time is required for the ASOPS technique’s repetitive pump-probe measurements to sweep through the full, approximately 12.5 nanoseconds of delay time. Fundamentally, the generated waveform is one that should have a timebase in the delay timeframe. In the raw data, there may be microseconds or nanoseconds of lab time between digital samples of the waveform, while in delay time, this corresponds to picoseconds and femtoseconds.

The assignment of a proper time axis in the delay timeframe, or more precisely, the conversion of the sampling rate from lab to delay time frame, is of importance for obtaining the correctly scaled frequency spectrum. In performing the numerical FFT analysis of the experimental time-domain waveforms, the FFT software (see §3.4.1) produces a result that is an array of frequency amplitudes, where each position in the array is assumed to correspond to a frequency being a specific fraction of the sampling rate at which the waveform was acquired. While the present waveforms were acquired over several milliseconds (per individual scan) in our lab-time, they represent an ultrafast process that is actually occurring on a picosecond and sub-picosecond timing level. It is based on this ultrafast timescale that the Fourier results and frequency assignments must be calculated. It can be convenient, then, to convert a waveform such as that shown in 3.5 having time units in milliseconds, over to the proper timescale. This has the benefit of showing a ‘true’ representation of the THz waveform, enabling direct comparisons with such waveforms acquired on traditional delay-line based instruments. Further, this of course enables various time-domain based analyses. For example, one may wish to obtain a direct time-domain measurement of the FID ring-down time or to track down the sources of reflection peaks, by finding their optical pathlength given the delay time to their arrival, the speed of light and the indices of various materials in the beam path.

The conversion of the lab-time sampling rate to one in delay time, and the closely related problem of assigning a delay-time axis to the acquired waveforms in resolved in a straightforward manner. Recall from chapter 2, that the ASOPS effect can be viewed from the perspective of a time-scaling or time dilation effect. The full range of the delay scan is the time period between subsequent pulses of the pump laser. And this delay time is explored at the rate of the repetition rate offset; that is, it is scanned in an amount of time equal to the inverse of the repetition rate, so 100 Hz offset yields 10 ms scans for example. This can be expressed as a simple scale factor, relating a lab-time period to a ‘true’ delay time period:

$$S = \frac{f_r}{\Delta f} \tag{3.45}$$

where f_r is the repetition rate of the pump laser (typically $\sim$80 MHz herein), Δf the offset in repetition rates between the pump and probe lasers (typically 100 Hz herein), and S is the ratio of lab time duration to delay time duration. For the typical frequencies noted here, $S \approx 8 \cdot 10^5$. That is, a $\sim$10 ms duration (in lab time) scan reduces by a factor of $S = 8 \cdot 10^5$ to 12.5 ns of delay, as we expect.

Similarly, S scales the digitizer sampling rate:

$$f_{ASOPS} = f_{ADC} * S \tag{3.46}$$

where f_{ADC} is the rate (in lab time) at which the digitizer acquires samples of the time-domain waveform, and f_{ASOPS} is the, S-scaled acquisition rate in delay time. For the 125 MSa/s digitizer rate employed, as noted above in §3.3.1.2, for the water vapor scans presented herein, and the typical S-factor value, we find that $f_{ASOPS} = 1^{14}$ samples per second! That is, the effective delay-time sampling rate for the water vapor scans presented here is at $\sim$100 TSa/s (terasamples per second). This is the sampling rate that is used to provide the frequency axis of the FFT results below.

More immediately, for our present purpose of displaying the time-domain waveform in delay time units, each subsequent data point is treated as arriving an amount of time later equal to the sampling time, which is merely the inverse of the calculated $\sim$100 TSa/s rate, or a value of $1 \cdot 10^{-14}$ s (10 fs) between subsequent points in the time-domain waveform. In equation form,

$$\tau_{ASOPS} = \frac{\tau_{ADC}}{S} \tag{3.47}$$

where τ_{ASOPS} is the time between adjacent sampled points in the delay-time waveform and is simply the inverse of f_{ASOPS}, and τ_{ADC} is the time between subsequent samples in the lab-time waveform and similarly, is the inverse of f_{ADC}. These simple timing relationships, used every time a THz waveform is processed, have been coded into a pair of MATLAB functions, ‘asopsRate.m’ and ‘timebase.m’, included in the appendix, §A.2 and §A.3. The first function, ‘asopsRate.m’, implements eqs. (3.45) and (3.46) to simply calculate the delay-time sampling rate, typically used to assign the frequency axis to FFT output, as discussed further in §3.4.1. Another use of the scaled sampling is for the generation of a delay-time axis for an originally lab-

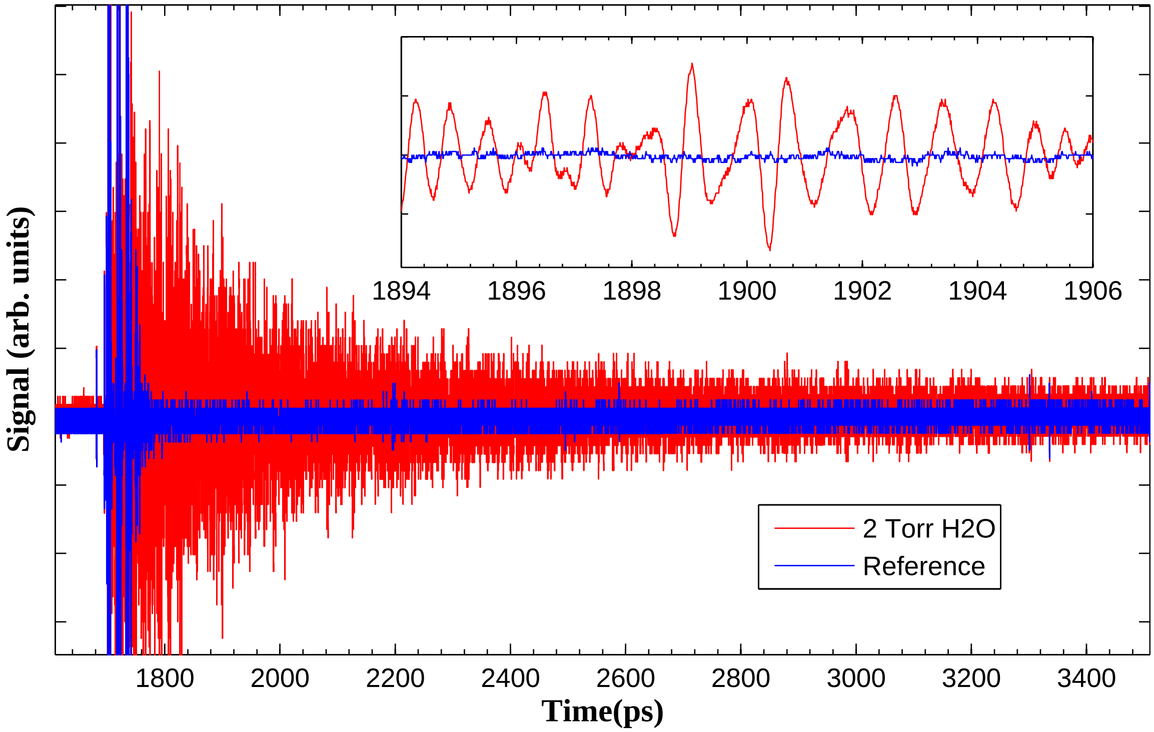

Figure 3.6: The time-domain THz waveform for both of water vapor and a reference scan. The main view is zoomed-in to the period at and just after the main THz pulse. The inset shows a further-zoomed period, just after the main pulse, so as to clearly show the continued THz-frequency ringing from the water vapor.

time waveform. This is achieved with the 'timebase.m' function. It accepts the scaled rate of 'asopsRate.m' and calculates a new time array for a waveform, to replace the lab-time, hardware-generated axis from the original acquisition. These two functions have been used to perform the timebase conversion for a water vapor time-domain scan, like that in Figure 3.5 (this scan from the 2-detector arrangement, otherwise similar).

The delay-time waveform is shown in Figure 3.6; it should be noted that this is a zoomed-in view spanning 1900 ps in the main figure window and 12 ps in the inset window. The main zoomed in view is selected to illustrate the substantial difference in the time-domain signal between the reference and water vapor waveforms. A problem in trying to plot this many points is the aliasing and undersampling and otherwise poor translation of almost 200,000 data points into small figure—this contributes to making the data appear much noisier than it really is. For this reason, the inset view has been provided, spanning only 12ps and showing that there is clearly a water FID well above the background signal level. This FID signal, based on the converted time axis, can clearly be seen to span at least $\sim$ 1 ns in time before falling down to noise levels. The MATLAB script used to generate this figure is also included in the appendix, §3.6. It should further be noted that the overall signal level of the sample waveform is much reduced from that of the reference; between this diminished time-domain amplitude and the time-domain ringing long after the initial THz pulse, we can be confident of seeing clean, distinct spectral features following the Fourier analysis discussed in §3.4 concerning the second part of the overall analysis process, that is, of the discrete Fourier transform of the data.

Prior to the Fourier analysis, in the usual data analysis, there are two remaining aspects to the waveform preparation in this first part of the overall process. In particular the proper portion of the waveform should be selected for further analysis and further, the waveform may benefit from 'windowing', that is, apodization, to prevent frequency domain ringing. While these two forms of processing are of course done prior to FFT analysis, they are motivated primarily by their effect upon the FFT results, so as noted above, we will first discuss the FFT processing.

3.4 Discrete Fourier Transform

In the sections above, there was an introductory explanation to the theory of Fourier analysis. There are a few important aspects about the above equations to note, because of their practical impact upon THz-TDS. First, these equations are all analytical and assume a function $f(x)$ that is mathematically 'well-behaved', including that it is a continuous function. Experimentally acquired data, as noted in 2, consists of discretely sampled time points. The data does not have a pre-supposed functional form as in the tutorial example equations above. So the actual numerical implementation of Fourier analysis will require accommodation for this aspect of the data; this is addressed below in section 3.4.1. Secondly, in the standard discussion of Fourier analysis above, the analysis is treating the function $f(x)$ over the domain $[-\pi,\pi]$. This domain is given by the periodicity of the harmonic components; the combination of harmonic components results in an anharmonic but periodic waveform. Our THz data will be over a variable period of time and will be a single waveform, not a periodic function. This actual time range of the data is handled in numerical implementations of the Fourier transform. The waveform data, as a single scan, can be thought of as a single period of a repeating scan. That is what one would obtain in reversing the Fourier analysis from frequency to time data if one looked at the time range outside of the original dataset.

3.4.1 Numerical Algorithm for Fourier Analysis

As noted above in Figure 3.2, a discrete Fourier transform is required to analyze the time-domain waveform to yield a measure of its frequency domain components. A discrete Fourier transform (DFT) implements the Fourier transform as discussed in §3.1.2, but for discontinuous, though regularly sampled points in a waveform. In terms of procedure, we utilize one of many commercially available software packages available for the task. Specifically, for the present analysis of water vapor spectra, the MATLAB software package [79] and its built-in 'fft' Fourier transform function are utilized. Additional code, for a software 'wrapper' of sorts, has been made for the present analysis—it is the 'fft_plus.m' function, included and discussed further in the appendix, §A.6.

The calculation of the DFT is notably different from the Fourier analysis equations previously discussed herein. The discrete DFT of a signal x_n (n being a sampling index), can be stated as [80]:

$$X_k = \sum_{n=0}^{N-1} x_n e^{-j(2\pi/N)kn} \tag{3.48}$$

where there are N number of (e.g., time-domain) sample index values n. The left-hand side result X_k is the DFT where the individual discrete Fourier series coefficients are indexed by k, meant to be a frequency index. As we increment k by integer values, we see on the right-hand side of (3.48) that the increment in frequency is $(1/T)$ Hz or $2\pi/T$ rad/s, as $nN = T$, the total waveform time duration. It is from a basis of these incremented frequencies, appropriate weighted, that one can reconstruct a likeness of the original, discretely sampled data.

Unfortunately, direct use of (3.48) to perform a DFT on a waveform can be computationally intensive, prohibitively so [81]. The amount of computing operations to perform a DFT on a signal waveform with n elements scales as n^2. Algorithms that achieve a DFT result in a faster manner are generally referred to as 'fast Fourier transforms' or FFT for short. The computing requirements for FFT algorithms scale as $n \log n$, thus providing a large time-savings, especially for longer records. As a point of reference, the waveforms transformed as part of the water vapor spectral analysis in this chapter are typically on the order of 500,000 to over 1 million samples in length—so the speed-up afforded by improved FFT algorithms is definitely important. As a specific example, a $\sim$1 million point water vapor scan processed in the present effort, including a high level of zero-padding (see §3.4.3), required several minutes of computation time on the author's well-equipped laptop, even crashing it once! The thousands of times longer waits and larger computing demands for direct evaluation of the DFT equation in (3.48) would be prohibitive.

There are actually a variety of FFT algorithms available; for in-depth details and references, the interested reader is referred to [80]. MATLAB's FFT functions are based [82] on a software library called 'FFTW' [83] [84]; this is in turn based on the widely used 'Cooley-Tukey algorithm' [85]. Regardless of the specific FFT mathematical algorithm or software package employed, the end result is the DFT of our time-domain waveform, thus providing the contributions of various frequencies to measured spectra. However, there are many ways in which that spectral content can be scaled and quantified, and that is the subject of the next section.

3.4.2 The FFT and Measures of Spectral Content

The time-domain waveform signal, as acquired, is a voltage level that is (ideally) linearly proportional, though the electro-optic detection scheme discussed in chapter 2, to the electric field of the THz pulses (and the square root of their power). The basic output from and proper usage of the chosen software package, MATLAB, and its 'fft' function are generally described in good detail on documentation websites, etc. [82] [81] [86] [87].

In general, the output from a FFT computer software package must be properly scaled, and have correct frequencies assigned to it, in order to obtain experimentally accurate amplitude and phase spectra. This processing requires several small steps and for example, varies depending on whether there are an even or odd number of data points in the spectrum and one requires measures of amplitude, power, power spectral density, etc. To assist in this regard for the present application of the THz spectroscopy of water vapor, a new MATLAB function, called 'fft_plus' has been written to serve as a 'wrapper' around the regular 'fft' function of that software package. The code for this simple, but useful, function is included in the appendix, §A.6; the interested reader may also benefit from the extensive comments and further references therein.

In terms of the practical application of these details, it should be noted that the initial output of such routines is a set of complex-valued amplitudes for each of the calculated frequency bins; this is the amplitude *and* phase information that make THz-TDS such a powerful technique. The data consists of positive and *negative* frequencies from 0 Hz (DC) up to the Nyquist frequency, or nearly so (transforms of records with an odd number of points lack a bin for the Nyquist frequency). For real-valued signals, as generally should be observed in laboratory experiments, the positive and negative frequency information are redundant and can be combined (doubled) to yield a measure of the amplitude contribution of each frequency component in the transformed waveform. This initial amplitude information is in the standard form of a complex quantity, $a+bi$; the real-valued amplitude (or magnitude) and corresponding phase are recovered by simple application of equations 3.16 and 3.17 from §3.1.2.

This amplitude information is then directly proportional to the measured voltage and thus, the THz electric field. These values can then be squared for a measure proportional to the field's power. The custom processing script in §A.6 handles these details and offers a simple way to select for amplitude, power, or other measures of spectral content. In general, because of the referencing of sample and background, the proportionality constants are divided out and we can obtain quantitative measures of a sample's absorption.

In this regard, it should be known that there are a variety of ways in which the frequency-domain Fourier analysis results may be labeled and presented in the scientific literature. For un-referenced waveforms, typically to compare sample and reference scans to each other, the amplitude may be plotted on a linear or sometimes base-10 logarithmic scale, in which case it may be referred to as the amplitude or 'relative amplitude', for example. Alternatively, its square may be plotted as a measure of power, then typically presented on a base-10 logarithmic scale and referred to as the power in some form or perhaps the 'FFT intensity', herein as 'log relative power' in arbitrary units. In all of these cases, because the proportionality constants to actual fields and powers are typically not measured, these results are in 'arbitrary units', though not always explicitly noted as such.

In performing the referencing of sample spectra, as discussed further in §3.5.1, these sample amplitudes or power levels are divided by those of the reference spectrum. The natural logarithm of the ratio of corresponding amplitudes may be taken and plotted as a measure of 'amplitude absorption'; this is the same, to within a factor of 2 as a Beer-Lambert's law absorption (because of the electric field to power square relationship). Similarly, a ratio of amplitude-squares may be taken as a measure of transmission, or further, a base-10 logarithm of this taken to yield the absorbance. The latter is the preferred method for frequency domain plots herein, where it is referred to as the 'relative absorbance' to emphasis that the proportionality between acquired voltage and THz field is not measured (though it isn't necessary either for most spectroscopy).

3.4.3 Zero-Padding the Waveform

In FFT processing, there is a distinction between the length of the input waveform record, referred to as the window length, and the length of the output, referred to as the transform length [81]. FFT routines typically run (even) faster if the size of the record to process is a power of 2. In this case, the number of computing operations scales even faster, then as $3n\log_2 n$, thus providing an even more substantial speed advantage over direction evaluation of the DFT equation in 3.48. While one's original datasets to be transformed may not necessarily be a power of 2, they can be chopped down to size to accommodate this length, or they can be padded at their end with additional numbers, zeroes, to reach the next power of 2.

Such an artificial extension of the scan duration has benefits beyond the speed of the FFT. Recall from 3.1.4.1, that the frequency resolution scales with the duration of the scan. As the scan is artificially lengthened, the spectral resolution is increased. Zero-padding, while a common technique in processing THz spectra, does not add any new information to the spectrum [57], rather the zero-padding is effecting an interpolation of the frequency-domain data. This provides a numerical means to fit the peaks in the spectrum [36] and assists in locating spectral peaks; this latter aspect is discussed further in §3.5.2. Through the interpolation of the frequency-domain data, zero-padding improves the accuracy of the amplitude measurements in the Fourier transform [88]. The DFT produces Fourier components for discrete frequency bins; if a real-world signal frequency component falls between bins (as is the case with a continuum of THz frequency content), then the accuracy of the amplitude estimate is affected. It should be stressed that the zero-padding *does not* improve the spectral resolution of the instrument; that is set by the experimental duration of the waveforms acquired. However, the zero-padding can improve the accuracy of the amplitude measurements for frequency content that should fall within the bandwidth of the experimental measurements.

The effect of zero-padding upon the frequency-domain spectrum is plotted in Figure 3.7, where data point markers have been applied to show the actual underlying data beneath the curves. Here we present a zoomed-in view of a single water vapor peak at approximately 0.752 THz. The input to the FFT routine was a full $\sim$10,000 ps duration time-domain waveform. In the absence of zero-padding, the frequency resolution following the transform would be 95.3 MHz. However, the additional levels of zero-padding to this original dataset have artificially increased the resolution substantially. At the highest level shown in the figure, an additional 7 powers of 2 *beyond* the next power of 2, the new frequency resolution has been increased substantially, to 745 kHz.

The figure makes clear that, while there is no new 'real' information present, the increasing levels of zero-padding provide increasingly dense levels of interpolation between the original frequency-domain data points. Given the linewidth of this and other spectral peaks in this sample, the highest level of zero-padding presented provides a more than adequate interpolation of the whole peak. It should be noted that Figure 3.7 was made using the MATLAB script 'test_zeroPad.m' as described in the appendix, A.7. This script provides an easy means to select other datasets, select different levels of zero-padding, and generate additional figures for such comparisons and optimization. Such high levels of zero-padding also assist in finding the locations of peaks, as discussed further below in 3.5.2.

3.4.4 Selecting the Waveform Time Window

One can truncate the measured time-domain waveforms to avoid unwanted reflections, before Fourier analysis, or in an attempt to improve the signal-to-noise performance by excluding the time portion in which the sample-induced oscillations in the THz field have effectively ended. In general, this shouldn't necessarily be pushed to extremes as the low-frequency coverage can be helped by extending the reflection-free time window [70]. However, for the present study and instrumentation, having exceptionally long time windows (i.e., several nanoseconds instead of a few tens of picoseconds), effecting a decrease in low-frequency coverage is generally not of concern.

The effect off truncating the time-domain waveforms is illustrated for the present application of the THz spectroscopy of water in Figures 3.8 and 3.9. In this case, the potential time-domain concern is an instrument-based reflected THz pulse later in the scan as seen previously in Figure 3.5. The pulse arrives about 4 nanoseconds, in delay-time (roughly 4 milliseconds in lab time), following the main THz pulse. The concern

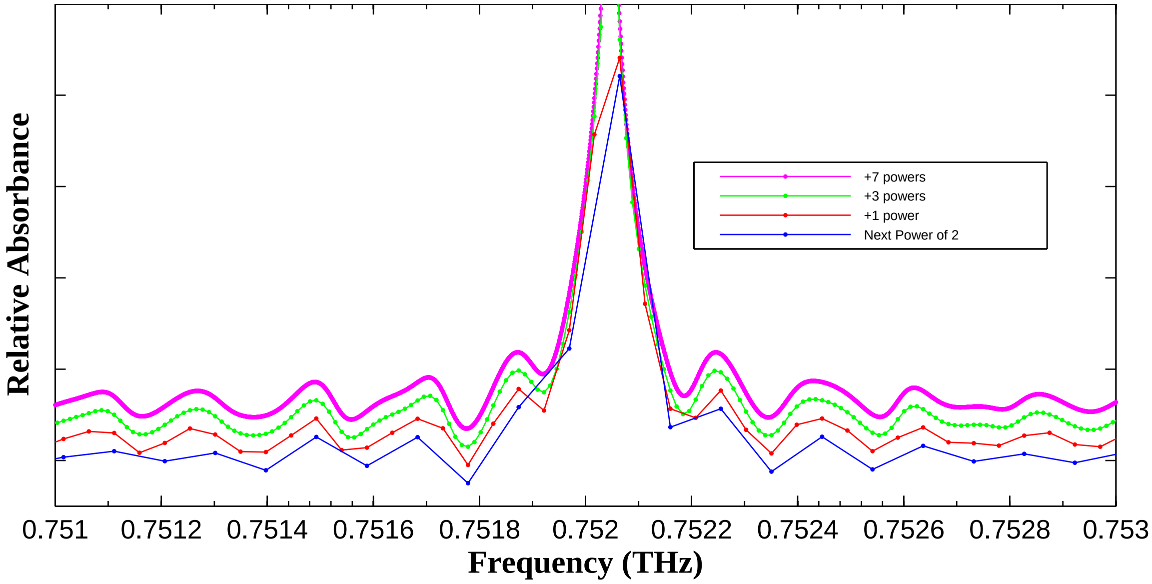

Figure 3.7: Comparison of zero-padding levels upon a water vapor spectrum. Higher levels provide increasingly dense interpolation of the frequency-domain data, with the highest level shown providing more than adequate coverage of the peak shape given the sample peak linewidth.

is that inclusion of this reflection pulse data in the DFT processing may have some negative effects upon the resulting spectrum (e.g., frequency domain ringing or oscillations in the Fourier component amplitudes.

Figure 3.8 shows a time-domain waveform for a water sample scan (no reference shown). Color-coded ‘cuts’ in time have been overlaid upon one another to stress which temporal information is included in the Fourier analysis that yields the corresponding frequency-domain spectra in Figure 3.9. Note that that the different temporal periods are stacked upon one another from longest on bottom to shortest on top (that is, the plots are stacked from bottom to top in the order that they appear in the legend, top to bottom). All time-domain waveforms start at a delay time of 0 ps, i.e., the beginning of the scan record. Four conditions were considered: first, the essentially full delay scan of 0 to 10000 ps, as this makes use of all acquired information and provides the highest (pre-zero-padded) instrumental spectral resolution. Secondly, a record reaching to a delay time off 6560 ps is considered, as this includes the reflection pulse, but excludes the remainder of the scan, which generally appears to be near-zero noise from the instrument. The motivating question here is whether excluding this noise signal may improve the spectrum. Thirdly, a record to 6440 ps, or a delay time just before the reflection pulse is taken. This presents a good point of comparison to the second case, extending just before the reflection—thus largely isolating any spectral effects of the reflection itself. And lastly, a time record to 4000 ps of delay is taken. This time point is the approximate end of the THz field oscillations from water sample. If there is any benefit to excluding either or both of the reflection pulse and the long stretches of near-zero signal, then it should be apparent in the water vapor spectrum derived from this shorter time period, optimized about the duration of the water sample's THz signal.

As an aside, it should be noted that it is exactly this type of flexibility in later processing and analysis, that perhaps makes this first part of the overall experimental procedure shown in Figure 3.2, the 'THz Time-Domain Waveform Prepation', the most important. In particular, proper acquisition of the time-domain records and quality of the instrumentation underlie all later analyses, which can be re-performed and optimized upon the same initial dataset(s). It is this thinking that motivated the time and effort put into the experimental design of the instrumentation, as generally described in chapter 2.

Returning to Figure 3.9, we can see the frequency-domain effects of the different extents of the delay scans shown in Figure 3.8; note that the spectra have been offset slightly from each other along the vertical axis for clarity. In this figure, we have zoomed-in to a narrow frequency range about a water vapor spectral peak at approximately 0.752 THz, chosen as it was moderate in intensity relative to the overall set of water peaks observed. This zoomed-in view enables us to more easily inspect for frequency-domain ringing about the peak position, while still being wide enough to observe any more spread out effects. Indeed, about the base of the spectrum associated with the full scan of 10,000 ps, there is some small amount of ringing. This level of ringing is relatively small, at least for the present application of measuring the peak THz frequencies of water vapor rotational transitions; this may be of some additional concern if the present goal was to measure peak areas in a quantitative manner. Overall, then, this generally eases concerns about making use of the full delay range of the instrument.

The small frequency-domain ringing effects associated with the full scan, interestingly, are significantly reduced even in the time-domain scan reaching to 6560 ps, past the reflection pulse. The ringing immediately about the base of the peak is largely gone. However, inspection of the low-frequency side of the peak shows what are likely periodic bunches of additional ringing. In retrospect, this ringing may also be visible to some extent in the spectrum associated with the full delay scan.

Further reducing the delay-time portion, to an extent ending at 6440 ps, or just before the reflection, seems to have eliminated the bunches of ringing previously observed on the low-frequency side of the peak. However, for reasons not yet fully understood, the transform of this time span seems to have re-introduced a small amount of ringing about the base of the peak. And finally, looking at the shortest span of delay time considered, that to 4000 ps or the effective end of the THz field oscillations from the water vapor sample, we do not see any clear frequency-domain ringing.

Overall, the length of the time duration included in the Fourier analysis can have an effect upon the amount of frequency domain ringing observed. At the shorter scan durations, the (pre-zero-padded) spectral resolution is diminished. This effect can be seen simply by observing the spacing in data markers in Figure

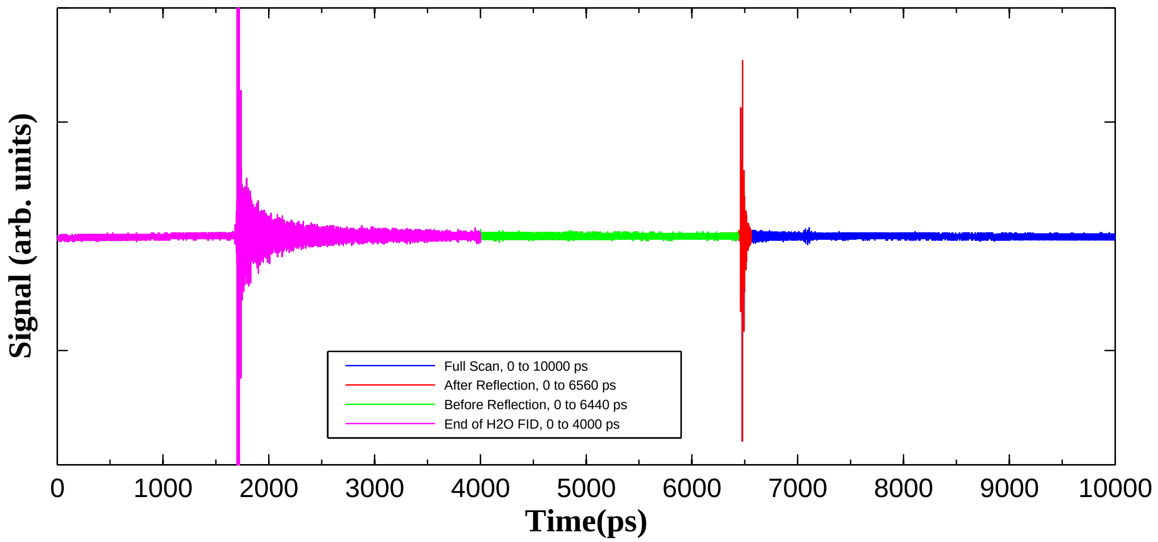

Figure 3.8: A time-domain THz waveform from a water vapor sample. Different extents of the delay scan are highlighted, with shorter extents plotted over the longer durations of the scan. These different durations of the waveform are each Fourier transformed, with their spectra plotted in 3.9, to look for duration-dependent changes in the FFT result, particularly upon inclusion of the reflection pulse at ∼6500 ps. Note that the y-axis is zoomed so as to clip the full extent of the main THz pulse.

3.9. Also of concern is that ringing in longer-duration scans may affect the accurate assignment of peak frequencies. As a compromise choice in our initial effort, the scan duration of 5000 ps is used later herein in §3.5.2 and 3.5.3 for the analysis of peak center positions (along with much higher zero-padding as discussed therein).

It should be noted that the numerical processing and figure generation for Figures 3.8 and 3.9 were carried out a MATLAB script such that this sort of analysis can easily be performed during further work on water vapor or on any future samples. The script, 'test_timecut.m', is included and discussed further in the appendix, §A.5 for reference to the interested reader.

3.4.5 'Windowing': Apodizing the Waveform

A practical issue arising in the Fourier analysis of time-domain signals, particularly when truncating the waveforms as above, is that of 'windowing', also known as 'apodization' [43]. At the edges of a signal to be Fourier transformed, the signal should go towards zero in a smooth fashion. If the signal is sufficiently nonzero at its edges in the time-domain, sample-related information may be lost (i.e., a truncation error) and this edge may be seen as a sharp (i.e., high-frequency content) discontinuity in the Fourier analysis. Such edges can result in undesirable ringing in the frequency domain, and distort spectral line-shapes, thus affecting frequency measurements of peaks and the measurement of peak areas.

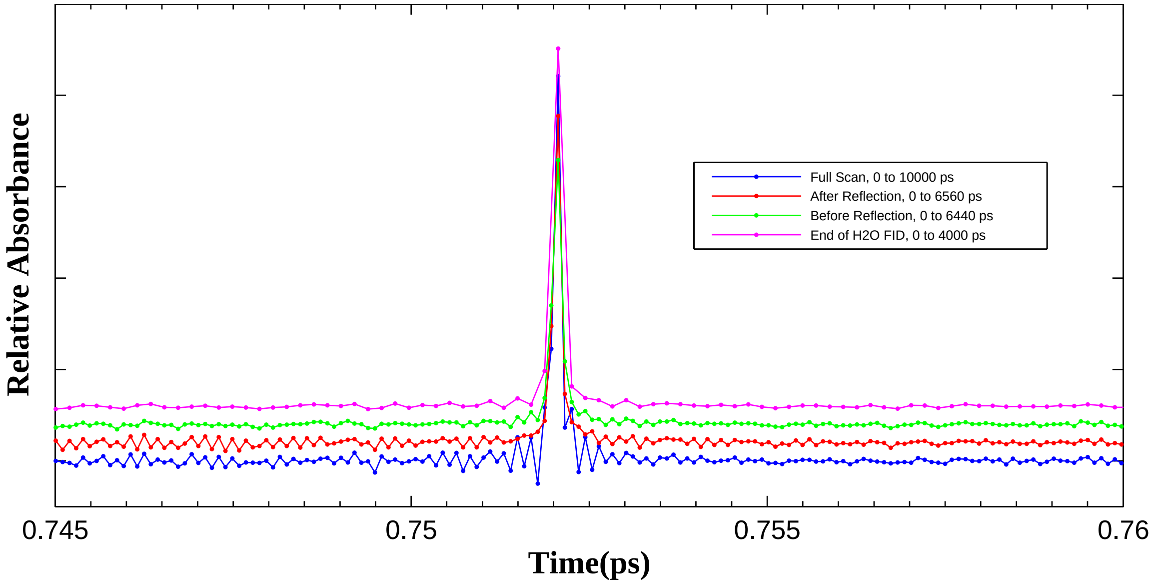

Figure 3.9: The water vapor FFT results from the differing extents of scan duration that were illustrated in Figure 3.8 (colors matched between figures). The shorter scans generally have less frequency-domain ringing, albeit at a cost of instrument spectral resolution. See the main text for further details.

The practical issue, then, is that the THz-TDS data should start from a zero baseline and end on a zero baseline, otherwise this would be interpreted by a Fourier transform as a discontinuity and result in incorrect frequency components. In general, THz-TDS scans do start at a zero-baseline prior to the arrival of the THz pulse. As long as a sufficient time duration of data is acquired, the THz waveform will return to zero as well; this condition is generally well met in the present case of ASOPS THz-TDS, as long scans are a primary motivation for the technique. However, if this condition is not met, then the time-domain data should have a 'window' applied; essentially the data is multiplied by a time domain curve that scales the data down to a zero baseline at both of start and positions. The scaling of the experimental data can be done in a linear or exponential manner; there are a variety of apodization or windowing functions commonly used. For the quantitative reliability of the resulting frequency domain data, e.g., in peak area measurements, such windowing should of course be done in a consistent manner across all sample scans.

Windowing applied to the edges of a full THz-TDS scan, like that shown in the longest of Figure 3.8, will not have a significant effect upon the frequency-domain results. Effects may be noticeable if the windowing if so great that the reflection pulse is diminished, then the results will be similar to that discussed above in §3.4.4; at that point, one would basically be excluding the original experimental signal with near-zero-padded data.

However, if a portion of the water vapor FID signal is isolated from the middle region of the time delay scan, after the main THz pulse, then apodization can have significant effects. Such a reduced-delay portion

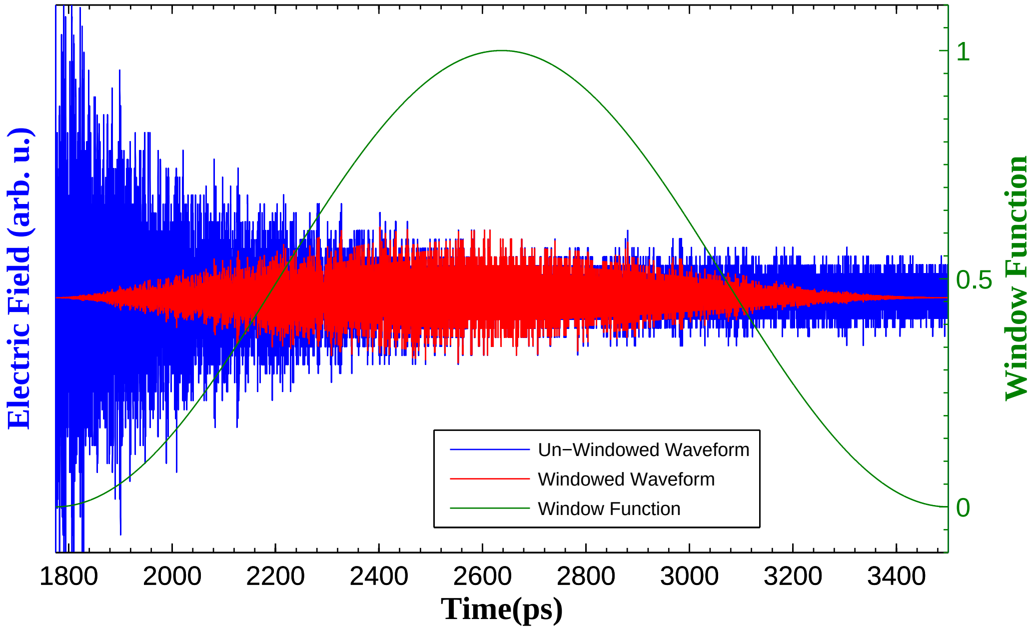

Figure 3.10: Windowing in the time domain. The waveform is the THz signal from water vapor, shortly after the main THz peak. A Hanning window type is illustrated on the scale at right, and the resulting, windowed waveform shown over the original data.

of a water vapor time-domain signal is shown in Figure 3.10. Overlaid on the time-domain data is a window function (known as a Hanning window [89]), scaled from zero to 1, with the resulting, windowed time-domain signal shown in red. It is clear from simple inspection of the figure that the once large truncations that would occur at the time extents of the figure (1775 and 3500 ps), would no longer occur with the apodized signal. Indeed, significant effects are observed in the corresponding frequency-domain spectra, as plotted in Figure 3.11. Here, a zoomed-in view of the resulting water spectra (without referencing) is shown at ∼2.1 to 2.5 THz. The ‘un-windowed spectrum’ is generated from the ‘un-windowed waveform’ of Figure 3.10 and likewise for the windowed spectrum.

The two spectra in Figure 3.11 show significant differences. The un-windowed spectral peaks all show a serious peak-splitting effect, which is not accurate for these water vapor lines. Further, while the un-windowed peaks are of greater amplitude than those from the windowed data, these peaks are also significantly noisier and have distorted line-shapes, notably about their bases, in addition to the splitting. Overall, the windowed spectrum is much ‘cleaner’ and more suitable for finding frequency peaks, for example. Further, it should be noted that this type of essentially background-free THz FID measurement of the water vapor signal is an important area to pursue in future research, and may yield better signal levels at longer delay scans and higher resolutions.

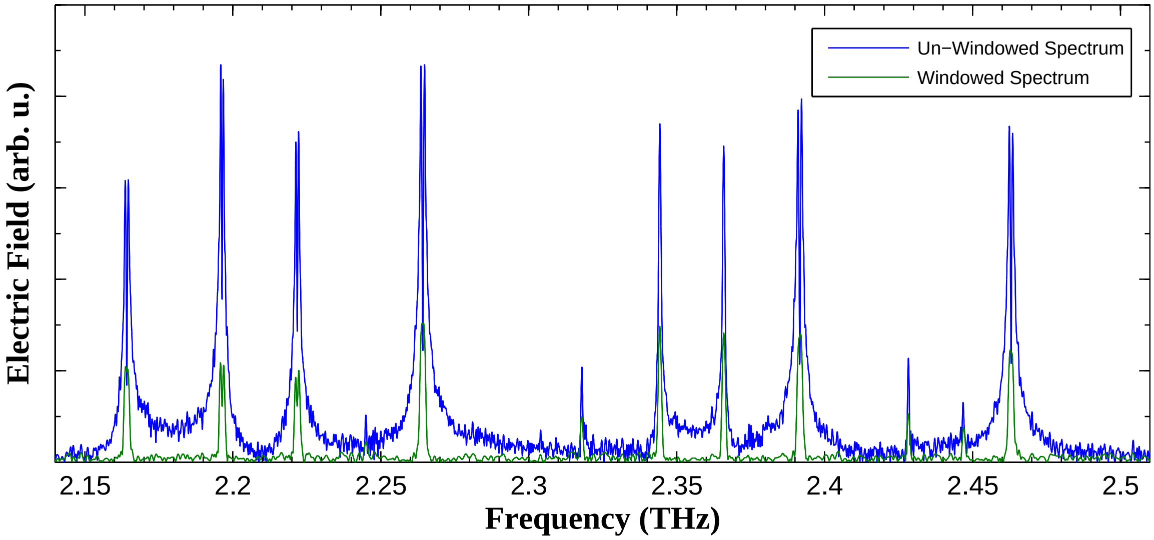

Figure 3.11: Frequency domain results of the time-domain windowing performed in Figure 3.10. Note that the time range considered excludes the main THz peak, so these spectral peaks derive only from the later ringing signal from the water vapor, and no referencing has been performed.

For the interested reader, it should be noted that Figures 3.10 and 3.11 and their underlying data were processed and generated automatically with a (MATLAB) script. The script used (‘test_apodize_field.m’) is included in the appendix, §A.10, and was designed to be readily re-used for future studies in optimizing this sort of apodized, THz FID measurement.

3.5 Spectrum Analysis

Referring back to the overall experimental procedure, as discussed in §3.2 and shown at lower-right in Figure 3.2, we see that the third part of the overall procedure is that of the spectrum analysis. It is in this portion of the overall procedure that the effects of the instrumentation can be accounted for through the use of a background spectrum, and that analyses of the spectra can then be performed. For example, for generating spectroscopic line lists, as pursued in the present research for the case of water vapor, one would require to find the frequencies of the peak centers. Other studies, such as those concerned with finding pressure-broadening coefficients or line strengths, for example, may be interested in the peak linewidths or their heights and/or areas. The present discussion is focused on following the overall analysis algorithm for finding peak frequencies so as to produce spectroscopic line lists. This is demonstrated herein on water vapor, however this analysis and the associated mathematical tools created and discussed herein can be equally well applied to other gaseous samples. Further, linewidths are discussed in the context of verifying instrument spectral resolution, and peak fitting generally discussed.

3.5.1 Referencing the Spectrum

In absorption spectroscopy, the amount of incoming light absorbed by the sample, as a function of frequency or wavelength, is recorded and plotted. By its very nature then, the technique requires knowledge of the amount of light available to be absorbed, in the absence of a sample in the experimental beam path. Indeed, any instrumental factor along the beam path is of importance—including the light source and its spectrum, as well as the wavelength/frequency-dependent response of the detector and any optical losses though the components of the system. These effects are controlled for, however, when a reference scan, lacking sample, is obtained for ratioing against that of a sample. These scans are quite familiar to readers who have used FT-IR spectrometers and such background scans are equally important for absorption spectroscopy with the THz-TDS technique. Indeed, we saw in eqs. (3.32) and (3.33) above in §3.1.3 how the ratios of the Fourier component amplitudes and differences of the phases, between sample and reference scans, are necessary in THz-TDS to extract the dielectric properties of an unknown sample, and referenced scans for the present THz spectroscopy of water vapor are obtained by the same amplitude ratio equation.

The process of referencing a water vapor THz spectrum is illustrated in Figures 3.12 and Figure 3.13, where we have un-referenced or ‘raw’ scans and a referenced scan, respectively. First, in Figure 3.12 a pair of raw scans is shown for a water vapor sample and its reference (empty gas cell) scan. The data is taken from the dual-detector instrument configuration, with 1000 averaged scans and with the time-domain waveforms selected from 0 to 5000 ps, and zero-padding to the next power of two in the number of datapoints. The FFT amplitudes from each scan were squared as a measured of relative power and plotted on a log scale. The reference scan is plotted on top, so the absorption lines from the water vapor sample, can clearly be seen in relation to it. It should be noted that the spectral lines actually are of a finite width; as with other figures herein, the number of datapoints within the plotted range is so large that the figure image must be undersampled. The oscillations clearly seen in both spectra are from multiple reflections of the THz pulse, both on long and short timescales; importantly, they largely match and cancel out in the referencing. Plotting the scans in this manner also allows us to easily observe the power dynamic range of the spectrometer in this configuration. This is observed from the height of the peak THz signal at $\sim$1 THz relative to that of the noise floor at higher frequencies; this noise, beyond the bandwidth of the emitter is treated as the electronic noise floor at all frequencies, including beneath the peak signal at $\sim$1 THz. The power dynamic range calculated as such is approximately 30-35 dB, for this averaged data derived from 1000 scans.

The two scans shown in Figure 3.12 are referenced against each other by dividing their relative powers

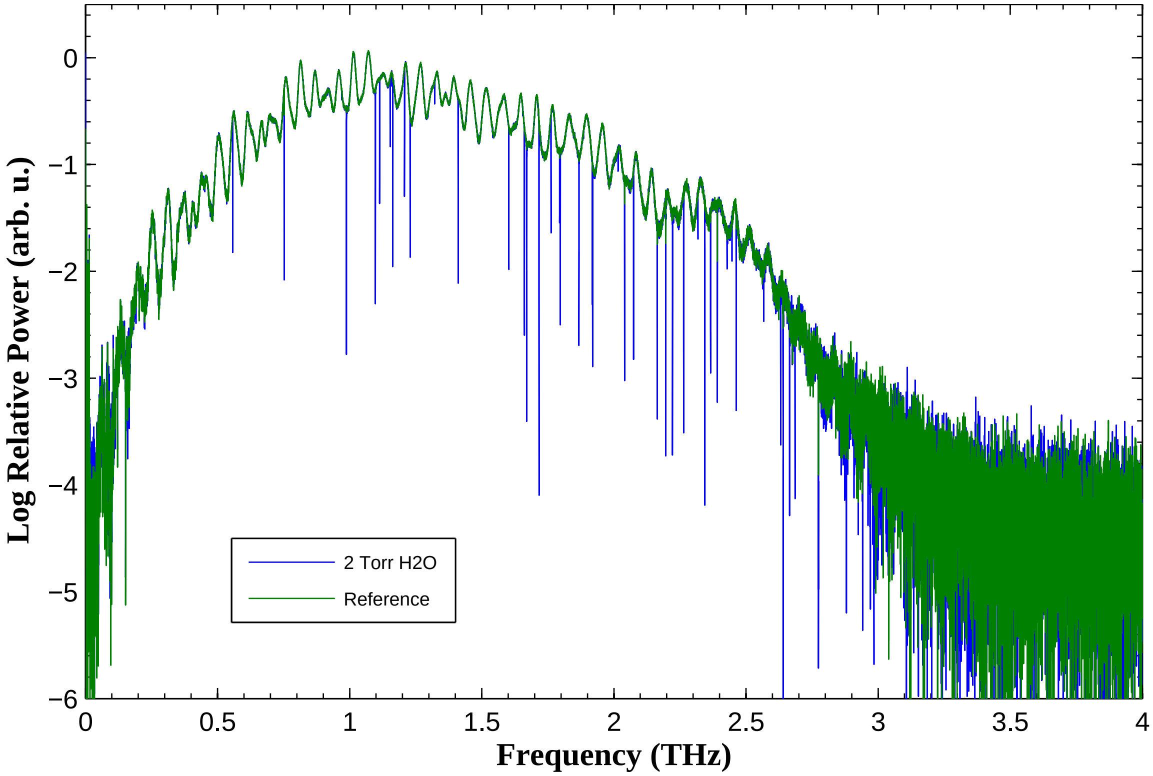

Figure 3.12: Comparison of water vapor and reference spectra; note the sharp water vapor absorption lines dipping down beneath the curve of the reference spectrum. Both sample and reference have a wavy baseline, likely from multiple THz pulse reflections in the instrument. The baseline largely divides out between sample and reference, as shown in the referenced spectrum in Figure 3.13

.

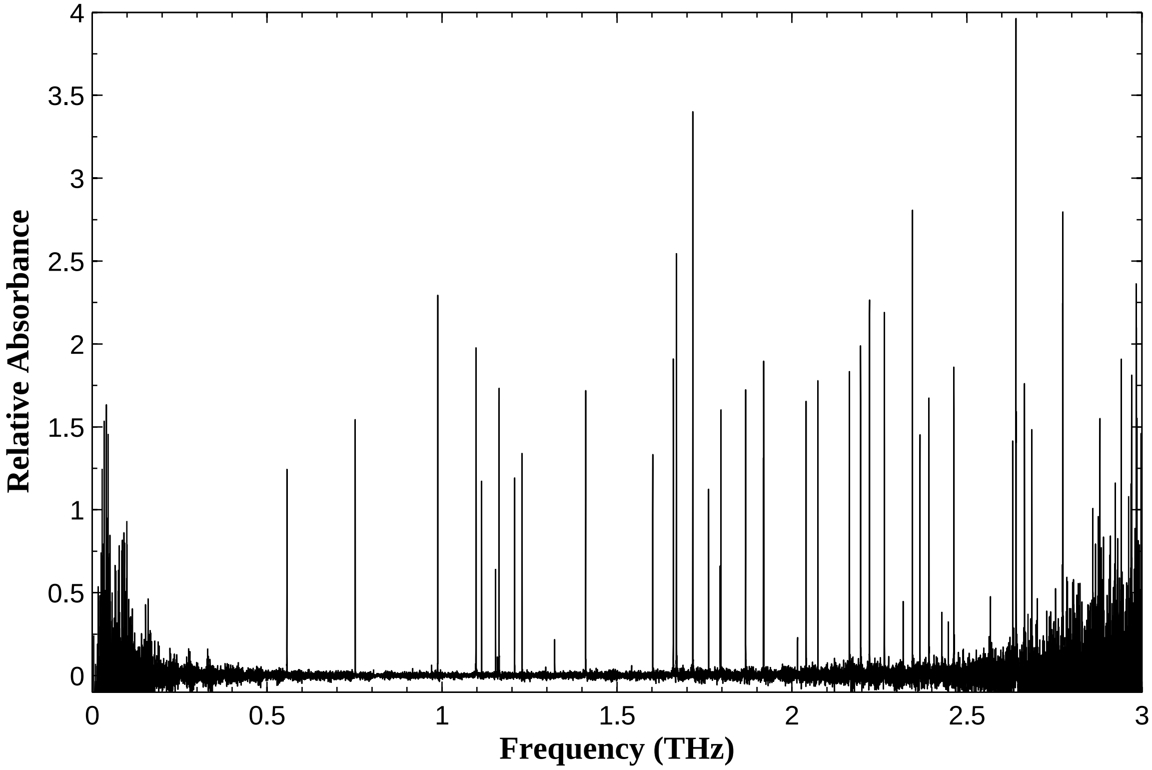

Figure 3.13: A referenced water vapor spectrum, the result of dividing the relative power of the water vapor and reference scans of Figure 3.12. The wavy baseline of the un-referenced data has disappeared. The noise levels are low enough for productive measurement of water vapor rotational transitions in the range of ~0.25-2.6 THz.

(that is, the squares of their FFT amplitudes) as in 3.32 in §3.1.3; the negative, base-10 log of the ratio is taken to yield absorbance values and plotted as the referenced scan in Figure 3.13. It is clear upon inspection that the large, background curve of the spectra in Figure 3.12 is gone, yielding a flat baseline, with sharp transitions remaining (now positive-going absorbance values because of the negative base-10 logarithm taken). For the interested reader, it should be noted that these data were processed and figures generated with a (MATLAB) script, 'test_background.m' included in the appendix, §A.9. This script is designed so that it can be easily re-used in future efforts to perform this backgrounding function on different scans and with different FFT parameters, etc.

There are a few important aspects of Figure 3.13 which should be noted. First is that, as with Figure 3.12, the high number of sample points plotted requires undersampling, such that the spectral lines do indeed appear to be lines. As discussed further below in §3.5.4, and as seen in numerous figures herein, the spectral lines are nonetheless of a finite linewidth. More importantly, Figures 3.12 and 3.13, taken together, provide a clear demonstration of the bandwidth of the instrumental bandwidth. Just as the raw spectra in Figure 3.12 are increasingly noisier above ~ 2.5 THz and below ~ 200 GHz, the referenced spectrum in 3.13 shows a substantial increase in noise in these spectral regions. These noise levels set the useable instrumental bandwidth of the instrument; from Figure 3.13 it presently is ∼0.25-2.6 THz. This bandwidth is as expected for the thickness of electro-optic detection crystal utilized and other factors; bandwidth concerns are discussed further in chapters 2 and 5. For the present application of the THz spectroscopy of water vapor, the present bandwidth and sensitivity of the instrument are clearly sufficient to identify numerous water vapor rotational transitions; finding the frequencies of these peaks is the focus of the next section, and indeed of this chapter.

3.5.2 Finding Spectral Peak Frequencies

There are different approaches available for the identification of spectral peaks. A common approach is to fit a standard line-shape to each peak, such that the peak location is a result of the best-fit parameters of the peak fitting. Indeed, this approach was followed in an early (lower-resolution) THz-TDS spectroscopy study of water vapor by van Exter et al. [36]. The authors there assumed a Lorentzian line shape and derived peak positions from fitting the THz spectra as such. However, they also pursued an alternative method of finding peak centers, by using extra zero-padding in the Fourier transform. As was discussed in §3.4.3, zero-padding provides an artificial increase in spectral resolution by interpolating between datapoints, and as observed in the plots of Figure 3.7, the highest levels of zero-padding used therein, basically 'completed' the shape of the spectral peak. In this same manner, van Exter et al. were able to obtain line centers, found to be the same as those from the analysis based on Lorentzian curve-fitting. As such, a zero-padding-based analysis was employed in the present effort. The spectrum resulting from a high-level of zero-padding is simply searched for the highest datapoints; the locations of these datapoints are the peak frequencies.

The spectral peak finding analysis was performed upon THz-TDS data from the single, balanced-detector arrangement, with similar acquisition parameters as noted above in §3.3.1. The time domain data was taken from 0 to 5000 ps, despite the reduction in spectral resolution, out of concern that etalon features from the reflected pulse may be affecting the measured peak locations to a small extent; this possibility should be explored further in the future. The data were not apodized, given the relatively flat baseline of the time-domain waveform, as discussed in §3.4.5, including for the 0 to 5000 ps portion cut-out for the present analysis. The data were heavily zero-padded; a zero-padding level of 7 powers of 2 beyond the next power of 2 was used (i.e., a 'num_zeroPad' value of 8 was passed to the 'fft_plus' Fourier analysis function). Peaks were identified with an automatic-peak finding routine; the results are discussed further in the next section, §3.5.3.

As a note to the interested reader, the data were prepared into the frequency domain spectrum with the assistance of the 'test_zeroPad.m' MATLAB script previously used in §3.4.3 for examining the effect of different levels of zero-padding upon water vapor spectra; the script is described further in the Appendix, §A.7. As a perhaps simpler alternative, the 'test_background' script used to produce Figure 3.13 could also be used; it is also in the appendix, §A.9. As usual, the 'fft_plus' Fourier function was utilized; it was set to return power values, (i.e., 'case_output' value of 3) to yield simple squares of the Fourier amplitude, proportional to power. These were referenced in the 'num_zeroPad' script to yield relative absorbance plots. These peaks were then located with a custom 'wrapper' for MATLAB's 'findpeaks' peak-finding command; the 'peakAnalyzer' custom script is included and described further in the appendix, §A.8. These scripts, including the peak-finding routine, can easily be utilized for future studies with the present instrumentation.

3.5.3 Results of Peak Frequency Analysis

The results of the peak-finding analysis described in §3.5.2 are plotted in Figures 3.14 and 3.15 and tabulated in Table 3.1. In order to better show the water spectra and their peak assignments, the overall spectrum, previously plotted at once in 3.13 has been split in two portions, one from 0.5-2 THz (Figure 3.14), the other from 2-2.5 THz (Figure 3.15); as discussed in §3.5.1, this is essentially all of the instruments available bandwidth, given its current configuration. These peak-finding (and figure creation) were performed in the 'peakAnalyzer' custom script noted above and included, with further description, in the appendix, §A.8. Of note, the noise levels of the higher bandwidth range of 2-2.5 THz was such that a slightly higher threshold for peak detection was used in this region, relative to the first, but as seen in the figures, clean peaks are nonetheless obviously visible in both frequency ranges.

Of course, it is important to compare the peak locations found by the present instrumentation and analysis to widely accepted values in the literature. For water vapor, and many other common atmospheric gases, a major resource in this regard is the HITRAN (**hi**gh **tran**smission) spectroscopic database [18] [90]. It should be noted that this database also draws line information from the widely regarded 'JPL catalog' [91]. The peak center frequencies measured in the present study were compared against the accepted values in the HITRAN database. Corresponding pairs of peaks are included in 3.1, along with the frequency differences between the presently measured peaks and the accepted values, as well as line strength and transition information.

As note to the interested reader, the line strengths are reported in units of cm/mol. This is actually a simplification of the 'full' units which are wavenumbers per cross section density, or $\mathrm{cm}^{-1}/(\mathrm{molecule} \cdot \mathrm{cm}^{-2})$ (at a standard temperature of 296 K); these units are defined in a paper describing the 1996 version of the HITRAN database [92]. The transition information in 3.1 represents the upper-state and lower-state 'local quanta' associated with the transitions. At these relatively low frequencies, the transitions are of course all purely changes in rotational states, so the 'global quanta', or vibrational states of the transitions are all

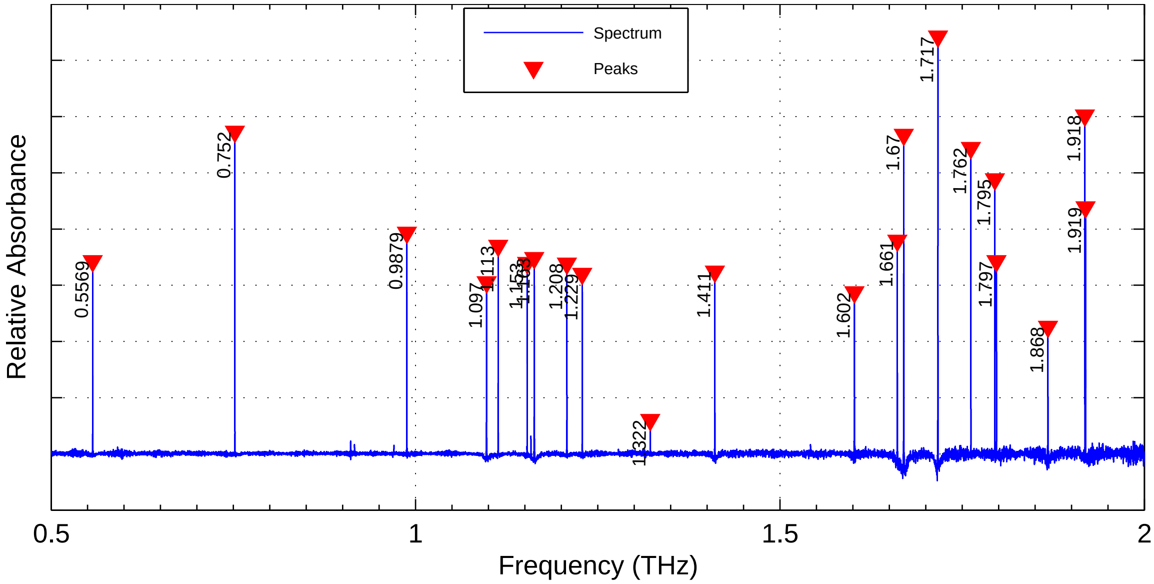

Figure 3.14: The experimental THz-TDS spectrum of water vapor, from 0.5-2 THz, plotted to show the peak center frequencies. The peak centers are found by using a high level of zero-padding in the FFT so as to interpolate the frequency-domain data, then locating maximum values.

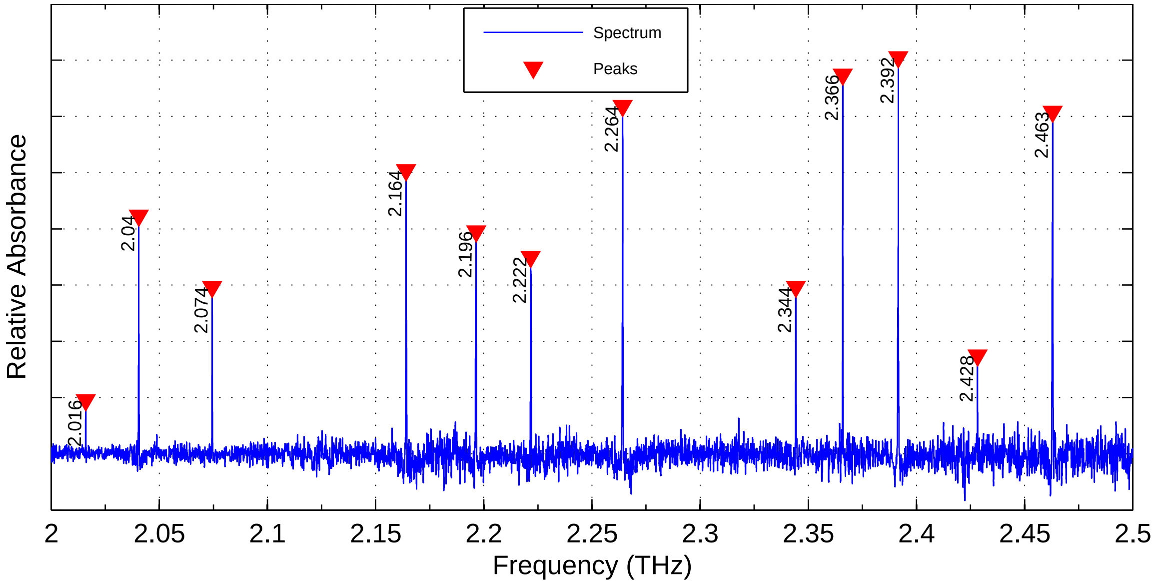

Figure 3.15: The experimental THz-TDS spectrum of water vapor, continued from Figure 3.14, to show the 2-2.5 THz spectral region and the peak center frequencies in the range. The noise levels are slightly higher, relative to the 0.5-2 THz region, but peak centers are nonetheless easily found.

Line Number	HITRAN wavenumber (cm-1)	HITRAN Frequency (THz)	Measured Frequency (THz)	Frequency Difference (MHz)	Line Intensity (cm/mol)	Transition Upper	Lower
1	18.577385	0.5569360	0.5569305	5.5	18.577385	1 1 0	1 0 1
2	25.085124	0.7520331	0.7520287	4.4	25.085124	2 1 1	2 0 2
3	32.953690	0.9879268	0.9879274	-0.7	32.953690	2 0 2	1 1 1
4	36.604150	1.0973648	1.0974219	-57.1	36.604150	3 1 2	3 0 3
5	37.137125	1.1133430	1.1133381	4.9	37.137125	1 1 1	0 0 0
6	38.464169	1.1531268	1.1531270	-0.2	38.464169	3 1 2	2 2 1
7	38.790556	1.1629116	1.1628653	46.3	38.790556	3 2 1	3 1 2
8	40.282490	1.2076387	1.2076374	1.3	40.282490	4 2 2	4 1 3
9	40.987981	1.2287888	1.2287884	0.3	40.987981	2 2 0	2 1 1
10	44.099344	1.3220651	1.3220643	0.8	44.099344	6 2 5	5 3 2
11	47.053149	1.4106179	1.4106133	4.7	47.053149	5 2 3	5 1 4
12	53.444280	1.6022192	1.6022136	5.6	53.444280	4 1 3	4 0 4
13	55.405255	1.6610078	1.6609488	58.9	55.405255	2 2 1	2 1 2
14	55.702029	1.6699048	1.6699006	4.2	55.702029	2 1 2	1 0 1
15	57.265273	1.7167697	1.7168268	-57.1	57.265273	3 0 3	2 1 2
16	58.775425	1.7620429	1.7620413	1.6	58.775425	6 3 3	6 2 4
17	59.867711	1.7947888	1.7947838	5.0	59.867711	6 2 4	6 1 5
18	59.946767	1.7971589	1.7971570	1.9	59.946767	7 3 4	7 2 5
19	62.301394	1.8677488	1.8676580	90.8	62.301394	5 3 2	5 2 3
20	63.993782	1.9184853	1.9184857	-0.4	63.993782	5 2 3	4 3 2
21	64.022941	1.9193595	1.9193557	3.7	64.022941	3 2 2	3 1 3
22	67.245953	2.0159830	2.0159865	-3.5	67.245953	8 3 5	8 2 6
23	68.062986	2.0404770	2.0404745	2.5	68.062986	4 3 1	4 2 2
24	69.195617	2.0744324	2.0744222	10.2	69.195617	4 1 3	3 2 2
25	72.187672	2.1641320	2.1640066	125.4	72.187672	3 1 3	2 0 2
26	73.262212	2.1963459	2.1964527	-106.8	73.262212	3 3 0	3 2 1
27	74.109615	2.2217504	2.2216677	82.7	74.109615	5 1 4	5 0 5
28	75.523901	2.2641496	2.2642126	-63.0	75.523901	4 2 3	4 1 4
29	78.195775	2.3442504	2.3442270	23.4	78.195775	7 2 5	7 1 6
30	78.917917	2.3658996	2.3659456	-46.0	78.917917	3 3 1	3 2 2
31	79.774278	2.3915727	2.3915882	-15.5	79.774278	4 0 4	3 1 3
32	80.997619	2.4282475	2.4282412	6.3	80.997619	9 3 6	9 2 7
33	82.154605	2.4629331	2.4629830	-49.9	82.154605	4 3 2	4 2 3

Table 3.1: A comparison of the presently determined peak frequencies for water vapor to accepted values from the HITRAN database [18]. Note that the 'line number' field is for internal reference. The transition notation is JK_aK_c. The average frequency deviation between the new centers and those in HITRAN is approximately 27.0 MHz.

fixed during the transition. Further, given the temperature of the sample (room), the energy levels of the water molecule and the sensitivity of the spectrometer, all transitions occur on the ground state vibrational manifold, or ‘0 0 0’, as in all three normal vibrational modes of water are in their lowest state.

Regarding the rotational transitions, the notation is JK_aK_c, where J is the total angular momentum (excluding nuclear spin) and K_a and K_c are labels for asymmetric tops, such as water, derived from the energy levels of prolate and oblate tops, respectively [19]. The notation employed by the HITRAN database for water, and other molecules is described further in the paper on its 2004 version [93]. The water molecule has a dipole moment in the molecular plane, along its z or b-axis. In addition to the selection rule on J values of $\Delta J = 0, \pm 1$, the *b*-type transitions of water are associated with the selection rules of $\Delta K_a = \pm 1(\pm 3, ...)$ and $\Delta K_c = \pm 1(\pm 3, ...)$.

Of great importance to the present effort in the THz spectroscopy of water, is of course the accuracy of the measured line center positions, relative the values of the standard HITRAN database. As shown in Table 3.1, the average absolute deviation of presently measured centers from the HITRAN values is approximately 27.0 MHz.

The average (absolute) frequency deviation from the widely accepted HITRAN values was 27.0 MHz. This result compares quite favorably to the original THz-TDS paper on the spectroscopy of water vapor by van Exter et al. [36], wherein their measured line centers had an estimated error of ±1 GHz. Those results were acquired on a traditional delay-line based spectrometer and a scan duration of 200 ps, already much longer than the delay scans typically acquired on such instruments. Further, the line centers had a systematic deviation of approximately 1 GHz, attributed by the authors to an error in the calibration of their delay line. In the present effort, the calibration of the delay line is replaced by the stability of the repetition rates of the pump and probe lasers, and the measurement of the pump laser rate by a referenced frequency counter. It should also be noted that the work of Bartels et al. [40] on a 1 GHz-resolution ASOPS system, that a comparison was performed against the HITRAN database for water vapor, with those authors reporting good agreement for frequencies up to 2.5 THz and noting that differences between their line centers and the database were below their resolution limit (of 1 GHz). In a more recent paper from that group, Klatt et al. [15] reported a mean deviation of line positions, relative to the HITRAN database, of 142 MHz, with individual line deviations reaching up to 461 MHz at most. The authors noted the most likely error source to be a systematic calibration error in the relationship between delay-time and lab-time, due to problems in the laser repetition rate locking electronics. Overall, the 27 MHz performance level of the present study compares favorably.

3.5.4 Fitting Spectral Linewidths

An important aspect to the present THz spectroscopy of water vapor is to demonstrate the technical capabilities of the instrument. A motivating aspect of the instrument's construction was the higher spectral resolution it would offer, thus enabling better line center measurements. As an initial real-sample demonstration of the instrument spectral resolution, a water peak (as plotted in Figures 3.13 and 3.14, was isolated and numerically fit to find a measure of its linewidth. A full 10,000 ps scan from the dual-detector configuration of the instrument was used for the fitting analysis (with zero-padding only to the next power of 2), and a peak at 1.153 THz was chosen, as it is of moderate intensity and exhibited minimal issues with frequency-domain ringing and distortion.

At the sample pressure of approximately 2 Torr, the overall linewidth is expected to be just below the instrumental resolution of 100 MHz that is associated with 10,000 ps scans, so an instrument-limited spectral linewidth of about 100 MHz is expected. This pressure was chosen to nearly match the expected linewidth to the instrument resolution, but to not exceed it, while maximizing the optical depth of the sample for strong absorption features. The true linewidth of spectral peak will be the convolution of various homogeneous and inhomogeneous broadening mechanisms [19], notably pressure broadening and Doppler broadening, respectively. The HITRAN database provides information on self-broadening; for the transition at 1.153 THz and 296K, the self-broadened half width at half-maximum is 0.538 cm^{-1}/atm, yielding an expected full-width pressure-broadening contribution to the linewidth of about 85 MHz. A calculation of Doppler broadening finds a full-width contribution of about 3 MHz. In cases where the pressure- and Doppler-broadening effects are of similar magnitude, a convolution of their line shapes, Lorentzian and Gaussian, respectively, into a Voigt line-shape function, is required. However, given the present order of magnitude difference in contributions and the approximate nature of the analysis, it is thus appropriate to model the peaks as having Lorentzian line-shapes; this line-shape was also utilized in previous THz-TDS studies of water vapor (e.g., [36], [15]). Such a fitting was made and is plotted over the original data points, as shown in Figure 3.16.

As seen in the figure, there are not many experimental data points over the peak. There are three points on the central portion of the peak and perhaps a few more about the base; this is expected as the peak's Lorentzian linewidth is close to or less than the size of the frequency bins in the spectrum. The fitting result for the Lorentzian linewidth is $\Delta\nu_{1/2}$ = 98.8 MHz, with 95% confidence bounds of 88.7 to 108.9 MHz; the somewhat large bounds are reasonable given the low number of datapoints available. Future efforts should re-visit this test, once better control of the experimental pressure is achieved (see discussion in chapter 5), and measure samples at both of lower and especially higher pressures to further verify the spectral resolution performance. However, the present result is nonetheless an initial verification of the instrument performance.

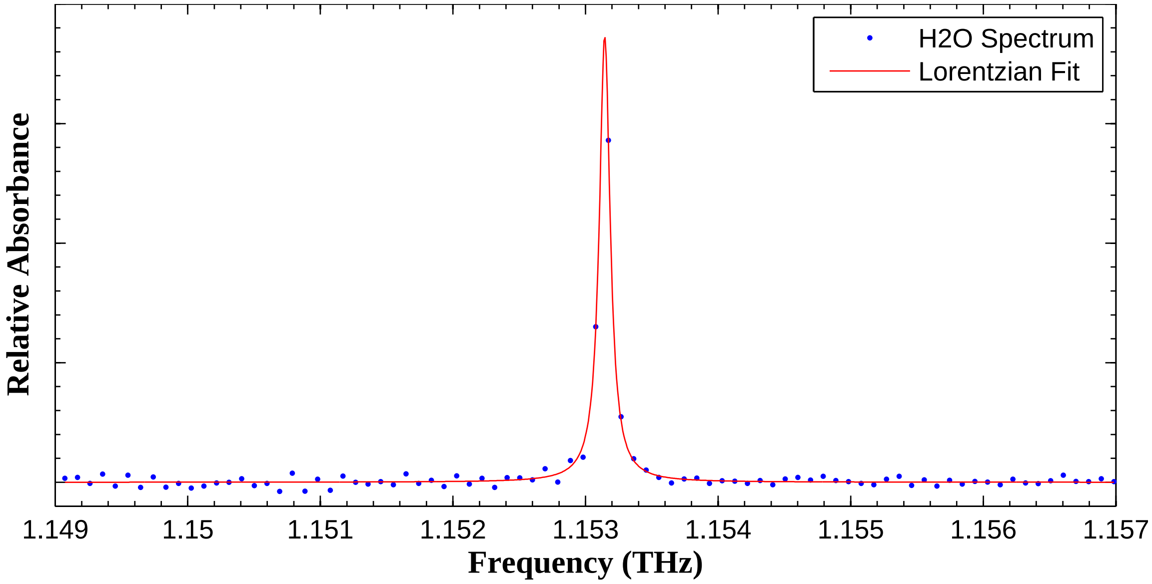

Figure 3.16: Lorentzian fit to a water vapor peak, obtained from a long (10,000 ps) waveform and zero-padding only to the next power of 2 in the scan record length. The linewidth was fitted as 98.8 MHz; see main text for further details.

For the interested reader, it is noted that the curve-fitting was carried out in MATLAB using non-linear least squares fitting in the 'Curve Fitting Toolbox' and a custom equation for the fitting, that is, the Lorentzian line-shape function [94]:

$$L(x) = \frac{1}{\pi} \frac{\frac{1}{2}\Gamma}{(x-x_0)^2 + (\frac{1}{2}\Gamma)^2} \tag{3.49}$$

where Γ is the full width at half maximum and x_0 is the peak center (these may also be noted, in the context of spectroscopy [19], as $\Delta\nu_{1/2}$ and ν_0, respectively).

The referenced scan data was first prepared using the 'test_background.m' script (included in the appendix, §A.9). The results from this first script were further processed by a new script 'peakOne_createFit.m', which isolated the desired peak and called a fitting function based on MATLAB's curve fitting toolbox; the script and fitting function are discussed further and included in the appendix, §A.11.

Chapter 4

Applications in Materials Science

The ASOPS THz-TDS instrument is versatile in its potential areas of application beyond gas-phase spectroscopy and we have pursued collaborations in this regard. In this chapter, we discuss two areas in materials science and condensed matter physics where we have applied the present instrumentation. In the first example below, in §4.1, we present the details of an all-optical (i.e., non-THz) use of the instrumentation. Here, the virtual delay line capability of our instrument is used in an optical pump-probe experiment to measure ultrafast, time-dependent changes in the reflectance of a sample in response to the heat generated from a pump pulse. These time-domain waveforms can be modeled so as to extract the size-dependent heat conduction properties of the sample. Such data can inform efforts to engineer the thermal properties of a material on a nanoscale so as to create thermal metamaterials for a wide array of practical uses. And in the second example below, in §4.2, we return to THz spectroscopy, but of a very different sample. Specifically, we use our spectrometer's THz pulse itself as the pump pulse to excite a coherent magnon mode in a candidate spintronics material. As the material's electrons precess in a coordinated fashion, the sample produces a long-duration THz ringing signal that we record much as we would in a regular THz-TDS experiment.

4.1 Measurement of Thermal Conductivity

Phonons represent the units or quanta of excitation of lattice vibrations in a crystalline material. These quasiparticles can be thought of as the 'quanta of sound waves' [95] and determine the thermal properties of crystalline matter [96]. Phonons, in being particle-like, have an associated mean free path (MFP), or average distance between collisions, and this property is a major factor in a material's thermal conductivity. When the size of a piece of material is close to the length of the MFPs associated with its phonon modes, then size effects in its heat conduction properties can result [97]. For example, nanowires and other nanostructured materials have been designed to have reduced thermal conductivity (e.g., [98]). In general, thermal energy moves down gradients in temperature at a rate proportional to the magnitude of the gradient; the constant of proportionality is the coefficient of thermal conductivity (κ, typically in units of W $m^{-1}K^{-1}$ and this is a simple statement of what is known as Fourier's law of heat conduction. In bulk material, the thermal properties, such as the conductivity, are determined by the material's phonon modes. However, by structuring matter on a nanoscale, on a level comparable to the mean path lengths of phonons, the conductivity can be altered; one is essentially creating a thermal metamaterial. For example, in the work of Pernot et al. [98], 'nanodot barriers' were engineered in order to scatter phonon modes, thus reducing thermal conductivity.

The ability to engineer the thermal properties of materials promises many applications. For example, controlling the thermal conductivity of materials may enable better heat management on computer chips and more efficient thermoelectric materials for energy applications such as recovering waste heat in machinery or powering spacecraft, or enable new materials for traditional engines to achieve higher efficiencies. Important to this approach, though, is knowledge of the phonon wavelengths and mean free paths, so that material structures can be designed on these spatial scales. Our collaborator, Professor Minnich of Caltech's Engineering and Applied Science Division, achieved a breakthrough in creating the first experimental technique capable of measuring MFP distributions in many materials and on a wide range of length scales [97].

4.1.1 Experimental Measurement of Phonon Mean Free Paths

Professor Minnich's technique is based on the size effects in heat conduction that can occur when a temperature gradient is created on a length scale similar to that of a material's MFPs. With such a highly local heat source, the conduction or heat flux away from that area will be reduced relative to the Fourier's Law behavior of the material that would be observed with a larger-scale source. The explanation is that there would be phonon MFPs longer than the length scale of the heated spot, thus carrying the thermal energy away from the spot with a low probability of scattering in that spot; such scattering is necessary for dissipating the energy and reaching thermal equilibrium, so the thermal conductivity is reduced. This transport of thermal energy away from the heat source is then known as 'nonlocal heat conduction' and is said to be 'ballistic' transport as opposed to the usual 'diffusive transport'.

The principle of the technique is by changing the size of a heated spot on a material, and monitoring changes in the thermal conductivity of the sample at that spot, then one could figure out the MFPs of the phonon modes that were affected. Further theoretical details are discussed various references, i.e., [97] [99] [100]. The focus of the remainder of this section is primarily upon the experimental aspects. In particular is the question of how to create localized heating and to do so in such a way as to measure the conductance of heat away from that spot.

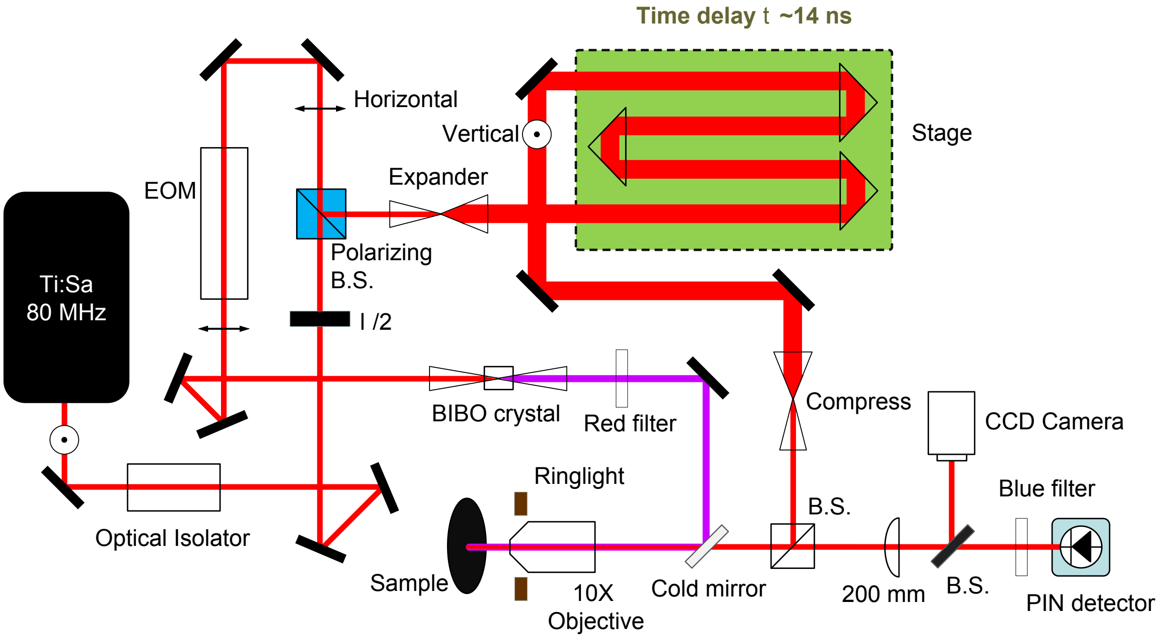

Figure 4.1: A traditional TTR instrument, as employed in the Minnich lab. Pump-probe delays are achieved via the use of a long range, quadruple-pass optical delay line; the beam is magnified for the delay line, to minimize delay-dependent changes in laser spot size. The optical pump pulses are doubled in a nonlinear crystal (BIBO) to enable clean spectral rejection of these pulses in the detection of the 800 nm probe pulses. (Figure courtesy of Xiangwen Chen)

As of that time, there was already a ‘transient thermoreflectance’ (TTR) technique wherein a laser beam is used to heat a local (∼micron-level) spot and the reflectance of another, probe beam, is used to monitor temperature, as the reflectance varies with temperature in a way that can be characterized well [101]. By adding to the procedure the variation of the pump beam size, and calculating thermal properties at each step in size [102], the wavelength distribution of MFPs can be determined.

The experimental design of a traditional TTR instrument, as used presently in the Professor Minnich’s group, is shown in Figure 4.1. The key point of the design is that both of pump and probe beams, with a relative delay, are delivered to the same spot on a sample, and with a controlled spot size. As the delay of the probe is varied relative to the heating, or pump, pulse, the sample will be encountered at a different different and its reflectivity altered. The samples typically tested in the present work include both of gallium arsenide and silicon. Both however, are coated with thin layers (typically several tens of nm or less) of aluminum as the thermoreflectance layer, as the aluminum provides a uniform temperature-reflection response across samples and prevents unintended material excitations from the beam. Notably, the changes in pump-probe delay time are achieved with a very long, traditional mechanical delay stage. And it is for replacing this delay stage with an ASOPS system that our collaboration started.

4.1.2 Experimental Design of an ASOPS-based TTR Instrument

The virtual delay line of the ASOPS instrument achieves its time-delay scanning without any mechanical stage motion. And with full-delay scans acquired at the repetition rate offset frequency, scan are collected at a very fast rate. With sufficient signal-to-noise (which is higher for TTR vs THz work), one can require all needed data potentially with only a few seconds of data acquisition time, while maintaining sub-picosecond timing resolution over $>$10 ns of pump-probe delay time. In scaling delay-time events to a slower lab-time frequency, experiments can now be done with low bandwidth electronics. This stands in contrast to the high-frequency modulation and lock-in recovery schemes of traditional, delay-line based TTR measurements.

The benefits of ASOPS for traditional (non-size-varied) TTR measurements have already been recognized [103], Professor Minnich was interested in expanding upon this by performing the size-dependent TTR work for finding phonon MFPs, though doing so with our ASOPS-based system. One important technical note, though, does present itself. The pump and probe beams must somehow be isolated before detection, for clean detection of the delay-dependent probe thermoreflectance signals. In the traditional TTR instrument with long delay line, as used by the Minnich group, a 2-color scheme was employed; see Figure 4.1. The beam from a single $\sim$800nm ultrafast laser is split, and a portion nonlinearly converted to SHG as a pump beam, so that the blue pump beam can be separated easily with filters from the red, delayed probe beam. In the Blake Group ASOPS THz-TDS spectrometer, there is insufficient power for that kind of nonlinear conversion, nor is it easy to substantially change the wavelength of the lasers. As such, additional way of separating the pump and probe beams, including upon spatial separation and polarization were designed and tested; these are the focus of §4.1.2.1 and 4.1.2.2, respectively.

4.1.2.1 Pump and Probe Separation by Noncollinear Beams

A schematic of the ASOPS-TTR system is shown in Figure 4.2. The overall goal of this setup is to overlap the pump and probe beams upon the sample and having well-characterized and controlled spot sizes on the sample at that intersection point. The overlap of beams in this experimental design is achieved through the use of a pair of microscope objects oriented at an angle to each other, thus the description of this section as using noncollinear beams.

The ‘synchronization system’ noted at top is much the same as the ASOPS THz-TDS instrument as shown in Figure 2.4, with the notable difference that the ‘THz Detection & Recording’ subsystem, as highlighted in Figure 2.6, is now removed. An early version of the TTR instrument (the noncollinear version discussed in the present section) is visible and noted at bottom left in the photo of the overall ASOPS instrumentation in Figure 2.5.

The integration of the TTR instrument with the ASOPS system is actually quite straightforward; one only requires access to each of the pump and probe beams. A pair of flip mirrors were inserted into the ASOPS THz-TDS instrument, one each for the pump and probe beams. Referring to Figure 2.4 for positioning, the pump flip mirror was inserted into the pump beam line between the first (from laser) lens and the preceding beam sampler. The probe beam flip mirror was positioned just before the pair of high-reflection mirrors immediately prior to the beam input to the purge enclosure. Both flip mirrors directed their beams across the table to additional turning optics into the TTR setup. Pairs of irises were fixed in the TTR setup for easy re-alignment when the flip mirrors were used; the beams were merely 'walked' with a pair of input mirrors in the TTR setup.

Following the pump beam path in Figure 4.2, this beam was directed first to an optical isolator so as to prevent large back-reflections to the laser. The beam was then directed through a half-wave plate and polarizer to rotate the polarization horizontal (to pass the later polarizing beam splitter) and clean up its polarization. The beam was then re-sized by a pair of telescopes, the first a cylindrical lens pair to adjust astigmatism, the second spherical, with one lens moveable, as a variable telescope to control the pump beam size upon the back aperture of a microscope objective, thus controlling the focused spot size on the sample. The sample was monitored with a CCD camera and tube lens positioned to receive either of un-polarized back reflected light or the illumination from a ring light placed around the microscope objective. In this overall design, the metallized, mirror-like sample reflects almost all pump light back upon the path along which it arrived. Sending this much light back to the laser may cause instabilities in its operation, thus the laser is protected by the optical isolator at the input to the TTR setup.

Following the probe beam path, it was directed first through a pair of cylindrical lenses to correct for any beam astigmatism at this point; the lenses were generally fixed once this correction had been done in initial alignment, even between uses of the flip mirrors. The beam was then passed through a pair of spherical lenses, where one lens could be moved along the optical path, as an adjustable telescope to control the beam size into the back aperture of the microscope objective, thus controlling the probe beam spot size. Following the lenses, the probe beam was split on a non-polarizing beam splitter, directing light to both of a microscope objective for focusing on the sample, as well as to one of the balanced photodiodes (with power adjustment from a polarizer, for proper detector balancing), as a reference signal. The portion of the beam directed at the sample was collected on reflection from the metallized (i.e., mirror-like) sample surface with a pair of lenses and directed to the other photodiode of the balanced detector, as the sample signal. In collecting the probe beam at an angle with respect to the pump beam, we essentially avoid the collection of pump light along the probe path, despite the light in the two beams having the same wavelength. This spatial separation of pump

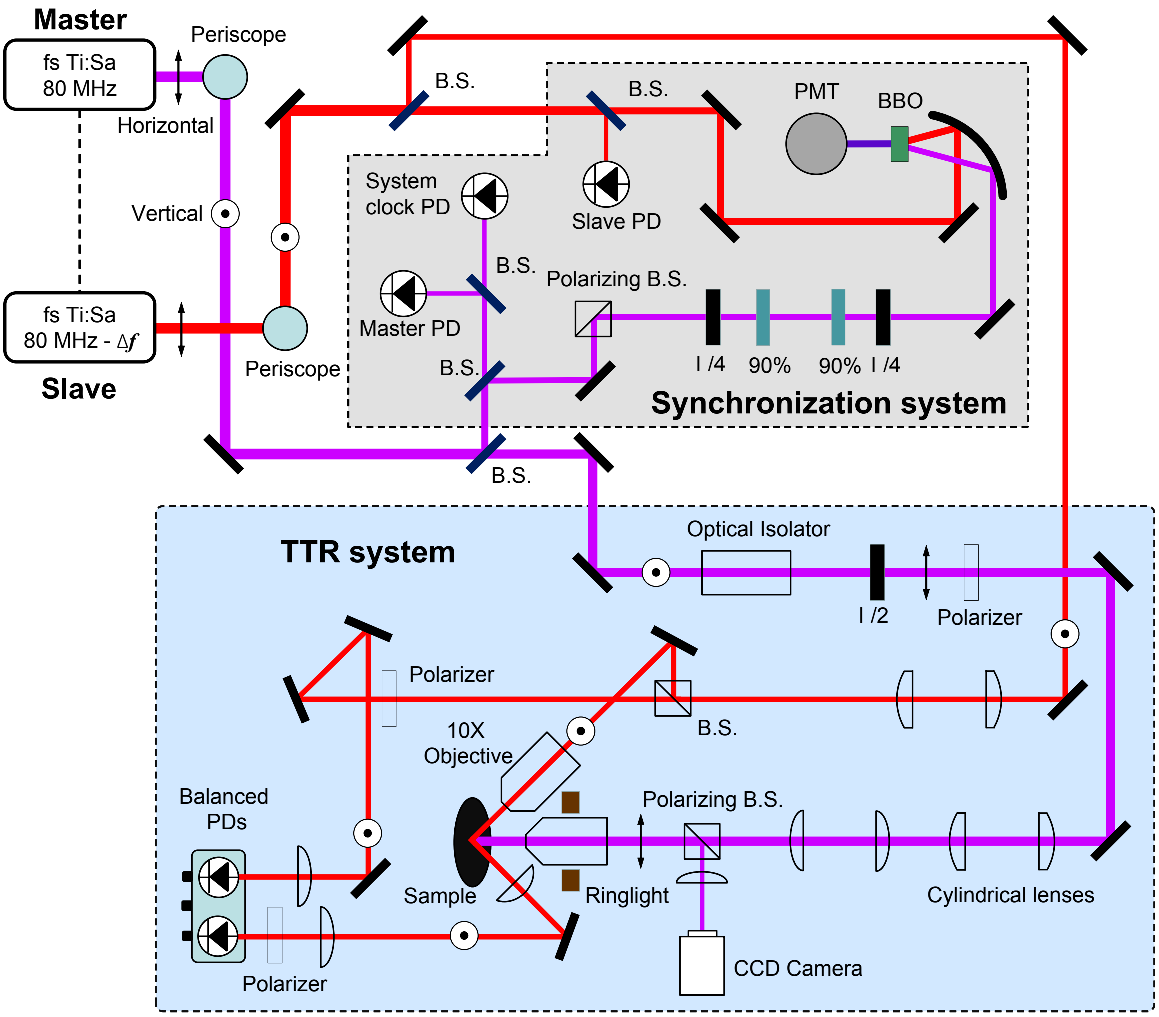

Figure 4.2: The complete ASOPS-based TTR instrument. The pump and probe beams of the ASOPS system (optical beams, before THz emission) are redirected to the TTR system, at bottom. Note that the two beam colors are for the reader's ease; the pulses are of the same wavelength. Separation of pump and pump in reflection from the sample is achieved via different angles of incidence and spatial filtering.

and probe beams is the major benefit of this experiment design.

In terms of the electronics and operation of the TTR instrument, an oscilloscope was connected to the balanced photodetector; sometimes the same digitizer as in the ASOPS setup (see §2.11) was used. The trigger signal for data acquisition could be acquired from the cross-correlator and PMT as in the ASOPS THz-TDS instrument, or from the sharp leading edge of the TTR signal itself. CCD camera images, for selecting a sampling spot, were acquired on a laptop computer. Samples were mounted on a metal plate and suspended in front of the pump beam microscope objective.

Upon testing this experimental apparatus, some practical challenges became apparent. The noncollinear pump-probe geometry makes it difficult to overlap the pump and probe beams at a known size. It is generally advantageous to overlap the pump and probe beam at a mutual focus; at such a beam waist the beam diameter is more tolerant to positioning errors. In taking beam size measurements with a scanning-slit beam profiler, we found the noncollinear geometry made it hard to take measurements of both beam sizes while ensuring those measurements corresponded to the same position. In this regard, a home-built scanning razor-edge beam profiler (e.g., [104–106]) would probably have helped make the measurements. However, it was found that controlling the spot position was also difficult. To overlap pump and probe, the 10X objective for the probe beam (see Figure 4.2) was moved; moving this optic, though, also changes the size of the probe beam at the overlap point with the pump beam. It was determined that a collinear pump-probe geometry had the potential to be easier to align while providing more reliable data, despite the challenge of separating spectrally overlapping pump and probe beams.

4.1.2.2 Pump and Probe Separation by Polarization

Given the issues noted above in the alignment and measurement of the pump and probe beam spots, the noncollinear TTR instrument setup in Figure 4.2 was replaced with a different design, the collinear arrangement of Figure 4.3. In moving to a collinear arrangement, we do encounter the problem that a simple spatial separation of pump and probe beams is no longer possible, as it was in the noncollinear arrangement. Further, a collinear arrangement with lasers having the same wavelength precludes the use of filters, dichroic mirrors, and the like for separating the two beams. In order to prevent the pump beam from overwhelming the detection of the probe beam, we therefore use the polarization property of light as a basis for separating the beams.

The beginning portions of the pump and probe beam paths in the collinear setup of Figure 4.3 are much as they were in the noncollinear arrangement as was depicted in Figure 4.2. The notable exception to this statement is that the pump beam, following the optical isolator and half-wave plate, is rotated to a vertical

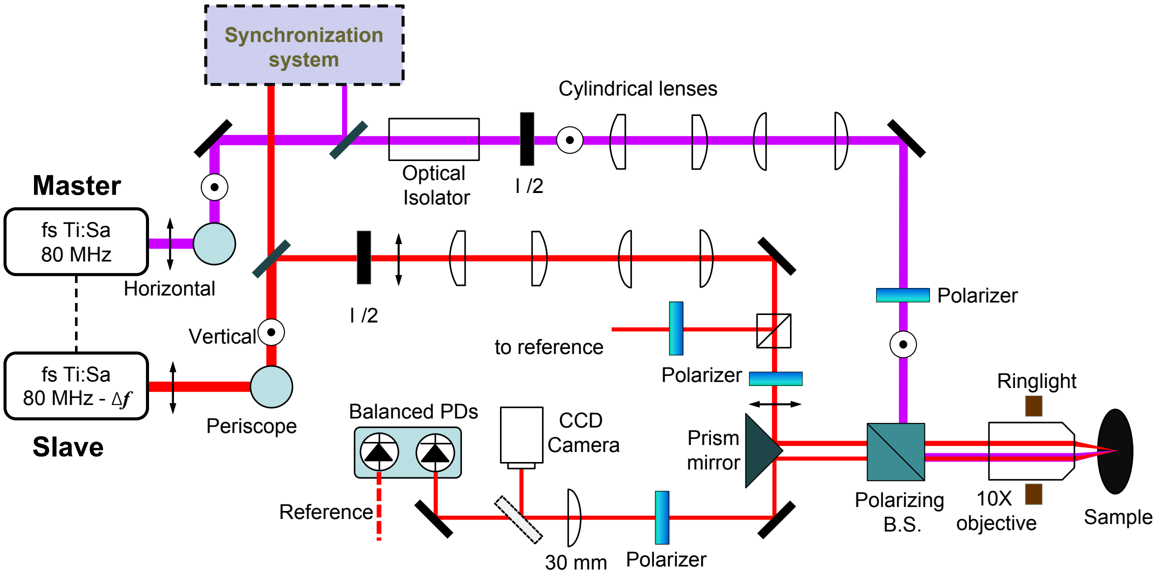

Figure 4.3: The newer version of the ASOPS-based TTR instrument, now in a collinear pump-probe geometry. The pump and probe beams of the ASOPS system (optical beams, before THz emission) are redirected to the TTR system as before (with the ASOPS synchronization as before). The two beam colors are of the same wavelength, as in Figure 4.2. Separation of pump and pump in reflection from the sample, though, is now achieved based on cross-polarization of the two beams with respect to each other.

polarization instead of horizontal. As before, though, the concern is in setting the polarization at the beginning of the setup to achieve a desired reflection or transmission upon a later polarizing beam splitter. In the present case, the pump beam is desired to reflect not transmit, hence the 90° difference in polarization. In the present case, the pump beam is directed to a polarizing beam splitter directly in front of a single microscope objective. The pump beam is reflected into the objective and focused upon the sample. The reflected pump light is reflected off of the sample and, as in the noncollinear arrangement, is sent back along it's input path and rejected by the optical isolator from continuing back to the source laser.

The probe beam polarization is also rotated differently in the collinear setup, so that it will transmit through the polarizing beam splitter. In this design, though, a prism mirror is used to direct the probe beam towards the objective, while also receiving its reflection off the sample and passing it towards the balanced detector. The prim mirror has mirrored sides with the useable mirror surface extending to a fine edge (the edge facing towards the objective in Figure 4.3. The prism mirror thus allows the incoming and outgoing probe beams to pass very close together so that they may both fit into the back aperture of the microscope objective. However, in entering the objective along a beam path that is slightly offset from the objective's optical axis, the probe beam is actually not quite collinear with pump beam. In some ways, this 'collinear' design is similar to the noncollinear design, except that the angle between the pump and probe beams is much smaller, such that the two beams can be passed through the same microscope objective while still being separated from one another. Upon exiting the objective, the probe beam is passed through a polarizing beam splitter, and reflect by the other face of the prism mirror towards the balanced detector, with power adjustment from a polarizer for proper detector balancing. In this arrangement, the CCD camera is now placed on the probe path, where it can observe the sample under illumination from the ring light surrounding the objective or from the probe light. Overall, this design has proven much easier to operate and control than the noncollinear design. The parallel alignment of the pump and probe beams through the same objective ensures they co-focus and the small angle between the beams enables straightforward measurement of their sizes at their point of overlap.

4.1.3 Results

Both of the noncollinear and collinear TTR instrument designs have an as-yet unresolved technical challenge in the measurement of accurate thermal conductivity curves. Specifically, both approaches suffer from a noisy baseline. When the sample is illuminated with the probe beam, and the pump beam blocked, there should ideally be zero signal from the balanced detector. Alternatively, there could be a nonzero, though fixed value for an unbalanced detector. However, under experimental tests, this baseline has often, though not always, been observed to be very noisy, with noise levels potentially reaching the same level as the signal itself.

The individual TTR scans themselves are relatively short. The laser repetition offset for such scans is no lower than the 100 Hz as used in the THz scans of Chapter 3, and is often in the range of several hundred hertz, as time resolution >1 picosecond is acceptable for the GaAs and Si samples studied so far. Baseline noise is generally not observed within a scan, but it does occur between scans and over the several second to few minute timescales over which we have attempted to average the TTR signals. The noise problem generally seems to fall within the lower baseband frequency region from a few hundred hertz to less than 1 Hz. For the proper fitting of thermal conductivity values to the experimental TTR curves, this shifting baseline poses a problem, as it is important to have a proper baseline value for each curve, and not an effective or average value for a set of scans.

Likely sources of noise include mechanical vibrations in the surrounding building, that couple into the table surface. If this is indeed a source of noise, this is then almost certainly exacerbated by present lack of table-floating capability. Acoustic noise in the room may also contribute. On longer timescales, temperature fluctuations are likely to be the culprit. Indeed, we have performed long-term (hours-scale) tests were the baseline signal was monitored while room temperature was simultaneously recorded. There does seem to be a correlation, with the two generally moving together. Nonetheless, and perhaps adding support to the theory of external noise, there are times when the system appears ‘calm’ and reasonable measurements can

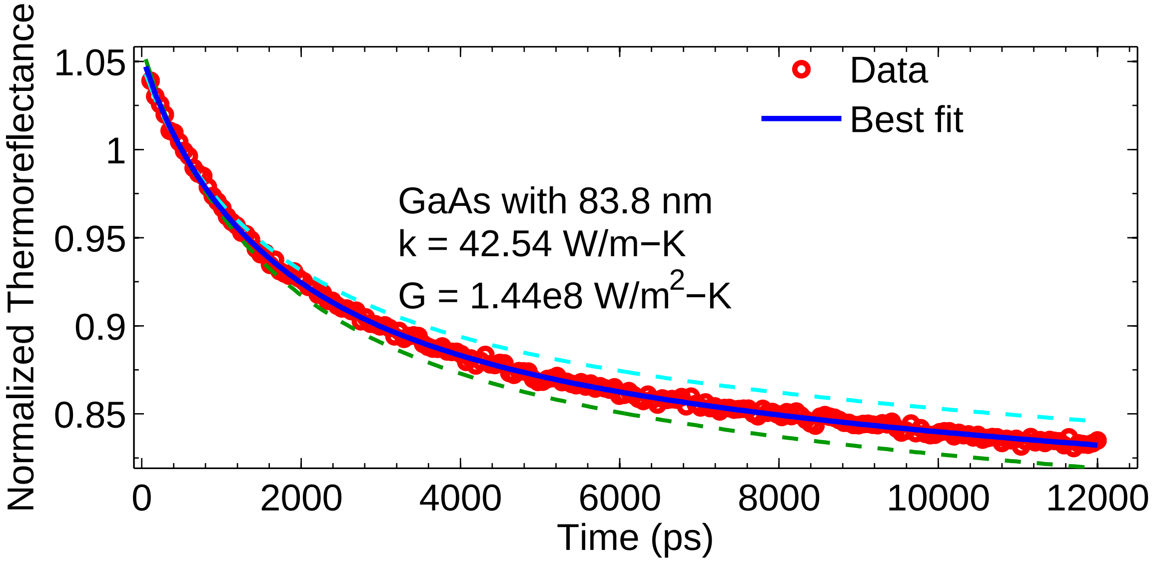

Figure 4.4: The result of the fitting routines for the transient thermoreflectance time-domain data; the sample is GaAs. The experimental data is plotted in red, with the original sharp rise from the pump pulse excluded from the analysis. See text for details.

be acquired; the issue of baseline noise is discussed further in 4.1.4.

An example of a fitted thermoreflectance curve for gallium arsenide is shown in 4.4. The specific sample was a piece of GaAs metallized with 83.8 nm of aluminum, as measured by x-ray reflectometry. The data was acquired with a repetition offset rate of 608 Hz, with 512 scans averaged; the collinear TTR setup was used with pump spot size of 30μm diameter, and a probe size of 14μm. The fitted thermal conductivity of 42.54 W/mK is indeed in good agreement with prior literature values [107]; the interested reader is referred to [99, 100]for details of the fitting procedure and theory.

4.1.4 Future ASOPS TTR Work

We generally are encouraged by the reasonable results that are *sometimes* produced by the present collinear TTR instrumental design. The relatively low frequency noise of the TTR signal baseline illustrates well one of the drawbacks of the ASOPS technique—in that, depending on the offset frequency, it may shift one's delay time signal too low in the lab timeframe. In general, one should try to avoid measuring signals in the baseband frequency region. The extent of the ASOPS time and frequency scaling could be reduced by using a larger repetition rate offset, thus shifting the signal of interest to a higher (lab timeframe) frequency range. However, in order to shift the presently lowest signals of interest to a high enough frequency range to avoid most of the noise would likely require a reduction in time resolution to approximately $\geq$ 10 ps; this is a level of time resolution that is no longer acceptable in general.

An alternative approach, and that which will likely be taken is to try a combination of reducing the noise source, avoiding the noise, and accounting for it. Reducing the noise applies mainly to the low frequency shifts in baseline signal that seem related to the temperature. The laboratory temperature has been an issue for the lab in general since our research group moved in a couple of years ago, following a major building renovation. The use of the amplified laser system can cause the room temperature to rise by a few to several degrees. Further, we have observed temperature spikes of several degrees overnight, with no apparent cause. We arranged for additional forced-air ducts to be supplied to the lab to help better regulate the temperature; these are now in place and the temperature seems to generally hold within a degree Fahrenheit.

In terms of avoiding the noise, it should be noted that the present optical table cannot be floated, due to a disabled leg. Addressing this issue and floating the table may go a long ways to addressing much of the lower baseband noise that we see, particularly in the range of a few hertz to a few hundred hertz. Much of the noise is relatively slow, and it is anticipated that much of the noise that would remain after floating the table would be particularly slow, given the mass of the table and its dampening properties. Noise remaining after this point might possibly be able to be accounted for. We have typically tried averaging scans for several seconds to a few minutes, and this is clearly enough time to have to worry about low frequency noise. We generally tried taking scans by averaging a baseline value, as sort of a reference scan. Then a sample scan would be taken. However, by the time the sample scan was started, let alone taken, the baseline may already have shifted. And one could also see this by taking a sample scan and then going back to repeat a baseline measurement. For the proper fitting of thermal conductivity values to the experimental TTR curves, it is important to have a proper baseline value for each curve, and not an effective or average value. As such, we could try splitting up the required signal averaging time and interspersing baseline checks within the set of sample scans. In this manner, we could measure the baseline more frequently, therefore being aware of higher frequency noise, and thus having a more accurate baseline value for each nearby period of signal averaging. Such a scheme could be automated with a simple computer control program and a computer-controllable optical shutter to block the pump as needed to measure the baseline.

4.2 Watching a Coherent Magnon in a Spintronics Material

Magnetoelectronics, more commonly known as spintronics, is a form of electronics based on the manipulation of the spin of the charge carriers instead of upon the charge carriers themselves (i.e., electrons and holes) [108]. An goal in this area of study is to better understand the interaction of light and matter in creating and manipulating non-equilibrium spin state populations, so that this technology may be employed as a basis for highly efficient computing [109].

Some experiments study all-optical generation and monitoring of spin waves and other phenomena. For example, Satoh et al. [110] used strong ultrafast optical pulses to generate, via the inverse Faraday effect, spin waves or patterns of spins precessing about their equilibrium magnetization direction, and used the resulting Faraday effect upon optical pulses as a detection mechanism. However, many coherent magnon modes have their natural resonance frequencies in the THz region. The optical techniques of pumping spin waves, including the inverse Faraday effect, can then be seen as impulsive stimulated Raman scattering [111]. In these cases, pumping the emission with THz wavelengths would be a much more direct route to the generation and manipulation of these states and allow the direct study of the magnetic dipole interaction between the applied field and the samples' spins [112].

In particular, a paper by Zhou et al. [16] came to our attention, demonstrating the use of oscillator-based THz emitters to pump a magnetic dipole transition at 0.299 THz in an anti-ferromagnetic yttrium iron oxide $YFeO_3$ crystal. The impulsive THz field, that is the magnetic field of the relatively weak THz pump, torqued the magnetic moment of the material's spins, setting up their precession. The THz waveform was recorded via typical THz-TDS electro-optic sampling. Fourier analysis of the original pulse portion of the THz waveform showed an absorption at 0.299 THz, while an FT of an overlapping, later portion of the THz waveform instead showed a sharp emission just at 0.299 THz. This has clear parallels to the THz spectroscopy of water in §3, particularly as shown in Figure 3.6, wherein the initial time-domain signal was attenuated in the presence of the water vapor sample. However, after the main THz peak had passed, the water sample continued to produce a time-domain ringing signal. Upon FFT of just that later signal, distinct spectral peaks were observed. Returning to the Zhou et al. work, polarization-based THz-TDS measurements revealed the emission to have circular polarization. The emission was identified as a free induction decay and was observed to have time-domain oscillations that continued for up to at least 60 ps. Unfortunately , that was the maximum time delay scan showed. We figured this would be a good sample to test further.

We formed an initial collaboration with Professor Jongseok Lee of GIST in S. Korea; Prof. Lee was able to supply the same type of *c*-cut yttrium orthoferrite $YFeO_3$ crystal as was used in Zhou et al. [16]. We simply placed the sample at the beam waist in the THz beam path, the same waist about which the gas cell is placed, and then acquired time-domain scans. A portion of the time domain scan for the $YFeO_3$ emission is included in Figure 4.5, and an FFT result is included in Figure 4.6. Referring to the time-domain scan, we can see a cropped portion of the initial instrument THz pulse at left, followed by the long-term 300 GHz; which appears to go on for at least ∼200 ps, well in excess of the 60 ps time record reported in Zhou et al. [16] (note that the waveform here is filtered in the frequency domain to remove a 6 kHz spurious oscillation in the equipment during this scan, and smoothed with a moving average as a low pass to preserve the 300 GHz content).

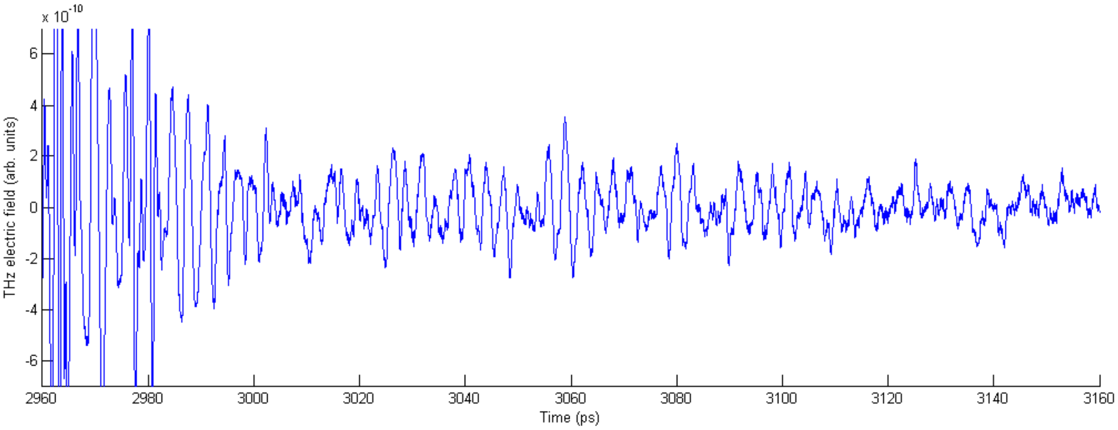

Figure 4.5: Time-Domain plot of the $YFeO_3$ emission; most of the original THz pulse is excluded here. This waveform has been further processed - see main text. It appears that multiple reflections in the instrument may be piling up on each other in the time domain. Nonetheless, the emission can be seen to continue for longer than the 60 ps previously reported [16].

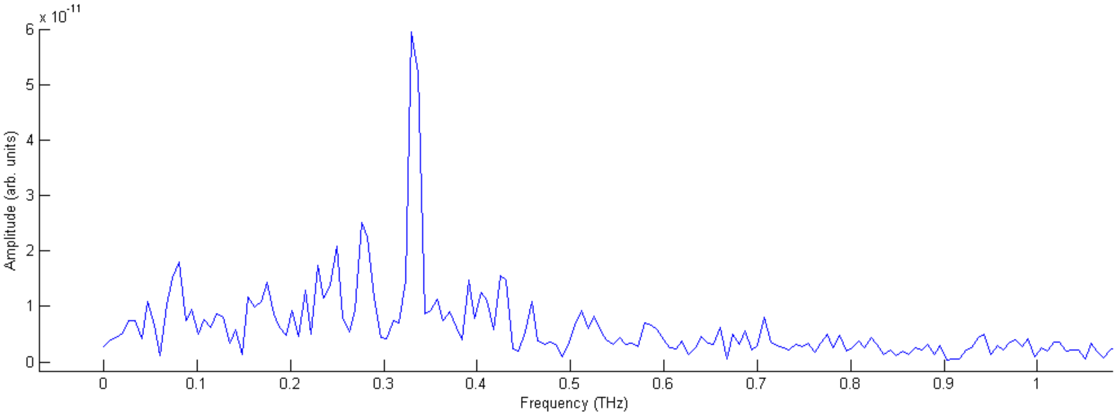

Figure 4.6: The spectrum of the $YFeO_3$ emission time-domain data in Figure 4.5. The longer time-domain scan possible with the present instrument is indeed useful for accurate characterization of the long-term coherent emission. Further improvements to the instrument signal levels and scan processing will be of help.

However, the waveform presented here is not nearly as clean; it seems that we have multiple reflections in the system piling up on each other in the time domain; this is something that should be addressed in future work if this is to be pursued further.

Chapter 5

Future Directions for ASOPS and Higher Resolution THz Spectroscopy

As seen in chapters 2 and 3 concerning the development and application the Blake Group THz-TDS spectrometer, we have already demonstrated the instrument to have a long delay scan capability, high spectral resolution and high frequency accuracy in assigned peak centers. The capabilities already demonstrated make the instrument sufficiently capable to begin routine laboratory use on a variety of samples including for example, solid-phase room temperature samples to take some of the usage strain from the high-power THz spectrometer also in the Blake Group, to beginning gas-phase studies of small molecules of astronomical interest. However looking forward, there are many technical and scientific items on the 'to-do' list, in both of the short- and long-term; more than enough to keep at least a few new students busy for some time to come! In that regard, this chapter constitutes something of a road map of what could be to come in the further technical development and scientific application of the present ASOPS THz-TDS spectrometer. For simplicity in organizing this guide, a distinction is made, as much as possible, between technical items in instrument development, and areas motivated more directly by a specific scientific application. We start the discussion off with a guide to the technical improvements to consider.

5.1 Technical Improvements to the Blake Group ASOPS THz-TDS Instrument

Building the present ASOPS THz-TDS instrument was very much an educational experience for the author and for the rest of the group as well. In developing the instrumentation, as with any project such as this, various design compromises were made in the interest of its timely development and testing. Further, with much of this equipment and underlying theory new to us, there were certain aspects of the design and potential improvements that only became apparent to us in hindsight. And of course, the past few years have seen rapid growth in the THz literature, with many new improvements reported to major components, including the electronics, emitters, detectors and so forth. From the privileged position of writing this thesis, though, the author can now finally address some of these issues that should be considered for future improvements to the instrumentation.

5.1.1 Improve Data Acquisition Averaging Capability

A relatively straightforward, but very important technical improvement to the instrument concerns improving the averaging capabilities of the data acquisition system. As discussed in chapter 2, the ‘THz Detection & Recording’ subsystem utilizes a 16-bit, 180 MSa/s, dual channel digitizer (AlazarTech model ATS9462) to acquire the THz and cross-correlator signals. Up until the present, the digital oscilloscope software (‘Alazar DSO’) that was supplied with the card has been the primary point of data acquisition for all ASOPS THz work. That is, all signal alignment and acquisition was carried out in the card manufacturer’s software on the host/control computer. Importantly, sample averaging has been carried out with the software’s built-in averaging and co-adding software plug-ins. However, there are at least three important problems in this regard.

First, and overall, the averaging and other processing of the time-domain waveforms from the card is crucial to all analysis and results that follow. Given the focus of our group on academic research in chemical physics and spectroscopy, it is generally advisable, as much as feasible, that we rely on acquisition software that we have either written ourselves, or for which we have access to the original source code. This is so that we may verify the exact operation of the card or software and spot any behavior that may affect our particular application. This leads us to the second, very much related point, that it has come to the author’s attention that the acquisition software’s included averaging plug-in apparently averages data in a 16-bit environment. Given that the bit depth of the data at collection, in a single scan, is already 16 bits, and that we wish to acquire even deeper averaging in the future, the 16-bit averaging environment presents the possibility that after a number of scans (variable depending on coding and signaling) that we may fail to see a benefit from continued averaging, due to the limitations of the bit depth. Averaging software that performs its math operations in a higher-bit (e.g., 32-bit or greater) environment should preclude these issues. An important side note is that the use of the plug-in seems to reduce rate of scan averaging and acquisition by a factor of 2; this should be pursued if the standard software is to be continued to be used.

As a third point of concern, the supplied averaging software generally cannot be interrupted. Once a scan with some number of averages, however large, has been started, it is the author’s understanding that the set of scans must be successfully finished if the averaged data is to be maintained and presented to the user. For a total averaged set of a few scans or even few dozens of scans, there is not really any problem. However, if one wishes for example, to acquire a million-scan average at a scan rate of 100 Hz, this would require at least 2.8 hours. If anything happens to the system in the meantime, even on the very last scan in the group, then the user could lose all data. Instead a ‘segmented averaging’ scheme should be implemented, as utilized in the Blake Group’s chirped-pulse Fourier-transform microwave spectroscopy work (e.g., [1]). Therein, data is collected in averaged batches, which are then saved to file. The final averaged scan is an average of these smaller intermediates. If anything goes wrong in such an intermediate scan, it can be excluded from the averaging and all other proper files retained for actual use, thus diminishing lost time. Such a capability will require our own custom-wrote code, but the manufacturer supplies an easy to use C/C++ language software development kit (SDK), with plenty of example code pertaining to averaging; this can be used as a starting point. Such averaging could have a dramatic effect on the present performance, especially given that most scans included herein had either of 1,000 or at most 10,000 averages.

It should also be noted that well-written averaging code potentially underlies many other future improvements to the instrument. In order to evaluate and choose between a set of different instrumental configurations that one may try, it will be important to take realistic scans, including with deep averages. In this case, it is important that the experimenter can trust the functioning of their averaging (and other data processing) code so that any differences in outcomes can appropriately be assigned to the experimental conditions, and the best option correctly chosen. Reliable, deep averaging will generally help us to confirm that the instrument signal-to-noise performance in electric field scales as the root of the number of scans or of time (or power, the square of the field, in a linear scaling). It would also be worthwhile to do additional testing to confirm that the signal is linear with the probe power and also that it scales properly with increased sample pressures (provided pressure is better controlled and measured, as discussed below in §5.1.9.

5.1.2 Instrument ‘Loop-Stop Code’

The instrument is generally very stable when both of the slow and fast PLLs are engaged. However, slowly, over hours, the instrument can might drift out of its locking range, the PLL lock can be lost and the instrument may head towards unlocked oscillation of the fast piezo. This of course makes data acquired during such to be unusable, and a segmented averaging scheme as discussed above in §5.1.1, would help to make the best use of scans that were acquired before this problem occurred. It is of concern to the author, though, that if the instrument is left unattended and this oscillation occurs and is left for some time, that eventually this may lead to damage of the PZT mirror assembly in the laser. If this occurs, it would be highly likely to put the laser out of order and require an expensive service visit. As an alternative, the author has a preliminary version of a ‘loop stop’ or ‘lock protect’ program (name still uncertain) that should prevent such a catastrophic problem. The program is written in C/C++ and is designed to run on the host/control computer, which is then connected to the SRS PID controller that runs both slow and fast loops. The program periodically polls the SRS unit, on the order of every few minutes or less, in order to check on the loop status. When the unit reports there is an issue, the program automatically shuts the loop control off and lowers the voltage to a good resting level. A feature to have the program automatically email the user—who may have left the acquisition unattended—has also been successfully tested. This loop protection code, along with a segmented averaging capability, will do much to enhance the usability and performance of the instrument.

5.1.3 Ease of Use Improvements to the Instrument

In order to maximize the scientific output of the instrument in the long-term and thus get the greatest benefit from the development work expended upon it, it is important that the instrument be made more user-friendly. Although usage instructions are contained herein, proper operation of the instrument nonetheless requires some training. While it is not necessarily the goal, nor should it definitely be for an academic research instrument such as this to be ‘turn-key’ like a commercial product, the instrument nonetheless can require too much start-up time for frequent use. The various RF power levels checks on parts of the circuit, for example, presently require unscrewing SMA cables and checking powers with a spectrum analyzer.

For certain cumbersome start-up (and shut-down) tasks, such as checking RF power levels, the author believes it worthwhile to invest the time, effort, and money to relive the burden on the experimenter and at least partially automate the process. In the present ASOPS instrument design, for example, the checking of RF power levels at key points, such as after the monitor photodiodes, could be improved and with no need for unscrewing cables. Instead RF crystal power meters could be installed at these points, or bias tees could be used to draw off the DC voltage level to a voltmeter. In either case, the sensors, appropriately amplified, can be monitored by a low-speed, moderate- to high-resolution digitizer and readings displayed on the host/control computer, much as the probe/slave laser stepper motor positioning is already handled. If there were any issues in the RF power levels, the instrument user could use these on-screen displays to spot the problem before taking any poor scans and to get near real-time feedback as they realigned the mirrors to direct power onto the monitor photodiodes, for example. Some components for this overall purpose have already been acquired and it is hoped that this is an area of future work that is addressed in the near future.

5.1.4 Setup Master Repetition Rate Control

In the present laser asynchronization control subsystem, as noted in §2.3.3, the master laser is left free-running, while the slave-laser follows it at a precise 100 Hz repetition rate offset. Typically, the master laser is stable to the $\sim$1 Hz level or minutes, but over longer scans or under particularly trying building conditions, the rep rate could change by 10s or even a few hundred hertz. This is starting to approach the level of drift, where it may become a concern for establishing an accurate delay timebase for longer-acquisition (i.e., highly averaged) scans. And this slightly changes the reference clock frequency that should be inputted to the DDS boards (which are clocked by the master laser). This situation can likely be remedied by using the 'galvo' mirror (really a slow, multi-wafer PZT stack) in the master laser in a third control loop (besides slave laser fast and slow loops), with this third loop locked to a low phase noise frequency synthesizer. The lock should be of low bandwidth so as to not interfere with the slave laser loops, let alone any resonances or limits to the slow PZT stack. The master laser repetition rate could still be monitored by one of the referenced frequency counters and/or the synthesizer it is locked against could itself be referenced against a 10 MHz Rubidium clock standard available in the laboratory.

5.1.5 Vibration Isolation Through Table-Floating

The present optical table upon which the instrument is built (see Figure 2.4) is not able to pneumatically 'floated'; at least one of the table legs' air bladders is damaged and the models are out of date. Fixing this problem may have some effect upon the ASOPS THz-TDS performance, but a particularly big benefit might be derived for the ASOPS TTR work. Recall that in §4.1.3, it was noted that substantial low-frequency noise (e.g., sub-hertz to few hundred hertz) was observed to interfere with the TTR measurements. The noise may have a time of day dependence (i.e., better in morning) that further suggests an environmental source. Floating the table would help to isolate it from the building and may reduce these sources of noise, allowing for better performance in all experiments done on the table. In this regard, it should be noted that each laser has had a water recirculating chiller underneath the table in order to maintain a constant temperature in the baseplates of the laser heads. These chillers each have a mechanical fan, and this of course produces noise. We have attempted to see if this contribute to the 'baseline' noise (as described in §4.1.3), by turning them on and off while monitoring the output of the balanced detector on a baseband spectrum analyzer. No significant effect has yet to be observed, but this should be re-checked if the arrangement of items around or on the table is changed or if the table is floated.

5.1.6 Measure Pulse Durations at Key Points

Pulse durations can limit instrumental bandwidth in detection of the electro-optic THz waveforms, as noted in §2.1.1. However, long pulses can also limit instrumental bandwidth in terms of the initial generation of THz radiation at the THz emitter. The Coherent Micra laser model, used for both of pump and probe lasers, is capable of producing pulses that can be compressed down to 15fs. The pulses produced presently in the instrument, though, are certainly much longer than that, perhaps approaching 100 fs. Estimates by the author and some testing with an auto-correlator to measure pulse duration, indicate that the pulses may be as much at 150 fs in duration at the detector or emitter. This is a very rough number, though, and it is hard to be quantitative in this regard, as we have require a quality auto-correlator for long term use. It is worth noting that in reference [41], 40 fs duration pulses, in pump and probe beams, were used for a moderate-resolution (i.e., 1 GHz) ASOPS-based THz-TDS spectrometer with more than 6 THz of bandwidth. The THz emitter utilized therein is similar to that which we presently used. The detector, though, was different, the subject of the next section. As for the pulse durations, if they are indeed too long in the present experimental setup, then pulse compression in either or both of the pump and probe beam lines may be necessary to improve bandwidth and noise performance.

5.1.7 Evaluate Different Detection Crystals and Schemes

The bandwidth of the current instrument configuration falls off quickly above 2.5 THz, though this is consistent with what other workers have seen when dealing much wider bandwidth (e.g., plasma) THz sources and detecting with 1 mm ZnTe EO crystals as in the present setup [113]. We should try the different thicknesses of ZnTe that are already in the lab from the amplified THz system. Further, we should try detection in GaP, as evaluated in the moderate-resolution ASOPS system noted above [41].

In general, though, the bandwidth can be limited by one or more of a few factors. The pump and pulse durations may be too long, and require checking as noted above. The detection crystal type and thickness may need to be changed. If both of these corrections fail to improve bandwidth, then system timing jitter may be the limiting factor, and this would only be fixed by improving the PLL circuitry. Problems with the PLL circuitry might be diagnosed by inserting the etalon optics (the ‘Delay Scan Calibration’ subsystem of Figure 2.6) into the system, improving the present PMT amplifier’s 1 MHz bandwidth, and carefully studying the cross-correlation width of the peaks in the ring-down; if they are too wide, as in hundreds of femtoseconds, then this may be a sign of a problem.

Returning to the electro-optic detection, there have been a few papers very recently, suggesting methods to improve the detectivity of the sampling [114] [115] [116]. In particular, Ahmed et al. [114] suggest a scheme to improve detectivity by a factor of $\sim$20 simply by inserting a sequence of Brewster windows into the EO probe beam path so as to increase its ellipticity. This may be a straightforward way in which to significantly improve the performance of the instrument.

5.1.8 Monitoring of Nitrogen-Purging in the THz Spectroscopy Area

We have experimentally observed that the amount water vapor in the THz enclosure can significantly affect the measured THz signal levels. This is of course the reason for the enclosure and the purging with dry nitrogen. However, in order to ensure consistently good system performance in this regard and ensure that the inside of the enclosure is actually as dry as it can be, it may be desirable to get a scientific grade hydrometer. Presently, a consumer-grade device is kept in the enclosure, but it seems quite imprecise and may have a high measurement floor. A USB-enabled device would be desirable, if possible, for easy monitoring by the host/control computer. Once we have better measurements in hand, we could decide, if necessary, upon more comprehensive purge box drying methods (e.g., Drie-rite containers, dehumidifiers).

5.1.9 Improve Sample Cell and Gas Handling Apparatus

The sample cell, and vacuum lines, used for the water vapor scans in chapter 3 were very basic. For example the cell was connected to the rest of the vacuum lines by plastic/tygon tubing held over compression fittings, with clamps. Whether it was the lines or the cells, that arrangement had issues in maintaining the $\sim$2 Torr level to even the $\sim$10% level. That is adequate for what was the then goal of measuring accurate line centers. However, for future gas-phase studies, better pressure is necessary. A new cell, better sealed, and with better pressure control will be necessary. The fit of a cell about the THz beam waist, between the enclosure's two 4f telescopes, is a bit complicated by the mounts that hold the OAPMs on either end and stick out bit; custom OAPM holders could be fabricated to set these edges of their mounts a small distance further back so as to accommodate slightly larger cells. It is planned that early gas-phase spectroscopy efforts would still take place in what is essentially a static gas cell. However, a slight controlled leak (to vacuum) system, with computer controlled sample gas backing pressure, and with feedback from the cell pressure, could be constructed in order to accurately hold sample pressure and purity to a $\sim$milli-torr level. This level of control would be definitely be useful, indeed likely required, for any high-accuracy and precision peak intensity measurements or studies of pressure-broadening coefficients, for example. In regards to the sample cell, it should be noted that its sample cells are presently made of polyethylene; better performance in both absorption and bandwidth would be had with other window materials, particularly a polyethylene cyclic olefin copolymer known as 'Topas' [117].

5.2 Scientific Applications for the Blake Group ASOPS THz-TDS Instrument

While building the present instrumentation, the focus of course was just on getting it to the point of being operational, such that the initial application of higher resolution water vapor spectroscopy could be pursued. Further, the ASOPS TTR work, as discussed in the section (really mini-chapter) of §4.1, was an important secondary priority. Now that the ASOPS THz-TDS instrument has reached a useable state, it is appropriate to look ahead to future scientific use of the spectrometer. Listed and described in this section are examples of potential scientific applications that should be pursued. Some projects would of course require additional improvements to the instrument, or benefit from improvements already suggested above in §5.1; where appropriate, such technical improvements have been discussed herein.

5.2.1 Pseudorotational Modes in THF

An interesting chemical physics project would be the THz spectroscopy of the tetrahydrofuran and a related molecule, 1,3-dioxolane, in the range of 0.3-3 THz. These molecules are of fundamental chemical physics interest due to their pseudorotation vibrational modes [118–120]; and the present spectrometer would offer the opportunity to improve upon decades-old FT-IR and dispersive measurements [121,122] of these systems. Further, we are, as a group looking towards THz-based coherent control experiments on these molecules, so a better understanding of the energy levels and potential energy surfaces of these molecules is an important first step. At sufficiently low pressures, we may be able to observe gas-phase free-induction decays from these vibrational modes instead of the usual rotational transitions of the gas phase.

5.2.2 Laboratory Molecular Astrophysics

One of the key areas of future work will be that of actually getting some laboratory astrophysics done with the instrument, as this is of course a primary motivation for its construction. A good place to start would be in scanning some classic astronomical ’weed’ molecules (as in they have strong transitions and are relatively abundant). Beyond scans on water, sulfur dioxide (SO_2) is another moderate to light asymmetric top with a rich spectrum that is well predicted to ∼MHz precision at high frequencies, so as to provide a good grounds for comparison with our measured line centers. Alcohols such as methanol (CH_3OH) and ethanol (C_2H_5OH) would also be excellent molecules to study with the ASOPS THz-TDS instrument before moving onto structurally related, but less-studied molecules. Such studies would benefit greatly if the bandwidth of the instrument was extended, as discussed above in §5.1.

Eventually, the entire ASOPS setup could be considered to be relocated over to the Blake group's other laboratory location, where microwave spectroscopy is primarily done. There it could more easily be integrated with the kind of equipment typically found on our microwave instruments such as pulsed nozzles and flow cells, so as to enable THz spectroscopy of transient or unstable species.

5.2.3 Additional ASOPS-TTR Measurements

As noted above in §5.1.5, in the collaborative project with the Minnich group, the TTR scans to date have been problematic because of low frequency noise in the instrument. However, there have been times when noise levels are low, perhaps due to environmental effects, and the data obtained with the ASOPS-TTR instrument are very good. Some of the results from our test scans of GaAs and Si match up well with the literature and other results measured on the Minnich lab's traditional TTR instrument. Once the noise-reduction issues are addressed, as described further in §4.1.4, we should be able to proceed quickly to obtaining reliable data on a routine basis. Additionally, there have been preliminary discussions with Prof. Minnich about ways in which we may be able to use pulse-picking schemes so as to achieve exceptionally long duration ASOPS scans for materials with very slow cooling curves (but still too fast for reliable, direct sampling).

Appendix A

MATLAB Scripts and Functions

The following sections contain the code for various MATLAB [79] scripts and functions discussed in the main text. For full details, the interested reader should refer to the sections of the main text as noted below for each function or script. The code is organized into sections, one for each function/script, and includes cursory notes about each block of code. The code itself includes line numbers at left (sometimes referenced in the main text), as well as comments - these are the lines and other snippets of text that are preceded by a '%
' symbol (this is the symbol for marking off comments in the MATLAB computer language). Each function or script, in the electronic copy, is saved as usual as a plain text file having a '.m' extension - this filename, as well as the identification of each block of code as a script or function, is included in the title of each section of this appendix.

It should be noted that many of these scripts and functions have very simple and short code. Indeed, in some case, there are only a few lines of code. These scripts and functions, however, were routinely called in the analysis of many or all THz spectra, so it is very convenient for them to be packaged into a more modular and ready-to-use script or function. In most cases, the code is heavily commented for ease of use and modification by others; in many cases, the amount of comments matches or even exceeds the amount of actual code. Blank lines and other groupings of code are utilized to improve human readability. Further, the code itself is generally *not* written for brevity or cleverness, or to squeeze out some extra measure of efficiency or speed of execution. Rather, the code has been written to be simple, modular, and more readily understood and modified by others, even if they are relatively new to this type of programming.

A.1 Script 'fig_timeWaveform.m', used to make Figure 3.5

This script was used to generate Figure 3.5 in §3.3.1.3. That figure is meant to be an example of a 'raw' time-domain waveform with little processing - it is the starting point for all subsequent processing including Fourier analysis and various spectral analysis techniques (whose scripts are also included herein). The general intent in this script is to load the dataset (in this case, 'cond_04_samp.mat' - a MATLAB file from the digitizer software) and then both of a 'main' plot of the entire waveform and an 'inset' plot showing a much zoomed-in view of the strongest time-domain waveform peak. As noted in the main text, the only processing herein involves setting the time values to start at zero (as the digitizer generally starts at a nonzero timestamp) - this is done in line # 34, and further to convert the timestamp values from units of seconds to milliseconds for convenient presentation, as done in line #36. Much of the rest of the code is for formatting the main and inset plots and saving the result to an EPS-format image for inclusion in this document. There are also many comments throughout the code, offering further explanation.

There are a few key features in this code that are worthy of further explanation here. Each '.mat'

MATLAB-format data file produced by the digitizer acquisition software contains two 1-dimensional matrices, one each for the signal values and the hardware-generated timestamp for each datapoint. The same-numbered elements of each matrix correspond; a typical acquisition produces approximately 1 million samples and thus the same number of elements in each matrix. The '.mat' files each contain both matrices and assign them specific variables names. The timestamp matrix is called 'T1' and the signal matrix is either of 'Y1' if a single-channel was used (i.e. a single balanced detector was employed) or 'M1' if a math-channel was used in conjunction with regular photodetectors on each of channels A and B (i.e. # 1 and 2) to calculated A-B after digitization. This pre-naming of the variables can cause issues if one wishes to eventually import many different files into a common workspace for comparative analysis. As such, in code line #31, the data is loaded into a variable name of the author's choice (e.g. 'samp') which becomes a structure-type of data whose elements are 'T1' and 'Y1' or 'M1' as assigned from the '.mat'-format input file. In this manner one can choose the variable name of the structured datatype as they see fit to avoid the situation of overwriting otherwise similarly named variables if one just tried directly loading many 'T1' and 'Y1' or 'M1' variables at once. More generally, one could create an array of such structured datatypes to easily handle many files and/or both of matched sample and reference scans at once.

Also of note herein are the numerous plotting-related commands. It is indeed true, of course, that one could simply use a bland 'plot' statement in MATLAB to generate a plain-looking figure and then proceed to use the GUI interface therein to add the various formatted axes, texts, etc. and scale and zoom the figure as desired before manually exporting the result to a file for inclusion in the present document. However, by putting in a little effort once to learn these commands and built up a simple 'reference' script as this (or even a custom plotting function), on can easily generate uniformly-formatted figures by the dozens at the touch of a 'run' button, limited only by the computing time required. As an alternative to writing these commands out, it should be noted that one could follow the manual formatting approach once and then use MATLAB's 'generate code' feature so that it creates the code that would've made the plot; that code then could be re-used with minor changes. However one wishes to proceed, it is important to understand that MATLAB uses a hierarchical system of 'handles' to refer to the elements of a figure. In assembling the figure, step-by-step, one generally proceeds in the following order:

1. Create the overall figure (initially a white box) as in code line #40, where the created figure has a handle variable name of 'sampFull_fig'. This is done with the 'figure' command at right, where one can also set basic parameters such as default units of measure and the overall size and position of the figure, important for printing it to a file later. Additional properties can be set, appropriately enough, by the 'set' command - see for example code line #41.

2. Create the main axes (e.g. x and y) upon which data will be plotted. The axes belong to the previously defined figure. This is noted in code line #44 where we create the axes with the 'axes' command, assign them to the handle variable name 'sampFull_axes_main' and supply the figure handle to specify it as the 'parent' figure in which these axes will be placed. As before, 'set' commands, one or many, can be used to further format the axes' properties.

3. Create the main plot - in that we tell MATLAB what to plot on the previously defined axes; this is shown in code line #48. Those axes are again the 'parent' of the plotted data, in this case 'samp.T1' and 'samp.Y1', the two different matrices for time and signal, respectively, from the 'cond_04_samp.mat', now stored as elements of the 'samp' structure datatype.

4. Create any inset plot(s) if desired, as in code lines #60-61. The inset is created in a manner similar to the above, with its own axes and plot handles having the original figure as their 'parent'. The important difference, making it an inset, is that its position and size settings place it in a different area of the parent figure (e.g. to the upper-right and smaller as in the present example).

5. Print the figure. In this case we are 'printing' to a file, specifically an EPS-format file (encapsulated postscript) for easy use in a LaTeXdocument. Using the 'print' command, one can specify the filename, type, and importantly the rendering engine. Be sure to use the 'painters' option to make sure the figure output is a vector graphic and not a raster graphic - the latter will typically not display well in publication quality documents.

Regarding the setting of the x- and y-axis numerical ranges to show, it is generally useful to plot the data with a simple, auto-scaled plot command once, and manually explore (zoom in and out of) the data to get a good guess of the desired numerical ranges, which could then be hard-coded, if desired, in a script. In many cases, for similar data, hard-coded limits can work well (e.g. 8-10 milliseconds of time, as used herein, to show full scans). Otherwise, the x- and y-axis scaling can be left to 'auto'.

The scripts begins:

```
1  % script for demonstrating the time-domain appearance of a THz-TDS waveform
2
3  %% 'HOUSE-KEEPING'
4
5  % Clear out previous data and commands
6  clc % clear commands
7  clear % clear workspace
8
9  %% USER INPUTS
10
11 % INPUT FILENAME
```

```
% Filename and Name for sample scan
filename_samp = ’cond_04_samp.mat’;
name_samp = ’Sample’;
% Also note, original data, assumed to have ’Y1’ signal data (voltage) and
% ’T1’ time axis data from digitizer (in units of seconds).

% ’refFull’ FIGURE SETTINGS
% output filename and figure size
sampFull_filename = ’fig_timeWaveform’;
% Note: size format is [width height] in inches
sampFull_size = [6 3];
% Full ref inset x (in milliseconds) and y limits
sampFull_inset_xLimits = [1.354 1.368368]; % [min max]
sampFull_inset_yLimits = [-.03968253968253968 .11904761904761912]; % [min max]

%% LOAD DATA FILE

% Load scan’s T1,Y1 data into a structure. The use of structures avoids an
% issue with multiple scans’ files having ’M1’ and ’Y1’ workspace variables.
samp = load(filename_samp);

% Set initial digitizer time to zero
samp.T1 = samp.T1-samp.T1(1);
% Convert time values from seconds to milliseconds
samp.T1 = samp.T1.*1000;
%% PLOT OF FULL REF DATA W/ZOOM INSET (AND SAVE PLOT IN EPS FILE)

% Create figure and name the window (separate from figure title)
sampFull_fig = figure;
set(sampFull_fig, ’Name’,’Example of THz TDS Waveform’,’NumberTitle’,’on’);

% Create main axes
sampFull_axes_main = axes(’Parent’,sampFull_fig);
set(sampFull_axes_main, ’box’, ’on’);

% Create main plot
sampFull_plot_main = plot(samp.T1, samp.Y1, ’Parent’, sampFull_axes_main);
set(sampFull_plot_main,’Color’,’k’);

% Format main axes (limits, labels, ticks)
set(get(sampFull_axes_main,’XLabel’),’fontsize’, 12, ’fontname’, ’times’, ’fontweight’, ’bold’); % x-axis label size and font
set(get(sampFull_axes_main,’YLabel’),’fontsize’, 12, ’fontname’, ’times’, ’fontweight’, ’bold’); % y-axis label size and font
set(get(sampFull_axes_main,’XLabel’),’String’,’Time(milliseconds)’); % x-axis label
set(get(sampFull_axes_main,’YLabel’),’String’,’Signal (arb. units)’); % y-axis label
set(sampFull_axes_main,’YTickLabel’,[]) % remove numbers from y-axis, as this plot is for qualitative, explanatory purposes
set(sampFull_axes_main,’XMinorTick’,’on’) % turn on minor ticks along the x-axis

% Create the inset (zoomed-in) plot
sampFull_axes_inset = axes(’Parent’,sampFull_fig,’position’, [0.35 0.6 0.5 0.3]); % fractional [left bottom width height]
sampFull_plot_inset = plot(samp.T1, samp.Y1, ’Parent’, sampFull_axes_inset);
set(sampFull_plot_inset,’Color’,’k’);
set(sampFull_axes_inset,’XLim’,sampFull_inset_xLimits); % for adjustment of x-axis limits
set(sampFull_axes_inset,’YLim’,sampFull_inset_yLimits); % for adjustment of y-axis limits
set(sampFull_axes_inset,’YTickLabel’,[]) % remove numbers from y-axis
```

```

% Trim down the excess space around the plot - whitespace management can be
% left to LaTeX.
set(sampFull_axes_main, 'LooseInset', [0,0,0,0]);

% Adjust the size and position of the overall figure, with regards to the
% printed output.
set(sampFull_fig, 'PaperUnits', 'inches');
set(sampFull_fig, 'PaperSize', sampFull_size); % [width height]
set(sampFull_fig, 'PaperPositionMode', 'manual');
set(sampFull_fig, 'PaperPosition', [0 0 sampFull_size(1) sampFull_size(2)]);
% [left bottom width height]

% 'Print' the figure to an EPS file Note: MathWorks recommends exporting as
% EPS for publication-quality graphics, see their website for more info on
% exporting figures:
% http://www.mathworks.com/help/matlab/creating_plots/
% choosing-a-graphics-format.html#f3-103427
print(sampFull_fig, '-dpdf', '-painters', '-noui', sampFull_filename);
%print(sampFull_fig, '-depsc2', '-painters', '-noui', sampFull_filename);
% -depsc2 for EPS level 2 color and -deps2 for EPS level 2 B&W
% -painters sets to render using vector-based Painter's algorithm
% -noui suppresses any user interface controls that may show up in figure
```

A.2 Function ‘asopsRate.m’

The conversion of the laboratory timeframe sampling rate of the digitizer to an effective delay timeframe ultrafast sampling rate is a simple timing relationship used in all analyses concerning ASOPS THz-TDS waveforms. For convenience, this relationship, expressed in eqs. (3.45) and (3.46), has been implemented in the present MATLAB function, for ease of frequent use.

As noted in the code’s comments, the user must pass the digitizer rate in MHz, pump laser repetition rate, also in MHz, and the repetition rate offset, the latter in Hz, as the usual offset is 100 Hz. The function then returns the delay timeframe sampling rate in terms of TSa/s, or terasamples per second. Overall, a very short, but very useful script. For further information, see the main text, §3.3.2.

```
function rate_asops = asopsRate(rate_adc,rate_pump,rate_offset)
%asopsRate(rate_sample,rate_pump,rate_offset)
%   'asopsRate' function returns the asops sampling rate in delay time,
%   in units of terasamples per second (TS/s)given the following arguments:
%   ---'rate_adc' digitizer (ADC) sampling rate in lab time (in MHz)
%   ---'rate_pump' pump laser repetition rate (in MHz)
%   ---'rate_offset' rep rate difference between pump and probe lasers (Hz)
%   (with probe laser assumed to be at a lower rep rate).

% Adjust arguments for units. 'rate_adc' and 'rate_pump' were specified as
% being in MHz, so need to multiply out now.
rate_adc = rate_adc*(10^6);
rate_pump = rate_pump*(10^6);
```

```

% ASOPS time scaling factor (delay to lab time)
scaleFactor = (rate_pump/rate_offset);

rate_asops = (rate_adc*scaleFactor)/(10^12);
end
```

A.3 Function ‘timebase.m’

Time-domain waveforms typically acquired by the digitizer have timestamps generated by the hardware. Alternatively, knowing the sampling rate, each datapoint is simply one sampling time period after another. The conversion of this time-axis to a delay timeframe is important in the time-domain analysis and presentation of scan data, as in the main text Figure 3.6, for example. The present MATLAB function is very simple and performs this frequent delay time-axis creation task. It accepts as input the delay timeframe sampling rate, as generated by the ‘asopsRate.m’ function described above in §A.2, as well as the number of points in the waveform. Starting at zero, this function simply creates a timebase vector, with subsequent values incremented by the delay timeframe sampling time per data point.

```
function time_delay = timebase(rate_asops,num_points)
% timebase(rate_asops,num_points)
%   'timebase' creates a time data vector for ASOPS scans, in delay time
%   with units of picoseconds (ps), from the following arguments:
%   ---rate_asops = ASOPS sample rate in delay time in units of terasamples
%   per second (TS/s)
%   ---num_points = number of points desired in output time data vector

% find time per sample in (ps), 'rate_asops' is in TS/s so inverse is in
% units of ps as desired
sampleTime = 1/rate_asops;

% create output variable for delay time vector
%time_delay = 0:sampleTime:(sampleTime*(num_points-1));
time_delay = 0:1:(num_points-1);
time_delay = time_delay*sampleTime;

end
```

A.4 Script ‘fig_delayWaterFID.m’, used to make Figure 3.6

A zoomed-in view of both of reference and sample (water vapor) waveforms was presented in Figure 3.6. Notably, this figure’s time axis was corrected to that of the delay timeframe, instead of the laboratory timeframe as previously shown in Figure 3.5. The main portion of the figure was actually a zoomed-in portion of the overall time range available, so as to emphasize the water FID signal relative to the flat reference time-domain waveform. The figure also has an inset portion, further zoomed-in, to clearly show the water FID signal at long delays (hundreds of picoseconds) following the initial THz pulse.

In generating a delay timeframe time axis for the waveform, this script makes use of the ‘asopsRate.m’ and ‘timebase.m’ functions described above in §A.2 and §A.3. The experimental data set employed is similar to that used for Figure 3.5; this dataset was obtained at similar pressure (approximately 2 Torr of water vapor at room temperature), though with a 2-detector arrangement instead of a single, balanced detector.

Looking at the code, we can see that the ‘asopsRate’ function was called in line # 55, and the ‘timebase’ function in line # 62. Of note, the data is processed in lines # 68-71 to remove any linear trend and mean (i.e. DC or 0 Hz) value, as is typically done in advance of FFT processing; this is effectively a simple base-lining step and has generally has no effect upon the THz spectral results.

A large portion of the code, particularly from line # 73 onwards, is simply for figure, plotting, and related formatting commands. In this regard, the present script has much in common with that in §A.1 used for the creation of the time domain waveform with a laboratory timeframe axis; the plots are otherwise quite similar.

```
1   % Script for creating Figure label = 'fig_delayWaterFID', a zoomed in view
2   % of the water FID (main plot) and very close view of FID oscillations
3   % (inset plot).
4
5   %% 'HOUSE-KEEPING'
6
7   % Clear out previous data and commands
8   clc % clear commands
9   clear % clear workspace
10  %close all % close all open figures
11
12  %% USER INPUTS
13
14  % INPUT FILENAMES
15  % Filename and Name for sample scan
16  filename_sample = 'cond_02_samp.mat';
17  name_sample = '2 Torr H2O';
18  % Filename and Name for reference scan
19  filename_ref = 'cond_02_ref.mat';
20  name_ref = 'Reference';
21  % Also note, original data, assumed to have 'M1' signal data (voltage) and
22  % 'T1' time axis data from digitizer (in units of seconds). And assumed
23  % that sample and reference data have same number of data points.
24
25  % DATA ACQUISITION PARAMETERS
26  rate_adc = 125; % digitizer (ADC) sampling rate in lab time (in MHz)
27  rate_pump = 79.9794; % pump laser repetition rate (in MHz)
28  rate_offset = 100; %rep rate difference between pump and probe lasers (Hz)
29
30  % 'fastOscCompare' FIGURE SETTINGS
31  % output filename and figure size
32  fastOscCompare_filename = 'fig_delayWaterFID';
```

```
% Note: size format is [width height] in inches
fastOscCompare_size = [6 4];
% 'fastOscCompare' main plot x (time in ps) and y limits
fastOscCompare_main_xLimits = [1610 3510]; % [min max]
fastOscCompare_main_yLimits = [-.000174 .000301]; % [min max]
% 'fastOscCompare' inset plot x (time in ps) and y limits
fastOscCompare_inset_xLimits = [1894 1906]; % [min max]
fastOscCompare_inset_yLimits = [-.00019 .0002]; % [min max]

%% LOAD DATA FILES

% Load scans' T1,M1 data into structures, one each for sample and ref. The
% use of structures avoids an issue with both scan files having 'M1' and
% 'M1' workspace variables.
sample = load(filename_sample);
ref = load(filename_ref);

%% CREATE DELAY TIME AXIS, DETREND SIGNAL DATA

% CREATE DELAY TIME AXIS
% Calculate sampling rate in TSa/s given 'data acquisition parameters'
% specified above
rate_asops = asopsRate(rate_adc,rate_pump,rate_offset);
% Create timebase for time-domain data in terms of delay time (in ps),
% given sampling rate and length of sample signal (M1) data; note it is up
% to user to make sure sample and reference scans have same number of
% points. Also note that because of this new timebase, the original 'T1'
% time data is not really required; though it can be useful to calculate
% the digitizer sampling rate if this is forgotten.
time_delay = timebase(rate_asops,length(sample.M1));

% DETREND THE DATA Before any FFT processing, it is often recommended to
% remove the mean value or linear trend from the signal data. This also
% helps for display purposes, in centering data (different scans) along y =
% 0 (across multiple scans).
sample.M1 = detrend(sample.M1); % remove any linear trend
sample.M1 = detrend(sample.M1, 'constant'); % remove mean value
ref.M1 = detrend(ref.M1); % remove any linear trend
ref.M1 = detrend(ref.M1, 'constant'); % remove mean value

%% 'fastOscCompare' PLOT OF REF OVER SAMPLE NEAR MAIN PULSE

% Create figure and name the window (separate from figure title)
fastOscCompare_fig = figure;
set(fastOscCompare_fig, 'Name','Plot of Ref over Sample Near Main Pulse - for fast
  osc','NumberTitle','on');

% Create main axes
fastOscCompare_axes_main = axes('Parent',fastOscCompare_fig);
set(fastOscCompare_axes_main, 'box', 'on');

% Plot sample and ref together as plot matrix
fastOscCompare_plot_main = plot(time_delay, [sample.M1; ref.M1], 'Parent',
  fastOscCompare_axes_main);
% Note: first plot (1) is Sample, 2nd (2) is Reference
% Name the plots (for legend)
set(fastOscCompare_plot_main(1),'DisplayName',name_sample);
set(fastOscCompare_plot_main(2),'DisplayName',name_ref);
```

```
% Set Plot Colors (to something better)
set(fastOscCompare_plot_main(1),’Color’,’r’);
set(fastOscCompare_plot_main(2),’Color’,’b’);
% Create Legend
fastOscCompare_legend = legend(fastOscCompare_axes_main,’show’);
% Force legend position, so as to avoid overlap with inset plot.
% Positioning format is [left bottom width height]
set(fastOscCompare_legend,’Position’,[0.710910062300654 0.2 0.108221476510067
  0.0730434782608696]);

% Create main title
%title(’title of plot’);

% Format main axes (limits,labels, ticks)
set(fastOscCompare_axes_main,’XLim’,fastOscCompare_main_xLimits); % for adjustment of
  x-axis limits
set(fastOscCompare_axes_main,’YLim’,fastOscCompare_main_yLimits); % for adjustment of
  y-axis limits
set(get(fastOscCompare_axes_main,’XLabel’),’fontsize’, 12, ’fontname’, ’times’,
  ’fontweight’, ’bold’); % x-axis label size and font
set(get(fastOscCompare_axes_main,’YLabel’),’fontsize’, 12, ’fontname’, ’times’,
  ’fontweight’, ’bold’); % y-axis label size and font
set(get(fastOscCompare_axes_main,’XLabel’),’String’,’Time(ps)’); % x-axis label
set(get(fastOscCompare_axes_main,’YLabel’),’String’,’Signal (arb. units)’); % y-axis
  label
set(fastOscCompare_axes_main,’YTickLabel’,[]) % remove numbers from y-axis, as this plot
  is for qualitative, explanatory purposes
set(fastOscCompare_axes_main,’XMinorTick’,’on’) % turn on minor ticks along the x-axis

% Create the inset (zoomed-in) plot
fastOscCompare_axes_inset = axes(’Parent’,fastOscCompare_fig,’position’, [0.35 0.6 0.6
  0.3]); % fractional [left bottom width height]
fastOscCompare_plot_inset = plot(time_delay, [sample.M1; ref.M1], ’Parent’,
  fastOscCompare_axes_inset);
% Set Plot Colors (to something better) - plot order for inset is same as
% main plot, so do not need to make another legend, just make sure colors
% below matach similar statements for main plot above.
set(fastOscCompare_plot_inset(1),’Color’,’r’);
set(fastOscCompare_plot_inset(2),’Color’,’b’);
% adjust inset x,y limits
set(fastOscCompare_axes_inset,’XLim’,fastOscCompare_inset_xLimits); % for adjustment of
  x-axis limits
set(fastOscCompare_axes_inset,’YLim’,fastOscCompare_inset_yLimits); % for adjustment of
  y-axis limits
set(fastOscCompare_axes_inset,’YTickLabel’,[]) % remove numbers from y-axis
set(fastOscCompare_axes_inset,’XMinorTick’,’on’) % turn on minor ticks along the x-axis

% Trim down the excess space around the plot - whitespace management can be
% left to LaTeX.
set(fastOscCompare_axes_main, ’LooseInset’, [0,0,0,0]);

% Adjust the size and position of the overall figure, with regards to the
% printed output.
set(fastOscCompare_fig, ’PaperUnits’, ’inches’);
set(fastOscCompare_fig, ’PaperSize’, fastOscCompare_size); % [width height]
set(fastOscCompare_fig, ’PaperPositionMode’, ’manual’);
set(fastOscCompare_fig, ’PaperPosition’, [0 0 fastOscCompare_size(1)
  fastOscCompare_size(2)]);
```

```
% [left bottom width height]

% 'Print' the figure to an EPS file Note: MathWorks recommends exporting as
% EPS for publication-quality graphics, see their website for more info on
% exporting figures:
% http://www.mathworks.com/help/matlab/creating_plots/
% choosing-a-graphics-format.html#f3-103427
print(fastOscCompare_fig, '-dpdf', '-painters', '-noui', fastOscCompare_filename);
%print(fastOscCompare_fig, '-djpeg100','myfile.jpg')
% -dpdf for PDF, -depsc2 for EPS level 2 color and -deps2 for EPS level 2 B&W
% -painters sets to render using vector-based Painter's algorithm
% -noui suppresses any user interface controls that may show up in figure
```

A.5 Script ‘test_timecut.m’ for Evaluating the FFT of Different Scan Durations

This script, ‘test_timecut.m’, was used to create Figures 3.8 and 3.9 in §3.4.4. It is designed to allow the user to easily check the effect upon a spectrum of changing the extent of the scan duration that is supplied for the Fourier transform. It automatically produces the two figures, one showing via color-coding the different extents of the scan duration selected, as in Figure 3.8, the other showing the resulting spectra as in 3.9. Note that the spectra are plotted as a base-10 log of the ratio of the squares of the FFT amplitudes. Further note that the spectra are intentionally offset or staggered in the vertical direction for clarity. The source data and level of zero-padding can be easily changed; the latter being of use to investigating the effect of the different scan durations upon the search for peak frequencies.

```
% script for testing the effect of changing the time range to FFT (and
% generate figures)

%% 'HOUSE-KEEPING'

% Clear out previous data and commands
clc % clear commands
clear % clear workspace
%close all % close all open figures

%% USER INPUTS

% INPUT FILENAMES
% Filename and Name for sample scan
filename_sample = 'cond_02_samp.mat';
name_sample = '~2 Torr H2O';
% Filename and Name for reference scan
filename_ref = 'cond_02_ref.mat';
name_ref = 'Reference';
% Also note, original data, assumed to have 'M1' signal data (voltage) and
% 'T1' time axis data from digitizer (in units of seconds). And assumed
```

```
% that sample and reference data have same number of data points.

% DATA ACQUISITION PARAMETERS
rate_adc = 125; % digitizer (ADC) sampling rate in lab time (in MHz)
rate_pump = 79.9794; % pump laser repetition rate (in MHz)
rate_offset = 100; %rep rate difference between pump and probe lasers (Hz)

% TIME CUTTING OF SCANS
% in units of ps
% Note that cells are used here to enable easy evaluation of 'n' different
% conditions in terms of start and stop times for FFT analysis.
% NOTE - by convention here, list longest spans of time first.
time_delay_start = {0 0 0 0};
time_delay_stop = {10000 6560 6440 4000};
%time_delay_name = cell(1,length(time_delay_stop));
time_delay_name = {'Full Scan' 'After Reflection' 'Before Reflection' 'End of H2O FID'};
% Plot colors for the scans, in order. [r g b] 0 to 1
time_delay_color = {[0 0 1] [1 0 0] [0 1 0] [1 0 1]};
% Color for ref scan
refColor = [0.5 0.5 0.5];
% Name for ref scan
refName = 'Reference';

% Have user enter # of conditions above, good self check, as opposed to
% using length(time_delay_stop), etc.
numTimecuts = 4;

% FFT PARAMETERS
num_zeroPad = 1; % argument for 'fft_plus' function, uses next power of 2 on pad
case_output = 3; % arg for 'fft_plus', sets output type, type 3 = power

% 'timecutsCompare' FIGURE SETTINGS
% output filename and figure size
timecuts_filename = 'fig_timecutsCompare';
% Note: size format is [width height] in inches
timecuts_size = [6 3];
% 'timecutsCompare' plot x (time in ps) and y limits
timecuts_axes_xLimits = [0 10000]; % [min max]
timecuts_axes_yLimits = [-0.001 0.001];
% Legend size and position.
% Positioning format is [left bottom width height]
timecuts_legendSize = [0.28 0.2 0.3155 0.1];
% Legend fontsize
timecuts_legendFontSize = 5;

% 'timecutsFFTcompare' FIGURE SETTINGS
% output filename and figure size
timecutsFFT_filename = 'fig_timecutsFFTcompare';
% Note: size format is [width height] in inches
timecutsFFT_size = [6 3];
% 'timecutsCompare' plot x (freq in THz) and y limits
timecutsFFT_axes_xLimits = [0.745 .760]; % [min max]
timecutsFFT_axes_yLimits = [-0.25 2.5];
% Legend size and position.
% Positioning format is [left bottom width height]
timecutsFFT_legendSize = [0.6 0.6 0.3155 0.1];
% Legend fontsize
timecutsFFT_legendFontSize = 5;
```

```
%% LOAD DATA FILES, PROCESS CONDITION NAMES

% Load scans’ T1,M1 data into structures, one each for sample and ref. The
% use of structures avoids an issue with both scan files having ’M1’ and
% ’Y1’ workspace variables.
sample = load(filename_sample);
ref = load(filename_ref);

% Modify condition labels for legend, etc. by appending time values
for j = 1:numTimecuts
time_delay_name{j} = [time_delay_name{j} ’, ’ num2str(time_delay_start{j}) ’ to ’ num2str(time_delay_stop{j}) ’ ps’];
end

%% CREATE DELAY TIME AXIS, DETREND SIGNAL DATA

% CREATE DELAY TIME AXIS
% Calculate sampling rate in TSa/s given ’data acquisition parameters’
% specified above
rate_asops = asopsRate(rate_adc,rate_pump,rate_offset);
% Create timebase for time-domain data in terms of delay time (in ps),
% given sampling rate and length of sample signal (Y1) data; note it is up
% to user to make sure sample and reference scans have same number of
% points. Also note that because of this new timebase, the original ’T1’
% time data is not really required; though it can be useful to calculate
% the digitizer sampling rate if this is forgotten.
time_delay = timebase(rate_asops,length(sample.M1));

% DETREND THE DATA Before any FFT processing, it is often recommended to
% remove the mean value or linear trend from the signal data. This also
% helps for display purposes, in centering data (different scans) along y =
% 0 (across multiple scans).
samp_signal = detrend(sample.M1); % remove any linear trend
samp_signal = detrend(samp_signal, ’constant’); % remove mean value
ref_signal = detrend(ref.M1); % remove any linear trend
ref_signal = detrend(ref_signal, ’constant’); % remove mean value

%% PERFORM TIME CUTS

% CUT OUT DESIRED TIME PORTIONS Using cells to store cut poritions as cut
% out portions will all be of different lengths, hard to scale/handle
% arrays for that situation.
time_delay_part = cell(1,numTimecuts);
samp_signal_part = cell(1,numTimecuts);
ref_signal_part = cell(1,numTimecuts);
% Loop through all conditions and store cut-out portions.
% Note that there are ways to do this without such redundant usage of
% memory, but this nonetheless works fine.
for j = 1:numTimecuts
[ time_delay_part{j}, samp_signal_part{j} ] = timecut(time_delay,samp_signal,time_delay_start{j},time_delay_stop{j});
[ time_delay_part{j}, ref_signal_part{j} ] = timecut(time_delay,ref_signal,time_delay_start{j},time_delay_stop{j});
end
% Note that it is OK to re-use time_delay_part between sample and ref
% cut-outs, as corresponding pairs of sample and ref will be the same.
```

```
%% ’timecutsCompare’-INITIAL PLOTTING OF SELECTED TIME PORTIONS FOR COMPARISON
% Plot the time-domain data, with color codes, so user can see extent of
% different time portions. Only sample (not ref) for each timecut will be
% presented. A full-delay ref scan will be plotted last in its user-spec’d
% ’refColor’.

% Create figure and name the window (separate from figure title)
timecuts_fig = figure;
set(timecuts_fig, ’Name’,’Plot of Different Waveform Portions’,’NumberTitle’,’on’);
%plot(time_delay,samp_signal,’r’,time_delay_part,samp_signal_part,...
%’g’,time_delay,ref_signal,’b’)

% Create main axes
timecuts_axes = axes(’Parent’,timecuts_fig);
set(timecuts_axes, ’box’, ’on’);

% Format main axes (limits,labels, ticks)
set(timecuts_axes,’XLim’,timecuts_axes_xLimits); % for adjustment of x-axis limits
set(timecuts_axes,’YLim’,timecuts_axes_yLimits); % for adjustment of y-axis limits
set(get(timecuts_axes,’XLabel’),’fontsize’, 12, ’fontname’, ’times’, ’fontweight’, ’bold’); % x-axis label size and font
set(get(timecuts_axes,’YLabel’),’fontsize’, 12, ’fontname’, ’times’, ’fontweight’, ’bold’); % y-axis label size and font
set(get(timecuts_axes,’XLabel’),’String’,’Time(ps)’); % x-axis label
set(get(timecuts_axes,’YLabel’),’String’,’Signal (arb. units)’); % y-axis label
set(timecuts_axes,’YTickLabel’,[]) % remove numbers from y-axis, as this plot is for qualitative, explanatory purposes
set(timecuts_axes,’XMinorTick’,’on’) % turn on minor ticks along the x-axis

% Plot all of the timecut portions (sample scans, not refs)
timecuts_plot = zeros(1,numTimecuts);
hold(timecuts_axes,’all’); % this has to go here and can’t go much up above or somehow gets reset
for j = 1:numTimecuts
   timecuts_plot(j) = plot(time_delay_part{j},samp_signal_part{j},’Parent’,timecuts_axes);
   % Name the plots for Legend
   set(timecuts_plot(j),’DisplayName’,time_delay_name{j});
   % Set plot colors (so they’re different!)
   set(timecuts_plot(j),’Color’,time_delay_color{j});
end

% Add a full time record ref plot to the sample scans
%timecuts_refplot = plot(time_delay,ref_signal,’Parent’,timecuts_axes);
%set(timecuts_refplot,’DisplayName’,refName);
%set(timecuts_refplot,’Color’,refColor);

% Create Legend
timecuts_legend = legend(timecuts_axes,’show’);
% Force legend position, so as to avoid overlap with inset plot.
% Be careful to specify ’Fontsize’ before ’Position’ (which is also size) or
% Matlab may ignore the desired size if it is too small for the default
% font size that hasn’t been changed yet.
set(timecuts_legend,’FontSize’,timecuts_legendFontSize,’Position’,timecuts_legendSize);

% Create main title
%title(’title of plot’);

% Trim down the excess space around the plot - whitespace management can be
```

```
% left to LaTeX.
set(timecuts_axes, ’LooseInset’, [0,0,0,0]);

% Adjust the size and position of the overall figure, with regards to the
% printed output.
set(timecuts_fig, ’PaperUnits’, ’inches’);
set(timecuts_fig, ’PaperSize’, timecuts_size); % [width height]
set(timecuts_fig, ’PaperPositionMode’, ’manual’);
set(timecuts_fig, ’PaperPosition’, [0 0 timecuts_size(1) timecuts_size(2)]);
% [left bottom width height]

% ’Print’ the figure to a PDF file
% See MathWorks website for more info on exporting figures:
% http://www.mathworks.com/help/matlab/creating_plots/...
%choosing-a-graphics-format.html#f3-103427
print(timecuts_fig, ’-dpdf’, ’-painters’, ’-noui’, timecuts_filename);
%print(fastOscCompare_fig, ’-djpeg100’,’myfile.jpg’)
% -dpdf for PDF, -depsc2 for EPS level 2 color and -deps2 for EPS level 2 B&W
% -painters sets to render using vector-based Painter’s algorithm
% -noui suppresses any user interface controls that may show up in figure

%% FOURIER ANALYSIS

% Calculate the FFTs for all timecut waveforms.
% Note that the ’freqaxis’ for both of ref and sample
% will be the same so it is OK to re-use. It is assumed herein, and coded
% as such, that ref and samp will be taken under exact same acquisition and
% rep rate parameters.
freqaxis_part = cell(1,numTimecuts);
samp_fft_part = cell(1,numTimecuts);
ref_fft_part = cell(1,numTimecuts);
sratio_part = cell(1,numTimecuts);
for j = 1:numTimecuts
[ref_fft_part{j} freqaxis_part{j}] = fft_plus(ref_signal_part{j}, rate_asops, num_zeroPad, case_output);
[samp_fft_part{j} freqaxis_part{j}] = fft_plus(samp_signal_part{j}, rate_asops, num_zeroPad, case_output);

% Calculate the referenced data (reverse log)
% Also add stepped offset for display purposes
sratio_part{j} = (-log10(samp_fft_part{j}./ref_fft_part{j}))+0.1*(j-1);
end

%% ’timecutsFFTcompare’- COMPARISON OF FFT RESULTS FOR DIFFERENT TIMECUTS

% Create figure and name the window (separate from figure title)
timecutsFFT_fig = figure;
set(timecutsFFT_fig, ’Name’,’Plot of Different Waveform Portions’,’NumberTitle’,’on’);

% Create main axes
timecutsFFT_axes = axes(’Parent’,timecutsFFT_fig);
set(timecutsFFT_axes, ’box’, ’on’);

% Format main axes (limits,labels, ticks)
set(timecutsFFT_axes,’XLim’,timecutsFFT_axes_xLimits); % for adjustment of x-axis limits
set(timecutsFFT_axes,’YLim’,timecutsFFT_axes_yLimits); % for adjustment of y-axis limits
set(get(timecutsFFT_axes,’XLabel’),’fontsize’, 12, ’fontname’, ’times’, ’fontweight’, ’bold’); % x-axis label size and font
```

```
set(get(timecutsFFT_axes,'YLabel'),'fontsize', 12, 'fontname', 'times', 'fontweight',
  'bold'); % y-axis label size and font
set(get(timecutsFFT_axes,'XLabel'),'String','Time(ps)'); % x-axis label
set(get(timecutsFFT_axes,'YLabel'),'String','Signal (arb. units)'); % y-axis label
set(timecutsFFT_axes,'YTickLabel',[]) % remove numbers from y-axis, as this plot is for
  qualitative, explanatory purposes
set(timecutsFFT_axes,'XMinorTick','on') % turn on minor ticks along the x-axis

% Plot all of the timecut portions (sample scans, not refs)
timecutsFFT_plot = zeros(1,numTimecuts);
hold(timecutsFFT_axes,'all'); % this has to go here and can't go much up above or
  somehow gets reset
for j = 1:numTimecuts
   timecutsFFT_plot(j) =
     plot(freqaxis_part{j},sratio_part{j},'Parent',timecutsFFT_axes,...
        'MarkerSize',5,'Marker','.');
   % Name the plots for Legend
   set(timecutsFFT_plot(j),'DisplayName',time_delay_name{j});
   % Set plot colors (so they're different!)
   set(timecutsFFT_plot(j),'Color',time_delay_color{j});
end

% Create Legend
timecutsFFT_legend = legend(timecutsFFT_axes,'show');
% Force legend position, so as to avoid overlap with inset plot.
% Be careful to specify 'Fontsize' before 'Position' (which is also size) or
% Matlab may ignore the desired size if it is too small for the default
% font size that hasn't been changed yet.
set(timecutsFFT_legend,'FontSize',timecutsFFT_legendFontSize,...
'Position',timecutsFFT_legendSize);

% Create main title
%title('title of plot');

% Trim down the excess space around the plot - whitespace management can be
% left to LaTeX.
set(timecutsFFT_axes, 'LooseInset', [0,0,0,0]);

% Adjust the size and position of the overall figure, with regards to the
% printed output.
set(timecutsFFT_fig, 'PaperUnits', 'inches');
set(timecutsFFT_fig, 'PaperSize', timecutsFFT_size); % [width height]
set(timecutsFFT_fig, 'PaperPositionMode', 'manual');
set(timecutsFFT_fig, 'PaperPosition', [0 0 timecutsFFT_size(1) timecutsFFT_size(2)]);
% [left bottom width height]

% 'Print' the figure to a PDF file
% See MathWorks website for more info on exporting figures:
% http://www.mathworks.com/help/matlab/creating_plots/...
%choosing-a-graphics-format.html#f3-103427
print(timecutsFFT_fig, '-dpdf', '-painters', '-noui', timecutsFFT_filename);
%print(fastOscCompare_fig, '-djpeg100','myfile.jpg')
% -dpdf for PDF, -depsc2 for EPS level 2 color and -deps2 for EPS level 2 B&W
% -painters sets to render using vector-based Painter's algorithm
% -noui suppresses any user interface controls that may show up in figure
```

A.6 Function ‘fft_plus.m’ for Discrete Fourier Transforms

This is the primary function, wrapped around MATLAB’s built-in ’fft’ function, used to perform the discrete Fourier transform upon all experimental data.

```matlab
function [ output_fft output_freqaxis ] = fft_plus(data_signal, rate_sample, num_zeroPad, case_output)
%FFT_PLUS Provides additional features around Matlab’s ’fft’ command.
%   FFT_PLUS - v2.0 by Daniel Holland. (Previous version called ’fft_ssb’).
%   Calculates the discrete Fourier transform of a signal using Matlab’s
%   built-in ’fft’ function. Provides options for proper handling of sample
%   rate, output frequency axis, zero-padding, and output type - e.g.
%   complex, amplitude, power, etc.

% FUNCTION ARGUMENTS
%--- ’data_signal’ = signal vector
%--- ’rate_sample’ = sample rate (determines frequency axis)
%--- ’num_zeroPad’ = Specifies extent, if any, of zero-padding. Zero = no
%zero padding, 1 = pad to first power of 2, 2 = to second, etc.
%--- ’case_output’ = Integer to specify output type as follows:
% 0 = Complex FFT results - ALL FREQUENCIES (INCLUDING NEGATIVE)
% 1 = Complex FFT results - DC TO POSITIVE FREQUENCIES
% 2 = Amplitude (real value, ’abs()’ value of FFT complex value)
% 3 = power (simple square of amplitude)
% 4 = Power (sum squared amplitude definition of total power in wave)
% 5 = Power Spectral Density (linear power per Hz, based on time-integral
% squared amplitude)
% Note: all outputs, except 0 = complex FFT, are single-sided.

%% NOTES AND REFERENCES

% GENERAL NOTE REGARDING CODING STYLE Please note that this code was not
% written with brevity as a goal. Rather it was written for readability and
% modularity. The ’case_output’ argument of this function specifies the
% output type - this function is written around a large case structure
% based on this selection. There is much repetition of code between case
% options in this function. This is done intentionally so users can easily
% understand, modify, or re-use the code.

% HANDLING OF OUTPUT VALUES AND FREQUENCY AXIS All output, with the
% exception of case 0, is single-sided data - appropriately scaled by a
% factor of 2. Frequency axes are rearranged to run from DC to Nyquist
% (even # FFT points) or to a half step below Nyquist (odd # of FFT
% points). The frequency axis of case 0 includes both of positive and
% negative frequencies and is shifted so as to place zero frequency in the
% middle.

% REFERENCES

% (1) A webpage/wiki "Unpacking the MATLAB fft" by the Seismology Group at
% UOregon was very helpful in explaining the proper scaling of the output
% data and setting of the frequency axis. The function is largely based on
% this reference. Link:
% http://blogs.uoregon.edu/seis/wiki/unpacking-the-matlab-fft/

```

```
% (2) The MathWorks (MATLAB company) Documentation Center page, "Fast
% Fourier Transform" explains the practical basics, as well as some of the
% theory of FFTs, link:
% http://www.mathworks.com/help/matlab/math/fast-fourier-transform-fft.html

% (3) The MathWorks Documentation Center page on the 'fft' function
% supplements the above, link:
% http://www.mathworks.com/help/matlab/ref/fft.html

% (4) The MathWorks Documentation Center page on "Power Spectral Density
% Estimates Using FFT" informed this function's power output option. Link:
% http://www.mathworks.com/help/signal/ug/psd-estimate-using-fft.html

% (5) The MathWorks Documentation Center page on "Amplitude Estimation and
% Zero Padding" informs this function's option of using zero-padding and is
% important to spectroscopy, link:
% http://www.mathworks.com/help/signal/ug/amplitude-estimation-and-zero-padding.html

% (6) Short presentation online, "FFT Normalisation for Beginners",
% concering total power in wave, link:
% http://www.hep.ucl.ac.uk/~rjn/saltStuff/fftNormalisation.pdf

%% PERFORM THE FFT, INITIAL PROCESSING OF RESULTS

% The size of the orignal time-series data is the window length; this can
% be extended with zero padding.

length_signal = length(data_signal);
if (num_zeroPad > 0) % user wants zero-padding
    num_fftPts = 2^(nextpow2(length_signal)+(num_zeroPad-1));
else % user does not want zero-padding
    num_fftPts = length_signal;
end

% Perform the fft, with number of points as calculated above.
F = fft(data_signal,num_fftPts);

% Calculate frequency step size
deltaFreq = rate_sample/num_fftPts;

% Calculate the Nyquist frequency
Nyq = rate_sample/2;

% Create the (inital) frequency axis (correct spacing, but runs to sample
% frequency)
f = (0:(num_fftPts-1))*deltaFreq;
% Adjust frequency axis to have negative frequencies (i.e. only <= Nyquist
% frequency content).
f(f>Nyq) = f(f>Nyq)-(Nyq*2);
% Alternatively (to above), could have done below, as the vector elements
% in the range of (floor(end/2)+2:end) are/correspond to negative
% frequencies (for both even/odd # of fft points)(and mirror the positive
% frequency terms).
%f(floor(end/2)+2:end) = f(floor(end/2)+2:end) - (Nyq*2);

%% CONVERT FFT RESULTS TO SELECTED OUTPUT TYPE

switch case_output
```

```

    case 0 % COMPLEX FFT RESULTS - ALL FREQUENCIES (INCLUDING NEGATIVE)
        % Values for this case already calculated above, just pass along.

        output_fft = F;
        output_freqaxis = f;

    case 1 % COMPLEX FFT RESULTS - DC TO POSITIVE FREQUENCIES
        % Similar to case 0 above, but only pass DC and positive
        % frequencies. Useful for real signals, which is the usual
        % application.

        % note to self, set up like case 0 but also mult DC and Nyquist (if
        % present by 2)
         % Set output frequency axis as positive frequencies.
        output_freqaxis = f(f>=0);
        % Alternatively (to above), could have used fact that vector
        % elements in range of (1:ceil(end/2)) are the DC and positive
        % frequencies (for both even/odd # of fft points). Would also need
        % to account for Nyquist component in case of even # fft points.
        %output_freqaxis = f(1:(ceil(end/2)+(1-mod(num_fftPts,2))))

        % Pass along complex Fourier terms as they are (no amp(), etc.)
        output_fft = F(f>=0);
        % Normalize to window length
        output_fft = output_fft/length_signal;

        % Double non-unique frequency components (i.e. those other than
        % DC and, if present, Nyquist) as taking single sideband spectrum
        % of a real signal.
        output_fft(2:ceil(num_fftPts/2)) = output_fft(2:ceil(num_fftPts/2))*2;

    case 2 % AMPLITUDE
        % Need to select only DC and positive frequencies for axis. And to
        % take real amplitude of complex Fourier coefficients.

        % Set output frequency axis as positive frequencies - same as in
        % complex case (#1) above.
        output_freqaxis = f(f>=0);

        % Take real amplitude of complex Fourier terms (in elements
        % corresponding to positive frequencies as above for frequency
        % axis)(and could instead select such elements with 'ceil', 'mod',
        % etc. as alternatively suggested above).
        output_fft = abs(F(f>=0));
        % Normalize to window length
        output_fft = output_fft/length_signal;
        % Multiply non-unique components by 2 as in above case.
        output_fft(2:ceil(num_fftPts/2)) = output_fft(2:ceil(num_fftPts/2))*2;

    case 3 % POWER (simple square of amplitude)
        % Square the amplitude values and divide by the number of FFT points.

        % Set output frequency axis as positive frequencies - same as in
        % complex case (#1) above.
        output_freqaxis = f(f>=0);

        % Take the amplitudes as in amplitude case above, square, divide by
```

```
        % number of FFT points.
        output_fft = abs(F(f>=0)).^2;

        % Multiply non-unique components by 2 as in above case.
        output_fft(2:ceil(num_fftPts/2)) = output_fft(2:ceil(num_fftPts/2))*2;

    case 4 % POWER (sum squared amplitude)
        % Square the amplitude values and divide by the number of FFT points.

        % Set output frequency axis as positive frequencies - same as in
        % complex case (#1) above.
        output_freqaxis = f(f>=0);

        % Take the amplitudes as in amplitude case above, square, divide by
        % number of FFT points.
        output_fft = (1/num_fftPts).*abs(F(f>=0)).^2;

        % Multiply non-unique components by 2 as in above case.
        output_fft(2:ceil(num_fftPts/2)) = output_fft(2:ceil(num_fftPts/2))*2;

    case 5 % POWER SPECTRAL DENSITY (linear power per Hz)
        % Very similar to power case above, but scale differently for 'per
        % Hz' spectral density.

        % Set output frequency axis as above.
        output_freqaxis = f(f>=0);

        % Take the amplitudes as in power case above, but change
        % pre-factor.
        output_fft = (1/(rate_sample*num_fftPts)).*abs(F(f>=0)).^2;

        % Multiply non-unique components by 2 as in above case.
        output_fft(2:ceil(num_fftPts/2)) = output_fft(2:ceil(num_fftPts/2))*2;

    otherwise % user selected undefined value for 'case_output'
        % Let use know of the problem and pass along zeros.

        disp('Error in fft_plus function: improper case_output value')
        output_freqaxis = 0;
        output_fft = 0;

end

end
```

A.7 Script ‘test_zeroPad.m’

This script was used to make Figure 3.7, comparing the effect upon the spectrum of different levels of zero padding. Further, it was used to create the spectra upon which the peak finding analysis was performed, as described in sections 3.5.2 and 3.5.3. This script can be easily modified to select other datasets, select different levels of zero-padding, and generate additional figures for such comparisons and optimization.

```
% script for testing the effect of changing the amount of zeropadding prior
% to FFT (and generate figures)

%% 'HOUSE-KEEPING'

% Clear out previous data and commands
clc % clear commands
clear % clear workspace
%close all % close all open figures

%% USER INPUTS

% INPUT FILENAMES
% Filename and Name for sample scan
filename_sample = 'cond_02_samp.mat';
name_sample = '~2 Torr H2O';
% Filename and Name for reference scan
filename_ref = 'cond_02_ref.mat';
name_ref = 'Reference';
% Also note, original data, assumed to have 'M1' signal data (voltage) and
% 'T1' time axis data from digitizer (in units of seconds). And assumed
% that sample and reference data have same number of data points.

% DATA ACQUISITION PARAMETERS
rate_adc = 125; % digitizer (ADC) sampling rate in lab time (in MHz)
rate_pump = 79.9794; % pump laser repetition rate (in MHz)
rate_offset = 100; %rep rate difference between pump and probe lasers (Hz)

% TIME CUTTING OF SCANS
% in units of ps
time_delay_start = 0;
time_delay_stop = 5000;

% FFT PARAMETERS AND LEVELS OF ZERO-PADDING
% arg for 'fft_plus', sets output type, type 3 = power
case_output = 3;
% argument for 'fft_plus' function, uses next power of 2 on pad
num_zeroPad = [1 2 3 4];
% Have user enter # of conditions below, good self check, as opposed to
% using length(num_zeroPad), etc.
num_zeroPad_Levels = 4;
% Names for the different zero padding levels
zeroPad_name = {'Next Power of 2' '+1 power' '+2 powers' '+3 powers'};
% Plots colors for the scans, in order. [r g b] 0 to 1
zeroPad_color = {[0 0 1] [1 0 0] [0 1 0] [1 0 1]};

% 'zeroPadsCompare' FIGURE SETTINGS
% output filename and figure size
zeroPad_filename = 'fig_zeroPadsCompare';
% Note: size format is [width height] in inches
zeroPad_figSize = [6 3];
% 'timecutsCompare' plot x (freq in THz) and y limits
zeroPad_axes_xLimits = [0.751 .753]; % [min max] for both figure and ticks
zeroPad_axes_xStep = 0.0002; % major tick mark step size
zeroPad_axes_yLimits = [-0.25 2.5];
% Legend size and position.
% Positioning format is [left bottom width height]
zeroPad_legendSize = [0.6 0.6 0.3155 0.1];
```

```
% Legend fontsize
zeroPad_legendFontSize = 5;

%% LOAD DATA FILES

% Load scans' T1,M1 data into structures, one each for sample and ref. The
% use of structures avoids an issue with both scan files having 'M1' and
% 'Y1' workspace variables.
sample = load(filename_sample);
ref = load(filename_ref);

%% CREATE DELAY TIME AXIS, DETREND SIGNAL DATA

% CREATE DELAY TIME AXIS
% Calculate sampling rate in TSa/s given 'data acquisition parameters'
% specified above
rate_asops = asopsRate(rate_adc,rate_pump,rate_offset);
% Create timebase for time-domain data in terms of delay time (in ps),
% given sampling rate and length of sample signal (Y1) data; note it is up
% to user to make sure sample and reference scans have same number of
% points. Also note that because of this new timebase, the original 'T1'
% time data is not really required; though it can be useful to calculate
% the digitizer sampling rate if this is forgotten.
time_delay = timebase(rate_asops,length(sample.M1));

% DETREND THE DATA Before any FFT processing, it is often recommended to
% remove the mean value or linear trend from the signal data. This also
% helps for display purposes, in centering data (different scans) along y =
% 0 (across multiple scans).
samp_signal = detrend(sample.M1); % remove any linear trend
samp_signal = detrend(samp_signal, 'constant'); % remove mean value
ref_signal = detrend(ref.M1); % remove any linear trend
ref_signal = detrend(ref_signal, 'constant'); % remove mean value

%% PERFORM TIME CUTS, SHOW SIMPLE FIGURE FOR CHECKING

% PERFORM THE TIMECUT
[time_delay_part, samp_signal_part] = ...
timecut(time_delay,samp_signal,time_delay_start,time_delay_stop);
[time_delay_part, ref_signal_part] = ...
timecut(time_delay,ref_signal,time_delay_start,time_delay_stop);
% Note that it is OK to re-use time_delay_part between sample and ref
% cut-outs, as corresponding pairs of sample and ref will be the same.

% CREATE SIMPLE FIGURE FOR QUICK CHECKING OF TIMECUT

% Create figure and name the window (separate from figure title)
timecuts_fig = figure;
set(timecuts_fig, 'Name','Plot of time-cut for zero-pad test','NumberTitle','on');

% Create the plot - full sample in red/back, full ref in blue/front and
% timecut portion in green/middle
timecuts_plot = plot(time_delay,samp_signal,'r',time_delay_part,samp_signal_part,...
'g',time_delay,ref_signal,'b');

%% FOURIER ANALYSIS
% Calculate the FFTs for all levels of zero-padding.

```

```
% Note that the ’freqaxis’ for both of ref and sample will be the same so
% it is OK to re-use. It is assumed herein, and coded as such, that ref and
% samp will be taken under exact same acquisition and rep rate parameters.
freqaxis_part = cell(1,num_zeroPad_Levels);
samp_fft_part = cell(1,num_zeroPad_Levels);
ref_fft_part = cell(1,num_zeroPad_Levels);
sratio_part = cell(1,num_zeroPad_Levels);
for j = 1:num_zeroPad_Levels
[ref_fft_part{j} freqaxis_part{j}] = ...
fft_plus(ref_signal_part, rate_asops, num_zeroPad(j), case_output);
[samp_fft_part{j} freqaxis_part{j}] = ...
fft_plus(samp_signal_part, rate_asops, num_zeroPad(j), case_output);

% Calculate the referenced data (reverse log)
% Also add stepped offset for display purposes
sratio_part{j} = (-log10(samp_fft_part{j}./ref_fft_part{j}))+0.1*(j-1);
%sratio_part{j} = (-log10(samp_fft_part{j}./ref_fft_part{j}));
end

%% ’zeroPadsCompare’- COMPARISON OF FFT RESULTS FOR DIFFERENT TIMECUTS

% Create figure and name the window (separate from figure title)
zeroPad_fig = figure;
set(zeroPad_fig, ’Name’,’Plot of Differently Zero-Padded FFTs’,’NumberTitle’,’on’);

% Create main axes
zeroPad_axes = axes(’Parent’,zeroPad_fig);
set(zeroPad_axes, ’box’, ’on’);

% Format main axes (limits,labels, ticks)
set(zeroPad_axes,’XLim’,zeroPad_axes_xLimits); % for adjustment of x-axis limits
set(zeroPad_axes,’YLim’,zeroPad_axes_yLimits); % for adjustment of y-axis limits
set(zeroPad_axes,’XTick’,zeroPad_axes_xLimits(1):zeroPad_axes_xStep:...
zeroPad_axes_xLimits(2)) % set major ticks
set(get(zeroPad_axes,’XLabel’),’fontsize’, 12, ’fontname’, ’times’, ...
’fontweight’, ’bold’); % x-axis label size and font
set(get(zeroPad_axes,’YLabel’),’fontsize’, 12, ’fontname’, ’times’, ...
’fontweight’, ’bold’); % y-axis label size and font
set(get(zeroPad_axes,’XLabel’),’String’,’Frequency (THz)’); % x-axis label
set(get(zeroPad_axes,’YLabel’),’String’,’Relative Absorbance’); % y-axis label
set(zeroPad_axes,’YTickLabel’,[])
% remove numbers from y-axis, as this plot is for qualitative, explanatory purposes
set(zeroPad_axes,’XMinorTick’,’on’) % turn on minor ticks along the x-axis

% Plot all of the timecut portions (sample scans, not refs)
zeroPad_plot = zeros(1,num_zeroPad_Levels);
% this has to go here and can’t go much up above or somehow gets reset
hold(zeroPad_axes,’all’);
for j = num_zeroPad_Levels:-1:1 % countdown so densest points in back
   zeroPad_plot(j) = plot(freqaxis_part{j},sratio_part{j},’Parent’,zeroPad_axes,...
        ’MarkerSize’,5,’Marker’,’.’);
   % Name the plots for Legend
   set(zeroPad_plot(j),’DisplayName’,zeroPad_name{j});
   % Set plot colors (so they’re different!)
   set(zeroPad_plot(j),’Color’,zeroPad_color{j});
end

% Create Legend
```

```
zeroPad_legend = legend(zeroPad_axes,’show’);
% Force legend position, so as to avoid overlap with inset plot.
% Be careful to specify ’Fontsize’ before ’Position’ (which is also size) or
% Matlab may ignore the desired size if it is too small for the default
% font size that hasn’t been changed yet.
set(zeroPad_legend,’FontSize’,zeroPad_legendFontSize,’Position’,zeroPad_legendSize);

% Create main title
%title(’title of plot’);

% Trim down the excess space around the plot - whitespace management can be
% left to LaTeX.
set(zeroPad_axes, ’LooseInset’, [0,0,0,0]);

% Adjust the size and position of the overall figure, with regards to the
% printed output.
set(zeroPad_fig, ’PaperUnits’, ’inches’);
set(zeroPad_fig, ’PaperSize’, zeroPad_figSize); % [width height]
set(zeroPad_fig, ’PaperPositionMode’, ’manual’);
set(zeroPad_fig, ’PaperPosition’, [0 0 zeroPad_figSize(1) zeroPad_figSize(2)]);
% [left bottom width height]

% ’Print’ the figure to a PDF file
% See MathWorks website for more info on exporting figures:
% http://www.mathworks.com/help/matlab/creating_plots/...
%choosing-a-graphics-format.html#f3-103427
print(zeroPad_fig, ’-dpdf’, ’-painters’, ’-noui’, zeroPad_filename);
%print(fastOscCompare_fig, ’-djpeg100’,’myfile.jpg’)
% -dpdf for PDF, -depsc2 for EPS level 2 color and -deps2 for EPS level 2 B&W
% -painters sets to render using vector-based Painter’s algorithm
% -noui suppresses any user interface controls that may show up in figure
```

A.8 Function ‘peakAnalyzer.m’

This script was used for finding peaks in processed spectra.

```
function [ peakFreqs ] = peakAnalyzer(freq,signal,minFreq,maxFreq,...
peakThreshold,peakSpacing,manyPeaks)
%’peakAnalyzer’ performs spectral peak location and analysis
%   The function will accept signal and frequency datasets, find the peaks,
%   output their locations, make plots, etc.

% found helpful info on peak analysis, in general, at MathWorks website,
% link: http://www.mathworks.com/help/signal/examples/peak-analysis.html
% also, useful info on ’findpeaks’ MATLAB function, at:
% http://www.mathworks.com/help/signal/ref/findpeaks.html

% narrow down the size of the source data in ’signal’, using ’minFreq’ and
% ’maxFreq’ specified range
signal = signal(freq>=minFreq & freq<=maxFreq);
freq = freq(freq>=minFreq & freq<=maxFreq);

% look for peaks
[pks,locs] = findpeaks(signal,’MINPEAKHEIGHT’,peakThreshold,’MINPEAKDISTANCE’,...
```

```
peakSpacing,’NPEAKS’,manyPeaks);

% record the peak frequencies
peakFreqs = freq(locs);

% MAKE A PLOT OF THE ORIGINAL DATA AND THE FOUND PEAKS

% Create figure and name the window (separate from figure title)
peaks_fig = figure;
set(peaks_fig, ’Name’,’Plot of Spectrum and Found Peaks’,’NumberTitle’,’on’);

% Create main axes
peaks_axes = axes(’Parent’,peaks_fig);
set(peaks_axes, ’box’, ’on’);

% Format main axes (limits,labels, ticks)
%set(zeroPad_axes,’XLim’,zeroPad_axes_xLimits); % for adjustment of x-axis limits
%set(zeroPad_axes,’YLim’,zeroPad_axes_yLimits); % for adjustment of y-axis limits
%set(zeroPad_axes,’XTick’,zeroPad_axes_xLimits(1):zeroPad_axes_xStep:...
%zeroPad_axes_xLimits(2)) % set major ticks
set(get(peaks_axes,’XLabel’),’fontsize’, 12, ’fontname’, ’times’, ...
’fontweight’, ’bold’); % x-axis label size and font
set(get(peaks_axes,’YLabel’),’fontsize’, 12, ’fontname’, ’times’, ...
’fontweight’, ’bold’); % y-axis label size and font
set(get(peaks_axes,’XLabel’),’String’,’Frequency (THz)’); % x-axis label
set(get(peaks_axes,’YLabel’),’String’,’Relative Absorbance’); % y-axis label
% remove numbers from y-axis, as this plot is for qualitative, explanatory purposes
set(peaks_axes,’YTickLabel’,[])
set(peaks_axes,’XMinorTick’,’on’) % turn on minor ticks along the x-axis

% make a plot of the original data and the found peaks
hold(peaks_axes,’all’);
peaks_plot_spectrum = plot(freq,signal,’DisplayName’,’Spectrum’);
peaks_plot_foundPeaks = plot(freq(locs),pks,’rv’,’MarkerFaceColor’,’r’, ...
’DisplayName’,’Peaks’); grid on
xlabel(’Frequency (THz)’); ylabel(’Relative Absorbance’)
%title(’Find All Peaks’);

% label plot points
strValues = strtrim(cellstr(num2str(peakFreqs(:),4))); % #4 is for precision
text(freq(locs),pks,strValues,’VerticalAlignment’,’bottom’, ...
’HorizontalAlignment’,’Right’,’FontSize’,7,’Rotation’,89)
% Note that rotation for ’text’ directly above is set to 89, not 90, as 90
% triggers a rotation of the whole printed/PDF page.

% Create legend
peaks_legend = legend(peaks_axes,’show’);
%legend(’Spectrum’,’Peaks’)
% Set legend position, Positioning format is [left bottom width height]
set(peaks_legend,’FontSize’,6,’Position’,[0.4 0.87 0.2 0.1]);

% Trim down the excess space around the plot - whitespace management can be
% left to LaTeX.
set(peaks_axes, ’LooseInset’, [0,0,0,0]);

% Adjust the size and position of the overall figure, with regards to the
% printed output.
set(peaks_fig, ’PaperUnits’, ’inches’);
```

```
set(peaks_fig, 'PaperSize',[6 3]); % [width height]
set(peaks_fig, 'PaperPositionMode', 'manual');
set(peaks_fig, 'PaperPosition', [0 0 6 3]);
% [left bottom width height]

% 'Print' the figure to a PDF file
% See MathWorks website for more info on exporting figures:
% http://www.mathworks.com/help/matlab/creating_plots/...
%choosing-a-graphics-format.html#f3-103427
print(peaks_fig, '-dpdf', '-painters', '-noui', 'peakAnalyzer.pdf');
%print(fastOscCompare_fig, '-djpeg100','myfile.jpg')
% -dpdf for PDF, -depsc2 for EPS level 2 color and -deps2 for EPS level 2 B&W
% -painters sets to render using vector-based Painter's algorithm
% -noui suppresses any user interface controls that may show up in figure

end
```

A.9 Script ‘test_background.m’

This script was used for backgrounding acquired spectra and displaying this, as well as original data.

```
% This script is for processing raw time domain data and producing
% frequency domain data for both of reference and sample scans, as well as
% referenced sample data and plots for the above. This script is very
% similar to the 'test_timecut.m' and 'test_zeroPad.m' scripts with the
% main exceptions that it only evaluates one time-cut range and one level
% of zero-padding, and then produces figures geared for the purpose of
% looking at both of raw data (ref and samp) and referenced sample data in
% the frequency domain.

%% 'HOUSE-KEEPING'

% Clear out previous data and commands
clc % clear commands
clear % clear workspace
%close all % close all open figures

%% USER INPUTS

% INPUT FILENAMES
% Filename and Name for sample scan
filename_sample = 'cond_02_samp.mat';
name_sample = '2 Torr H2O';
% Filename and Name for reference scan
filename_ref = 'cond_02_ref.mat';
name_ref = 'Reference';
% Also note, original data, assumed to have 'M1' signal data (voltage) and
% 'T1' time axis data from digitizer (in units of seconds). And assumed
% that sample and reference data have same number of data points.

% DATA ACQUISITION PARAMETERS
rate_adc = 125; % digitizer (ADC) sampling rate in lab time (in MHz)
rate_pump = 79.9794; % pump laser repetition rate (in MHz)
rate_offset = 100; %rep rate difference between pump and probe lasers (Hz)
```

```

% TIME CUTTING OF SCANS
% in units of ps
time_delay_start = 0;
time_delay_stop = 5000;

% FFT PARAMETERS
num_zeroPad = 1; % argument for 'fft_plus' function, uses next power of 2 on pad
case_output = 3; % arg for 'fft_plus', sets output type, type 3 = power

% 'rawFFTCompare' FIGURE SETTING
% This figure compares the 'raw' (as in not yet referenced) reference and
% sample scans after FFT.
% output filename and figure size
rawFFT_filename = 'fig_rawFFTcompare';
% Note: size format is [width height] in inches
rawFFT_figSize = [6 4];
% 'timecutsCompare' plot x (freq in THz) and y limits
rawFFT_axes_xLimits = [0 4]; % [min max] for both figure and ticks
rawFFT_axes_xStep = 0.5; % major tick mark step size
rawFFT_axes_yLimits = [-6 0.5];
% Legend size and position.
% Positioning format is [left bottom width height]
rawFFT_legendSize = [0.2 0.2 0.2 0.1];
% Legend fontsize
rawFFT_legendFontSize = 7;

% 'refdScan' FIGURE SETTING
% This figure shows a wide bandwidth portion of a referenced sample scan.
% output filename and figure size
refdScan_filename = 'fig_refdScan';
% Note: size format is [width height] in inches
refdScan_figSize = [6 4];
% 'timecutsCompare' plot x (freq in THz) and y limits
refdScan_axes_xLimits = [0 3]; % [min max] for both figure and ticks
refdScan_axes_xStep = 0.5; % major tick mark step size
refdScan_axes_yLimits = [-.1 4];
% Legend size and position.
% Positioning format is [left bottom width height]
refdScan_legendSize = [0.2 0.2 0.2 0.1];
% Legend fontsize
refdScan_legendFontSize = 7;

%% LOAD DATA FILES

% Load scans' T1,M1 data into structures, one each for sample and ref. The
% use of structures avoids an issue with both scan files having 'M1' and
% 'Y1' workspace variables.
sample = load(filename_sample);
ref = load(filename_ref);

%% CREATE DELAY TIME AXIS, DETREND SIGNAL DATA

% CREATE DELAY TIME AXIS
% Calculate sampling rate in TSa/s given 'data acquisition parameters'
% specified above
rate_asops = asopsRate(rate_adc,rate_pump,rate_offset);
% Create timebase for time-domain data in terms of delay time (in ps),
```

```
% given sampling rate and length of sample signal (Y1) data; note it is up
% to user to make sure sample and reference scans have same number of
% points. Also note that because of this new timebase, the original ’T1’
% time data is not really required; though it can be useful to calculate
% the digitizer sampling rate if this is forgotten.
time_delay = timebase(rate_asops,length(sample.M1));

% DETREND THE DATA Before any FFT processing, it is often recommended to
% remove the mean value or linear trend from the signal data. This also
% helps for display purposes, in centering data (different scans) along y =
% 0 (across multiple scans).
samp_signal = detrend(sample.M1); % remove any linear trend
samp_signal = detrend(samp_signal, ’constant’); % remove mean value
ref_signal = detrend(ref.M1); % remove any linear trend
ref_signal = detrend(ref_signal, ’constant’); % remove mean value

%% PERFORM TIME CUTS, SHOW SIMPLE FIGURE FOR CHECKING

% PERFORM THE TIMECUT
[time_delay_part, samp_signal_part] = ...
timecut(time_delay,samp_signal,time_delay_start,time_delay_stop);
[time_delay_part, ref_signal_part] = ...
timecut(time_delay,ref_signal,time_delay_start,time_delay_stop);
% Note that it is OK to re-use time_delay_part between sample and ref
% cut-outs, as corresponding pairs of sample and ref will be the same.

% CREATE SIMPLE FIGURE FOR QUICK CHECKING OF TIMECUT
% Create figure and name the window (separate from figure title)
timecuts_fig = figure;
set(timecuts_fig, ’Name’,’Plot of time-cut for zero-pad test’,’NumberTitle’,’on’);
% Create the plot - full sample in red/back, full ref in blue/front and
% timecut portion in green/middle
timecuts_plot = plot(time_delay,samp_signal,’r’,time_delay_part,...
samp_signal_part,’g’,time_delay,ref_signal,’b’);
timecuts_legend = legend(’Full Sample Signal’,’Selected Sample Signal’, ...
’Full Ref Signal’);
%% FOURIER ANALYSIS
% Calculates the FFTs for sample and reference scans.

% Note that the ’freqaxis’ for both of ref and sample will be the same so
% it is OK to re-use. It is assumed herein, and coded as such, that ref and
% samp will be taken under exact same acquisition and rep rate parameters.

[ref_fft_part, freqaxis_part] = ...
fft_plus(ref_signal_part, rate_asops, num_zeroPad, case_output);
[samp_fft_part, freqaxis_part] = ...
fft_plus(samp_signal_part, rate_asops, num_zeroPad, case_output);

% Calculate the referenced data
% (using a reverse log base 10)
sratio_part = (-log10(samp_fft_part./ref_fft_part));

%% ’rawFFTCompare’ FIGURE - COMPARISON OF UN-REF’D, FFT’D REF, SAMPLE SCANS

% Create figure and name the window (separate from figure title)
rawFFT_fig = figure;
set(rawFFT_fig, ’Name’,’Plot of Differently Zero-Padded FFTs’,’NumberTitle’,’on’);

```

```
% Create main axes
rawFFT_axes = axes('Parent',rawFFT_fig);
set(rawFFT_axes, 'box', 'on');

% Plot the sample spectrum
zeroPad_plot_samp = plot(freqaxis_part,log10(samp_fft_part),...
'Parent',rawFFT_axes,'DisplayName',name_sample);
%zeroPad_plot_samp = ...
%semilogy(freqaxis_part,samp_fft_part,'Parent',rawFFT_axes,'DisplayName',name_sample);
hold(rawFFT_axes,'all');
% Plot the reference spectrum
zeroPad_plot_ref = ...
plot(freqaxis_part,log10(ref_fft_part),'Parent',rawFFT_axes,'DisplayName',name_ref);
%zeroPad_plot_ref = ...
%semilogy(freqaxis_part,ref_fft_part,'Parent',rawFFT_axes,'DisplayName',name_ref);

% Create Legend
zeroPad_legend = legend(rawFFT_axes,'show');
% Force legend position, so as to avoid overlap with inset plot.
% Be careful to specify 'Fontsize' before 'Position' (which is also size) or
% Matlab may ignore the desired size if it is too small for the default
% font size that hasn't been changed yet.
set(zeroPad_legend,'FontSize',rawFFT_legendFontSize,'Position',rawFFT_legendSize);

% Format main axes (limits,labels, ticks)
set(rawFFT_axes,'XLim',rawFFT_axes_xLimits); % for adjustment of x-axis limits
set(rawFFT_axes,'YLim',rawFFT_axes_yLimits); % for adjustment of y-axis limits
% set major ticks
set(rawFFT_axes,'XTick',rawFFT_axes_xLimits(1):rawFFT_axes_xStep:rawFFT_axes_xLimits(2))
% x-axis label size and font
set(get(rawFFT_axes,'XLabel'),'fontsize', 12, 'fontname', 'times', 'fontweight', 'bold');
% y-axis label size and font
set(get(rawFFT_axes,'YLabel'),'fontsize', 12, 'fontname', 'times', 'fontweight', 'bold');
set(get(rawFFT_axes,'XLabel'),'String','Frequency (THz)'); % x-axis label
set(get(rawFFT_axes,'YLabel'),'String','Log Relative Power (arb. u.)'); % y-axis label
% remove numbers from y-axis, as this plot is for qualitative, explanatory purposes
%set(rawFFT_axes,'YTickLabel',[])
set(rawFFT_axes,'XMinorTick','on') % turn on minor ticks along the x-axis
set(rawFFT_axes,'YMinorTick','on') % turn on minor ticks along the y-axis

% Create main title
%title('title of plot');

% Trim down the excess space around the plot - whitespace management can be
% left to LaTeX.
set(rawFFT_axes, 'LooseInset', [0,0,0,0]);

% Adjust the size and position of the overall figure, with regards to the
% printed output.
set(rawFFT_fig, 'PaperUnits', 'inches');
set(rawFFT_fig, 'PaperSize', rawFFT_figSize); % [width height]
set(rawFFT_fig, 'PaperPositionMode', 'manual');
set(rawFFT_fig, 'PaperPosition', [0 0 rawFFT_figSize(1) rawFFT_figSize(2)]);
% [left bottom width height]

% 'Print' the figure to a PDF file
% See MathWorks website for more info on exporting figures:
% http://www.mathworks.com/help/matlab/creating_plots/...
```

```
%choosing-a-graphics-format.html#f3-103427
print(rawFFT_fig, '-dpdf', '-painters', '-noui', rawFFT_filename);
%print(fastOscCompare_fig, '-djpeg100','myfile.jpg')
% -dpdf for PDF, -depsc2 for EPS level 2 color and -deps2 for EPS level 2 B&W
% -painters sets to render using vector-based Painter's algorithm
% -noui suppresses any user interface controls that may show up in figure

%% 'refdScan' FIGURE - REFERENCED, FFT'D SAMPLE SCAN DISPLAY

% Create figure and name the window (separate from figure title)
refdScan_fig = figure;
set(refdScan_fig, 'Name','Plot of Differently Zero-Padded FFTs','NumberTitle','on');

% Create main axes
refdScan_axes = axes('Parent',refdScan_fig);
set(refdScan_axes, 'box', 'on');

% Plot the referenced sample spectrum
refdScan_plot_sratio = plot(freqaxis_part,sratio_part,'k','Parent',refdScan_axes, ...
'DisplayName','Referenced Scan');
%hold(refdScan_axes,'all');

% Create Legend
%refdScan_legend = legend(refdScan_axes,'show');
% Force legend position, so as to avoid overlap with inset plot.
% Be careful to specify 'Fontsize' before 'Position' (which is also size) or
% Matlab may ignore the desired size if it is too small for the default
% font size that hasn't been changed yet.
%set(refdScan_legend,'FontSize',refdScan_legendFontSize,'Position',refdScan_legendSize);

% Format main axes (limits,labels, ticks)
set(refdScan_axes,'XLim',refdScan_axes_xLimits); % for adjustment of x-axis limits
set(refdScan_axes,'YLim',refdScan_axes_yLimits); % for adjustment of y-axis limits
set(refdScan_axes,'XTick',refdScan_axes_xLimits(1):refdScan_axes_xStep:...
refdScan_axes_xLimits(2)) % set major ticks
% x-axis label size and font
set(get(refdScan_axes,'XLabel'),'fontsize', 12, 'fontname', 'times', ...
'fontweight', 'bold');
% y-axis label size and font
set(get(refdScan_axes,'YLabel'),'fontsize', 12, 'fontname', 'times', ...
'fontweight', 'bold');
set(get(refdScan_axes,'XLabel'),'String','Frequency (THz)'); % x-axis label
set(get(refdScan_axes,'YLabel'),'String','Relative Absorbance'); % y-axis label
% remove numbers from y-axis, as this plot is for qualitative, explanatory purposes
%set(rawFFT_axes,'YTickLabel',[])
set(refdScan_axes,'XMinorTick','on') % turn on minor ticks along the x-axis
set(refdScan_axes,'YMinorTick','on') % turn on minor ticks along the y-axis

% Create main title
%title('title of plot');

% Trim down the excess space around the plot - whitespace management can be
% left to LaTeX.
set(refdScan_axes, 'LooseInset', [0,0,0,0]);

% Adjust the size and position of the overall figure, with regards to the
% printed output.
set(refdScan_fig, 'PaperUnits', 'inches');
```

```
set(refdScan_fig, 'PaperSize', refdScan_figSize); % [width height]
set(refdScan_fig, 'PaperPositionMode', 'manual');
set(refdScan_fig, 'PaperPosition', [0 0 refdScan_figSize(1) refdScan_figSize(2)]);
% [left bottom width height]

% 'Print' the figure to a PDF file
% See MathWorks website for more info on exporting figures:
% http://www.mathworks.com/help/matlab/creating_plots/...
%choosing-a-graphics-format.html#f3-103427
print(refdScan_fig, '-dpdf', '-painters', '-noui', refdScan_filename);
%print(fastOscCompare_fig, '-djpeg100','myfile.jpg')
% -dpdf for PDF, -depsc2 for EPS level 2 color and -deps2 for EPS level 2 B&W
% -painters sets to render using vector-based Painter's algorithm
% -noui suppresses any user interface controls that may show up in figure
```

A.10 Script 'test_apodize_field.m'

This script was used to test the effects of windowing or apodization in the time-domain, and for creating Figures 3.10 and 3.11 in §3.4.5. The code cuts out a portion of the time-domain data, first producing a simple plot of the original and cut-out data, so the user can confirm they have selected the desired portion of the time-domain record (e.g. the water FID emission following the main THz pulse). A second plot is created, showing a zoomed-in view of the selected data, overlaid with a window function, and the resulting windowed data. Both the windowed and un-windowed time-domain data are processed with the 'fft_plus.m' FFT function described in A.6. No referencing is performed, as it is expected that the typical usage case will involved the THz FID signal following a main THz pulse. The resulting electric field components of both datasets are plotted together in a third figure for comparison. This script was designed so that it can readily be utilized in future efforts towards optimizing THz FID measurements; these will almost certainly require such apodization.

```
% Script for performing FFT analysis with support for windowin/apodization.
% This code is meant for the calculation of sample field data; there is no
% provision for referencing or reference scans. Overall, code is meant for
% use on portion of waveform following initial THz pulse.

%% 'HOUSE-KEEPING'

% Clear out previous data and commands
clc % clear commands
clear % clear workspace
%close all % close all open figures

%% USER INPUTS

% INPUT FILENAMES
% Filename and Name for sample scan
```

```
filename_sample = ’cond_02_samp.mat’;
name_sample = ’˜2 Torr H2O’;
% Filename and Name for reference scan
filename_ref = ’cond_02_ref.mat’;
name_ref = ’Reference’;
% Also note, original data, assumed to have ’M1’ signal data (voltage) and
% ’T1’ time axis data from digitizer (in units of seconds). And assumed
% that sample and reference data have same number of data points.

% DATA ACQUISITION PARAMETERS
rate_adc = 125; % digitizer (ADC) sampling rate in lab time (in MHz)
rate_pump = 79.9794; % pump laser repetition rate (in MHz)
rate_offset = 100; %rep rate difference between pump and probe lasers (Hz)

% TIME CUTTING OF SCANS
% in units of ps
time_delay_start = 1775;
time_delay_stop = 3500;

% FFT AND WINDOW PARAMETERS
num_zeroPad = 4; % argument for ’fft_plus’ function, uses next power of 2 on pad
case_output = 2; % arg for ’fft_plus’, sets output type, type 2 = amplitude
windowParam = 1; %0 to 1, rect to Hann for @Tukey window

% ’winDataTime’ FIGURE SETTINGS
% output filename and figure size
winDataTime_filename = ’fig_winDataTime.pdf’;
% Note: size format is [width height] in inches
winDataTime_size = [6 3.5];
% ’winDataTime’ main plot x (time in ps) and y limits
winDataTime_xLimits = [1775 3500]; % [min max], match this with time cut
winDataTime_wave_yLimits = [-.000174 .0002]; % [min max]
winDataTime_win_yLimits = [-.1 1.1];
% legend position
winDataTime_legendSize = [.5 .17 .2 .1]; % [left bottom width height]
% legend fontsize
winDataTime_legendFontSize = 7;

% ’winDataFFT’ FIGURE SETTING
% This figure compares the FFT results for windowed and non-windowed
% waveforms.
% output filename and figure size
winDataFFT_filename = ’fig_winDataFFT.pdf’;
% Note: size format is [width height] in inches
winDataFFT_figSize = [6 3];
% ’timecutsCompare’ plot x (freq in THz) and y limits
winDataFFFT_axes_xLimits = [2.14 2.51]; % [min max] for both figure and ticks
winDataFFT_axes_xStep = 0.5; % major tick mark step size
winDataFFT_axes_yLimits = [-.434 .245];
% Legend size and position.
% Positioning format is [left bottom width height]
winDataFFT_legendSize = [.8 .782 .09 .08];
% Legend fontsize
winDataFFT_legendFontSize = 7;

%% LOAD DATA FILES

% Load scans’ T1,M1 data into structures, one each for sample and ref. The
```

```
% use of structures avoids an issue with both scan files having 'M1' and
% 'Y1' workspace variables.
sample = load(filename_sample);
ref = load(filename_ref);

%% CREATE DELAY TIME AXIS, DETREND SIGNAL DATA

% CREATE DELAY TIME AXIS
% Calculate sampling rate in TSa/s given 'data acquisition parameters'
% specified above
rate_asops = asopsRate(rate_adc,rate_pump,rate_offset);
% Create timebase for time-domain data in terms of delay time (in ps),
% given sampling rate and length of sample signal (Y1) data; note it is up
% to user to make sure sample and reference scans have same number of
% points. Also note that because of this new timebase, the original 'T1'
% time data is not really required; though it can be useful to calculate
% the digitizer sampling rate if this is forgotten.
time_delay = timebase(rate_asops,length(sample.M1));

% DETREND THE DATA Before any FFT processing, it is often recommended to
% remove the mean value or linear trend from the signal data. This also
% helps for display purposes, in centering data (different scans) along y =
% 0 (across multiple scans).
samp_signal = detrend(sample.M1); % remove any linear trend
samp_signal = detrend(samp_signal, 'constant'); % remove mean value
ref_signal = detrend(ref.M1); % remove any linear trend
ref_signal = detrend(ref_signal, 'constant'); % remove mean value

%% PERFORM TIME CUTS, SHOW SIMPLE FIGURE FOR CHECKING

% PERFORM THE TIMECUT
[time_delay_part, samp_signal_part] = ...
timecut(time_delay,samp_signal,time_delay_start,time_delay_stop);
[time_delay_part, ref_signal_part] = ...
timecut(time_delay,ref_signal,time_delay_start,time_delay_stop);
% Note that it is OK to re-use time_delay_part between sample and ref
% cut-outs, as corresponding pairs of sample and ref will be the same.

% CREATE SIMPLE FIGURE FOR QUICK CHECKING OF TIMECUT
% Create figure and name the window (separate from figure title)
timecuts_fig = figure;
set(timecuts_fig, 'Name','Plot of time-cut for checking','NumberTitle','on');
% Create the plot - full sample in red/back, full ref in blue/front and
% timecut portion in green/middle
timecuts_plot = plot(time_delay,samp_signal,'r',time_delay_part,samp_signal_part,'g', ...
time_delay,ref_signal,'b');
timecuts_legend = legend('Full Sample Signal','Selected Sample Signal', ...
'Full Ref Signal');

% Rescale time axis so it starts at zero
%time_delay_part = time_delay_part - time_delay_part(1);

%% FOURIER ANALYSIS W/ AND W/O WINDOWING/APODIZATION

% CREATE AND APPLY THE WINDOW
% Create the window function
%0 to 1, rect to Hann
time_window = window(@tukeywin,length(time_delay_part),windowParam);
```

```
time_window = time_window'; % transpose to row vector to match data
% apply window function calculated above
samp_signal_part_windowed = time_window.*samp_signal_part;

% Calculate the FFTs
% w/o windowing
[samp_fft freqaxis] = fft_plus(samp_signal_part, rate_asops, num_zeroPad, case_output);
% w/ windowing
[samp_fft_windowed freqaxis] = fft_plus(samp_signal_part_windowed, rate_asops, ...
num_zeroPad, case_output);
% Note that the 'freqaxis' for both of windowed and non-windowed data
% will be the same so it is OK to re-use. The windowing just scales the
% y-axis (signal) of the original time-domain data; the x-axis (timing)
% data is left alone.

%% 'winDataTime' - PLOT OF WINDOWING FUNCTION W/ ORIGINAL AND WINDOWED DATA

% plot the windowing function over the original data for checking
winDataTime_fig = figure;
set(winDataTime_fig, 'Name','Signal Data and Windowing','NumberTitle','on');

% Plot un-windowed data and window function together on double y-axis plot
% for more info on double y-axis plotting, see:
% http://www.mathworks.com/help/matlab/ref/plotyy.html
[winDataTime_axes,winDataTime_plot_prewin,winDataTime_plot_window] = ...
plotyy(time_delay_part,samp_signal_part,time_delay_part,time_window);
% Name the plots (for legend), (1) is non-windowed,(2) is the window
set(winDataTime_plot_prewin,'DisplayName','Un-Windowed Waveform');
set(winDataTime_plot_window,'DisplayName','Window Function');
% Add a plot for the windowed waveform
hold(winDataTime_axes(1),'all');
winDataTime_plot_postwin =
  plot(time_delay_part,samp_signal_part_windowed,'Parent',winDataTime_axes(1), ...
'Color',[1 0 0]);
set(winDataTime_plot_postwin,'DisplayName','Windowed Waveform');

% Create Legend
winDataTime_legend = legend(winDataTime_axes(1),'show');
set(winDataTime_legend,'FontSize',winDataTime_legendFontSize, ...
'Position',winDataTime_legendSize);

% Create main title
%title('Comparison of Signal Data and Window Function')

% Format main axes (limits,labels, ticks)
set(get(winDataTime_axes(1),'Ylabel'),'String','Electric Field (arb. u.)')
set(get(winDataTime_axes(2),'Ylabel'),'String','Window Function')
set(get(winDataTime_axes(1),'XLabel'),'String','Time(ps)'); % x-axis label
% for adjustment of x-axis limits,apparently don't need to specify (1)or(2)
set(winDataTime_axes,'XLim',winDataTime_xLimits);
% for adjustment of y-axis limits, on waveform axis
set(winDataTime_axes(1),'YLim',winDataTime_wave_yLimits);
% for adjustment of y-axis limits, on window axis
set(winDataTime_axes(2),'YLim',winDataTime_win_yLimits);
set(get(winDataTime_axes(1),'XLabel'),'fontsize', 12, 'fontname', 'times', ...
'fontweight', 'bold'); % x-axis label size and font
set(get(winDataTime_axes(1),'YLabel'),'fontsize', 12, 'fontname', 'times', ...
'fontweight', 'bold'); % y-axis label size and font
```

```
set(get(winDataTime_axes(2),'YLabel'),'fontsize', 12, 'fontname', 'times', ...
'fontweight', 'bold'); % y-axis label size and font
% turn on minor ticks along the x-axis
set(winDataTime_axes(1),'XMinorTick','on')
% turn on minor ticks along the y-axis for the window function
set(winDataTime_axes(2),'YMinorTick','on')
% remove numbers from y-axis, as this plot is for qualitative, explanatory purposes
set(winDataTime_axes(1),'YTickLabel',[])
%set(winDataTime_axes(2),'YTickLabel',[])

%set(handle_data,'LineStyle','--')
%set(handle_window,'LineStyle',':')

% Trim down the excess space around the plot - whitespace management can be
% left to LaTeX.
%set(winDataTime_axes, 'LooseInset', [0,0,0,0]);

% Adjust the size and position of the overall figure, with regards to the
% printed output.
set(winDataTime_fig, 'PaperUnits', 'inches');
set(winDataTime_fig, 'PaperSize', winDataTime_size); % [width height]
set(winDataTime_fig, 'PaperPositionMode', 'manual');
%set(winDataTime_fig, 'PaperPosition', [0 0.1*winDataTime_size(2) ...
% winDataTime_size(1) 0.9*winDataTime_size(2)]);
set(winDataTime_fig, 'PaperPosition', [0 0 winDataTime_size(1) winDataTime_size(2)]);
% [left bottom width height]

% 'Print' the figure to an EPS file Note: MathWorks recommends exporting as
% EPS for publication-quality graphics, see their website for more info on
% exporting figures:
% http://www.mathworks.com/help/matlab/creating_plots/...
%choosing-a-graphics-format.html#f3-103427
print(winDataTime_fig, '-dpdf', '-painters', '-noui', winDataTime_filename);
%print(fastOscCompare_fig, '-djpeg100','myfile.jpg')
% -dpdf for PDF, -depsc2 for EPS level 2 color and -deps2 for EPS level 2 B&W
% -painters sets to render using vector-based Painter's algorithm
% -noui suppresses any user interface controls that may show up in figure


%% 'winDataFFT' FIGURE - PLOT OF FFT RESULTS OF WINDOWED AND NON-WINDOWED DATA

% Create figure and name the window (separate from figure title)
windataFFT_fig = figure;
set(windataFFT_fig, 'Name','Plot of (Un-)Windowed Data','NumberTitle','on');

% Create main axes
winDataFFT_axes = axes('Parent',windataFFT_fig);
set(winDataFFT_axes, 'box', 'on');

% Plot the un-windowed spectrum
winDataFFT_plot_nowin = plot(freqaxis,samp_fft,'Parent',winDataFFT_axes, ...
'DisplayName','Un-Windowed Spectrum');
hold(winDataFFT_axes,'all');
% Plot the windowed spectrum
winDataFFT_plot_win = plot(freqaxis,samp_fft_windowed,'Parent',winDataFFT_axes, ...
'DisplayName','Windowed Spectrum');

% Create Legend
```

```
winDataFFT_legend = legend(winDataFFT_axes,'show');
% Force legend position, so as to avoid overlap with inset plot.
% Be careful to specify 'Fontsize' before 'Position' (which is also size) or
% Matlab may ignore the desired size if it is too small for the default
% font size that hasn't been changed yet.
set(winDataFFT_legend,'FontSize',winDataFFT_legendFontSize,'Position', ...
winDataFFT_legendSize);

% Format main axes (limits,labels, ticks)
set(winDataFFT_axes,'XLim',winDataFFFT_axes_xLimits); % for adjustment of x-axis limits
%set(winDataFFT_axes,'YLim',winDataFFFT_axes_yLimits); % for adjustment of y-axis limits
%set(winDataFFT_axes,'XTick',winDataFFFT_axes_xLimits(1):winDataFFFT_axes_xStep:...
%winDataFFFT_axes_xLimits(2)) % set major ticks
% x-axis label size and font
set(get(winDataFFT_axes,'XLabel'),'fontsize', 12, 'fontname', 'times', 'fontweight', 'bold');
% y-axis label size and font
set(get(winDataFFT_axes,'YLabel'),'fontsize', 12, 'fontname', 'times', 'fontweight', 'bold');
set(get(winDataFFT_axes,'XLabel'),'String','Frequency (THz)'); % x-axis label
set(get(winDataFFT_axes,'YLabel'),'String','Electric Field (arb. u.)'); % y-axis label
set(winDataFFT_axes,'YTickLabel',[]) % remove numbers from y-axis, as this plot is for qualitative, explanatory purposes
set(winDataFFT_axes,'XMinorTick','on') % turn on minor ticks along the x-axis
set(winDataFFT_axes,'YMinorTick','on') % turn on minor ticks along the y-axis

% Create main title
%title('title of plot');

% Trim down the excess space around the plot - whitespace management can be
% left to LaTeX.
set(winDataFFT_axes, 'LooseInset', [0,0,0,0]);

% Adjust the size and position of the overall figure, with regards to the
% printed output.
set(windataFFT_fig, 'PaperUnits', 'inches');
set(windataFFT_fig, 'PaperSize', winDataFFT_figSize); % [width height]
set(windataFFT_fig, 'PaperPositionMode', 'manual');
set(windataFFT_fig, 'PaperPosition', [0 0 winDataFFT_figSize(1) winDataFFT_figSize(2)]);
% [left bottom width height]

% 'Print' the figure to a PDF file
% See MathWorks website for more info on exporting figures:
% http://www.mathworks.com/help/matlab/creating_plots/...
%choosing-a-graphics-format.html#f3-103427
print(windataFFT_fig, '-dpdf', '-painters', '-noui', winDataFFT_filename);
%print(fastOscCompare_fig, '-djpeg100','myfile.jpg')
% -dpdf for PDF, -depsc2 for EPS level 2 color and -deps2 for EPS level 2 B&W
% -painters sets to render using vector-based Painter's algorithm
% -noui suppresses any user interface controls that may show up in figure
```

A.11 MATLAB Code for Linewidth Measurement

In §3.5.4, a water vapor spectral line was fit to a Lorentzian curve. This section of the appendix contains the two additional pieces of code, one script and one function, that were required for that analysis and the generation of Figure 3.16. As noted previously, the scan data was referenced with the use of ‘test_background.m’ script (also included in the appendix, §A.9). Following the completion of that script, the referenced scan data remained in the MATLAB workspace. The script included immediately below, ‘test_linewidth.m’ was then used to select two different spectral regions, each about a different peak of interest; the analysis of only the first of these peaks was shown in the main text, though both yielded similar linewidths. The script then passed the isolated peak data on to a fitting and figure plotting function, ‘peakOne_createFit.m’, also included below.

Before the call to the fitting/plotting function was included in the present script, the peak data of interest about 1.153 THz was fit with the graphical user interface of MATLAB’s Curve Fitting Toolbox, version 3.3.1. The option to use a ’custom equation’ was chosen as a standard Lorentzian curve was not available; the custom Lorentzian equation entered is listed in line # 19 of the function code below, and matches the Lorentzian equation in Equation 3.49 in the main text. The MATLAB toolbox used a nonlinear least squares method in the fitting; new ’StartPoint’ values were entered to achieve a fit. The ‘Generate Code’ option was then used to a create function that would repeat the same analysis. With some modification for printing, this auto-generated code became the ‘peakOne_createFit.m’ function included below.

It should be noted that the ‘peakOne_createFit.m’ function is presently designed for the particular peak studied and shown in Figure 3.16; certain values, such as the starting guesses in the curve fitting and the axes ranges for the figure, were hard-coded. However, with some straightforward modifications, these pieces of code could be modified to handle the automatic peak fitting of many peaks. New code could be designed to look for peaks on a supplied list, or the code could find peaks on its own and calculate starting guesses for the fitting. This would be of use to further checks on the spectral resolution performance of the instrument, as well as in automating the generation of experimental line lists and measurements of pressure-broadening, for example.

A.11.1 Script ‘test_linewidth.m’ for Linewidth Measurement

```matlab
% script to fit the Lorentzian linewidth of a pair of water vapor lines,
% already prepared in the Matlab workspace by the test_background.m script

% Two peaks:
% Peak One at 1.153 THz, range around = 1.149 to 1.157
% Peak Two at 1.229 THz, range around = 1.223 to 1.235
```

```
% Peak data should already be in the 'freqaxis_part' and 'sratio_part'
% workspace variables, as prepared by test_background.m script.

% Peak information (frequencies in THz)
% for peak one
peakOne_low = 1.149;
peakOne_high = 1.157;
% for peak two
peakTwo_low = 1.223;
peakTwo_high = 1.235;

% Extract just the peak area data into new variables
% Peak One
peakOne_freqaxis = freqaxis_part((freqaxis_part > peakOne_low)&(freqaxis_part <
  peakOne_high));
peakOne_sratio = sratio_part((freqaxis_part > peakOne_low)&(freqaxis_part <
  peakOne_high));
% Peak Two
peakTwo_freqaxis = freqaxis_part((freqaxis_part > peakTwo_low)&(freqaxis_part <
  peakTwo_high));
peakTwo_sratio = sratio_part((freqaxis_part > peakTwo_low)&(freqaxis_part <
  peakTwo_high));

% To verify have selected right time portions
figure
plot(peakOne_freqaxis,peakOne_sratio)
figure
plot(peakTwo_freqaxis,peakTwo_sratio)

% Used MATLAB's 'cftool' Curve-fitting tool, via its graphical interface.
% After fitting peak one, saved the fitting session, but also used the
% 'generate code' option to create a function, 'peakOne_createFit.m' that
% automatically performs the fit and produces a figure and prints out fit
% results (or returns to variables, depending on how the function is
% called).
peakOne_createFit(peakOne_freqaxis,peakOne_sratio)
% Modified this function above for better-lookig plot output.

% Used the fitting session of peak one as a template for peak two, merely
% adjusting the starting points (under 'Fit Options...') for the center and
% linewidth parameters. Fit results were good and linewidth similar at ~100
% MHz (fitting session saved). Could similarly create a function for peak
% two. However, general solution is to modify the 'peakOne_createFit'
% function for general use, adding function parameters so can pass initial
% guesses (or otherwise, add code so it can do better on its own). And also
% would need to adjust plotting features. Then could do large amounts of
% automated peak fitting.
```

A.11.2 Function ‘peakOne_createFit.m’ for a Lorentzian Fit to a Peak

```
function [fitresult, gof] = peakOne_createFit(peakOne_freqaxis, peakOne_sratio)
%CREATEFIT(PEAKONE_FREQAXIS,PEAKONE_SRATIO)
%  Create a fit.
%
```

```
%  Data for ’untitled fit 1’ fit:
%      X Input : peakOne_freqaxis
%      Y Output: peakOne_sratio
%  Output:
%      fitresult : a fit object representing the fit.
%      gof : structure with goodness-of fit info.
%
%  See also FIT, CFIT, SFIT.

% Note by Dan Holland, modified for better plotting
%% Fit: ’untitled fit 1’.
[xData, yData] = prepareCurveData( peakOne_freqaxis, peakOne_sratio );

% Set up fittype and options.
ft = fittype( ’(a*pi)*(g/2)./((g/2)ˆ2+(x-v).ˆ2)’, ’independent’, ’x’, ’dependent’, ’y’ );
opts = fitoptions( ft );
opts.Display = ’Off’;
opts.Lower = [-Inf -Inf -Inf];
opts.StartPoint = [0.9649 0.0001 1.153];
opts.Upper = [Inf Inf Inf];

% Fit model to data.
[fitresult, gof] = fit( xData, yData, ft, opts );

% Plot fit with data.
figure( ’Name’, ’Fitting Results and Fitted Data’ );
h = plot( fitresult, xData, yData );
set(gca, ’box’, ’on’);
grid off
legend( h, ’H20 Spectrum’, ’Lorentzian Fit’, ’Location’, ’NorthEast’ );
set(gca,’YLim’,[-0.1 2]); % for adjustment of y-axis limits
set(gca,’XLim’,[1.149 1.157]); % for adjustment of x-axis limits
set(gca,’XMinorTick’,’on’) % turn on minor ticks along the x-axis
set(gca,’YMinorTick’,’on’) % turn on minor ticks along the y-axis
% Label axes
set(gca,’YTickLabel’,[]) % remove numbers from y-axis, as this plot is for qualitative, explanatory purposes
set(get(gca,’XLabel’),’fontsize’, 12, ’fontname’, ’times’, ’fontweight’, ’bold’); % x-axis label size and font
set(get(gca,’YLabel’),’fontsize’, 12, ’fontname’, ’times’, ’fontweight’, ’bold’); % y-axis label size and font
set(get(gca,’XLabel’),’String’,’Frequency (THz)’); % x-axis label
set(get(gca,’YLabel’),’String’,’Relative Absorbance’); % y-axis label

% Trim down the excess space around the plot - whitespace management can be
% left to LaTeX.
set(gca, ’LooseInset’, [0,0,0,0]);

% Adjust the size and position of the overall figure, with regards to the
% printed output. Note, ’gcf’ call ’Gets the Current Figure’ handle.
set(gcf, ’PaperUnits’, ’inches’);
set(gcf, ’PaperSize’, [6 3]); % [width height]
set(gcf, ’PaperPositionMode’, ’manual’);
set(gcf, ’PaperPosition’, [0 0 6 3]);
% [left bottom width height]

% ’Print’ the figure to a PDF file
% See MathWorks website for more info on exporting figures:
```

```
% http://www.mathworks.com/help/matlab/creating_plots/...
%choosing-a-graphics-format.html#f3-103427
print(gcf, '-dpdf', '-painters', '-noui', 'peakOne_create.pdf');
%print(fastOscCompare_fig, '-djpeg100','myfile.jpg')
% -dpdf for PDF, -depsc2 for EPS level 2 color and -deps2 for EPS level 2 B&W
% -painters sets to render using vector-based Painter's algorithm
% -noui suppresses any user interface controls that may show up in figure
```

Bibliography

[1] Finneran, Ian A., D. B. Holland, P. B. Carroll, and G. A. Blake, "Development of a reduced-cost chirped pulse microwave spectrometer," in *The 68th Ohio State University International Symposium on Molecular Spectroscopy*, Columbus, Ohio, Jun. 2013, Oral Presentation. [Online]. Available: https://molspect.chemistry.ohio-state.edu/symposium/Abstracts/p515.html

[2] I. A. Finneran, D. B. Holland, P. B. Carroll, and G. A. Blake, "A direct digital synthesis chirped pulse Fourier transform microwave spectrometer," *Review of Scientific Instruments*, vol. 84, no. 8, p. 083104, 2013. [Online]. Available: http://link.aip.org/link/RSINAK/v84/i8/p083104/s1&Agg=doi

[3] J.-Y. Yu, C.-H. Kuo, D. B. Holland, Y. Chen, M. Ouyang, G. A. Blake, R. Zadoyan, and C.-L. Guo, "Wide-field optical sectioning for live-tissue imaging by plane-projection multiphoton microscopy," *Journal of Biomedical Optics*, vol. 16, no. 11, p. 116009, 2011.

[4] J.-Y. Yu, D. B. Holland, G. A. Blake, and C.-L. Guo, "The wide-field optical sectioning of microlens array and structured illumination-based plane-projection multiphoton microscopy," *Optics Express*, vol. 21, no. 2, pp. 2097–2109, Jan. 2013. [Online]. Available: http://www.opticsexpress.org/abstract.cfm?URI=oe-21-2-2097

[5] Yu, Jiun-Yann, D. Holland, G. Blake, and C.-L. Guo, "Temporal focusing generated via a height-staggered microlens array can be used for wide-field optical-sectioning microscopy," in *Conference on Lasers and Electro-Optics (CLEO) 2013*, San Jose, CA, Jun. 2013.

[6] Yu, Jiun-Yann, D. Holland, G. A. Blake, and C.-L. Guo, "Temporal focusing with structured illumination can be applied for high-frame-rate, wide-field optical-sectioning multiphoton microscopy," in *Focus on Microscopy 2013 Conference*, Maastricht, the Netherlands, Mar. 2013, Oral Presentation.

[7] Trivedi, V., T. V. Truong, L. A. Trinh, D. B. Holland, M. Liebling, and S. E. Fraser, "Dynamic three-dimensional imaging of developing zebrafish heart reveals changes in cellular shapes and gene expressions," in *The American Society for Cell Biology Annual Meeting*, San Francisco, CA, USA, Dec. 2012, Poster.

[8] Trivedi, V., T. Truong, L. Trinh, D. Holland, M. Liebling, and S. Fraser, “Dynamic three-dimensional imaging of cellular shape changes and gene expressions in the developing zebrafish heart,” in *EMBO Conference Series Morphogenesis and Dynamics of Multicellular Systems*, Heidelberg, Germany, Sep. 2012, Poster.

[9] Trivedi, Vikas, T. V. Truong, L. A. Trinh, D. B. Holland, M. Liebling, and S. E. Fraser, “Dynamic three-dimensional imaging of cellular shape changes and protein expression in the developing zebrafish heart,” in *57th Annual Meeting of the Biophysical Society*, Philadelphia, PA, USA, Feb. 2013, Oral Presentation. [Online]. Available: http://bps2013.conferencespot.org/1036-Plat/

[10] Truong, T. V., V. Trivedi, D. B. Holland, and S. E. Fraser, “Imaging proteins, cells, and tissues dynamics during embryogenesis with two-photon light sheet microscopy,” in *The American Society for Cell Biology Annual Meeting*, San Francisco, CA, USA, Dec. 2012, Poster.

[11] Truong, Thai V., D. B. Holland, V. Trivedi, and S. E. Fraser, “Imaging proteins, cells, and tissues dynamics during embryogenesis with two-photon light-sheet microscopy,” in *57th Annual Meeting of the Biophysical Society*, Philadelphia, PA, USA, Feb. 2013, Poster. [Online]. Available: http://bps2013.conferencespot.org/1726-Pos

[12] Truong, Thai V, V. Trivedi, L. Trinh, D. Holland, F. Cutrale, J. Choi, and S. E. Fraser, “Live 4D imaging of embryonic vertebrate heart with two-photon light sheet microscopy,” in *EMBO—EMBL Symposium: Seeing is Believing Imaging the Processes of Life*, Heidelberg, Germany, Oct. 2013, Poster Presentation.

[13] A. I. McIntosh, B. Yang, S. M. Goldup, M. Watkinson, and R. S. Donnan, “Terahertz spectroscopy: a powerful new tool for the chemical sciences?” *Chemical Society Reviews*, vol. 41, no. 6, pp. 2072–2082, Feb. 2012. [Online]. Available: http://pubs.rsc.org/en/content/articlelanding/2012/cs/c1cs15277g

[14] G. Sucha, “Rapid scanning time delays for ultrafast measurement systems,” in *Ultrafast Lasers: Technology and Applications*, ser. Optical Science and Engineering, M. E. Fermann, A. Galvanauskas, and G. Sucha, Eds. CRC Press, 2002, pp. 419–471.

[15] G. Klatt, R. Gebs, H. Schafer, M. Nagel, C. Janke, A. Bartels, and T. Dekorsy, “High-resolution terahertz spectrometer,” *Selected Topics in Quantum Electronics, IEEE Journal of*, no. 99, p. 110, 2011. [Online]. Available: http://ieeexplore.ieee.org/xpls/abs_all.jsp?arnumber=5487397

[16] R. Zhou, Z. Jin, G. Li, G. Ma, Z. Cheng, and X. Wang, “Terahertz magnetic field induced coherent spin precession in YFeO3,” *Applied Physics Letters*, vol. 100, no. 6, pp. 061 102–061 102–4, Feb. 2012. [Online]. Available: http://apl.aip.org/resource/1/applab/v100/i6/p061102_s1

[17] F. A. Miller, “Far infra-red spectroscopy,” in *Molecular Spectroscopy*. The Institute of Petroleum, 1968, pp. 5–27.

[18] L. Rothman, I. Gordon, Y. Babikov, A. Barbe, D. Chris Benner, P. Bernath, M. Birk, L. Bizzocchi, V. Boudon, L. Brown, A. Campargue, K. Chance, E. Cohen, L. Coudert, V. Devi, B. Drouin, A. Fayt, J.-M. Flaud, R. Gamache, J. Harrison, J.-M. Hartmann, C. Hill, J. Hodges, D. Jacquemart, A. Jolly, J. Lamouroux, R. Le Roy, G. Li, D. Long, O. Lyulin, C. Mackie, S. Massie, S. Mikhailenko, H. Mller, O. Naumenko, A. Nikitin, J. Orphal, V. Perevalov, A. Perrin, E. Polovtseva, C. Richard, M. Smith, E. Starikova, K. Sung, S. Tashkun, J. Tennyson, G. Toon, V. Tyuterev, and G. Wagner, “The HITRAN2012 molecular spectroscopic database,” *Journal of Quantitative Spectroscopy and Radiative Transfer*, vol. 130, pp. 4–50, Nov. 2013. [Online]. Available: http://linkinghub.elsevier.com/retrieve/pii/S0022407313002859

[19] P. F. Bernath, *Spectra of atoms and molecules*, ser. Topics in physical chemistry. New York: Oxford University Press, 1995.

[20] T. Phillips and J. Keene, “Submillimeter astronomy [heterodyne spectroscopy],” *Proceedings of the IEEE*, vol. 80, no. 11, pp. 1662–1678, Nov. 1992.

[21] J. Or, “Comets and the formation of biochemical compounds on the primitive earth,” *Nature*, vol. 190, no. 4774, pp. 389–390, Apr. 1961.

[22] various authors, “List of interstellar and circumstellar molecules,” 2014. [Online]. Available: http://en.wikipedia.org/wiki/List_of_interstellar_and_circumstellar_molecules

[23] M. Ohishi, “Observations of hot cores,” *IAU Symp.*, vol. 178, pp. 61–74, 1997.

[24] S. Widicus-Weaver and G. Blake, “1,3-dihydroxyacetone in sgr b2(n-LMH): the first interstellar ketose,” *Ap. J. (Letters)*, vol. 624, pp. L33–36, 2005.

[25] N. R. Crockett, E. A. Bergin, S. Wang, D. C. Lis, T. A. Bell, G. A. Blake, A. Boogert, B. Bumble, S. Cabrit, E. Caux, C. Ceccarelli, J. Cernicharo, C. Comito, F. Daniel, M.-L. Dubernet, M. Emprechtinger, P. Encrenaz, E. Falgarone, M. Gerin, T. F. Giesen, J. R. Goicoechea, P. F. Goldsmith,

H. Gupta, R. Gsten, P. Hartogh, F. Helmich, E. Herbst, N. Honingh, C. Joblin, D. Johnstone, A. Karpov, J. H. Kawamura, J. Kooi, J.-M. Krieg, W. D. Langer, W. D. Latter, S. D. Lord, S. Maret, P. G. Martin, G. J. Melnick, K. M. Menten, P. Morris, H. S. P. Mller, J. A. Murphy, D. A. Neufeld, V. Ossenkopf, J. C. Pearson, M. Prault, T. G. Phillips, R. Plume, S.-L. Qin, P. Roelfsema, R. Schieder, P. Schilke, S. Schlemmer, J. Stutzki, F. F. S. van der Tak, A. Tielens, N. Trappe, C. Vastel, H. W. Yorke, S. Yu, and J. Zmuidzinas, "Herschel observations of EXtra-Ordinary sources (HEXOS): the terahertz spectrum of orion KL seen at high spectral resolution," *Astronomy and Astrophysics*, vol. 521, p. L21, Oct. 2010.

[26] M. C. Beard, G. M. Turner, and C. A. Schmuttenmaer, "Terahertz spectroscopy," *The Journal of Physical Chemistry B*, vol. 106, no. 29, pp. 7146 – 7159, 2002. [Online]. Available: http://pubs.acs.org/doi/abs/10.1021/jp020579i

[27] P. Jepsen, D. Cooke, and M. Koch, "Terahertz spectroscopy and imaging - modern techniques and applications," *Laser & Photonics Reviews*, vol. 5, no. 1, pp. 124–166, Jan. 2011. [Online]. Available: http://doi.wiley.com/10.1002/lpor.201000011

[28] C. Ruchert, C. Vicario, and C. P. Hauri, "Spatiotemporal focusing dynamics of intense supercontinuum THz pulses," *Physical Review Letters*, vol. 110, no. 12, p. 123902, Mar. 2013. [Online]. Available: http://link.aps.org/doi/10.1103/PhysRevLett.110.123902

[29] Q. Wu, M. Litz, and X.-C. Zhang, "Broadband detection capability of ZnTe electro-optic field detectors," *Applied Physics Letters*, vol. 68, p. 2924, 1996. [Online]. Available: http://link.aip.org/link/APPLAB/v68/i21/p2924/s1&Agg=doi

[30] P. C. M. Planken, H.-K. Nienhuys, H. J. Bakker, and T. Wenckebach, "Measurement and calculation of the orientation dependence of terahertz pulse detection in ZnTe," *Journal of the Optical Society of America B*, vol. 18, no. 3, pp. 313–317, Mar. 2001. [Online]. Available: http://josab.osa.org/abstract.cfm?URI=josab-18-3-313

[31] Q. Wu and X.-C. Zhang, "7 terahertz broadband GaP electro-optic sensor," *Applied Physics Letters*, vol. 70, no. 14, pp. 1784–1786, Apr. 1997. [Online]. Available: http://apl.aip.org/resource/1/applab/v70/i14/p1784_s1

[32] A. Dreyhaupt, S. Winnerl, T. Dekorsy, and M. Helm, "High-intensity terahertz radiation from a microstructured large-area photoconductor," *Applied Physics Letters*, vol. 86, p. 121114, 2005. [Online]. Available: http://link.aip.org/link/APPLAB/v86/i12/p121114/s1&Agg=doi

[33] M. A. Allodi, S. Ioppolo, M. J. Kelley, B. A. McGuire, and G. A. Blake, "The structure and dynamics of carbon dioxide and water containing ices investigated via THz and mid-IR spectroscopy," *Physical Chemistry Chemical Physics*, vol. 16, no. 8, pp. 3442–3455, Jan. 2014. [Online]. Available: http://pubs.rsc.org/en/content/articlelanding/2014/cp/c3cp53767f

[34] M. v. Exter, C. Fattinger, and D. Grischkowsky, "Highbrightness terahertz beams characterized with an ultrafast detector," *Applied Physics Letters*, vol. 55, no. 4, pp. 337–339, Jul. 1989.

[35] M. Van Exter and D. Grischkowsky, "Characterization of an optoelectronic terahertz beam system," *IEEE Transactions on Microwave Theory and Techniques*, vol. 38, no. 11, pp. 1684–1691, 1990.

[36] M. v. Exter, C. Fattinger, and D. Grischkowsky, "Terahertz time-domain spectroscopy of water vapor," *Optics Letters*, vol. 14, no. 20, pp. 1128–1130, Oct. 1989. [Online]. Available: http://ol.osa.org/abstract.cfm?URI=ol-14-20-1128

[37] P. Y. Han, M. Tani, M. Usami, S. Kono, R. Kersting, and X. C. Zhang, "A direct comparison between terahertz time-domain spectroscopy and far-infrared Fourier transform spectroscopy," *Journal of Applied Physics*, vol. 89, no. 4, pp. 2357–2359, Feb. 2001.

[38] M. A. Allodi, R. A. Baragiola, G. A. Baratta, M. A. Barucci, G. A. Blake, P. Boduch, J. R. Brucato, C. Contreras, S. H. Cuylle, D. Fulvio, M. S. Gudipati, S. Ioppolo, Z. Kauchov, A. Lignell, H. Linnartz, M. E. Palumbo, U. Raut, H. Rothard, F. Salama, E. V. Savchenko, E. Sciamma-OBrien, and G. Strazzulla, "Complementary and emerging techniques for astrophysical ices processed in the laboratory," *Space Science Reviews*, vol. 180, no. 1-4, pp. 101–175, Dec. 2013. [Online]. Available: http://link.springer.com/article/10.1007/s11214-013-0020-8

[39] D. C. Edelstein, R. B. Romney, and M. Scheuermann, "Rapid programmable 300 ps optical delay scanner and signal-averaging system for ultrafast measurements," *Review of Scientific Instruments*, vol. 62, no. 3, p. 579, 1991. [Online]. Available: http://link.aip.org/link/RSINAK/v62/i3/p579/s1&Agg=doi

[40] A. Bartels, R. Cerna, C. Kistner, A. Thoma, F. Hudert, C. Janke, and T. Dekorsy, "Ultrafast time-domain spectroscopy based on high-speed asynchronous optical sampling," *Review of Scientific Instruments*, vol. 78, p. 035107, 2007. [Online]. Available: http://link.aip.org/link/RSINAK/v78/i3/p035107/s1&Agg=doi

[41] G. Klatt, R. Gebs, C. Janke, T. Dekorsy, and A. Bartels, "Rapid-scanning terahertz precision spectrometer with more than 6 THz spectral coverage," *Optics Express*, vol. 17, no. 25, pp.

22 847–22 854, Dec. 2009. [Online]. Available: http://www.opticsexpress.org/abstract.cfm?URI=oe-17-25-22847

[42] R. Gebs, G. Klatt, C. Janke, T. Dekorsy, and A. Bartels, “High-speed asynchronous optical sampling with sub-50fs time resolution,” *Optics Express*, vol. 18, no. 6, pp. 5974–5983, Mar. 2010. [Online]. Available: http://www.opticsexpress.org/abstract.cfm?URI=oe-18-6-5974

[43] H. V. Malmstadt, H. V. Enke, S. R. Crouch, and G. Horlick, *Optimization of Electronic Measurements*, ser. The Malmstadt-Enke Instrumentation for Scientists Series. Menlo Park, Calif: W. A. Benjamin, 1974, vol. 4.

[44] P. Elzinga, F. Lytle, Y. Jian, G. King, and N. Laurendeau, “Pump probe spectroscopy by asynchronous optical-sampling,” *Applied Spectroscopy*, vol. 41, no. 1, pp. 2–4, Jan. 1987.

[45] P. A. Elzinga, R. J. Kneisler, F. E. Lytle, Y. Jiang, G. B. King, and N. M. Laurendeau, “Pump/probe method for fast analysis of visible spectral signatures utilizing asynchronous optical sampling,” *Applied Optics*, vol. 26, no. 19, pp. 4303–4309, Oct. 1987. [Online]. Available: http://ao.osa.org/abstract.cfm?URI=ao-26-19-4303

[46] J. D. Kafka, J. W. Pieterse, and M. L. Watts, “Two-color subpicosecond optical sampling technique,” *Optics Letters*, vol. 17, no. 18, pp. 1286–1288, 1992. [Online]. Available: http://ol.osa.org/abstract.cfm?URI=ol-17-18-1286

[47] C. Janke, M. Frst, M. Nagel, H. Kurz, and A. Bartels, “Asynchronous optical sampling for high-speed characterization of integrated resonant terahertz sensors,” *Optics letters*, vol. 30, no. 11, pp. 1405 – 1407, 2005.

[48] T. Yasui, E. Saneyoshi, and T. Araki, “Asynchronous optical sampling terahertz time-domain spectroscopy for ultrahigh spectral resolution and rapid data acquisition,” *Applied Physics Letters*, vol. 87, no. 6, p. 061101, Aug. 2005.

[49] M. Brown, G. Fiechtner, J. Rudd, D. Zimdars, M. Warmuth, and J. Gord, “Water-vapor detection using asynchronous THz sampling,” *Applied spectroscopy*, vol. 60, no. 3, pp. 261 – 265, 2006.

[50] A. Bartels, A. Thoma, C. Janke, T. Dekorsy, A. Dreyhaupt, S. Winnerl, and M. Helm, “High-resolution THz spectrometer with kHz scan rates,” *Optics Express*, vol. 14, no. 1, pp. 430–437, Jan. 2006. [Online]. Available: http://www.opticsexpress.org/abstract.cfm?URI=oe-14-1-430

[51] P. Goldsmith, *Quasioptical systems: Gaussian beam quasioptical propagation and applications*. Piscataway NJ: IEEE Press, 1998.

[52] R. Shelton, “Active phase stabilization, synchronization and phase locking of mode locked Ti:Sapphire lasers,” Ph.D. dissertation, University of Michigan, 2002.

[53] S. M. Foreman, “Femtosecond frequency combs for optical clocks and timing transfer,” Ph.D. dissertation, University of Colorado, Boulder, 2007.

[54] (2010) AD9912 data sheet. Analog Devices. [Online]. Available: http://www.analog.com/static/imported-files/data_sheets/AD9912.pdf

[55] T. C. Briles, D. C. Yost, A. Cingz, J. Ye, and T. R. Schibli, “Simple piezoelectric-actuated mirror with 180 kHz servo bandwidth,” *Optics Express*, vol. 18, no. 10, pp. 9739–9746, May 2010. [Online]. Available: http://www.opticsexpress.org/abstract.cfm?URI=oe-18-10-9739

[56] F. Peter, S. Winnerl, S. Nitsche, A. Dreyhaupt, H. Schneider, and M. Helm, “Coherent terahertz detection with a large-area photoconductive antenna,” *Applied Physics Letters*, vol. 91, no. 8, Aug. 2007.

[57] X.-C. Zhang and J. Xu, *Introduction to THz wave photonics*. New York: Springer, 2010.

[58] J. H. Moore, C. C. Davis, and M. A. Coplan, *Building Scientific Apparatus*, 3rd ed. Westview Press, 2002.

[59] M. Naftaly and R. Dudley, “Terahertz reflectivities of metal-coated mirrors,” *Applied Optics*, vol. 50, no. 19, pp. 3201 – 3204, 2011.

[60] T. Bauer, J. S. Kolb, T. Loffler, E. Mohler, H. G. Roskos, and U. C. Pernisz, “Indium-tin-oxide-coated glass as dichroic mirror for far-infrared electromagnetic radiation,” *Journal of Applied Physics*, vol. 92, no. 4, p. 2210, 2002. [Online]. Available: http://link.aip.org/link/JAPIAU/v92/i4/p2210/s1&Agg=doi

[61] Y. Shen, T. Watanabe, D. A. Arena, C.-C. Kao, J. B. Murphy, T. Y. Tsang, X. J. Wang, and G. L. Carr, “Nonlinear cross-phase modulation with intense single-cycle terahertz pulses,” *Physical Review Letters*, vol. 99, no. 4, p. 043901, Jul. 2007. [Online]. Available: http://link.aps.org/doi/10.1103/PhysRevLett.99.043901

[62] P. F. Bernath, “The spectroscopy of water vapour: Experiment, theory and applications,” *Physical Chemistry Chemical Physics*, vol. 4, no. 9, pp. 1501–1509, Apr. 2002. [Online]. Available: http://xlink.rsc.org/?DOI=b200372d

[63] P. Hamm and M. Zanni, *Concepts and Methods of 2D Infrared Spectroscopy*. Cambridge University Press, 2011.

[64] E. Hecht, "The superposition of waves," in *Optics*, 4th ed. Reading, Mass: Addison-Wesley, 2002, ch. 7, pp. 281–324.

[65] ——, "Wave motion," in *Optics*, 4th ed. Reading, Mass: Addison-Wesley, 2002, ch. 2, pp. 10–35.

[66] G. B. Arfken and H.-J. Weber, *Mathematical methods for physicists*, 5th ed. San Diego: Harcourt/Academic Press, 2001.

[67] G. P. Tolstov and R. A. Silverman, *Fourier series*. New York: Dover, 1976.

[68] M. Born and E. Wolf, *Principles of optics: electromagnetic theory of propagation, interference and diffraction of light*, 7th ed. Cambridge ; New York: Cambridge University Press, 1999.

[69] J. Shan, J. I. Dadap, and T. F. Heinz, "Circularly polarized light in the single-cycle limit: The nature of highly polychromatic radiation of defined polarization," *Optics Express*, vol. 17, no. 9, pp. 7431–7439, Apr. 2009. [Online]. Available: http://www.opticsexpress.org/abstract.cfm?URI=oe-17-9-7431

[70] G. Arjavalingam, Y. Pastol, J. M. Halbout, and G. Kopcsay, "Broad-band microwave measurements with transient radiation from optoelectronically pulsed antennas," *IEEE Transactions on Microwave Theory and Techniques*, vol. 38, no. 5, pp. 615–621, 1990.

[71] M. Tani, Y. Hirota, C. Que, S. Tanaka, R. Hattori, M. Yamaguchi, S. Nishizawa, and M. Hangyo, "Novel terahertz photoconductive antennas," *International Journal of Infrared and Millimeter Waves*, vol. 27, no. 4, pp. 531–546, 2006. [Online]. Available: http://www.springerlink.com/content/d65l1077375r108w/abstract/

[72] E. Hecht, *Optics*, 4th ed. Reading Mass.: Addison-Wesley, 2002.

[73] M. Krger, S. Funkner, E. Brndermann, and M. Havenith, "Uncertainty and ambiguity in terahertz parameter extraction and data analysis," *Journal of Infrared, Millimeter, and Terahertz Waves*, vol. 32, no. 5, pp. 699–715, 2011. [Online]. Available: http://link.springer.com/10.1007/s10762-010-9669-1

[74] L. Duvillaret, F. Garet, and J. Coutaz, "A reliable method for extraction of material parameters in terahertz time-domain spectroscopy," *Selected Topics in Quantum Electronics, IEEE Journal of*, vol. 2, no. 3, pp. 739 – 746, 1996.

[75] P. U. Jepsen and B. M. Fischer, “Dynamic range in terahertz time-domain transmission and reflection spectroscopy,” *Optics letters*, vol. 30, no. 1, pp. 29 – 31, 2005. [Online]. Available: http://www.opticsinfobase.org/abstract.cfm?id=82107

[76] I. Pupeza, R. Wilk, and M. Koch, “Highly accurate optical material parameter determination with THz time-domain spectroscopy,” *Optics Express*, vol. 15, no. 7, pp. 4335–4350, Apr. 2007. [Online]. Available: http://www.opticsexpress.org/abstract.cfm?URI=oe-15-7-4335

[77] G. M. Alber and A. G. Marshall, “Effect of sampling rate on Fourier transform spectra: Oversampling is overrated,” *Applied Spectroscopy*, vol. 44, no. 7, pp. 1111–1116, Jul. 1990. [Online]. Available: http://as.osa.org/abstract.cfm?URI=as-44-7-1111

[78] L. J. Karssemeijer, S. Ioppolo, M. C. v. Hemert, A. v. d. Avoird, M. A. Allodi, G. A. Blake, and H. M. Cuppen, “Dynamics of CO in amorphous water-ice environments,” *The Astrophysical Journal*, vol. 781, no. 1, p. 16, Jan. 2014. [Online]. Available: http://iopscience.iop.org/0004-637X/781/1/16

[79] MATLAB, *MATLAB Release R2013a (version 8.1.0.604 win64).* Natick, Massachusetts: The MathWorks, Inc., 2013.

[80] C. S. Burrus, T. W. Parks, and J. F. Potts, *DFT/FFT and convolution algorithms: theory and implementation*, ser. Topics in digital signal processing. New York: Wiley, 1984.

[81] (2014) Fast Fourier transform. MathWorks Inc. [Online]. Available: http://www.mathworks.com/help/matlab/math/fast-fourier-transform-fft.html

[82] (2014) fft: Fast Fourier transform. MathWorks Inc. [Online]. Available: http://www.mathworks.com/help/matlab/ref/fft.html

[83] M. Frigo and S. G. Johnson. (2014) FFTW home page. [Online]. Available: http://www.fftw.org/

[84] ——, “FFTW: an adaptive software architecture for the FFT,” *Proceedings of the International Conference on Acoustics, Speech, and Signal Processing*, vol. 3, pp. 1381–1384, 1998.

[85] J. W. Cooley and J. W. Tukey, “An algorithm for the machine computation of the complex Fourier series,” *Mathematics of Computation*, vol. 19, pp. 297–301, Apr. 1965.

[86] (2014) Power spectral density estimates using FFT. MathWorks Inc. [Online]. Available: http://www.mathworks.com/help/signal/ug/psd-estimate-using-fft.html

[87] Unpacking the MATLAB fft. University of Oregon Seismology Group. [Online]. Available: http://blogs.uoregon.edu/seis/wiki/unpacking-the-matlab-fft/

[88] (2014) Amplitude estimation and zero padding. MathWorks Inc. [Online]. Available: http://www.mathworks.com/help/signal/ug/amplitude-estimation-and-zero-padding.html

[89] (2014) Hann (hanning) window-MATLAB hann. MathWorks Inc. [Online]. Available: http://www.mathworks.com/help/signal/ref/hann.html

[90] (2014) HITRAN on the web: Home page. Harvard-Smithsonian Center for Astrophysics and V.E. Zuev Institute of Atmospheric Optics. [Online]. Available: http://hitran.iao.ru/

[91] H. Pickett, R. Poynter, E. Cohen, M. Delitsky, J. Pearson, and H. Muller, "Submillimeter, millimeter, and microwave spectral line catalog," *Journal of Quantitative Spectroscopy and Radiative Transfer*, vol. 60, pp. 883–90, 1998.

[92] L. Rothman, C. Rinsland, A. Goldman, S. Massie, D. Edwards, J.-M. Flaud, A. Perrin, C. Camy-Peyret, V. Dana, J.-Y. Mandin, J. Schroeder, A. McCann, R. Gamache, R. Wattson, K. Yoshino, K. Chance, K. Jucks, L. Brown, V. Nemtchinov, and P. Varanasi, "The HITRAN molecular spectroscopic database and HAWKS (HITRAN atmospheric workstation): 1996 edition," *Journal of Quantitative Spectroscopy and Radiative Transfer*, vol. 60, no. 5, pp. 665–710, Nov. 1998. [Online]. Available: http://www.sciencedirect.com/science/article/pii/S0022407398000788

[93] L. Rothman, D. Jacquemart, A. Barbe, D. Chris Benner, M. Birk, L. Brown, M. Carleer, C. Chackerian, K. Chance, L. Coudert, V. Dana, V. Devi, J.-M. Flaud, R. Gamache, A. Goldman, J.-M. Hartmann, K. Jucks, A. Maki, J.-Y. Mandin, S. Massie, J. Orphal, A. Perrin, C. Rinsland, M. Smith, J. Tennyson, R. Tolchenov, R. Toth, J. Vander Auwera, P. Varanasi, and G. Wagner, "The HITRAN 2004 molecular spectroscopic database," *Journal of Quantitative Spectroscopy and Radiative Transfer*, vol. 96, no. 2, pp. 139–204, Dec. 2005. [Online]. Available: http://linkinghub.elsevier.com/retrieve/pii/S0022407305001081

[94] E. W. Weisstein, "Lorentzian function – from Wolfram MathWorld." [Online]. Available: http://mathworld.wolfram.com/LorentzianFunction.html

[95] D. A. McQuarrie, *Statistical mechanics*. Sausalito, Calif: University Science Books, 2000.

[96] D. L. Goodstein, *States of matter*. Mineola, N.Y.: Dover Publications, 2002.

[97] A. J. Minnich, J. A. Johnson, A. J. Schmidt, K. Esfarjani, M. S. Dresselhaus, K. A. Nelson, and G. Chen, “Thermal conductivity spectroscopy technique to measure phonon mean free paths,” *Physical Review Letters*, vol. 107, no. 9, p. 095901, 2011. [Online]. Available: http://link.aps.org/doi/10.1103/PhysRevLett.107.095901

[98] G. Pernot, M. Stoffel, I. Savic, F. Pezzoli, P. Chen, G. Savelli, A. Jacquot, J. Schumann, U. Denker, I. Mnch, C. Deneke, O. G. Schmidt, J. M. Rampnoux, S. Wang, M. Plissonnier, A. Rastelli, S. Dilhaire, and N. Mingo, “Precise control of thermal conductivity at the nanoscale through individual phonon-scattering barriers,” *Nat Mater*, vol. 9, no. 6, pp. 491–495, Jun. 2010. [Online]. Available: http://dx.doi.org/10.1038/nmat2752

[99] A. J. Minnich, “Exploring electron and phonon transport at the nanoscale for thermoelectric energy conversion,” Ph.D. dissertation, Massachusetts Institute of Technology, 2011. [Online]. Available: http://dspace.mit.edu/handle/1721.1/67593

[100] A. J. Schmidt, “Optical characterization of thermal transport from the nanoscale to the macroscale,” Ph.D. dissertation, Massachusetts Institute of Technology, 2008. [Online]. Available: http://dspace.mit.edu/handle/1721.1/44798

[101] D. G. Cahill, “Analysis of heat flow in layered structures for time-domain thermoreflectance,” *Review of Scientific Instruments*, vol. 75, no. 12, pp. 5119–5122, Dec. 2004. [Online]. Available: http://scitation.aip.org/content/aip/journal/rsi/75/12/10.1063/1.1819431

[102] A. J. Schmidt, X. Chen, and G. Chen, “Pulse accumulation, radial heat conduction, and anisotropic thermal conductivity in pump-probe transient thermoreflectance,” *Review of Scientific Instruments*, vol. 79, p. 114902, 2008. [Online]. Available: http://link.aip.org/link/RSINAK/v79/i11/p114902/s1&Agg=doi

[103] V. A. Stoica, Y.-M. Sheu, D. A. Reis, and R. Clarke, “Wideband detection of transient solid-state dynamics using ultrafast fiber lasers and asynchronous optical sampling,” *Optics Express*, vol. 16, no. 4, pp. 2322–2335, Feb. 2008. [Online]. Available: http://www.opticsexpress.org/abstract.cfm?URI=oe-16-4-2322

[104] M. Mauck, “Knife-edge profiling of q-switched Nd:YAG laser beam and waist,” *Applied Optics*, vol. 18, no. 5, pp. 599–600, 1979.

[105] J. M. Khosrofian and B. A. Garetz, “Measurement of a gaussian laser beam diameter through the direct inversion of knife-edge data,” *Applied Optics*, vol. 22, no. 21, pp. 3406–3410, Nov. 1983. [Online]. Available: http://ao.osa.org/abstract.cfm?URI=ao-22-21-3406

[106] M. A. de Araujo, R. Silva, E. de Lima, D. P. Pereira, and P. C. de Oliveira, “Measurement of gaussian laser beam radius using the knife-edge technique: improvement on data analysis,” *Applied Optics*, vol. 48, no. 2, pp. 393–396, Jan. 2009. [Online]. Available: http://ao.osa.org/abstract.cfm?URI=ao-48-2-393

[107] M. G. Holland, “Phonon scattering in semiconductors from thermal conductivity studies,” *Physical Review*, vol. 134, no. 2A, p. A471, 1964. [Online]. Available: http://prola.aps.org/abstract/PR/v134/i2A/pA471_1

[108] G. A. Prinz, “Magnetoelectronics,” *Science*, vol. 282, no. 5394, pp. 1660–1663, Nov. 1998. [Online]. Available: http://www.sciencemag.org/content/282/5394/1660

[109] M. R. Freeman and Z. Diao, “Spintronics: All-optical spin-wave control,” *Nature Photonics*, vol. 6, no. 10, pp. 643 – 645, 2012. [Online]. Available: http://www.nature.com/nphoton/journal/v6/n10/full/nphoton.2012.241.html

[110] T. Satoh, Y. Terui, R. Moriya, B. A. Ivanov, K. Ando, E. Saitoh, T. Shimura, and K. Kuroda, “Directional control of spin-wave emission by spatially shaped light,” *Nature Photonics*, vol. 6, no. 10, pp. 662–666, 2012. [Online]. Available: http://www.nature.com/nphoton/journal/v6/n10/full/nphoton.2012.218.html

[111] J. Nishitani, K. Kozuki, T. Nagashima, and M. Hangyo, “Terahertz radiation from coherent antiferromagnetic magnons excited by femtosecond laser pulses,” *Applied Physics Letters*, vol. 96, no. 22, p. 221906, 2010. [Online]. Available: http://link.aip.org/link/APPLAB/v96/i22/p221906/s1&Agg=doi

[112] M. Nakajima, A. Namai, S. Ohkoshi, and T. Suemoto, “Ultrafast time domain demonstration of bulk magnetization precession at zero magnetic field ferromagnetic resonance induced by terahertz magnetic field,” *Optics Express*, vol. 18, no. 17, pp. 18 260–18 268, Aug. 2010. [Online]. Available: http://www.opticsexpress.org/abstract.cfm?URI=oe-18-17-18260

[113] M. Massaouti, J.-M. Manceau, A. Selimis, and S. Tzortzakis, “An intense tunable femtosecond gas-plasma THz source: Application in spectroscopic studies of polycyclic aromatic hydrocarbons,”

Journal of Molecular Structure, vol. 1006, no. 1-3, pp. 28–33, Dec. 2011. [Online]. Available: http://linkinghub.elsevier.com/retrieve/pii/S0022286011004637

[114] S. Ahmed, J. Savolainen, and P. Hamm, “Detectivity enhancement in THz electrooptical sampling,” *Review of Scientific Instruments*, vol. 85, no. 1, p. 013114, Jan. 2014. [Online]. Available: http://scitation.aip.org/content/aip/journal/rsi/85/1/10.1063/1.4862657

[115] F. D. Brunner, J. A. Johnson, S. Grubel, A. Ferrer, S. L. Johnson, and T. Feurer, “Distortion-free enhancement of terahertz signals measured by electro-optic sampling. i. theory,” *JOSA B*, vol. 31, no. 4, pp. 904 – 910, 2014. [Online]. Available: http://www.opticsinfobase.org/abstract.cfm?uri=josab-31-4-904

[116] J. A. Johnson, F. D. Brunner, S. Grubel, A. Ferrer, S. L. Johnson, and T. Feurer, “Distortion-free enhancement of terahertz signals measured by electro-optic sampling. II. experiment,” *JOSA B*, vol. 31, no. 5, pp. 1035 – 1040, 2014. [Online]. Available: http://www.opticsinfobase.org/josab/upcoming_pdf.cfm?id=204877

[117] P. D. Cunningham, N. N. Valdes, F. A. Vallejo, L. M. Hayden, B. Polishak, X.-H. Zhou, J. Luo, A. K.-Y. Jen, J. C. Williams, and R. J. Twieg, “Broadband terahertz characterization of the refractive index and absorption of some important polymeric and organic electro-optic materials,” *Journal of Applied Physics*, vol. 109, no. 4, p. 043505, 2011. [Online]. Available: http://scitation.aip.org/content/aip/journal/jap/109/4/10.1063/1.3549120

[118] D. G. Melnik, T. A. Miller, and F. C. De Lucia, “Observation of bands among the four lowest pseudorotational states of 1,3-dioxolane,” *Journal of Molecular Spectroscopy*, vol. 221, no. 2, pp. 227–238, Oct. 2003. [Online]. Available: http://linkinghub.elsevier.com/retrieve/pii/S0022285203002236

[119] D. G. Melnik, S. Gopalakrishnan, T. A. Miller, and F. C. De Lucia, “The absorption spectroscopy of the lowest pseudorotational states of tetrahydrofuran,” *The Journal of Chemical Physics*, vol. 118, no. 8, p. 3589, 2003. [Online]. Available: http://link.aip.org/link/JCPSA6/v118/i8/p3589/s1&Agg=doi

[120] V. M. Rayon and J. A. Sordo, “Pseudorotation motion in tetrahydrofuran: An ab initio study,” *The Journal of Chemical Physics*, vol. 122, no. 20, p. 204303, 2005. [Online]. Available: http://link.aip.org/link/JCPSA6/v122/i20/p204303/s1&Agg=doi

[121] W. J. Lafferty, D. W. Robinson, R. V. S. Louis, J. W. Russell, and H. L. Strauss, “Far-infrared spectrum of tetrahydrofuran: Spectroscopic evidence for pseudorotation,” *The*

Journal of Chemical Physics, vol. 42, no. 8, p. 2915, 1965. [Online]. Available: http://link.aip.org/link/JCPSA6/v42/i8/p2915/s1&Agg=doi

[122] G. G. Engerholm, “Ring puckering in five-membered rings. II. the microwave spectrum, dipole moment, and barrier to pseudorotation in tetrahydrofuran,” *The Journal of Chemical Physics*, vol. 50, no. 6, p. 2446, 1969. [Online]. Available: http://link.aip.org/link/?JCP/50/2446/1&Agg=doi